Light-powered transmission in a bioinspired synthetic nerve



Charlotte Hoskin

Brasenose College

University of Oxford

A thesis submitted for the degree of

Doctor of Philosophy

Hilary Term 2021

Declaration

All work described within this thesis was carried out under the supervision of Professor Hagan Bayley, at the University of Oxford between July 2017 and April 2021. I declare that I am the sole author of this thesis and, except where otherwise stated, it describes exclusively my own research. I confirm that I have not previously submitted the work in this thesis for any other degree at the University of Oxford or at any other institution.

Charlotte Hoskin, 21st April 2021

Acknowledgements

I wish to thank the following people who contributed to the production of this thesis:

Firstly, Professor Hagan Bayley for the opportunity to join his group and whose creative and meticulous approach to science greatly advanced my development.

My special thanks go to Dr Vanessa Restrepo Schild for being a brilliant mentor, colleague and friend. For her invaluable assistance, encouragement and guidance in both the writing of this thesis and throughout the experimental work which preceded it.

Also thank you to my collaborators: Dr Javier Vinals, Dr Idil Cazimoglu and Dr Assala Al Samad for preparing and sharing key materials; Dr David Lunn and Dr Juan Liu for their creative input in the project; Professor Claire Vallance and Dr Linna Zhou for experimental assistance; the Chemistry Department Workshops for technical support; and my parents for proofreading this thesis.

To the funding bodies who enabled this research: the Biotechnology and Biological Sciences Research Council (BBSRC) and Engineering and Physical Sciences Research Council (EPSRC).

To Professor Elspeth Garman for her constant support, kindness and for being an inspiring presence throughout my time in Brasenose College.

To the Bayley and Booth groups, for insightful discussions and for being a joy to work with (particularly those in LG7). To all the lab friendships (Brian, Flo, Idil, Jack, Jeff, Juan, Matt, Mike, Pablo, Rav, Sandra, Thomas, Vane, Yujia) for the advice, encouragement and support both in and out of the lab. Additionally, to Sandra, Matt and Ale for helping me organise the lab retreats, sorry for roping you into it.

Finally, thanks to all my family and friends for their support during my DPhil. In particular to my parents, for their love and the never-ending supply of coffee and cake when writing in lockdown, to Antonin, Idil and Tanja for their friendships and humour, and to Emma and Weez for being my most enthusiastic cheerleaders. A special mention to all the people I met through sport at Oxford, in particular the OULC blues! To my fellow OAPs, Zoe and Molly for being such great (wine-loving) friends and Ziski for cycling round Oxfordshire in circles with me in lockdown. Also to OUTC and Georgie for the countless walks and cups of tea lounging in the clubhouse. Lastly, to my fellow SynBios (namely Gareth and Jesus) for their incredible friendships and continuous encouragement largely via dinners, beers and memes.

Abstract

Electronic devices which seamlessly interface with living tissues have considerable potential. However, conventional technologies are restricted by inherent mechanical, chemical, and electrical differences which exist at the biotic-abiotic interface. Innovative approaches are therefore required to overcome these limitations and enhance device functionality. This thesis details the fabrication of a new bioelectronic device - a synthetic nerve - which is soft, tetherless, and powered by light. Imitating neurobiological architectures, the synthetic (non-living) nerve is a cable-like bundle of synthetic axons that conveys sensory information over centimetre distances. The components of the neural device are nanolitre aqueous droplets and hydrogel fibres, connected through functionalised lipid bilayers. At the sensory end of the synthetic nerve, signalling is initiated by photochemically-driven proton pumps: archaerhodopsin-3 and bacteriorhodopsin. Following rapid phototransduction, bioelectrical signals are directionally transmitted along the conducting axon and into the synaptic terminals. Mimicking natural cells, chemical neurotransmitters are then released from these synaptic terminals, initiating functional outputs downstream. In this way, signalling within the synthetic nerve resembles the electrochemical communication used by living cells: conducting ions and translocating molecules in the process (albeit using different mechanisms). Parallel transmission of discrete electrochemical signals can be achieved by patterning the conducting pathways in 3-dimensions. Finally, photoinduced communication is demonstrated in a simple hybrid tissue. These light-powered synthetic nerves are a valuable contribution to the development of electrode-free, soft bioelectronics for applications in medicine, robotics or computing.

Contents

List of Abbreviations **x**

1 Introduction **1**
1.1 Biological membranes . . . 2
1.1.1 Structure . . . 2
1.1.2 Transport . . . 5
1.1.3 Electrochemical gradients . . . 6
1.2 Biological communication . . . 7
1.3 Synthetic cell mimics . . . 9
1.3.1 Droplet-based cells . . . 11
1.3.1.1 Droplet interface bilayers . . . 11
1.3.1.2 Droplet hydrogel bilayers . . . 12
1.3.1.3 Tuning the membrane . . . 13
1.3.1.4 Functional droplet bilayers . . . 14
1.3.2 Alternative synthetic cells . . . 17
1.4 Synthetic Tissues . . . 18
1.4.1 Constructing droplet networks . . . 18
1.4.2 Functional droplet networks . . . 20
1.5 Remote control . . . 23
1.6 Thesis Summary . . . 26

2 A Photosensing Module **28**
2.1 Introduction . . . 30
2.1.1 Photoreceptors . . . 30
2.1.2 Microbial rhodopsins . . . 31
2.1.3 Optogenetics . . . 39
2.1.4 Voltage Indicators . . . 40
2.1.5 Biosensors and Bioelectronics . . . 41
2.2 Results . . . 42
2.2.1 Materials preparation . . . 42
2.2.2 Light-driven proton pumps . . . 42
2.2.2.1 Bacteriorhodopsin . . . 42

2.2.2.2 Archaerhodopsin-3 . . . 44
2.2.3 Ion-conducting protein pores . . . 46
2.2.3.1 Alpha-hemolysin . . . 46
2.2.4 System design . . . 46
2.2.4.1 Photosensory module formation . . . 46
2.2.4.2 Electrical characterisation . . . 47
2.2.4.3 LED . . . 52
2.2.4.4 Environment . . . 53
2.2.4.5 Optical monitoring of pumping . . . 53
2.2.5 bR photosensory modules . . . 56
2.2.5.1 Sigma-bR output . . . 56
2.2.5.2 PM-bR output . . . 57
2.2.5.3 Orientation . . . 59
2.2.6 CM-aR3 photosensory modules . . . 60
2.2.6.1 CM-aR3 output . . . 61
2.2.6.2 Orientation . . . 62
2.2.6.3 Optimisation . . . 64
2.2.6.4 Characterisation . . . 72
2.2.7 EC-aR3 photosensory modules . . . 79
2.2.7.1 Oligomerisation . . . 79
2.2.7.2 EC-aR3 output . . . 80
2.2.7.3 Orientation . . . 81
2.2.7.4 Proton pumping . . . 83
2.2.8 Photosensory module comparison . . . 85
2.2.9 Quantitation of CM-aR3 in a photosensory module . . . 85
2.2.9.1 CM-aR3 trimer area . . . 85
2.2.9.2 Number of CM-aR3 trimers in solution . . . 86
2.2.9.3 Protein packing into the bilayer . . . 87
2.2.9.4 Summary of potential limitations . . . 89
2.2.9.5 Quantitation of proton pumping . . . 91
2.2.10 Chromophores . . . 91
2.2.11 Spectral mutant library . . . 94
2.2.11.1 Library design . . . 94
2.2.12 Proton release complex . . . 101
2.2.12.1 Mutations . . . 102
2.2.12.2 Proton pumping . . . 103
2.2.12.3 Time resolved absorption . . . 104
2.3 Conclusions . . . 106

3 A Synthetic Neuron **107**

3.1 Introduction . . . 109

3.1.1 Bioelectricity . . . 109

3.1.2 Signalling and communication in neurons . . . 111

3.1.3 Signalling and communication in synthetic cells . . . 113

3.1.4 Bioelectronics . . . 117

3.1.4.1 Bioelectric medicine . . . 117

3.1.4.2 Soft robotics . . . 120

3.1.4.3 Computing . . . 122

3.2 Results . . . 123

3.2.1 Design of a synthetic neuron . . . 123

3.2.2 Protein preparation and insertion . . . 126

3.2.3 Photosensory receptors . . . 127

3.2.3.1 Rapid pulse generation . . . 127

3.2.3.2 Wireless detection of signal transduction . . . 131

3.2.4 Signal transmission . . . 132

3.2.4.1 Biobattery . . . 132

3.2.4.2 Directional signalling over centimetre distances . . . 133

3.2.4.3 Different signalling mechanism . . . 141

3.2.5 Neurotransmission . . . 144

3.2.5.1 A synthetic synapse . . . 144

3.2.5.2 Protons as transmitters . . . 145

3.2.5.3 MANT-dATP as a neurotransmitter . . . 146

3.2.5.4 Chemical neurotransmission . . . 147

3.2.5.5 Electrochemical communication . . . 149

3.2.6 Downstream signalling . . . 152

3.2.6.1 A neighbouring cell . . . 153

3.2.6.2 Triggering a downstream response . . . 154

3.2.7 Synthetic myelination . . . 156

3.2.8 Device lifetime . . . 159

3.2.8.1 Photobleaching . . . 159

3.2.8.2 Synthetic neuron storage . . . 162

3.2.8.3 Improving stability using a copolymer . . . 163

3.3 Conclusion . . . 166

4 A Synthetic Nerve **167**
4.1 Introduction . . . 169
4.1.1 Patterning . . . 169
4.1.2 Synthetic nerves . . . 170
4.1.3 Hybrid Tissues . . . 171
4.2 Results . . . 172
4.2.1 Design of a synthetic nerve . . . 172
4.2.2 Constructing a synthetic nerve . . . 173
4.2.3 Stimulus patterning . . . 174
4.2.4 Photosensory droplet patterning . . . 175
4.2.5 A hybrid tissue . . . 180
4.3 Conclusion . . . 185

5 Future work **187**
5.1 Sensory transduction in a synthetic tissue . . . 188
5.1.1 Enhancing photosensory module functionality . . . 188
5.1.1.1 Strategies to increase protein insertion . . . 188
5.1.1.2 Alternative photosensory systems . . . 190
5.1.2 Alternative modules for neuronal stimulation . . . 191
5.1.3 Multi-responsive synthetic tissues . . . 192
5.2 Synthetic Tissue functionality . . . 192
5.2.1 Miniaturisation of the synthetic nerve . . . 192
5.2.2 Bio-mimetic mechanism of signal transmission . . . 193
5.2.3 Synthetic nerves for *in situ* biosynthesis . . . 193
5.2.4 Synthetic Organs . . . 194
5.2.5 Transfer to an aqueous environment . . . 194
5.2.6 Using synthetic nerves in hybrid tissues . . . 195
5.3 Synthetic tissue longevity . . . 197
5.3.1 Methods to enhance synthetic tissue stability . . . 197
5.3.1.1 Adding PEGylated lipids . . . 197
5.3.1.2 Using block copolymers . . . 198
5.3.1.3 Including an emulsion stabiliser . . . 198
5.3.2 Bioresorbable devices . . . 198
5.3.3 Methods to increase the lifetime of a synthetic nerve . . . 199
5.3.3.1 Addition of an uncoupler . . . 199
5.3.3.2 Incorporating ATP synthesis machinery into the structure . . . 199

6 Materials and Methods **201**
6.1 Materials . . . 201
6.2 Aqueous solutions . . . 202
6.3 Protein preparation . . . 203
6.4 Mutagenesis . . . 209
6.5 Dye and polymer preparation . . . 210
6.6 Lipid-in-oil solutions . . . 212
6.7 Chamber and cast design . . . 213
6.8 Absorbance . . . 216
6.9 Electrical characterisation . . . 216
6.10 Optical recordings . . . 226
6.11 Plate reader experiments . . . 228
6.12 Time-resolved absorption . . . 229
6.13 Synthetic tissue formation . . . 230
6.14 Flexibility experiments . . . 232
6.15 Cell experiments . . . 233
6.16 Replicates . . . 235
6.17 Display figure preparation . . . 236

References **238**

List of Abbreviations

2D . . . . . Two dimensions.

3D . . . . . Three dimensions.

4D . . . . . Four dimensions.

A . . . . . Axon.

AB . . . . . Aluminium box.

ACR . . . . . Anion channelrhodopsin.

AFM . . . . . Atomic force microscopy.

Ag/AgCl . . . Silver/silver chloride.

αHL . . . . . Alpha-hemolysin.

aR . . . . . Archearhodopsin.

ATP . . . . . Adenosine triphosphate.

ATR . . . . . All trans retinal.

BG . . . . . Background.

BLINK1 . . . Blue-light–induced K+ channel 1.

BLM . . . . . Black lipid membrane.

bR . . . . . Bacteriorhodopsin.

BS . . . . . Black sheets.

BZ . . . . . Belousov–Zhabotinsky.

C . . . . . Chamber.

CAD . . . . . Computer aided design.

CCR . . . . . Cation channelrhodopsin.

CD . . . . . Circular dichroism.

ChR . . . . . Channelrhodopsin.

CM . . . . . Claret membrane.

CMC . . . . . Critical micelle concentration.

CNC . . . . . Computer numerical control.

D . . . . . Dark.

DBS . . . . . Deep Brain Stimulation.

ddH_2O . . . . . Double distilled water.

DDM . . . . . n-Dodecyl β-D-maltoside.

DFT . . . . . Density functional theory.

DHB . . . . . Droplet hydrogel bilayer.

DIB . . . . . Droplet interface bilayer.

DNA . . . . . Deoxyribonucleic acid.

DNP . . . . . 2,4-Dinitrophenol.

DPBS . . . . . Dulbecco's phosphate-buffered saline.

DPhPC . . . . 1,2-diphytanoyl-sn-glycero-3-phosphocholine.

EC . . . . . E.coli.

ECM . . . . . Extracellular membrane.

EDTA . . . . . Ethylenediaminetetraacetic acid.

ES . . . . . Elastomeric sheath.

F_A . . . . . Absolute fluorescence value.

F_B . . . . . Background fluorescence value.

FBS . . . . . Fetal bovine serum.

FMN . . . . . Flavin mononucleotide.

F_T . . . . . Fluorescence value at a point in time.

GE . . . . . Ground electrode.

GEVI . . . . . Genetically engineered voltage indicator.

GFP . . . . . Green fluorescent protein.

GPCR . . . . . G-protein coupled receptor.

GUV . . . . . Giant unilamellar vesicle.

HEK . . . . . Human embryonic kidney cells.

HH . . . . . Hodgkin-Huxley.

His . . . . . Histidine.

hν . . . . . Light.

Hz . . . . . Hertz.

IPTG . . . . . Isopropyl β- d-1-thiogalactopyranoside.

IR . . . . . Infra-red.

IV . . . . . Current-voltage.

IVTT . . . . . In vitro transcription and translation.

k_p . . . . . Photocycle rate.

LB . . . . . Luria-Bertani.

LC . . . . . Living cells.

LED . . . . . Light-emitting diode.

MA . . . . . Multichannel amplifier.

MANT-dATP 3'-O-(N-Methylanthraniloyl)-2'-deoxyadenosine 5'-triphosphate.

MD . . . . . Molecular dynamics.

MES . . . . . 2-(N-morpholino)ethanesulfonic acid.

MicRhoDE . . Microbial Rhodopsin database for Diversity and Evolution.

MLV . . . . . Multilamellar vesicle.

N . . . . . Neighbouring cell droplet.

NA . . . . . No alpha hemolysin.

NP . . . . . No microbial rhodopsin protein.

N_pHR . . . . . Halorhodopsin from *Natronomonas*.

OD . . . . . Optical density.

OG . . . . . n-Octyl-β-D-Glucopyranoside.

Pa . . . . . Pascals.

PDB . . . . . Protein data bank.

PE-PEG . . . Polyethylene-block-poly(ethylene glycol).

PEG . . . . . Poly(ethylene glycol).

pH . . . . . Potential for hydrogen.

PM . . . . . Purple membrane.

PMMA . . . . Polymethyl methacrylate.

POPC . . . . . 1-palmitoyl-2-oleoyl-sn-glycero-3-phosphocholine.

pR . . . . . Proteorhodopsin.

PRC . . . . . Proton release complex.

Pre . . . . . Presynaptic droplet.

Pst . . . . . Postsynaptic droplet.

PVC . . . . . Polyvinyl chloride.

QM/MM . . . Quantum mechanical and molecular mechanisms.

RE . . . . . Recording electrode.

ret . . . . . Retinal.

RBP . . . . . Retinal binding pocket.

RNA . . . . . Ribonucleic acid.

rub . . . . . Bacterioruberin.

S . . . . . (Photo)sensory droplet.

SD . . . . . Standard deviation.

SLB . . . . . Supported lipid bilayer.

SN . . . . . Synthetic nerve.

SUV . . . . . Small unilamellar vesicle.

TMP . . . . . Transmembrane protein.

TP . . . . . Terrapin.

USB . . . . . Universal Serial Bus.

UV . . . . . Ultra-violet.

Vis . . . . . Visible.

VGC . . . . . Voltage-gated channel.

VGKC . . . . . Voltage-gated potassium channel.

VGSC . . . . . Voltage-gated sodium channel.

WT . . . . . Wild-type.

YG . . . . . Yellow-green.

1

Introduction

The minimal tissues described in this thesis were built from the bottom-up using only the basic elements (Fig. 1.1). Information provided in **Chapter 1** reflects the themes and features considered during the *de novo* design, as well as an overview of advances made with synthetic tissues, and their potential applications.

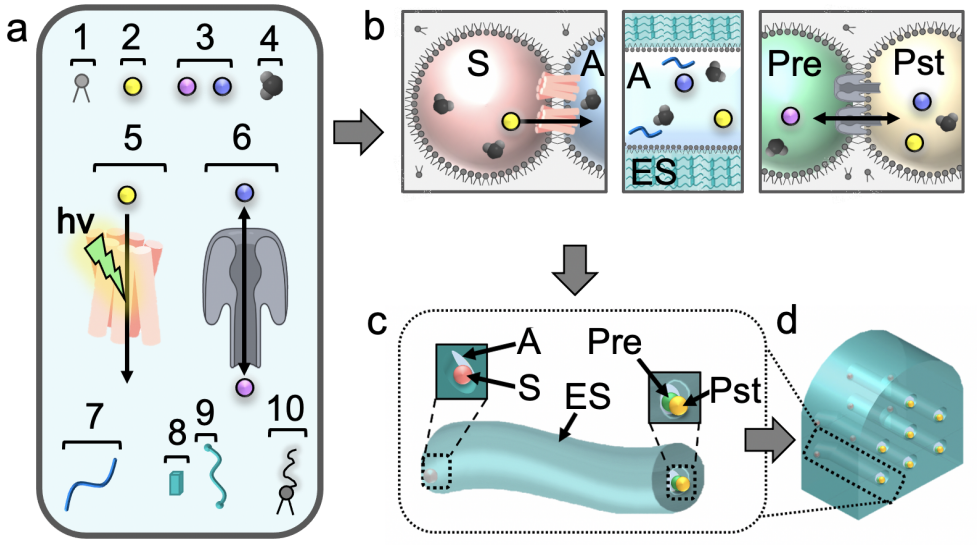


Figure 1.1: Synthetic nerve. a, Synthetic nerve elements: 1-Lipid. 2-Proton. 3-Ions and molecules. 4-Water. 5-Light-driven proton pump. 6-Protein pore. 7-Hydrogel monomer. 8-9-Elastomer crosslinker and monomer. 10 - copolymer **b,** Left to Right: Element assembly into a photosensory bilayer, myelinated hydrogel axon and a synaptic bilayer. S - photosensory droplet. A - axon, ES - elastometic sheath. Pre - presynaptic droplet, Pst - postsynaptic droplet. **c,** A synthetic neuron. **d,** A synthetic nerve.

1.1 Biological membranes

Biological complexity requires spatial organisation to perform many of the processes central to sustaining life. This is generally achieved by compartmentalisation; surrounding cells, or organelles, with a lipid membrane that physically separates their contents from the bulk environment.

1.1.1 Structure

Cell membranes have a specialised structure which facilitates their function. Initially devised by Singer and Nicolson in 1972, the fluid mosaic model is still widely used to describe the architecture of biological membranes; a patchwork layer of lipids, proteins, and carbohydrates that give the membrane its dynamic character (Fig. 1.3)[1]. The relative proportion of each component is membrane-specific. A standard membrane is several nanometers thick and held together by the interplay of lipid molecules: hydrophobic, hydrophilic and van der Waals interactions[2]. Further, the bilayer has a large resistance and capacitance when intact, which is also important for its functionality.

Lipids

Typically, biological membranes are formed from amphipathic lipid molecules which self-assemble into bilayers; the core contains the hydrocarbon tails and the polar heads face outwards (Fig. 1.3)[3,4]. This orientation protects the lipid tails from the surrounding aqueous solution. Even free lipid molecules congregate together when exposed to water, forming micelles or vesicles depending upon the lipid[3,4]. A micelle is a thermodynamically stable aggregate of conical lipid monomers; a single layer forms in which the heads face the aqueous solution. When lipid sheets fold to encapsulate a central aqueous droplet, a vesicle is formed.

Around half the mass of a membrane results from the lipid component. Each membrane has a distinct lipid composition that reflects its unique function[5] and determines its physical properties, such as its curvature and rigidity[5]. Composed from predominantly phospholipids, such as phosphatidylcholine, these biological

membranes are often referred to as phospholipid bilayers. Within each phospholipid molecule, the polar head (formed from a glycerol and phosphate) is linked to its non-polar tails via an alcohol group[5] (Fig. 1.2). These lipid tails pack together in the membrane; the tightness of packing is dependant upon the relative number of saturated and unsaturated fatty acid chains. Other lipids which are frequently included in the membrane are sphingolipids and non-polar sterols. Cholesterol is an important sterol component that regulates the stiffness of animal membranes. Consequently, it has a quite different structure to phospholipids: a hydroxyl group (forming the hydrophilic region) is joined to a four-ring steroid structure with a short hydrocarbon side chain[5] (Fig. 1.2).

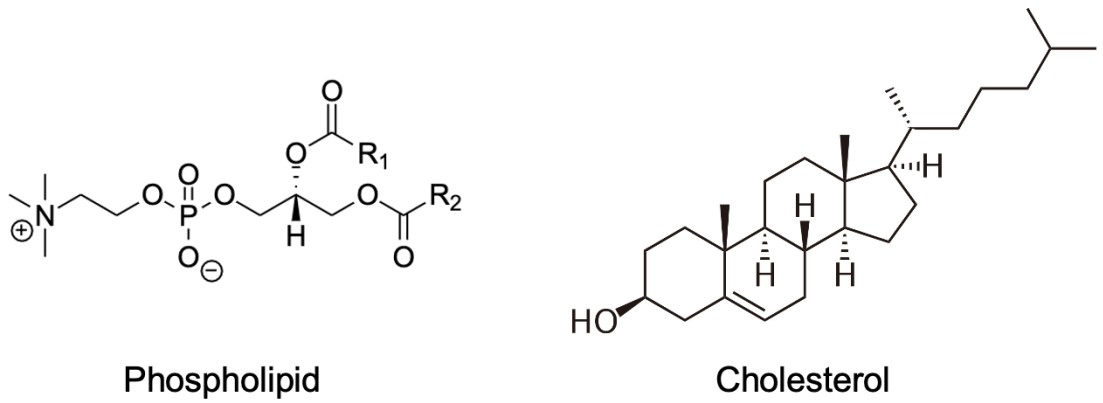


Figure 1.2: Lipid structure. Left: Structure of a phospholipid. Right: Structure of cholesterol. Drawn using ChemDraw.[6]

Inside these lipid bilayers, individual molecules may move (rotate, or laterally diffuse), within one leaflet; the non-polar tails must remain within the hydrophobic membrane core. Enzymes, such as flippases, enable transfer of lipid molecules between the different leaflets of a membrane. This dynamic nature of the lipid bilayer is important for many physiological functions for instance in self-repair where lipids re-position to close a minor hole. Arising from the movement of individual molecules, each leaflet of a biological membrane is composed of a different combination of lipids thereby introducing asymmetry into the bilayer[6]. Lipid asymmetry is functionally important, for instance in cell signalling and recognition, and reflects the roles of each leaflet within the membrane[5].

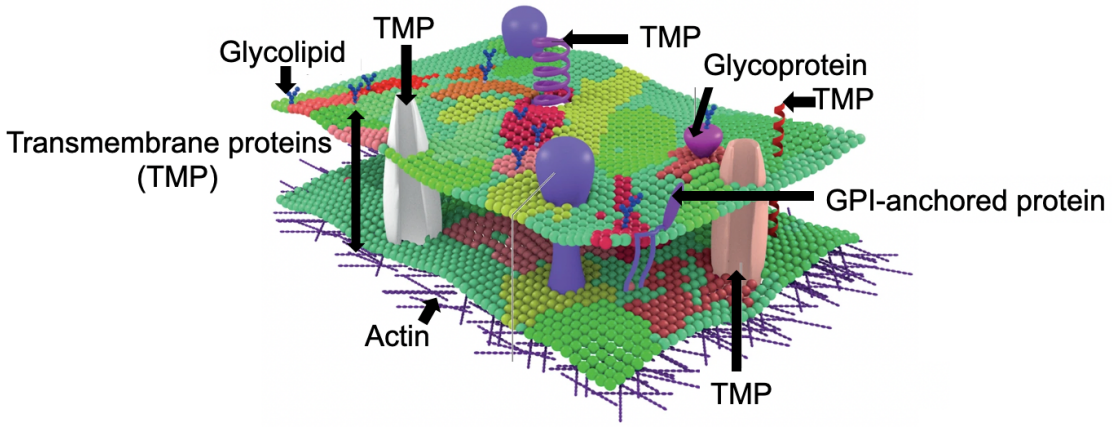


Figure 1.3: Fluid Mosaic Model. Schematic of a lipid membrane embedded with a range of integral and peripheral proteins, some of which contain sugar moieties: Transmembrane proteins (TMP), Actin, Glycolipid, GPI-anchored protein, Glycoprotein. Figure taken from Sezgin et. al. (Labels reproduced)[6]

Proteins

The second major component of biological membranes are proteins: these can be either integral or peripheral depending upon their interaction with the lipid bilayer (Fig. 1.3)[3,4,7]. The lipids which surround a particular protein play an important role in its function[2,5,8].

Similar to lipids, integral proteins are amphipathic; their hydrophobic membrane-spanning regions interact with the non-polar fatty acid tails, anchoring the protein to the bilayer[2,3,4]. Integral membrane proteins can either span just a segment of the membrane, or completely traverse it (up to twelve times) forming a transmembrane protein (TMP). Single-pass proteins typically have a hydrophobic segment around 20 residues long, whereas multi-pass ones are extensively folded with several hydrophobic sections embedded in the membrane; the hydrophilic regions are exposed at either side of the membrane[3,4].

On the other hand, peripheral proteins just associate at the surface of the membrane, attaching to lipids or integral proteins (Fig. 1.3). Since the protein-membrane interactions are weaker they can more easily dissociate from the membrane[3,4].

Whilst membrane proteins can laterally move within one leaflet of lipid bilayer, their rates of movement are generally slower than those of lipids and it is therefore

less significant. However, since these proteins either have a specific orientation, or associate with one leaflet, they introduce further asymmetry into the membrane[5].

Carbohydrates

Carbohydrates are the third major component of biological membranes[3,4]. Glycolipids and glycoproteins are formed when sugar molecules attach to lipids or proteins repectively. Since they are usually located on the external surface of cells they introduce more asymmetry into the biological membrane (Fig. 1.3). These additional chains consist of around 2-60 monosaccharide units and can be either straight or branched[3,4]. They form distinctive cellular markers playing an important role in cell communication, adhesion and recognition, for instance allowing immune cells to identify foreign cells[3,4]. Additionally these carbohydrate components are highly hydrophilic attracting large amounts of water to the surface of the cell.

1.1.2 Transport

Since biological membranes enable compartmentalisation, transport across them is a key feature. Most membranes are semi-permeable, with the lipid and protein constituents determining which species can move across it[3,4]. Whilst these biomolecules have some motility within the membrane, any gaps created as a result of this are minuscule which ensures it remains an effective barrier.

Small hydrophobic molecules may directly diffuse through the bilayer but larger, or hydrophilic, ones require proteins to facilitate their transmembrane transport as they cannot permeate the non-polar core of the bilayer at an appreciable rate (Fig. 1.3).

The protein components of the membrane dictate the substances to which it will be permeable, and which signalling molecules it can recognise. Membrane proteins are vital to the optimal functionality of the membrane[9]. Protein channels or pores provide a water-filled passage through which molecules can spontaneously diffuse down their electrochemical gradient; they may have gated selectivity filters, opening and closing upon stimulation. However, in order to transport molecules

against a gradient, external energy is required: this may be provided by ATP hydrolysis[3,4], mechanical deformation[4,10], a membrane potential[9], ligand binding[3,4] or even the presence of light[11]. These carrier proteins, which include protein pumps and exchangers, undergo tightly controlled conformational changes in order to facilitate transport across the membrane[3,4].

Whilst channels and carrier proteins are ideal for transporting specific small molecules, they are too small and selective to enable the transport of very large substances such as entire bacterial cells. For this, cells use bulk transport mechanisms, enclosing these substances in a separate biological membrane. Fusion of these vesicular compartments to the cell membrane enables the removal of waste products or the release of signalling molecules (known as exocytosis)[3,4]. Endocytosis is when large substances are transported into the cell: via phagocytosis (large particles), pinocytosis (extracelullar fluid) or receptor-mediated endocytosis[3,4].

Some peptidic, viral and bacterial components use alternative methods, disrupting the cell membrane to enable the transport of molecules across the bilayer.

1.1.3 Electrochemical gradients

By controlling the transport of ions and molecules, it is possible to determine the spaciotemporal distribution of these substances across the membrane. The ability to sustain concentration gradients and move materials against them, is crucial to cell health and maintenance. Since many substances are charged, their unequal distribution across a membrane results in an electrical, as well a chemical, gradient[3,4].

The synthetic tissues described in this thesis can generate electrochemical proton gradients, transporting hydrogen ions across the membrane. In nature, such gradients play key roles in storing energy. Mitchell's chemiosmotic theory, for which he won the Nobel Prize in 1978, postulated how specialised biological membranes, such as the mitochondria or chloroplast, couple synthesis of the energy-storage molecule ATP to proton gradient formation[12,13]. First, high-energy electrons (derived from a variety of sources e.g. sunlight) must move along the transport chain via a series of electron carriers. This process releases energy which is used

to pump protons across the membrane; the resulting ion accumulation establishes an electrochemical proton gradient. Functioning as a battery (energy source), this gradient drives ATP synthesis. Throughout nature these energy-rich proton gradients are used as a power source. In addition to ATP synthesis proton gradients can be used to drive numerous processes such as flagella rotation or metabolite transport[3,4,14,15].

Electrochemical gradients formed from other ions (primarily sodium, calcium, potassium and chloride) are also important in nature, for instance they play a key role in the function of electrically excitable cells: driving muscle contraction, nerve conduction or hormone secretion[3,4].

1.2 Biological communication

Since cells are separate compartments, they must communicate with one another in order to perform coordinated behaviours, as well as share information about the environment. For a particular cell to detect a signal it must have the appropriate receptor proteins (Fig. 1.4)[3,4].

Endocrine signalling

Endocrine glands release small molecules (called hormones) into the bloodstream which travel throughout the vascular system until reaching distant regions of the body (Fig. 1.4)[3,4]. As these hormones are relatively stable it enables them to transfer information over significant distances. One example is oxytocin which is released from the pituitary gland. Following transport in the blood stream, oxytocin induces responses in a number of different tissues e.g., the uterine muscles and mammary glands[3,4].

Paracrine signalling

Paracrine signalling is when cells, close in proximity, communicate via water soluble chemical messengers called cytokines (Fig. 1.4)[3,4,16]. The graded exposure of cells to these signals is important as they respond differently depending upon the

chemical concentration in their vicinity. It enables cells to locally co-ordinate their behaviours, for instance in blood clotting or tissue development[3,4].

Neural signalling

Neurons use electrical signals to transfer information along their axons; this is discussed in more detail in **Chapter 3**. However, these signals can't move between non-connected cells. Instead, once the electrical signals reach the axon terminals, they release neurotransmitters (by exocytosis of synaptic vesicles) which then bind to receptors on the post-synaptic membrane (Fig. 1.4)[3,4]. Following release, these neurotransmitters are quickly degraded or re-taken up by the signalling cell, resetting the system. Neurotransmission is a specialised type of paracrine signalling.

Autocrine signalling

Another variant of paracrine signalling is autocrine signalling, in which a cell signals to itself (Fig. 1.4). The local mediator binds to receptors either within its own membrane, or perhaps even within the cell itself (Fig. 1.4). In many cases, the chemical signal may have both an autocrine and paracrine effect. Whilst this type of signalling is important in the commitment of a cell fate during development, it also contributes to the uncontrolled proliferation of cells within a tumour[3,4,16].

Contact-dependant signalling

Alternatively, signalling may be direct; two cells may bind to one another because they carry complementary proteins on their surfaces (Fig. 1.4)[3,4]. When the cells bind to one another, this interaction changes the shape of one or both proteins, transmitting a signal. This type of contact-dependant signalling plays an essential role in the immune system, enabling cells to differentiate between pathogenic and healthy cells[3,4].

Direct signalling

In some instances, cells may communicate with their immediate neighbours via gap junctions (animals) or plasmodesmata (plants) which form small channels between them (Fig. 1.4)[3,4]. These water-filled channels connect the cytoplasm of cells transferring information about the state of once cell to interconnecting ones. This permits connecting cells to quickly co-ordinate their behaviour, for instance in the contraction of cardiomyocytes[3,4].

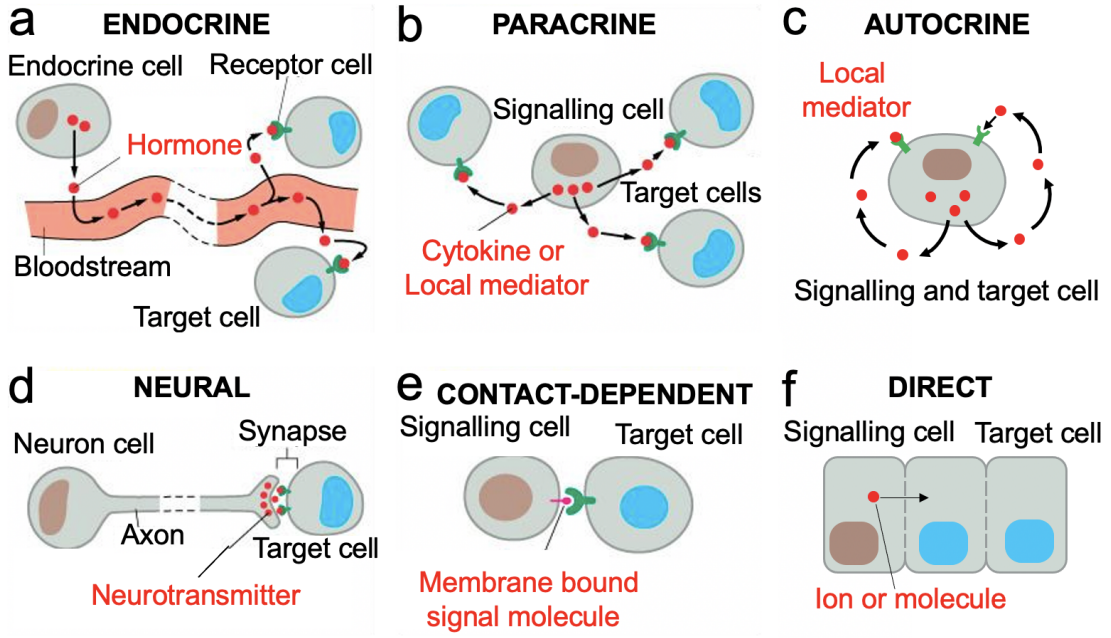


Figure 1.4: Cellular communication. Schematics of the different types of signalling used by biological cells to communicate. **a,** Endocrine signalling. **b,** Paracrine signalling. **c,** Autocrine signalling. **d,** Neural signalling. **e,** Contact-dependant signalling. **f,** Direct signalling. Figure is adapted from Alberts et. al. (Labels reproduced) (Part c and f were made by the author in the same style)[4]

1.3 Synthetic cell mimics

Synthetic cells are engineered artificial structures which loosely resemble living cells. This thesis focuses on a bottom-up approach to their fabrication; a myriad of building blocks are assembled to create a system which imitates the form and function of biological cells[17,18,19]. Since synthetic cells, built in this way, may include any natural or unnatural elements, they have the capacity to do more than simply

emulate nature. Whilst many of these synthetic structures are rudimentary, their characteristics are predictable and not constrained by nature. By building functional analogs of natural cells, scientists gain insights into the mechanisms surrounding the origin of life, and discover novel applications for such cell-like constructs, in their quest to recreate life. The alternative approach for the construction of synthetic cells is using a top-down approach where components are removed from a living cell leaving only the minimum parts which are essential for life[20,21].

Prior to building an synthetic cell from its basic elements, the important features central to a functional, multifaceted biological cell should be considered.

1. Compartmentalisation - Surrounding the cell with a finely tuned, semipermeable boundary enables it to control the interchange of materials with the bulk environment (Sections 1.1 1.2).

2. Genetic material - Including genetic material in an artificial cell enables features such as self-replication and *in situ* protein expression. These abilities are important for the longevity of such cells.

3. Energy production[22] - An important feature of a living cell is its ability to generate energy and link this to metabolic pathways. Energy production is key to achieving physiochemical homeostasis. Further, emulating these functions in artificial cells increases their lifetime.

4. Growth and Division[23] - Within unicellular organisms, cell growth and division is its way of reproducing. For multicellular organisms, it is how tissues grow and is important for their maintenance.

5. Flexibility - Cells adapt in order to respond to changing environmental conditions, for instance by undergoing changes to their shape, size, number or organisation. They may also respond to external cues by altering their internal biochemistry.

6. Communication[24] - Throughout nature, cells interact with one another in order to pass on information and coordinate their behaviour.

7. Motility[25] - Cell movement is a key function in organisms, for instance it is how predators catch prey.

Although a synthetic cell which possesses all fundamental properties of a living cell has not yet been created, recent advances suggest that this is an achievable goal.

1.3.1 Droplet-based cells

Within the field of synthetic biology, considerable effort has been devoted to the construction of artificial cells. The use of aqueous droplets as membrane-encapsulated "cellular" compartments is one avenue being explored. Advantages of synthetic cells built from aqueous droplets, include:

- their versatility,
- their modularity,
- the single bilayer between compartments facilitating functionalisation by protein insertion,
- the miniature compartments requiring only limited biological material and reagents enabling rare and expensive ones to be used,
- the parameters e.g. pH or protein orientation, can be easily controlled
- bilayer asymmetry, a key feature of biological membranes, can be easily recapitulated[26].

1.3.1.1 Droplet interface bilayers

When an aqueous droplet is formed in a lipid-containing oil, a lipid monolayer surrounds it (Fig. 1.5a)[27]. The oil typically consists of a hydrocarbon such as hexadecane and a non-hydrocarbon such as silicone oil. The latter is supplemented to match the density of the two phases and to promote monolayer formation. Bringing two such droplets together results in the spontaneous formation of a droplet interface bilayer (DIB) at the contact point (Fig. 1.5b). This droplet pair, connected by

a DIB, exists in a local energy minimum meaning they are thermodynamically unstable towards coalescence into a single droplet; they do, however, have high kinetic stability which makes them useful in a range of applications[27]. One way in which the kinetic stability of a DIB can be improved is by using a lipid-in-oil solution in which the lipid has poor solubility. For instance, the lipid DPhPC (diphytanoyl-sn-glycerol-3-phosphocholine), dissolved in a mixture of hexadecane and silicone oil, prefers to occupy space at the droplet interface due to its poor solubility in silicone oil; this strengthens the bilayer[27]. Alternatively, the lipid might be incorporated into the bilayers from vesicles inside the droplets; bilayer stability is improved when formed using this lipid-in method[28]. Other ways in which droplet stability has been enhanced include reducing the droplet size, adding a plastic sheet around the interface[29], forming droplets in a box[30] or by the addition of other components such as PEG groups[31], copolymers[32] and hydrogels[28,33,34]. Despite some instability, functional and robust DIBs have been formed in air[35], bent[36], transported to the top of Mount Fuji[37] and even dropped from height[38]. Analogous to biological membranes, the strength of these DIBs is derived from the hydrophobic effect, head-group interactions and the van der Waals forces between the phospholipid tail groups.

1.3.1.2 Droplet hydrogel bilayers

The use of aqueous droplets in conjunction with hydrogels, such as agarose or polyacrylamide, was initially explored using a droplet-hydrogel bilayer (DHB) system. Similar to with DIBs, both components are coated in a lipid monolayer and a bilayer spontaneously forms at the interface (Fig. 1.5c). The hydrogel component presents both fluid and solid capabilities, the first needed for function of biomolecular machinery located within the bilayer (and for flexibility), and the latter for improved stabilisation[27]. Hydrogel-hydrogel bilayers have also been successfully made with even better stability since the lipids are physically caged at the interface[39]. These hydrogel structures retained their shape when transferred to different aqueous solutions, exposed to air, or dropped[30,33].

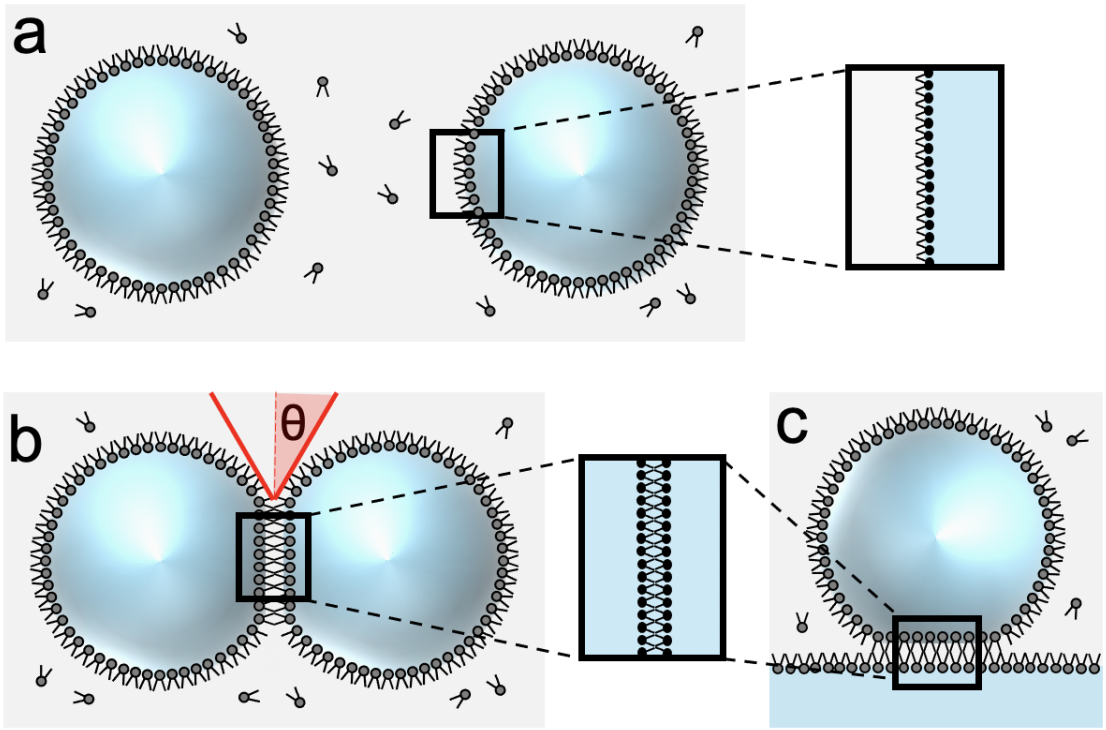


Figure 1.5: Construction of a droplet bilayer. **a,** Aqueous droplets become encapsulated with a lipid monolayer when in a lipid-in-oil environment. Zoom : A lipid monolayer. **b,** A droplet interface bilayer forms when two droplets are brought into contact. The contact angle (formed between them) is shown in red. **c,** A droplet hydrogel bilayer forms at the interface between a droplet and hydrogel. Zoom : A lipid bilayer.

1.3.1.3 Tuning the membrane

Whilst there is an incomplete understanding of the physicochemical properties of droplet bilayers, it is known that altering the membrane parameters can control bilayer formation. The contact angle between the two droplets can be adjusted by modifying the components present, for instance there is a linear dependence of the contact angle with respect to the increasing relative volume fraction of silicone oil (Fig. 1.5b)[40]. Other factors which effect bilayer adhesion include the lipid composition and concentration as well as the contents of the droplets themselves. Interestingly, some environmental parameters, such as temperature, weren't found to alter the interface size[40]. It has been assumed that the area of the bilayer, as well as the corresponding contact angle between droplets, reflects the strength of the bilayer. Moreover, understanding how different conditions affect the bilayer formation is

important when characterising proteins embedded within the membrane, as well as for the development of higher order, and more complex, structures[40].

1.3.1.4 Functional droplet bilayers

Droplet bilayer systems (DIBs and DHBs) are a form of minimal artificial cell (Fig. 1.6). Built from the bottom-up they are typically inexpensive to make and easy to handle.

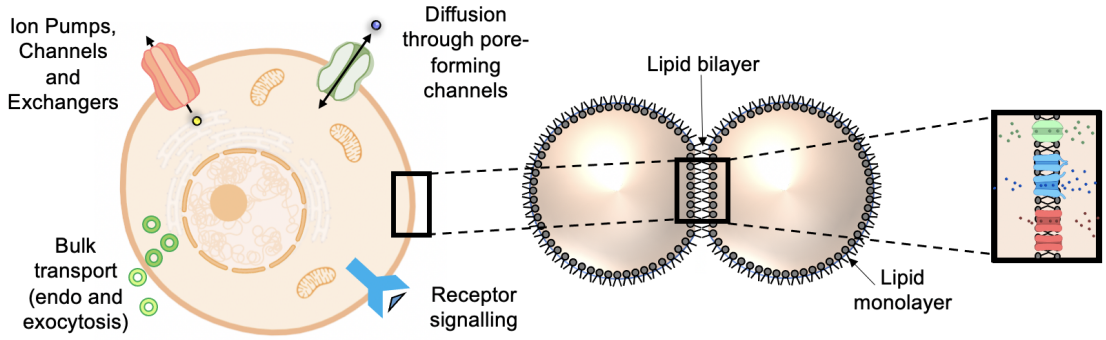


Figure 1.6: Membrane Transport. a, Left: Schematic of a biological cell. Different methods of membrane transport are depicted: Bulk transport; Ion pumps, channels and exchangers; Diffusion through open pores; Receptor signalling. Right: Schematic of a minimal synthetic cell (formed from a droplet pair joined by a lipid bilayer). Zoom: Both biological and synthetic cells contain lipid bilayers embedded with membrane proteins for transport: Pore (green), Receptor (blue) and Ion channel (red).

The single lipid bilayer connecting individual compartments facilitates the reconstitution of a myriad of different proteins: channels[38,41,42,43], pumps[31,44], transporters[45] and pores[44]. DNA based biomimetic channels have also been successfully reconstituted into droplet bilayers[46]. The method used to incorporate a protein into a droplet bilayer are dependent upon the protein itself and the purpose of the study[47,48]. Water soluble proteins such as alpha-hemolysin have previously been shown to spontaneously insert into the bilayer directly from solution[44,49,50]. However, most integral membrane proteins aren't water soluble so are purified into detergent micelles[31,44], liposomes[45,51] or cell membrane fragments[51] for insertion. For instance, the light-driven pump bacteriorhodopsin was shown to insert into the droplet bilayer, spontaneously and functionally, in the presence of a low concentration of detergent[31,44]. Here, it is thought that the detergent causes partial fragmentation

of the purple membrane with these smaller, more soluble fragments inserting spontaneously[31,44,48]. Proteins have also been directly inserted into the bilayer following cell-free *in vitro transcription/translation*[45,52,53]; again, insertion occurred spontaneously. Yet not all proteins can efficiently insert into the bilayer in a spontaneous manner, for example an applied potential of 100 mV was required for the bacterial outer membrane porin OmpG to functionally insert[26,48]. The rate of insertion might also be enhanced by adjusting the environmental conditions e.g., pH or salt concentration[48]. Following insertion, these proteins can be electrically interrogated by the addition of electrodes into the droplets (or hydrogel)[39,44,49]. Droplet bilayer systems are a robust approach used in understanding how bilayer properties and mechanics are related to protein function. Indeed, the biophysical properties of a number of membrane proteins have been studied using droplet systems, for example the gating of mechanosensitive channels[48].

Due to the remarkable ability to mechanically dissociate droplet bilayers, these systems have also been employed in sensing and screening applications. Since membrane proteins are important drug targets, functionalised droplet bilayers can be used for pharmacological studies. For instance, potential inhibitors for channel proteins have been rapidly screened: in succession and in parallel[27,41,48,54]. Alternatively, droplet bilayer systems have been used in protein translocation studies since the small droplet volume enables low concentrations of cargo to be detected[27,48,55]. A third screening application of bilayer systems is in single-molecule DNA sequencing[27,48,56]; this might be extended to proteins in the future.

By functionalising lipid bilayers it is also possible to control transport across them (Fig. 1.6, 1.7 a,e). Typically, proteins are incorporated into the droplet interface from vesicles or directly from the droplet solution (purified protein in the presence of a low concentration of detergent). However, including genetic material within the droplets enabled proteins to insert into the bilayer after expression *in situ* (Fig. 1.7c)[41,45,57]; this has even been remotely controlled with single droplet resolution[27]. Bulk transport mechanisms have also been demonstrated in droplet systems[58,59].

Similar mechanisms might be used to develop artificial droplet cells which can controllably form internal organelle-like structures, replicate, grow, and divide[60].

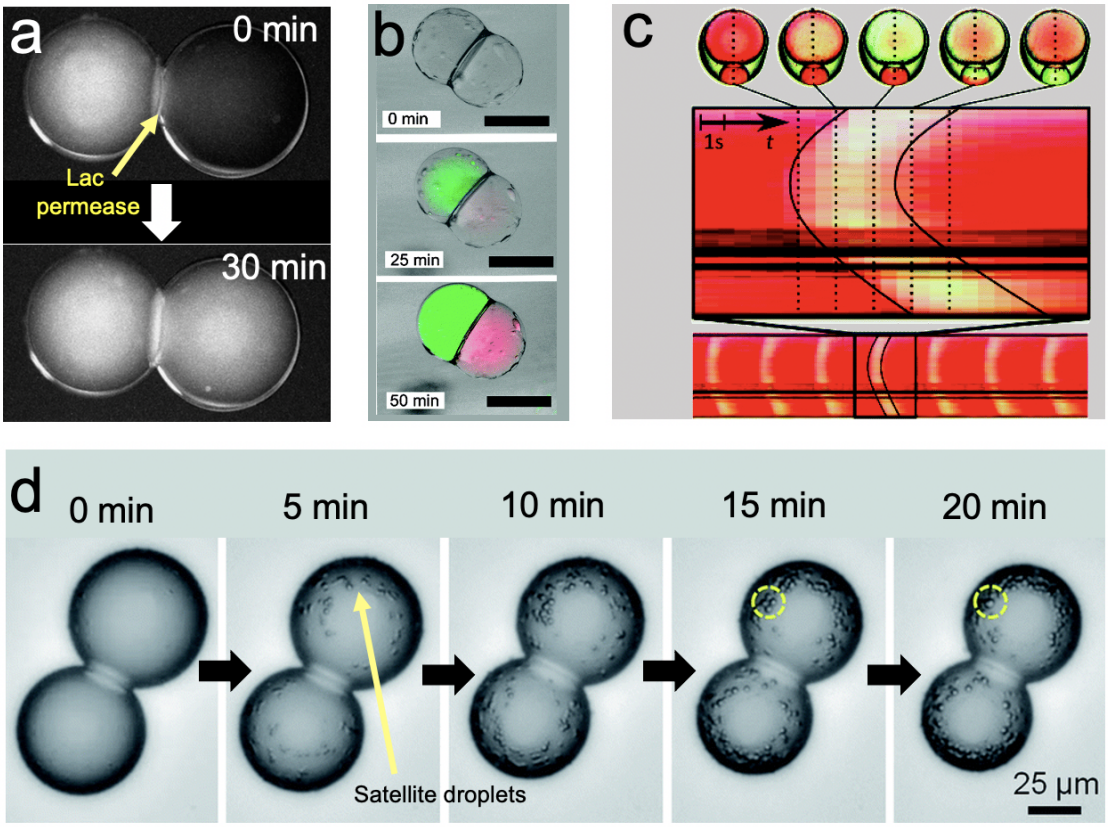


Figure 1.7: Droplet artificial cells perform simple biological functions. **a,** Active transport of bio-molecules (sugar) across a DIB was performed by lac permease (location indicated by the yellow arrow). **b,** Compartmentalisation was achieved. Images show that each droplet expressed a different protein and no transfer occurred between the spatially-segregated compartments. Scale bar = 200 μm. **c,** A BZ chemical reaction moved across a droplet pair: Line profiles of the BZ-droplet pair were collected in a single time-plot and the chemical wave (represented as a white stripe) expanded from the centre of the larger droplet propagating outwards across the lipid bilayer and into the smaller droplet (black lines are for visualisation). **d,** Images of a large droplet pair in which satellite droplets formed following condensation (indicated by the yellow arrow). As the larger droplets dehydrated, water was transferred to the hydrophilic interior of lipid micelles (present in the oil); the resulting satellite droplets grew (and merged, indicated by yellow circle) over time. Figure **'a'** taken from Findlay et. al[45], **'b'** from Elani et. al[61], **'c'** from Guzowski et. al[62] and **'d'** from Mruetusaturn et. al[59], Labels were reproduced and arrows added.

In addition, transport between droplet compartments permits the system to function as a microreactor. Aqueous droplets are ideal for biochemical reactions which require water to function. A compartmentalised droplet system might

facilitate a multi-step reaction which requires multiple (incompatible) environments, moving reagents and products between the compartments[27,57,63]. Transport between droplets has been achieved by diffusion through the bilayer itself[61,64] or by translocation through proteins functionally incorporated into the interface (Fig. 1.7a)[45,65]. Further, the oscillating Belousov– Zhabotinsky (BZ) reaction has been demonstrated in simple droplet systems. Here, the droplets were able to change shape or move[62,66,67]. Whilst simple droplet pairs have demonstrated some functional properties, as of yet there has been no systematic investigation into features such as their physical chemistry and much remains to be explored.

1.3.2 Alternative synthetic cells

There have been extensive efforts to construct synthetic cells from the bottom-up which are both biomimetic in structure and function. A myriad of material have been used to build such cells. Biological membranes are typically formed from a lipid bilayer filled with functional proteins. For this reason a popular synthetic cell mimic is the liposome (or vesicle), formed when a lipid bilayer encloses an aqueous solution[68]. Synthetic droplet cells are only encapsulated by a lipid monolayer which facilitates protein reconstitution[27,48]. Other materials have also been used to encapsulate aqueous compartments and form cell mimics: polymers, proteins, DNA and inorganic colloidal particles. Membrane-less synthetic cells have even been built by mixing biomolecules that self-assemble into hydrophilic droplets: coacervates.

Many important biological functions have been successfully imitated in synthetic cells built using these systems including: intercellular communication[69,70], movement[71,72], biochemical reaction cascades[61,73,74,75,76], DNA replication and protein synthesis[77,78,79,80,81,82,83,84], energy generation[15,85,86,87] and growth and division[78,88,89]. Synthetic cells have also been shown to communicate with living (animal or bacterial) cells, triggering a functional response[90,91]. For instance, artificial cells (proteoliposomes) converted a chemical signal into one recognised by living bacterial cells. This signal then activated genes in the bacterial cells, producing a functional output[91].

1.4 Synthetic Tissues

Since aqueous droplets are used as simple artificial cells, by extension, assembles of these droplets form minimal synthetic tissues. Connecting multiple droplets together introduces a number of interesting possibilities since droplet networks possess collective properties which surpass those of the droplet pair. Using a combination of natural and unnatural elements, synthetic tissues can be designed to imitate nature or include novel functionality. By using a simple modular approach, the properties and functions of the resulting tissues are predictable.

1.4.1 Constructing droplet networks

Droplets can be brought together in either two or three dimensions to form sophisticated droplet networks and synthetic tissues.

Manual assembly

The simplest approach is to manually form the droplets, using a syringe or pipette, before bringing them together either by hand or using a micromanipulator. It is straightforward to manually remove a specific droplet compartment of a 2D network and replace it (Fig. 1.8a)[44]. Whilst 3D networks have been made using hand-operated droplet assembly[92], it is slow and requires a high degree of dexterity restricting its use more advanced structures. The synthetic tissues described in this thesis were build by hand; droplets were pipetted into place.

Assisted assembly

One technique which was developed to assist in the placement of droplets involves the addition of paramagnetic beads[93]. In this way, multi-layered networks were constructed by positioning droplets into a pyramidal formation in a modular fashion. Other methods to assist in the assembly of droplet networks have also been explored, for instance the use of optical tweezers[94,95] or lasers[96].

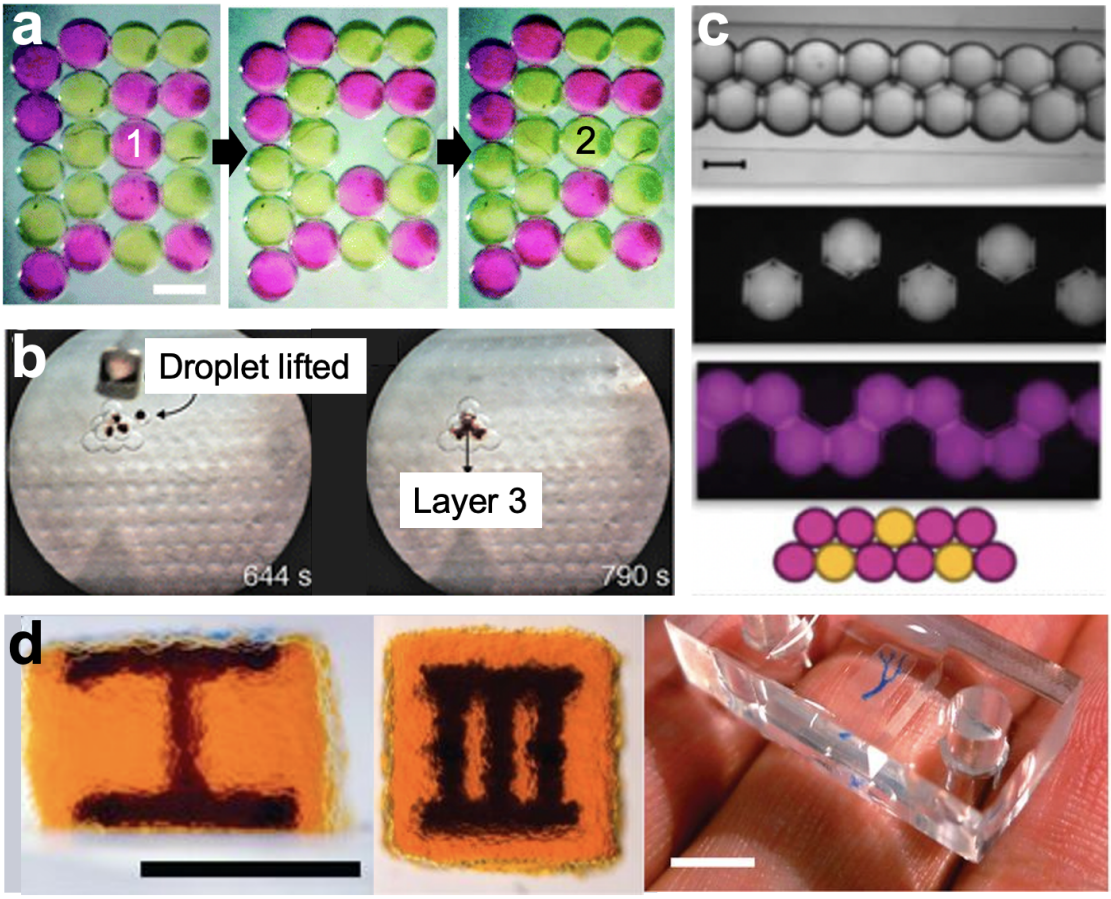


Figure 1.8: Making droplet networks a, Manual assembly using a pipette. A single droplet (pink, 1) was easily removed and replaced with a different droplet (yellow, 2). Scale bar = 700 μm. **b,** Magnetic beads enabled a magnet to assist in 3D structure formation. A droplet (+ magnetic beads) was picked up and place on top of the structure without any disruption to the network. **c,** Microfluidics was used to develop patterned networks. Two types of droplets were used and the pattern could be visualised. Scale bar = 400 μm. **d,** Printed networks can have a high level of patterning in 3D. Left: A network of droplets ($\approx$ 65 pL, two different coloured aqueous solutions) were printed into a 28 layer structure (each layer contained 24 x 24 droplets). Scale bar = 1 mm. Right: A branched network containing 20 layers (50 x 35 droplets) was also printed. Scale bar = 5 mm. Figures reproduced from **'a'** Holden et. al[44], **'b'**Elani et. al[97], **'c'** Wauer et. al[93], **'d'** Villar et. al[50] and labels added.

Microfluidic assembly

Automatic approaches have been developed in order to build large, complex 3D networks, rapidly screen conditions and produce multiple replicates[98,99]. These methods also enable smaller droplets to be made than is feasible by hand. One technique is microfluidic assembly. Here, immiscible liquids flow within microfluidic channels and aqueous droplet compartments are released. Using this technique,

simple patterned networks composed of thousands of individual compartments, all of pre-determined size and lipid composition, have been formed[57,97]. Whilst microfluidic chips have been shown to form extensive droplet arrays in a controlled manner, there are some drawbacks in that pattern development is limited and assembled networks can be difficult to extract from the container in which they are formed.

Droplet printing

A second automated method is the use of a droplet printer which can form extensive networks of pre-defined architectures ($>$ 100 droplets)[50]. The printer has two nozzles, each capable of ejecting one type of droplet into a lipid-containing oil bath. 3D structures are formed by layering droplets on top of one another; here, each droplet forms a lipid bilayer with its neighbouring ones. Therefore, the ideal packing arrangement of a printed structure would have each droplet with a space-filling trapezo-rhombic dodecahedron geometry[40]. Using this technique, large, synthetic tissue-like structures, with precisely patterned droplets, have be constructed[27,40,50].

1.4.2 Functional droplet networks

Synthetic tissues, built from the assembly of multiple droplet cells, hold significant promise. Individual compartments may contain an array of living or synthetic parts which give functional properties to the structure.

Signalling

A number of proteins have been used to facilitate transport between droplet compartments: transporters[45], channels[38,41,42,43,46,48], and pumps[44,48,100]. Using these tools, droplet networks have been built which carry signals through defined pathways, enabling inter-droplet communication (this is further discussed in **Chapter 3**). Remote control of signal initiated was achieved in simple droplet networks by including light-sensitive pumps[31,44]. However, these droplet systems only measured outputs. Different synthetic tissues were built which sent rapid electrical signals across droplet networks (upon an applied potential)[40,50,52]. Here, the signals were carried by ions which moved between droplets via protein pores

located at the interface. Molecules can also move through these protein pore-rich bilayers, sending signals via chemical messengers[65]. One droplet network used the propagated chemical signal to generate a functional output[65] but few examples of this exist. Instead of using transmembrane proteins, some chemical signals can pass directly between connected droplets by diffusing through the bilayer[61,64,66,67]. The Belousov–Zhabotinsky reaction has been used in 2D droplet networks to propagate signals as chemical waves (and spirals)[66,67]. Signalling using chemical waves is faster than methods which rely on diffusion over long distances.

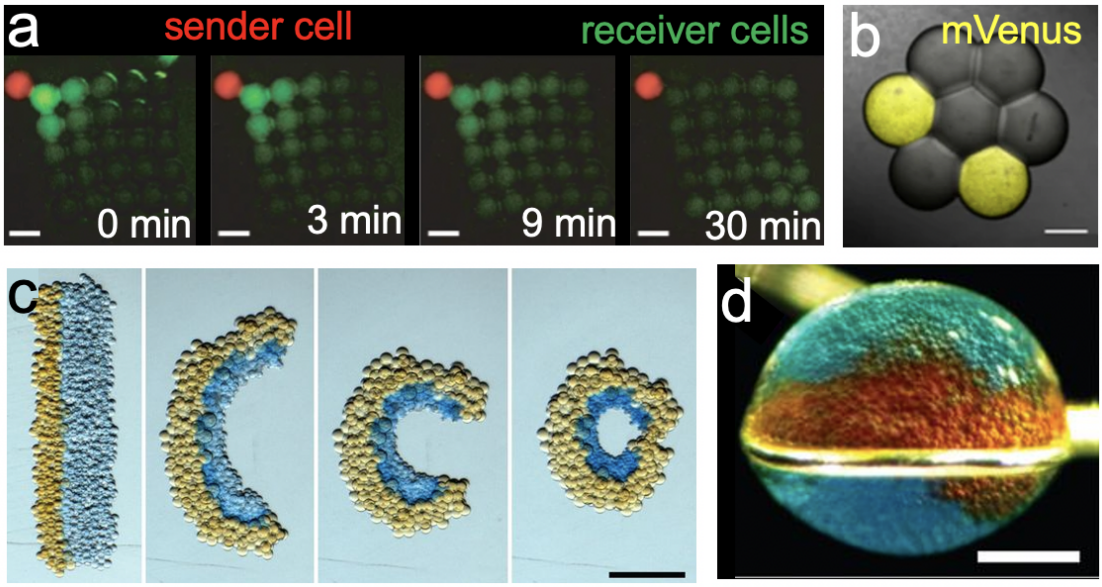


Figure 1.9: Functional droplet networks. a, Chemical signal transmission. Here, the signal (DFHBI) diffused from a sender droplet (red) across the lipid bilayers (via protein pores) to receiver cells and induced GFP production. Scale bar = 200 μm. **b,** Genetic information within droplets enabled controlled protein expression. Only the two droplets illuminated produced the fluorescent protein (yellow, mVenus). Scale bar = 250 μm. **c,** Patterning droplets enabled shape changes. Two droplet strips, with different osmolarities, were patterned into the network and the resulting flow of water across the bilayer induced a shape change in the network after formation (over hours). Scale bar = 250 μm. **d,** Printed droplets within an oil droplet were interfaced with bulk aqueous solution to enable communication with the environment. Scale bar = 400 μm. Figures reproduced from **'a'** Dupin et. al.[65], **'b'** Booth et. al.[27], **'c-d'** Villar et. al.[50] Labels are reproduced.

Synthesis

Droplet networks have also been used to perform a number of different synthesis reactions: genetic, chemical and biochemical. Firstly, cell-free transcription and

translation systems have been used to synthesise proteins *in situ*[52,53]. In one example, these proteins then inserted into the interconnecting droplet bilayers forming an ion-conducting pathway for rapid signalling[52]. Multi-step reactions have also been demonstrated in droplet networks[57,63,101] since the compartments allow different reaction conditions to be achieved. In another example, an enzymatic cascade reaction propagated along a droplet chain[64]. Synthetic droplets which can synthesis their own energy would be extremely useful. For this reason, single droplet have been built which use the energy from light to drive ATP synthesis[15].

Shape change

Also, synthetic tissues have been designed to self-fold[50,92]. Here, individual droplet compartments are patterned in 2D or 3D. In one example, high-salt and low-salt droplets were patterned so that as water moved down the osmotic gradient (after network formation), the structure changed shape[50]. In this way, networks folded into otherwise unattainable geometries. Reversible shape changes have also been demonstrated in droplet networks. Here, multiple stimuli-responsive elements were patterned into the structure enabling it to shrink and bend[92].

Aqueous facing

Many of the literature examples of functional synthetic tissues, especially droplet-based networks, are constrained by their requirement for an external oil environment and therefore are not readily deployed in physiological environments. Multisomes are droplet networks built within an oil drop immersed within a bulk aqueous solution[27]. Such structures can be formed manually[63,102] or by using automatic techniques such as microfluidics[33] and 3D printing[50]. Multisomes enable droplet networks to not only communicate between their individual compartments but also with the external solution[63,102]. The ability to detach these multisomes from the stabilising wire loops would be useful development in order for these structures to reach their potential. Hydrogels have also been used to aid transfer to an aqueous environment, enclosing the droplet networks[33,34,103]. Electrical and chemical communication have

been achieved by including protein pores in the lipid bilayers formed at the interface of the encapsulated aqueous droplets and the encasing hydrogel[34].

1.5 Remote control

The ability to control the biomimetic functionality of synthetic cells and synthetic tissues, both tightly and remotely, is yet to be fully explored. Aside from introducing spatiotemporal resolution, the addition of sensory elements into these systems enables tetherless command of the cellular events, even reaching regions of the networks otherwise inaccessible.

Light

Light is an ideal candidate for the remote control of synthetic systems since it can be applied in a tight and precise manner and can be easily patterned. Further, light can transmit high volumes of data extremely rapidly.

Optogenetics is a technique used to control neuronal activity (with high resolution) using light. These neurons are first genetically engineered to express photosensitive ion channels and pumps[104]. Similar light-driven proteins have also enabled the functions of synthetic cells and tissues to be remotely controlled. Power generating systems have been built which harvest light energy, using it to drive protein synthesis[15]. Light sensors have also been developed[44,100]. For instance, a minimal synthetic retina (built from an array of droplets packed with photochemically-driven proton pumps) detected static, moving and greyscale images[100].

A second method for using light to activate synthetic tissue functionality was designed in which a protein-expression system was under the control of a photosensitive promoter[52]. Remote activation initiated formation of a pathway through which electrical signals were transmitted[52]. Control of enzymatic reactions using light has also been shown within simple synthetic cells[74].

Magnetism

An alternative method to remotely control and manipulate specific components of a tissue is using magnetic actuation. The behaviour of specific cellular components, such as ion channels, has been demonstrated by activating magnetic nanoparticles[105]. Whilst the use of magnetism as a means to control synthetic tissue functionality is yet to be fully explored, the inclusion of magnetic elements has been used to facilitate the motility of entire synthetic structures[39,92].

Temperature

The environmental temperature is essential to ensure the correct form and function of biologically-relevant molecules. Since it is relatively easy to alter the external temperature of a system, thermoregulation is one possible means to remotely control synthetic structures. Within droplet networks, temperature is known to disrupt lipid membranes. Exploiting this instability, the temperature-dependant release of encapsulated multisome contents was demonstrated[102]. Further, the use of thermoresponsive materials has been explored to remotely control synthetic tissues[92,106]. For instance, patterning the responsive hydrogel components of a gripper, enabled the structure to undergo the reversible shape changes essential for function[92].

pH

Additionally, environmental pH also plays an important role in determining the structure of biomolecules, affecting their activity. One example of using pH to remotely control the activity of a synthetic system involved pH-sensitive lipid bilayers. For instance a multisome, built from such lipids, burst when the surrounding solution became more acidic; the droplet contents were released into the bulk solution[102]. In another example, coacervates, built from functionalised dipeptides, demonstrated the ability to undergo pH-dependant structural reconfiguration imitating metamorphosis[110].

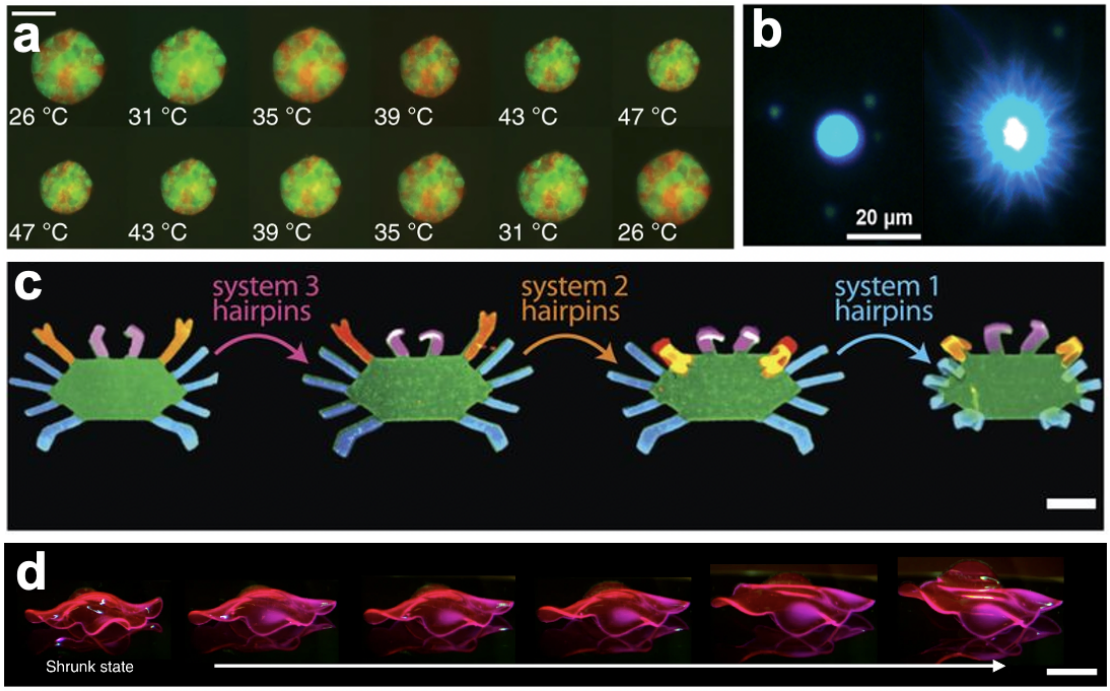


Figure 1.10: Remote control of synthetic constructs. **a,** Thermoresponsive synthetic tissue could contract or expand in response to temperature changes. Scale bar = 50 μm. **b,** Fluorescent microscopy images of a coacervate droplet. Acidifying the environment led to shape change of a coacervate artificial cell. Scale bar = 10 μm. **c,** The addition of DNA molecules led to controlled shape change of a hydrogel construct; only matching elements bent. Scale bar = 2mm. **d,** A thermo-responsive hydrogel ray swelled over time as the temperature decreased. Scale bar = 5 mm. Figures reproduced from **'a'** Gobbo et. al.[106], **'b'** Krishna Kumar et. al[107], **'c'** Cangialosi et. al.[108], **'d'** Nojoomi et. al.[109]

Molecular

The use of small molecule activators is another possible avenue for the remote control of synthetic structures. Specific DNA molecules, called hairpins, caused responsive hydrogel elements to swell to around 100 times in volume[108]. Using these molecular signals, a hydrogel flower and crab were formed in which only the regions with the matching sequence experienced any shape change[108]. Additionally, chemical molecules have been used to remotely activate synthetic droplet networks. Here, a two-droplet module was built which functioned in an aqueous environment. First, a prodrug was transported from one droplet to the other via protein pores embedded in the interface. It was then activated by enzymes in the second droplet. The droplet contents were then released in a controlled manner when a molecular

cation chelator, added to the bulk solution, opened an ion-sensitive pore[63].

Mechanical

Mechanical disturbance, such as the application of acoustic waves, may not seem like the obvious way to control synthetic systems as they might destabilise droplet bilayers. However, the mechanosensitive channel MscL was successfully reconstitute and activated in a droplet pair[43] without causing disruption to the membrane. Further, a DIB system in which the bilayer was placed nearby a vibrating hair, could transduce the mechanical stimulus into an electric signal[32]; a similar phenomenon has been shown in a DHB system[111].

1.6 Thesis Summary

Outlined in this thesis is the development of a minimal synthetic nerve which uses the external activation of light-driven proteins to propagate sensory information over centimetre distances. Inspired by the architecture of an afferent nerve, this synthetic (non-living) imitation, was constructed using only the components essential for function. Whilst it was designed to emulate biological tissues, it should be noted that it wasn't intended to be a perfect replicate. In the future, similar synthetic nerves might act as a novel alternative to conventional bioelectronic devices, for applications in medicine, soft robotics and computing.

Beginning with the development of photosensory droplets capable of wireless power generation, the manner in which several synthetic neurons are assembled, and then patterned into nerve bundles, is narrated. The design and systematic assembly of this synthetic tissue is detailed in the following chapters. **Chapter 2** describes the formation of a photosensory module, which enables the synthetic nerve to be powered by light. **Chapter 3** details the formation of a minimal synthetic afferent neuron; elaborating the use of this light-powered module to perform simple electrochemical communication. Signalling in these synthetic neurons are both rapid and directional. Moreover, they can release transmitters from their terminals which generate functional outputs downstream. Patterning these synthetic neurons

and assembling them into a nerve bundle enables the simultaneous transmission of discrete signals along parallel axons, as reported in **Chapter 4**. Ultimately, a simple hybrid tissue is built demonstrating photoinduced communication across the device-cell interface. Future developments of the synthetic nerve and other similar tissues, including possible applications, are outlined in **Chapter 5**. Finally, a detailed report of the experimental methods and materials is provided in **Chapter 6**.

2

A Photosensing Module

In soft bioelectronics, ideal devices would be remotely and wirelessly powered. **Chapter 2** outlines the formation of photosensory modules, formed when light-driven microbial rhodopsins (archaerhodopsin-3 and bacteriorhodopsin) insert into a droplet interface bilayer (Fig. 2.1). Using an external stimulus, these photoactivated proteins generate signals in a tetherless manner. In addition, the photosensory system was used to carry out an extensive biophysical characterisation of the light-driven protein archaerhodopsin-3, elucidating information surrounding its proton pumping mechanism and spectral properties.

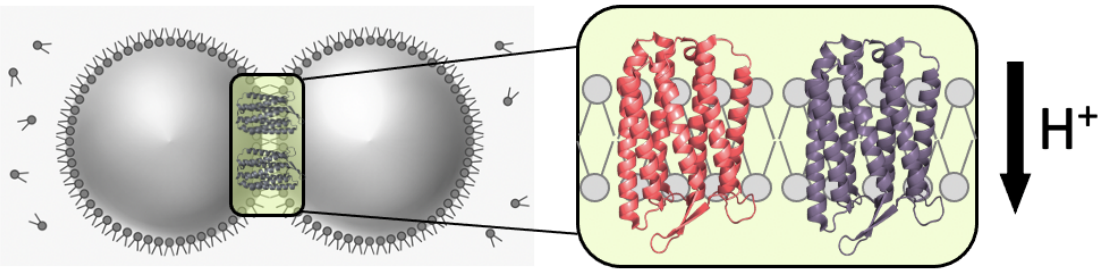


Figure 2.1: A photosensory module. Light-driven proteins insert into the droplet interface bilayer. Both archaerhodopsin-3 (pink) and bacteriorhodopsin (purple) pump protons (H^+) across the bilayer upon illumination (with yellow-green light).

Acknowledgement

The author led the development of the photosensory modules outlined in this chapter. The author would like to thank Dr Vanessa Restrepo Schild (**V.R.S**, Bayley Group, University of Oxford) for preliminary work on light-sensing bilayers and for technical training. Additionally, thanks to Dr Javier Vinals (**J.V**, Watts Group, University of Oxford) who expressed and purified the microbial rhodopsins and recorded their UV-Visible spectra. Alpha hemolysin pores were expressed by Idil Cazimoglu (**I.C**, Bayley Group, University of Oxford). Time-resolved absorption experiments were performed in collaboration with Dr Vanessa Restrepo Schild (**V.R.S**) and Professor Claire Vallance (**C.V**, University of Oxford). The author would also like to acknowledge the technical assistance of the Electrical and Mechanical Workshops (University of Oxford) and Tecella.

Publication

At the time of this thesis submission, a manuscript is in preparation detailing the work on archaerhodopsin-3 functionality described in this chapter.

- Vinals Camallonga, J., **Hoskin, C.E.G.**, Restrepo Schild, V., Bada Juarez, J., Crowther, O., Judge, P., Vallance, C., Bayley, H., and Watts, A. *Enhanced versatility and spectral tuning of Archaerhodopsin-3 through targeted mutation for biotechnological application.* (Joint 1st author).

2.1 Introduction

2.1.1 Photoreceptors

In all domains of life, organisms employ photoreceptor proteins to sense and respond to light[11]. The light-sensitivity (and colour) of photoreceptor proteins arise from bound chromophores[11]. In fact, protein classification is based on the chemical structure of the light-absorbing chromophore, with each family subdivided based on sequence similarities.

Rhodopsins are a large superfamily of photochemically active membrane proteins composed of an opsin apoprotein and a retinal chromophore. A common heptahelical architecture links the members of the rhodopsin family: the animal, microbial and heliorhodopsins. For animal and microbial rhodopsins their N-terminus faces the outside of the cell and the C-terminus the inside[11]; heliorhodopsins (only discovered in 2018) exhibit the reverse orientation[112,113]. Additionally, protein sequences differ greatly[114,115,116,117]; it is merely a result of convergent evolution that they all use retinal photochemistry[11,118]. Animals employ rhodopsin proteins for vision, and for non-visual applications such as to dictate the entrainable oscillations of the circadian clock[119] or in photoperiodism[119]. In microorganisms, rhodopsins function as light sensors and enable light energy to be harvested[11,120,121,122]. The function of heliorhodopsins is currently unknown.

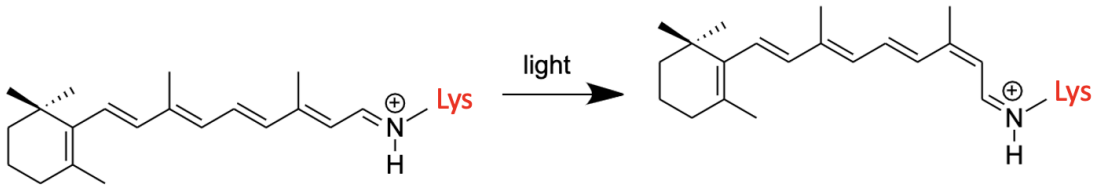


Figure 2.2: Retinal photoisomerisation Light provides the energy required to convert the all-trans retinal to its 13-cis isomer. The retinal chromophore is covalently linked to the ϵ-amine group of a lysine residue via a protonated Schiff base. Structures were drawn using ChemDraw[6].

At the core of rhodopsin function is retinal photoisomerisation. The retinal chromophore (vitamin A aldehyde) is attached to the ϵ-amino group of a lysine

residue via a Schiff base linkage[11,122] (Fig. 2.2). Retinal photoexcitation initiates the conversion of one isomeric form of the chromophore to another. In turn, this triggers the (small) protein structural changes required for function. Retinal photoisomerisation is one of the fastest and most efficient reactions found in nature[11]. Interestingly, exposure to light destroys animal rhodopsins such as those found in retinal rod cells. Here, isomerisation (11-cis to all-trans retinal) is irreversible as light causes the opsin and retinal to dissociate: bleaching. However, this phenomenon is not experienced by microbial rhodopsins. Isomerisation (all-trans to 13-cis retinal) triggers an ordered sequence of conformational (and spectroscopic) changes in the protein which cycles back to all-trans-retinal in the dark[123]. This process is discussed in more detail later (Fig. 2.4, 3.10).

2.1.2 Microbial rhodopsins

This thesis will focus on microbial rhodopsins. Their natural ubiquity means that genes encoding these proteins have been discovered in bacteria[116], archaea[115,121], unicellular eukaryotes[120,124,125] and even giant viruses[126,127]. So far, an excess of 7000 microbial rhodopsins have been identified from throughout the prokaryotic domain and in lower eukaryotes (Fig. 2.3)[128]. This protein family is a notable example of evolution where minor modifications to a single biomolecule result in diverse chemical functionality. These functions can be placed into two broad categories:

1. **Sensors** - These proteins detect light to gain information about the environment and regulate cellular processes. They typically have a slow photocycle, providing more efficient light detection as the signalling intermediates remain for longer; one cycle typically lasts milliseconds to seconds[114].

2. **Transducers** - These proteins harvest light energy by converting it into electrochemical potential energy to power cellular processes. Rhodopsin pumps and channels typically have photocycles lasting tens of milliseconds[114,121,129].

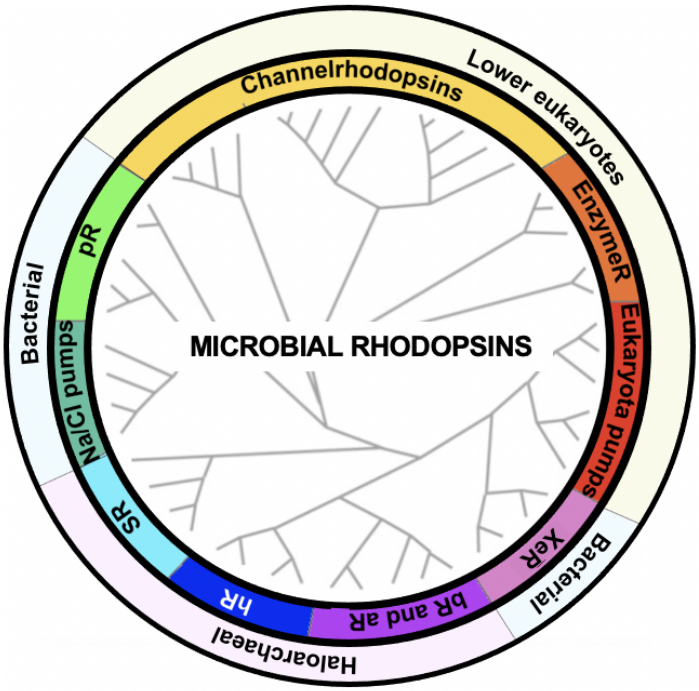


Figure 2.3: Microbial rhodopsin phylogenetic tree. Relationship between the different types of microbial rhodopsins which have been discovered. Figure adapted from Govorunova et. al.[128].

Due to their simplicity, these microbial proteins have been well characterised and utilised in a variety of applications as discussed later[130,131,132].

Bacteriorhodopsin

Discovered in 1971 in the purple membrane (PM) of *Halobacterium salinarum*, bacteriorhodopsin (bR) is the best characterised microbial rhodopsin[115]. This is primarily due to its simplicity, high chemical and thermal stability and ease of purification. Consequently it acts as a paradigm of photochemically-driven rhodopsin pumps, being widely used in the characterisation of novel homologues. Electron microscopy confirmed that bR has the heptahelical structure characteristic to microbial rhodopsins with the N-terminus facing out of the cell and the C-terminus inwards (Fig. 2.4a,b)[122,133]. Activated by green light ($\approx$ 570 nm), bR functions as an outward proton pump[115,133]. Within its native host, the role of bR

is to maintain a proton gradient across the membrane, providing energy to drive ATP synthesis and maintain other cellular processes in the absence of respiration.

Purple membrane

Within the PM, named for it signature colour, bR trimers arrange into a hexagonal crystal lattice[122,133]. Whilst trimerisation is important in enabling high-density packing of bR in the membrane, it is the monomers which form the functional unit of the bioenergetic protein (Fig. 2.4a). By weight, bR makes up around three quarters of the PM and is the sole protein constituent. Associated with each protein unit are ten haloarcheal lipids which have identical saturated dihydrophytol chains but differ in their polar head groups[122,134]. As with many membrane proteins the lipid-protein interactions play an important role in facilitating protein assembly and functionality[135]. Specific lipids fill the spaces between the hydrophobic protein surfaces providing flexibility to allow the protein to undergo key structural rearrangements.

Photocycle

The directional proton pumping of bR employs the Grotthuss mechanism; protons diffuse through a hydrogen bond network hopping between molecules by forming transient bonds[11]. Acting as a gate within the membrane, retinal imposes spacial and temporal control on proton transport further ensuring the uni-directional flow of protons out of the cell, even against large pH gradients. Additionally, geometrical changes to defined protein regions lead to modifications in the local environment of key residues. This alters their proton affinity and drives a specific sequence of events which results in a proton being pumped out of the cell[122]. The native lipids found within the purple membrane play an important role in the photocycle[136]

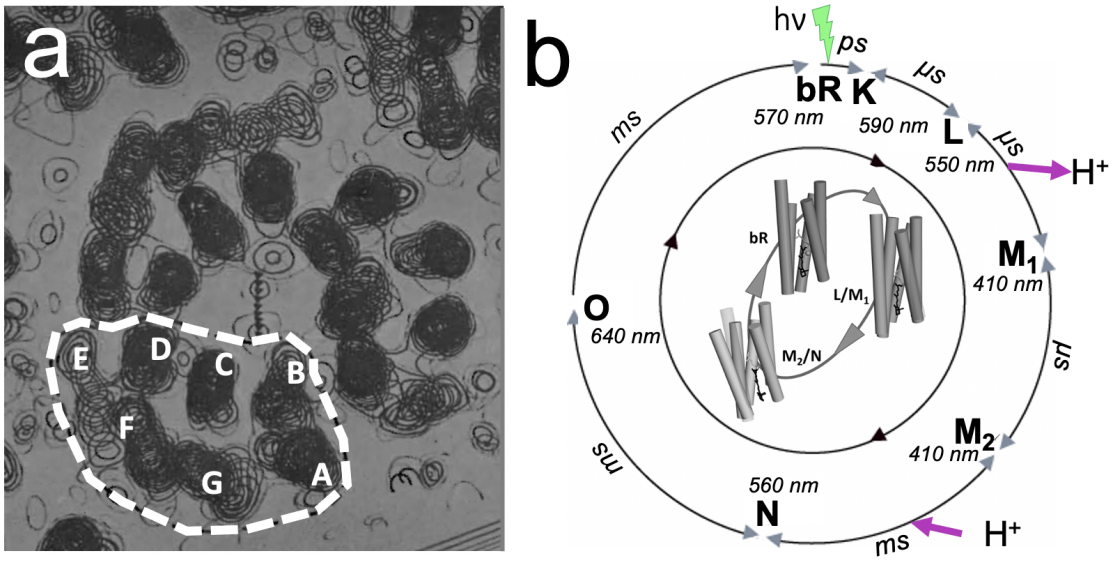


Figure 2.4: Bacteriorhodopsin. a, Crystal structure of bR in which one functional monomer is circled in white. The seven helices (A-G) are labelled. **b,** The bR photocycle. Key photo-intermediates are shown and the timescales of each intermediate step are noted alongside the absorbance of each intermediate. Proton release and uptake is shown in purple and light-absorption (hν) in green. Figure **'a'** was taken from Grigorieff et. al.[137], **'b'** adapted from Wickstrand et. al.[138]. Labels have been reproduced.

Proton transport in bacteriorhodopsin is accompanied by the thermal reisomerisation of the retinal chromophore in a cyclical process known as the photocycle. The conversion of these intermediates reflect the physical steps required to move a proton across the membrane, coupling charge transfer to conformational changes. A vast number of studies and experimental techniques have identified the key residues essential for proton pumping[11,122,138,139,140,141,142,143].

- The photocycle begins with the protein in the dark state. Here, a water molecule forms an extended hydrogen bonded network with the Schiff base and two key asparate residues (D85 and D96); this holds helices C and G apart (Fig. 2.4). Further, in this state the pKa of the Schiff base is stabilised at an elevated level than the closest proton acceptor (D85): pKa 13.5 and 2.2 respectively.

- The photocycle is initiated when the retinal photoisomerises. This gives rise to small structural re-configurations within the protein, reshaping the

retinal pocket. First the accessibility of the Schiff base to a key aspartate residue (D85) is improved by reducing the distance. Additionally a dipole shift occurs altering their respective pKa values which makes proton transfer to D85 favourable.

- Following this event, the retinal straightens away from D85 promoting the closure of the extracellular portion of the proton channel.
- Subsequently, the network of water molecules becomes disordered which reduces the rigidity of the extracellular section of the protein. This leads to proton release from the proton release complex (PRC): formed from two glutamate residues (E194 and E204) and some water molecules.
- Following proton release, the Schiff base is reprotonated; this is the rate-limiting step of the photocycle. A second aspartate residue (D96), located on the cytoplasmic side of the channel, donates the charge.
- A proton is consequently taken up from the cytoplasm to reprotonate D96.
- Finally, D85 is deprotonated via proton exchange to the proton release complex following the thermal re-isomerisation of retinal to its resting state configuration. The process can therefore occur again if another photon activates retinal photoisomerisation.

Archaerhodopsin

Expanding the family of archeal light-driven proton pumps are the archaerhodopsins (aR)[144]. Comparable to bR, aRs were found to tightly pack into trimers within crystalline membrane patches; such patches are named claret membrane (CM) for their characteristic colour[144]. The first aR discovered (aR1) produced a large signal output and displayed a high endogenous (native) fluorescence[144]. Three other aRs were subsequently discovered with similar properties: aR2, aR3 and aR4[145,146,147,148]. These CM-aR proteins exhibit over 80 % sequence homology to one another and ≈ 50-60 % similarity to bR[149]. A significant proportion of these

conserved residues lie in the proton pumping pathway which is logical since they are all outward-driven proton pumps.

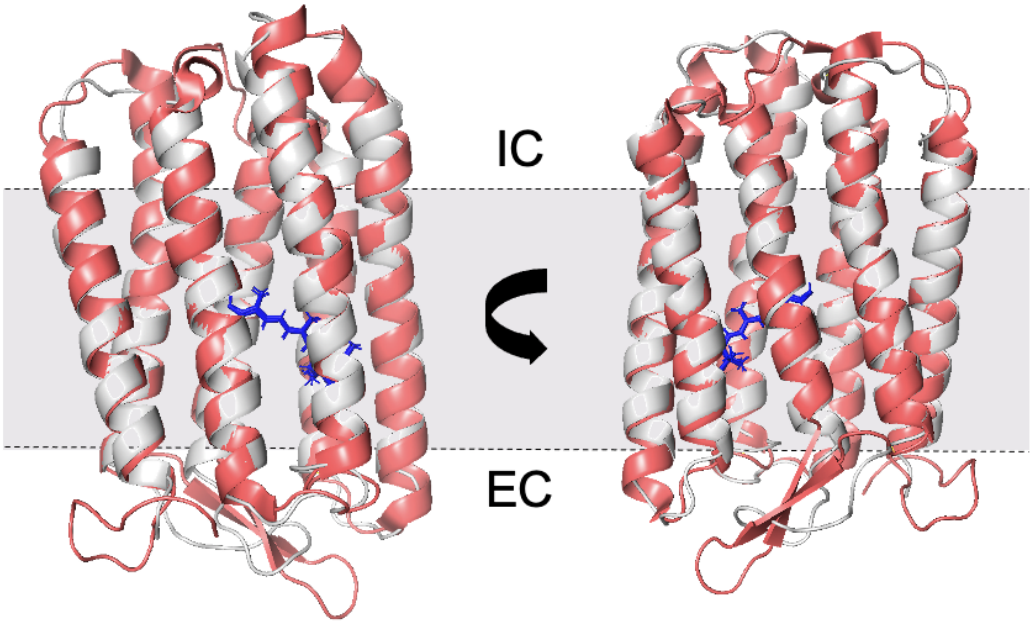


Figure 2.5: Proton pump structures. Overlay of the bacteriorhodopsin structure (white, 2BRD[122]) and archaerhodopsin-3 structure (pink, 6GUZ[150]). The retinal chromophores are shown in blue. The region of the protein which inserts into the bilayer is indicated by the grey box with the intracellular (in) and extracellular (out) faces labelled. Figure made in PyMol.

Alongside aR proteins, the CM contains haloarcheal lipids and a red-coloured carotenoid bacterioruberin[144], which gives the CM its colour. Not found in bR, the role of this carotenoid attracted interest. Since it is located at the monomer interface, a key role in oligomeric packing into trimers was proposed[144,149,151]. Further, it may protect the retinal chromophore against photobleaching and damage, which is supported by the enhanced production of bacterioruberin under light[152]. As the excited state is short-lived, and it isn't orientated with respect to retinal in a manner beneficial to energy transfer, bacterioruberin does not act as an antenna molecule for light harvesting[153]. The haloarcheal lipids located in the CM are a requisite for the correct conformational changes associated with the protein photocycle; proton uptake and release steps are reversed in delipidated aR proteins.

First identified in the claret membrane (CM) of *Halorubrum sodomense*, archaerhodopsin-3 (CM-aR3) is composed of 252 amino acids which assemble into a heptahelical protein with a molecular weight of $\approx$ 27 kDa[121]. The crystal structure of CM-aR3 closely overlays with that of bR (Fig. 2.5) however the latter lacks components such as an omega loop[150]. As this structure was only recently elucidated[150], information surrounding the mechanism and properties of CM-aR3 is limited. However, as observed with bR, the photocycle of CM-aR3 progresses through several photo-intermediates[121,129,150] (Fig. 3.10). Despite these comparisons, CM-aR3 has been found to generate higher photosignals than PM-bR. One explanation proposed was that key residues in the proton pumping pathway display altered pK_as. Alternatively, the proposed photocycle of CM-aR3[150] suggests that it might skip some of the bR intermediates enabling faster kinetics[121,129,154]. Despite the similarities between the crystal structures of CM-aR3 and PM-bR (Fig. 2.5), their subtle differences allow CM-aR3 to outperform PM-bR.

Channelrhodopsin

Remarkably, only one natural light-activated channel family has been found and it lacks any sequence homology to other known ion channels. Located within the eyespot of the green algae *Chlamydomonas reinhardtii*, channelrhodopsin (ChR) is involved in photoperception and phototaxis, enabling motile cells to locate desirable light conditions by ultimately depolarising the flagellar membrane[155]. Since its discovery in 2002[124], several more ChR variants have been identified[120,128,156]. Further, ChRs have been engineered to create a vast library of mutants with enhanced properties such as improved ion conductance or photocycle kinetics. Using cation channelrhodopsins (CCR) as the protein backbone, anion-conducting analogues were engineered by removing negatively charged residues from the channel pathway[128,157]. A year later, in 2015, naturally occurring anion channelrhodopsins (ACR) were isolated from the algae *Guillardia theta*[156128]. The catalogue of ACRs has since been expanded using both design and genome mining[128]. Besides ion

selectivity, ChRs also vary in photocycle kinetics, light sensitivity and activating wavelength; absorption peaks for known ChRs span 440 to 590 nm[11,155].

Whilst ChRs also exploit retinal photochemistry, these channels can flux ≈ 100 ions per second and exhibit increased light sensitivity compared to rhodopsin pumps[155]. The most extensively studied variant is ChR2 due to its superior channel characteristics[155]. Monomeric ChR2 is formed from a N-terminal membrane spanning domain (the characteristic heptahelical rhodopsin architecture) with an additional C-terminal intracellular domain, proposed to be involved in protein-protein interactions and signalling. It has low sequence homology to proton pumps like bR (15 - 20 %) but most of the essential amino acids are conserved[124]. As with proton pumps, the monomer forms the active unit; however ChR2 typically dimerises[158]. Extracellular hydrogen-bonding interactions on neighbouring helices, intracellular disulphide bonds and the presence of several internal water molecules, all play important roles in dimer formation.

Interestingly, the channel activity of ChR2 is a two photon reaction. The first opens the channel, with a rate constant of 5000 s^{-1}, and the second accelerates the photocycle further[159]. Photoisomerisation of retinal also results in a conformational change leading to channel opening and ion flux (of around 10-100 charges per photocycle) down their concentration gradient and across the membrane[158,159]. It is cation selective, allowing a variety of positively charged ions to pass along the water-filled polar channel: protons, lithium, sodium, caesium, potassium and calcium ions (permeability is in that order with inward rectification)[155]. Moreover, the channel isn't continuous but a series of cavities, two on the intracellular side and two on the extracellular side, which are linked by gates formed from an extended hydrogen-bonded network and several side-chain residues. The Schiff base of the retinal chromophore dictates the opening of the gates, controlling ion transport[128].

Whilst ChR2 functions predominately as a channel it has bifunctional characteristics and can also act as an outward proton pump; both are light initiated[155,160]. As with other rhodopsin pumps, the mechanism is insensitive to the ion electrochemical gradient whereas channel activity is highly sensitive.

Microbial rhodopsin summary

Sunlight drives virtually all life on Earth's surface so it is not surprising that nature has developed ways to harvest its energy. Microbial rhodopsins are a large family of retinal-binding proteins that provide light-driven ion transport and sensory functions to microorganisms; the summary table below is by no means complete and new members of this family are constantly being discovered.

Rhodopsin name	**Function**
Bacteriorhodopsin[122]	outward proton pump
Archaerhodopsin[121,150]	outward proton pump
Halorhodopsin[161]	inward chloride pump
Schizorhodopsins[162]	inward proton pumps
Xanthorhodopsin[153,163]	proton pump
Proteorhodopsins[116,129]	outward proton pump
Krokinobacter rhodopsin[164]	outward sodium (and proton) pump
Channelrhodopsin[120,124]	ion channel (can act as a pump)
Sensory rhodopsins[114,165]	phototaxis
Enzymerhodopsins[166]	light-regulation of enzymatic functions
Fungal rhodopsins[167]	proton pumps or sensors
Virus rhodopsins[168]	unknown
Xenorhodopsins[169,170]	inward proton pumps or sensors

2.1.3 Optogenetics

A major application of microbial rhodopsins has been for the modulation of neuronal activity *in vivo*, in a technique known as optogenetics. Francis Crick proposed the use of light to control the biochemical events of individual neuronal cells since the technique would be more specific than electrical stimulation, and faster than pharmaceuticals[171]. Following a combination of technological advances, and the discovery of optically-activated rhodopsins, in 2005 his vision was first demonstrated[172]. In this initial experiment, mammalian neurons were infected (*in vitro*) with a genetically engineered virus, resulting in the expression of the light-activated channelrhodopsin (ChR2) on the neuron surface. Illumination with blue light caused these neurons to fire action potentials demonstrating control over neuronal activity[172]. The high spatial and temporal precision with which individual cells can be selectively targeted has meant that optogenetics revolutionised the

field by addressing the key limitations. Optogenetics has enhanced knowledge of fundamental neuroscience and neurological pathologies, but also provided a means to treat many of these conditions.

The major protein used to activate neurons is channelrhodopsin-2 (ChR2)[131,132]. Archaerhodopsin-3 (CM-aR3) or *Natronomonas pharaonis* halorhodopsin (NpHR) are typically used to silence neuronal firing[121,131,132,173]. Both NpHR (an inward chloride pump) and CM-aR3 (an outward proton pump) can only transport a maximum of one charge across the membrane per captured photon, they require high levels of expression and increased light intensities in order to achieve neural photosuppression. Since this can result in undesirable side-effects, the discovery of anion channelrhodopsins (ACRs) may be the way forward[174]. ACRs offer unprecedented photoefficiency to silence neurons by light-gated chloride conduction offering both physiological relevance and higher ion flux. However, reports have indicated that following illumination, the photosignals generated by channelrhodopsins (e.g. ChR2) decrease and the protein can even become inactivated over time[120]. CM-aR3 doesn't experience this phenomena, recovering quickly after illumination, thereby aiding its use in optogenetics. In theory activating any photochemically-driven natural or synthetic protein would permit precise control over bioelectric signalling. One example of a synthetic light-gated potassium channel for use in optogenetics was BLINK1: the photosensory region of a (plant) blue-light receptor was fused to a potassium channel[175]. Its application was demonstrated in the guard cells of a plant *Arabidopsis thaliana* and upon illumination the channel opened and ions entered the cell. This caused the guard cells to swell, opening the stomata and enabling the plant to grow more quickly[176].

2.1.4 Voltage Indicators

Interestingly, the intrinsic fluorescence of such rhodopsins is also useful. A long-standing goal in neuroscience is to understand how the spatiotemporal patterns of neuronal firing underlie brain functionality. Mutations of microbial rhodopsins have been created in which their intrinsic fluorescence changes significantly with

voltage[177,178,179]. The protein, e.g., archaerhodopsin-3, is then expressed in the neuronal membranes of mammalian cells: acting as a genetically encoded voltage indicator (GEVI)[180]. Incredibly, by using GEVIs it was possible to record neural spikes in awake mice and flies with milisecond precision[181].

2.1.5 Biosensors and Bioelectronics

Several groups have been exploring the potential use of microbial rhodopsins as biosensors or bioelectronic devices. The inherent (structural, chemical and thermal) stability of the crystalline purple membrane makes bR a very attractive protein for these applications. It uses the light energy captured by its retinal chromophore to drive proton transport across the membrane, generating an electrochemical gradient. Exploiting this photoactivity, bR has been made into thin films or gels which can act as photovoltaic or solar cells[182], security inks[183] or even in optical computing[134]. However, the performance of these devices depend on the bR protein photocycle. For instance, a photovoltaic cell can only generate small currents due to the long photocycle of bR; aR3 might enhance device functionality since it has a faster photocycle[129,150].

Further, since bR is a wavelength specific photoactive pump, it can be employed in image detection. Through integration with other biomolecules, bR films have been used in retinal prosthesis to treat blindness[184]; they have the potential to reach higher resolution than conventional (semi-conductor based) implants. More recently, soft materials have been used to built devices such as biomimetic artificial retinas[31]. Here, using an array of bR pixels, detection of static, moving and greyscale images was achieved[31]. Mutagenesis has been used to investigate the spectral properties of bR, generating functional mutants which are activated by different wavelengths. This might prove useful to permit colour detection in these biosensors.

2.2 Results

2.2.1 Materials preparation

Briefly discussed here are the methods used to prepare the materials required for photosensory module construction; a more detailed description can be found within **Chapter 6** (Materials and Methods).

During the preparation process, four key aqueous solutions were used.

Solution	MES (Sigma, M3671)	NaCl (Sigma, S7653)	DDM (Sigma, D4641)	pH
A	100 mM	100 mM	0.1%	6.5
B	100 mM	100 mM	0.001%	6.5
C	None	100 mM	None	6.5
D	100 mM	100 mM	None	6.5

2.2.2 Light-driven proton pumps

In this thesis, two simple, electrogenic proteins were used to generate bioelectrical signals: bacteriorhodopsin (bR) and archaerhodopsin-3 (aR3). Several strategies were employed to prepare these proteins for reconstitution; further details on their expression and purification may be found within **Chapter 6** (Materials and Methods). Protein preparation was done in conjunction with **J.V**. For each experiment described in this thesis, a single protein expression and purification batch was used.

2.2.2.1 Bacteriorhodopsin

Bacteriorhodopsin (bR) is a well-characterised photochemically-driven protein, known to function as a proton pump. Moreover, it has previously been reconstituted into droplet bilayers generating signals upon illumination[31,44]. For these reasons, the output of a bR-containing droplet bilayer was used as a benchmark from which to compare the photoactivity of the homologous protein aR3.

Sigma-bR

Firstly, bR was prepared in the same manner as done for previous droplet bilayer experiments[31,44]. Lyophilised purple membrane (PM, containing bR) was purchased from Sigma. The Sigma-bR powder was dissolved directly into Solution A in which the detergent (DDM) was above the critical micelle concentration (CMC, 0.1 % (w/v) DDM). Here, detergent micelles surrounded a section of the PM crystals resulting in their partial dispersal into smaller fragments. The protein solution was then sonicated (30 minutes, water bath at 20 °C) to agitate the PM fragments and aid with micelle formation. Next, the protein was diluted (using Solution D) so that the final solution (Soution B) contained detergent (DDM) below the CMC (0.001 % (w/v) DDM). The final protein solution was concentrated using centrifugation to a Sigma-bR concentration of 0.15 - 0.25 mg mL^{-1} (measured using nanodrop). The Sigma-bR was stored at 4 ° C in the dark. Before each experiment, the solution was again sonicated and then vortexed to disrupt any subsequent PM aggregation.

```
SP|P96787|aR3   ---MDPIALQAGYDLLGDGRPETLWLGIGTLLMLIGTFYFLVRGWGVTDKDAREYYAVTI 57
SP|P02945|bR    MLELLPTAVEGVSQAQITGRPEWIWLALGTALMGLGTLYFLVKGMGVSDPDAKKFYAITT 60

SP|P96787|aR3   LVPGIASAAYLSMFFGIGLTEVTVGGEMLDIYYARYADWLFTTPLLLLDLALLAKVDRVT 117
SP|P02945|bR    LVPAIAFTMYLSMLLGYGLTMVPFGGEQNPIYWARYADWLFTTPLLLLDLALLVDADQGT 120

SP|P96787|aR3   IGTLVGVDALMIVTGLIGALSHTAIARYSWWLFSTICMIVVLYFLATSLRSAAKERGPEV 177
SP|P02945|bR    ILALVGADGIMIGTGLVGALTKVYSYRFVWWAISTAAMLYILYVLFFGFTSKAESMRPEV 180

SP|P96787|aR3   ASTFNTLTALVLVLWTAYPILWIIGTEGAGVVGLGIETLLFMVLDVTAKVGFGFILLRSR 237
SP|P02945|bR    ASTFKVLRNVTVVLWSAYPVVWLIGSEGAGIVPLNIETLLFMVLDVSAKVGFGLILLRSR 240

SP|P96787|aR3   AILGDTEAPEPSAGADVSAAD- 258
SP|P02945|bR    AIFGEAEAPEPSAGDGAAATSD 262
```

Figure 2.6: Sequence comparison between CM-aR3 and PM-bR. Alignment performed using the UniProt sequence alignment tool. Conserved residues are shown in yellow, helical regions are underlined and the Schiff Base lysine residue is in bold.

PM-bR

Additionally, bR was expressed within its native archeal host (*Halobacterium salinarum*) by **J.V** and purified as PM fragments[185]. This PM-bR protein was

purple in colour. PM-bR protein samples were then buffer exchanged (using a P3 BioSpin column) into Solution A (with a DDM detergent concentration of 0.1 % (w/v), higher than the CMC) and sonicated (30 minutes, water bath at 20 °C) for homogenisation. It is worth noting that during buffer exchange some protein was lost, sticking to the column and turning the white resin pale purple in colour. The PM-bR was then diluted (using Solution D) to a final solution in which the detergent was below the CMC (Solution B, 0.001% (w/v) DDM). PM-bR samples (0.15 - 0.25 mg mL^{-1} (measured using nanodrop) were stored at 4 ° C in the dark. PM-bR samples required regular agitation as they tended to aggregate: sonication and vortexing were used.

2.2.2.2 Archaerhodopsin-3

The predominant microbial rhodopsin used within this thesis was the light-driven proton pump archaerhodopsin-3 (aR3)[121,146,147], which displays high sequence similarity (> 80 %) to bR (Fig. 2.6). Due to their high comparability, aR3-containing droplet bilayers were prepared using a similar approach.

CM-aR3

Firstly, archaerhodopsin-3 (aR3) protein was expressed in the native archea *Halorubrum sodomense* (strain RD-26) and purified by **J.V** as fragments of the claret membrane (CM) (confirmed by AFM[186]). The CM-aR3 protein was red/pink in colour. Prior to use, samples were buffer exchanged into Solution A and sonicated (30 minutes, water bath at 20 °C). Since the detergent concentration was above the CMC, sonication aided micelle formation as well as agitated the CM fragments. The CM-aR3 solution was then diluted (as described for PM-bR) so that the detergent concentration was below the CMC to enable formation of the photosensory module. All CM-aR3 protein samples were stored at 4 °C in the dark with a final concentration of 0.15 - 0.25 mg mL^{-1} (measured using nanodrop) in Solution B. Prior to use, the CM-aR3 solution was further homogenised by gently vortexing to disrupt any aggregation; smaller fragments more favourably insert into artificial bilayers without breaking them. Interestingly, the homogenisation of the CM fragments

was relatively simple compared to PM-bR, most likely due to the requirement of a bacterioruberin carotenoid in oligomeric assembly.

In the absence of industrial bioreactors, it takes weeks to grow sufficient *Halorubrum sodomense* to purify miligrams of CM-aR3 protein. Whilst it is relatively slow, extracting CM-aR3 from its native host has several advantages such as natural chromophore incorporation during protein formation, endogenous lipids to aid folding [135] and the presence of the bacterioruberin carotenoid.

E.coli-expressed aR3

Fortunately, like bR, aR3 can be heterologously expressed within the bacteria *Escherichia coli (E.coli, EC)*: a simple, robust, and inexpensive system[187]. In comparison to the growth of *H. sodomense*, *E. coli* can grow and express large quantities of protein within days. Expression and purification of EC-aR3 was by **J.V** and the template plasmid used was WT Arch-3 in pET28b (addgene ID: 58487). The EC-aR3 had identical protein sequence to the CM-aR3 but was codon-optimised, contained a C-terminal histidine-tag (for protein stability and purification) and no CM (Fig. 2.6). Disadvantages of this expression method are that solely exogenous (non-native) lipids are present during protein formation and the final EC-aR3 protein lacks the bacterioruberin carotenoid. Since both play key roles in trimer formation, the EC-aR3 was monomeric (confirmed by a hypsochromic shift in absorbance, (Fig. 2.27[188]).

Expression of the EC-aR3 protein was visible to the naked eye as the media turned red/purple in colour. Following purification, the EC-aR3 was reconstituted into detergent micelles[127] since it could not be directly inserted into the DIB from a detergent-containing solution. Interactions between micelle lipids and EC-aR3 stabilised the protein, and increased the solubility of protein folding intermediates. Further, micelles have curved membranes which may imitate the native membrane assisting in reconstitution. EC-aR3 protein samples were treated as described for CM-aR3: buffer exchanged in Solution A, sonicated and then diluted to a final

protein concentration of 0.15 - 0.25 mg mL^{-1} (measured using nanodrop) in Solution B (6). All samples were stored at 4 ° C in the dark and gently vortexed before use.

2.2.3 Ion-conducting protein pores

Protein pores form solvent-filled channels in which ions and small molecules can passively diffuse across a membrane.

2.2.3.1 Alpha-hemolysin

In this thesis, the bacterial protein pore alpha-hemolysin (αHL) was used since it has been extensively studied in droplet bilayers[44,50,53,63]. Protocol for the transformation and expression of alpha hemolysin (αHL) was adapted by **I.C**, from Lind et. al.[189]. The protein was expressed in the native Staphylococcus aureus (Wood 46, ATCC). The αHL was purified as monomers, concentrated and stored at -80 ° C. Upon insertion into the bilayer, the monomers assembled to form the heptameric pore.

2.2.4 System design

Further details on the photosensory module experimental set-up can be found located in **Chapter 6**, Materials and Methods.

2.2.4.1 Photosensory module formation

Photosensory modules were composed of a droplet interface bilayer, formed between an aqueous droplet containing a photochemically-driven proton pump (the photosensory droplet, 200 nL, Solution A, 0.15 – 0.25 mg mL^{-1} bR or aR3) and a protein-free aqueous droplet (200 nL, Solution D). Protein spontaneously and vectorially inserted into the DIB from the photosensory droplet. To form such a module, aqueous droplets were encapsulated in a lipid monolayer by pipetting them into a lipid-in-oil solution (hexadecane and silicone oil (35:65) containing 10 mg mL^{-1} 1,2-diphytanoyl-sn-glycero-phosphatidylcholine (DPhPC)). After a few minutes (to allow for complete monolayer formation), they were gently brought together; a DIB formed within minutes (Fig. 2.1). A high lipid concentration

was used in photosensory module formation to minimise the frequency of droplet coalescence by having a large lipid excess within the solution.

2.2.4.2 Electrical characterisation

Ag/AgCl electrodes were added to the droplets to permit electrical characterisation of the module in response to light (Fig. 2.7). The electrodes were required to measure the signal output in 'real time'.

The ionic signal, generated by the microbial rhodopsin upon illumination, is carried by mobile ions in the aqueous droplets of the photosensory module. The electrodes, composed of a silver wire with a chlorinated tip, needed to be in contact with the (chloride-ion-containing) solution to work. In this case, compensating charge can be provided at the Ag/AgCl electrodes to enable the signal to travel through the external circuit and the output to be processed by the amplifier. Upon illumination, protons move across the bilayer and out of the photosensory droplet. At the electrode in the photosensory droplet, silver (Ag) is oxidised (to Ag^+) and a chloride ion (Cl^-) is picked up from solution. The electron (e^-) from the oxidation of silver moves through the external circuit to the other electrode as a measurable signal. At this electrode, a chloride ion (Cl^-) moves into solution to neutralise the positive charge arising from the protons pumped across the bilayer. The electron (e^-) then converts Ag^+ to silver (Ag) maintaining charge neutrality at the electrode.

Ag/AgCl electrodes are a good choice for these measurements because of their low noise levels generated during signal recording and low impedance. They have also been shown to function well in droplet and hydrogel systems in which picoampere signal outputs, generated by microbial rhodopsins, were recorded[31,44]. In addition, silver wire is cheap and easy to use. This technique, in which silver/silver chloride electrodes were used to record the signals generated by microbial rhodopsins, was developed by **V.R.S**.

Previous work with bR-rich DIBs performed all electrical recordings within a solid metal Faraday cage to minimise background noise and enable the picoampere (pA) signals to be detected[31,44]. The cage contained a platform (Mechanical

workshop, University of Oxford) which supported the amplifier headstage (Axopatch 200B, Axon Instruments), two micromanipulators (Narishige, NMN-21) and the experimental (PMMA) chamber. Ag/AgCl electrodes were prepared from silver wire (100 µm diameter, Sigma) with the tips incubated in sodium hypochlorite (NaClO, 10% active chlorine, Sigma) and coated with agarose (1% low-gelling, Sigma). Each electrode was connected, via a holder, to the amplifier headstage and to an independent micromanipulator to enable movement. PMMA chambers, filled with the lipid-in-oil, were positioned in the centre of the stage, directly below a fibre-couple LED bundle at a distance of 5 cm. Electrodes were immersed in the lipid-in-oil before droplets (200 nL, ≈700 μm diameter) were pipetted directly onto them. Signals were recorded with an amplifier (Axopatch 200B, Axon Instruments), connected to a digitizer (Digidata 1440 A, Axon Instruments) and analysed using Clampfit (version 10.3, Axon Instruments).

At the start and end of each electrical experiment the photoresponse of a DIB, formed between two protein-free droplets, was characterised. This was to ensure that no artifacts arose from photochemistry at the Ag/AgCl electrode surface. A major drawback of these electrodes in this system is that AgCl is sensitive to light and decomposes to form metallic silver. First a capacitance measurement (application of a triangular voltage waveform, ±15 mV, 30 s peak-to-peak) was taken to determine whether a DIB successfully formed; it was assumed that there was a bilayer if the capacitance was greater than 20 pF (Fig. 2.7c)[31]. The droplet pair was then illuminated, first with infrared (IR) light (LED Channel 1, 680 - 741 nm peaks at 722 nm, 16 ± 5.0 mW), or with ultraviolet (UV) light (355 - 390 nm peaks at 367 nm, 15 ± 3.9 mW), and then with yellow-green (YG) light (Channels 4 and 5, 490 - 608 nm peaks at 592 nm and 550 nm, 15 ± 4.5 mW) (Fig. 2.9). Electrodes which generated a signal upon illumination were discarded and fresh electrodes were made and tested.

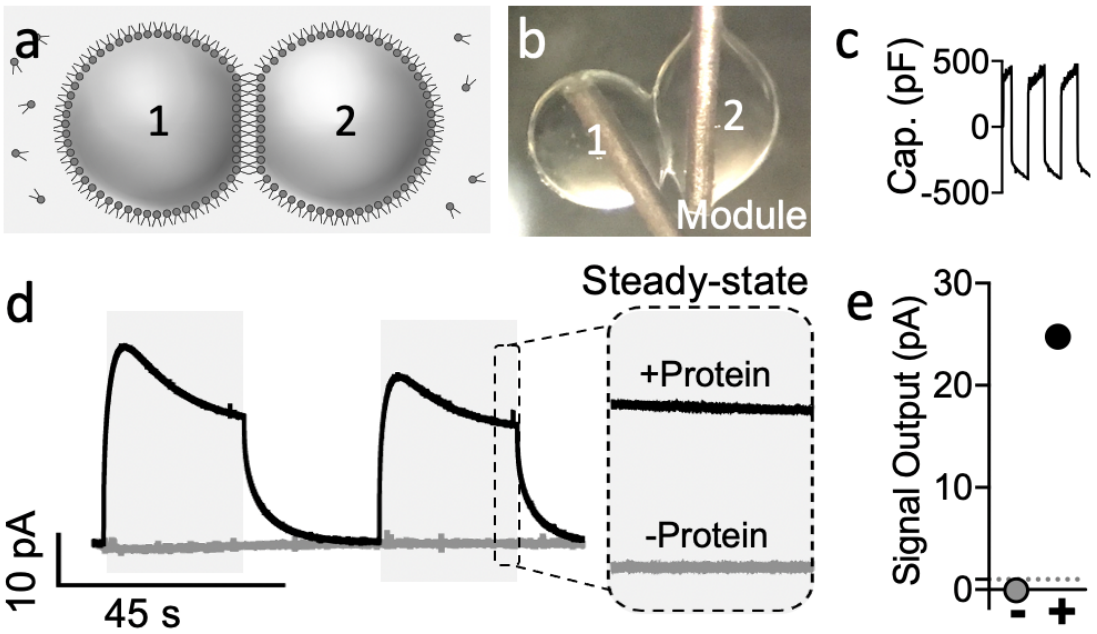


Figure 2.7: Monitoring protein photoactivity. **a,** Formation of a DIB. A photosensory (a1) and protein-free (a2) droplet are connected via a droplet interface bilayer (DIB). **b,** Photograph of a droplet pair (a photosensory module). Ag/AgCl electrodes are added to the droplets (200 nL). The photosensory droplet (b1) contains the recording electrode; the protein-free droplet (b2) the ground. **c,** Trace of the capacitance recorded (in the dark) across a DIB (mean ± SD, n = 3). A capacitance > 20 pF (dotted line) is taken to indicate bilayer formation. **d,** Signal output recorded across a DIB with (black, +protein) or without (grey, -protein) CM-aR3 upon illumination (YG light, 490 - 608 nm with peaks at 550 and 592 nm, 15 ± 4.5 mW, grey bars indicates when the light is on). The steady-state signal output is indicated by the dotted box. **e,** Chart of the mean steady-state output in 'd'. A 1.0-pA threshold (grey dotted line) was taken to indicate protein photoactivity; only when CM-aR3 (+protein) is present is a signal above the threshold produced.

A photosensory module (Fig. 2.1) was then made and characterised. Bilayer formation, between the photosensory and protein-free droplets, was confirmed by measurement of the capacitance (> 20 pF, application of a triangular voltage waveform, ±15 mV, 30 s peak-to-peak). The recording electrode was inserted into the photosensory droplet (unless otherwise specified). An arbitrary threshold value of 1.0-pA was set to indicate protein activity and is based on the baseline noise inherent to the amplifier (Fig. 2.7e). To ensure that the light-activated proteins didn't experience any photobleaching, their activity was recorded using YG light (550 and 592 nm, 15 ± 4.5 mW) at the start and end of the experiment

and compared. If there was a significant reduction in signal generation then the experiment was discarded and repeated.

When electrodes were included in the droplets, signals generated following proton pumping across the bilayer were recorded; both the magnitude and polarity of the steady-state signals was determined. Since protons are charged ions, pumping out of the photosensory droplet generated a positive terminal at the ground electrode and a negative terminal at the recording electrode; the latter located within the photosensory droplet. Therefore, electrons flowed towards the positively charged terminal generating the electron current. The conventional current flowed in the opposite direction, towards the negative (photosensory droplet) terminal, and was recorded by the amplifier. A positive signal was defined as one in which the conventional current flows into the recording electrode; the electron current flows into the ground electrode (Molecular Devices). If a photosensory module were to pump protons into the photosensory droplet, then a negative signal would be generated (Fig. 2.14, 2.16).

Several factors influenced the signal output of the photosensory modules, resulting in variability. Firstly, insertion of the microbial rhodopsins into the bilayer was stochastic, differing between experiments. Moreover, no two bilayers were of identical size, meaning not only the surface area but also bilayer-curvature varied. Interestingly, the capacitive current (arising from the bilayer itself) influenced the profile of the signal output generating a heterogeneous sample of signal behaviours, as expected from literature models[190,191]. This is due to the fact that the membrane acts as an insulator and forms both the capacitor and resistor within the circuit. Here, the entire signal charges the membrane capacitance and no signal flows across the membrane resistance. As the membrane capacitance becomes more charged, a larger fraction of the injected signal flowed across the membrane resistance. Once the capacitance was fully charged, the system reached a steady-state and the entire signal flowed across the membrane resistance. Therefore, the values of the bilayer capacitance and resistance will determine the signal profile recorded by the amplifier. For instance, a bilayer with a small surface area is likely to have a low capacitance

meaning that overshoot signals (where the transitional signal exceeds the steady-state and baseline) may be generated (Fig. 2.8). Likewise a bilayer with a large surface area may generate undershoot signals (where the transitional signal doesn't rise above the steady-state nor dip below the baseline). (Fig. 2.8).

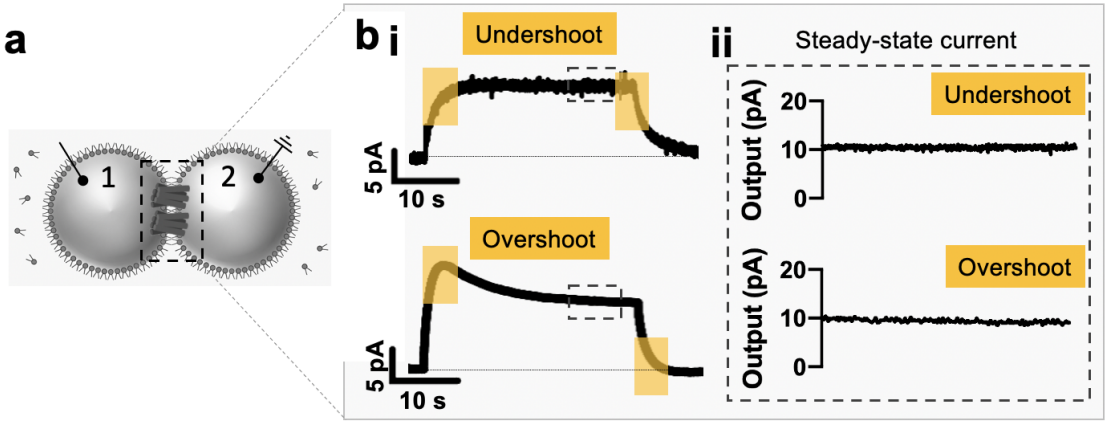


Figure 2.8: Shape of the signal trace. a, Schematic of a CM-aR3-containing DIB. The recording electrode is located within the photosensory droplet (a1, + CM-aR3) and the ground electrode within the protein-free droplet (a2). **b,** (i) Two potential signal profiles recorded across the DIB in 'a' upon illumination (YG light, 490 - 608 nm with peaks at 550 and 592 nm, 15 ± 4.5 mW). Top: An undershoot signal (orange boxes) is observed; transitional signals don't exceed the steady-state (when the light is turned on) or the baseline (when the light is turned off). Bottom: An overshoot signal (orange boxes) is observed; transitional signals exceed the steady-state (when the light is turned on) and the baseline (when the light is turned off). Dotted boxes indicate the steady-state level. (ii) Steady-state signal of the undershoot and overshoot traces shown in 'i' (5 s long). The output is constant irrespective of the rest of the signal profile. Figure adapted from the authors manuscript in progress[192].

Within seconds, the signals generated when a photosensory module is illuminated reach a steady-state level; both the undershoot and overshoot signals are transient. In cases where an overshoot signal was observed, the initial illumination pulse typically reached a greater transient peak than subsequent pulses (Fig. 2.26), most likely due to the protein becoming light adapted and having insufficient time to recover. For the work discussed in this thesis, it is only the steady-state signal magnitude which is of interest. Therefore, it is of no concern whether the bilayer causes an overshoot or undershoot signal when the protein-containing bilayer is illuminated. For each experiment described in this thesis, a single protein expression and purification batch was used.

Unless otherwise stated, experiments had a minimum of three biological replicates (measurements were taken from distinct samples but protein was from the same protein expression and purification batch) and were the average of three technical replicates (measurements taken from the same sample).

2.2.4.3 LED

Since the proteins used in the photosensory modules are light-driven, a fibre-coupled LED (PM100A Compact Power Meter Console, Thorlabs) was used as an illumination source (at a distance of 5 cm from the samples). The LED bundle used was composed of 7 distinct LED fibres covering light in the region of 355 - 741 nm; each can be independently controlled. The maximum and relative output of each LED was taken using a spectrometer (Fig. 2.9). Whilst each LED had a distinct peak, they covered a broad region of the spectrum (Fig. 2.9). Further, each LED had a different maximum output.

Since photosensory proteins described in this thesis are activated by yellow-green light, LEDs 4 (yellow, 576 - 608 nm peaks at 592 nm) and 5 (green, 490 - 594 nm peaks at 550 nm) were simultaneously used, at a combined output of 15.0 ± 4.5 mW (Fig. 2.9). Controls were performed in which the photosensory module was illuminated with non-activating wavelengths of light: IR (LED 1, red, 680 - 741 nm peaks at 722 nm, 16 ± 5.0 mW) or UV (LED 2, purple, 355 - 390 nm peaks at 367 nm, 15 ± 3.9 mW) (Fig. 2.9). The illumination protocol, including both pulse frequency and LED wavelength, was controlled from a computer by using the manufacture's software (see **Chapter 6** for more details).

For action spectrum experiments, in which the LED wavelength needed to be restricted, bandpass filters (ThorLabs) were used. These filters allowed light of only a narrow wavelength band to pass through (±10 nm); in turn, filters allowing light at 390 nm, 430 nm, 490 nm, 530 nm, 560 nm, 590 nm, 630 nm and 660 nm were fitted. Here, all LED channels (1-7) were simultaneously run with each LED output at 0.2 ± 0.1 mW (i.e. the same) (Fig. 2.9).

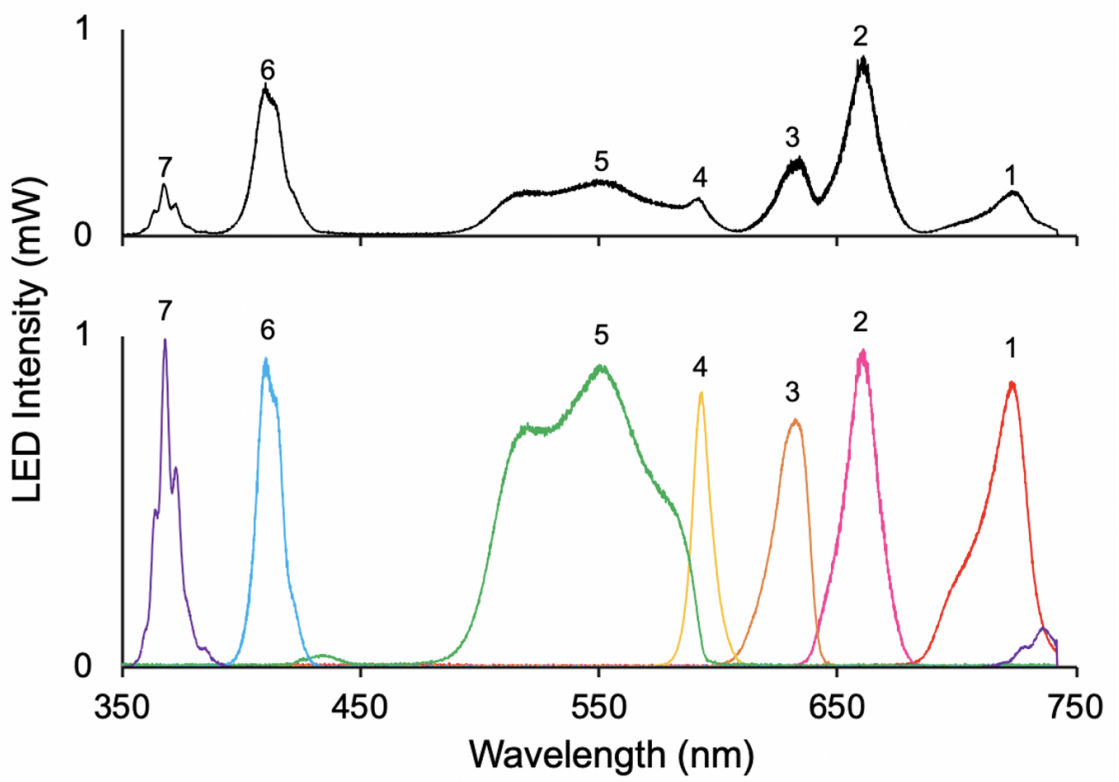


Figure 2.9: LED spectrograph. The LED bundle is composed of 7 distinct fibre-coupled LEDs, each of which is controlled by a separate channel on the software (Mightex). Spectral information for all LED channels was obtained using an Optical Spectrum Analyser (Thorlabs). LED channel 1 (740 nm, Red), 2 (656 nm, Pink), 3 (625 nm, Orange), 4 (590 nm, Yellow), 5 (560 nm, Green), 6 (410 nm, Blue), 7 (365 nm, Purple). Top: All LED channels are simultaneously turned on and run at 10 mA. Some LED channels generated higher outputs than others. Bottom: Each LED channel was separately turned on (illuminating at their maximum output) and the resulting traces of all seven LEDs superimposed. Some LED channels illuminate at a broader wavelength than others. Figure is taken from the authors manuscript in progress[193]

2.2.4.4 Environment

Electrical recordings were done at 24.5 ± 3.4 °C and 32.4 ± 8.6 % humidity (recorded using a USB Temperature and Humidity sensor, ThorLabs). Both factors fluctuated greatly during the day (temperature (20 - 29 ° C) and humidity (20 - 50 %)); extremes led to droplet instability coalescence.

2.2.4.5 Optical monitoring of pumping

An alternative method was developed in which information surrounding the directionality and magnitude of proton pumping signals could be obtained without

the inclusion of electrical tethers.

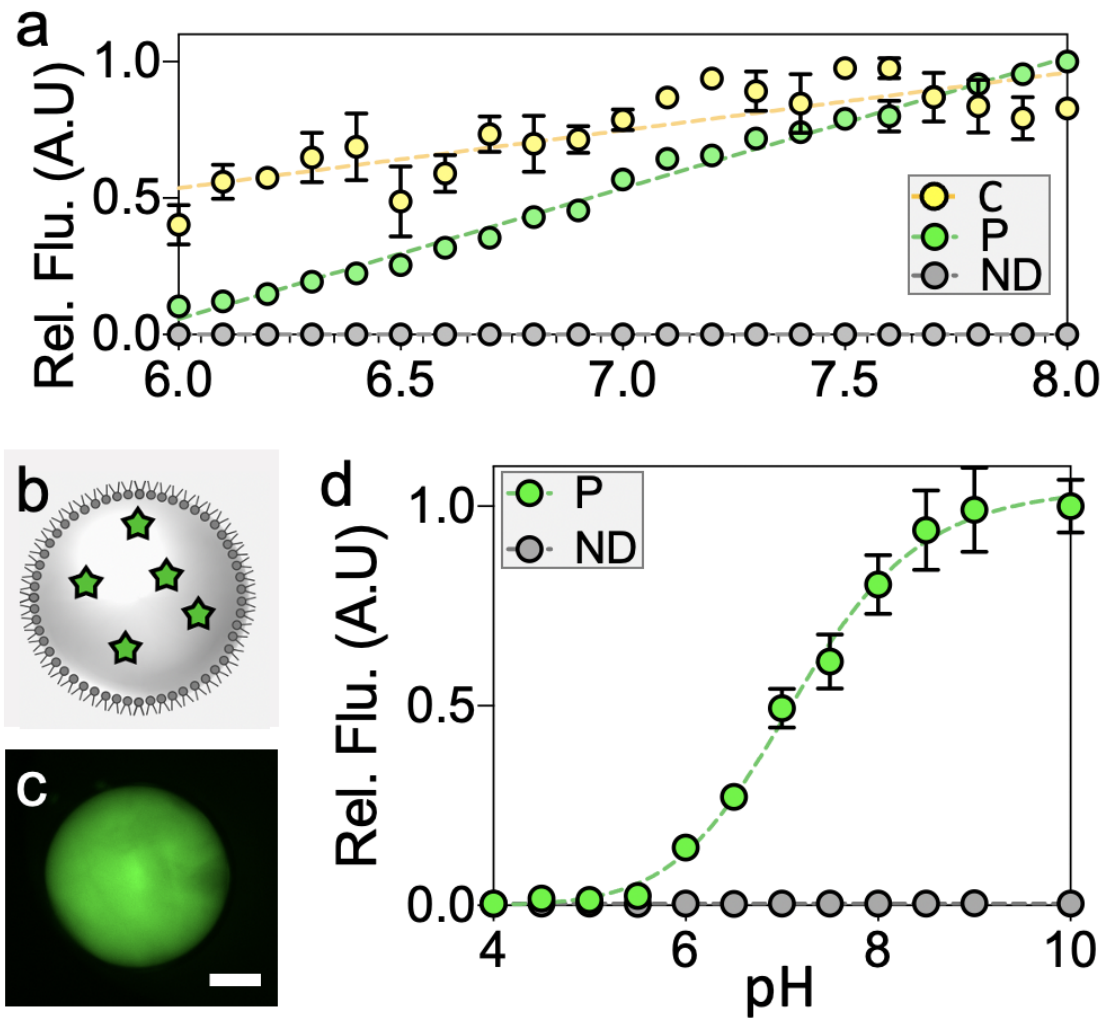


Figure 2.10: Pyranine calibration curves. a, Calibration curve of the pH-sensitive dyes carboxyfluorescein (C, yellow) and pyranine (P, green) in bulk. The fluorescence output (mean ± SD, n = 8) is plotted relative to the maximum recorded for that dye. A control was also shown containing buffer and no dye (ND, grey). **b,** Schematic of a pyranine (green star) containing droplet. **c,** Epifluorescent image of a droplet containing pyranine (100 μM pyranine, 100 mM NaCl, pH 6.5, minus background). Scale bar = 200 μm. **d** Relative fluorescence intensity (mean ± SD) of a spectrum of droplets (200 nL), with pH values that increase stepwise, was plotted against their pH (n=16). Droplets were imaged in the presence (green, P) or absence (grey, ND) of pyranine. The sigmoidal curve fit (as described in Equation 2.1) generated a pKa value of 7.3; literature values indicate the pKa of pyranine is 7.2 - 7.3[149]. Figure is adapted from the authors manuscript in progress[193]

First, the fluorescence intensity of two pH sensitive dyes (in bulk solution in the absence of buffer) were monitored at a number of discrete pHs (pH 6-8 at intervals of 0.1): carboxyfluorescein (Fig. 2.10a) and pyranine (Fig. 2.10b). Plotting

fluorescence intensity (recorded by a plate reader) against pH, generated a calibration curve for each of the dyes (mean ± SD, n = 8). For pyranine, a linear trend was observed (in this pH region) in which fluorescence intensity increased proportionally with pH; the trend for carboxyfluorescein was much noisier (Fig. 2.10).

For this reason, the pH-sensitive dye pyranine was then incorporated into protein-free aqueous droplets (in the absence of buffer, Fig. 2.10 a-b). Droplet pH was increased using a stepwise approach (from pH 5.5 to pH 10) and the relationship with fluorescence intensity plotted to form a calibration curve (pKa = 7.31, n=16, Fig. 2.10c-d). Fluorescence intensity was plotted relative to the maximum output (Fig. 2.10d). Considering that fluorescence intensity increased with pH, it was possible to quantify the changes in proton concentration which occurred following pumping[149,194]. Droplet (200 nL) pH can be determined from the fluorescence output, using the Equation 2.1 of the calibration curve (relative intensity against pH): A = 0.0 ± 0.0, B = 1.0 ± 0.0, C = 7.1 ± 0.0 and D = 0.7 ± 0.0.

$$pH = log_{10}\frac{(B-A)}{(Fluorescence-A)}) + log_{10}C - 1 \tag{2.1}$$

In order to calculate droplet fluorescence, first the background fluorescence (F_B) of the system was established. Pyranine-free droplets (Solution C) were imaged using epifluroescence microscopy (n = 16 droplets) to get the background fluorescence. Intensity was determined by plotting the droplet cross-section and calculating the mean (n = 3 technical replicates). For this calibration curve experiment the background fluorescence (F_B) was 21.7 ± 1.8 A.U (mean ± SD, n = 16, Fig. 2.11); it was 22.3 ± 4.5 A.U across all experiments in this thesis. Next, the same process was repeated for each pyranine-containing droplet (+100 μM pyranine) to determine the absolute fluorescence intensity (F_A) (Fig. 2.11). Finally, droplet fluorescence intensity at that point in time (F_T) was calculated by subtracting the background fluorescence (F_B) from the absolute fluorescence (F_A) (Fig. 2.11). By monitoring changes in fluorescence intensity over time, it was possible to quantify the pH changes that arose from proton pumping using the calibration curve (Fig. 2.11). Only small pH changes (< 1 pH unit) were expected to occur when photosensory

modules were illuminated overnight (as CM-aR3 only pumps one proton per photon absorbed and the bilayer contains $\approx 10^5$ - 10^6 proteins, (see 'Quantitation of CM-aR3'). Therefore, buffer was excluded from the droplets to ensure that even these small fluorescence changes could be observed (Solution C, 100 mM NaCl, pH 6.5).

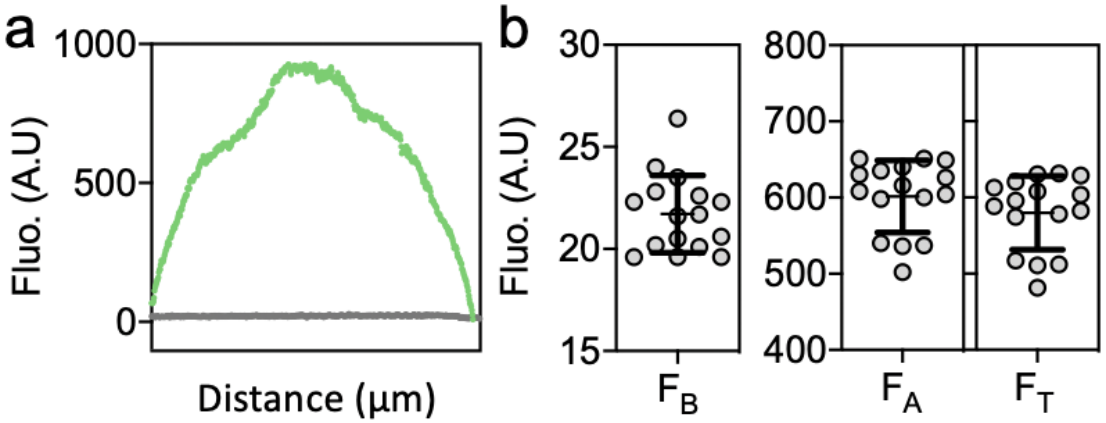


Figure 2.11: Calculating pyranine fluorescence. a, Lines plotted across a droplet (see 2.10c) in the presence (green) or absence (grey) of pyranine (100 μM, Solution C) **b,** Left: The background fluorescence (F_B) is the fluorescence intensity of droplets containing no pyranine (ND, grey, mean ± SD, n = 16 droplets with n = 3 technical replicates). Middle: The absolute fluorescence (F_A) is the fluorescence intensity of droplets containing pyranine (P, green mean ± SD, n = 16 droplets with n = 3 technical replicates). Right: The real fluorescence at a point in time (F_T) is the actual fluorescence intensity (F_A) minus the background fluorescence (F_B) (mean ± SD, n = 16).

2.2.5 bR photosensory modules

Bacteriorhodopsin (bR) is a 27kDa, photochemically-driven proton pump[115]. Since it is the best characterised microbial rhodopsin, it has been previously reconstituted into artificial bilayers (including DIBs)[31,44,195]. Further, this work demonstrated that bR retained its light-driven pumping activity following reconstitution into the artificial bilayers.

2.2.5.1 Sigma-bR output

Previous work carried out in the Bayley Group, used Sigma-bR (bought as lyophilised PM)[31,44]. For this reason photosensory modules were first made using Sigma-bR to enable comparison with the literature. These experiments found that Sigma-bR inserted into droplet bilayers as small membrane fragments (confirmed by AFM[196]).

Upon illumination (YG light, 490-608 nm, peaks at 550 and 592 nm, 15 ± 4.5 mW), Sigma-bR photosensory modules pumped protons across the bilayer (into the protein-free droplet), generating positive signals greater than the 1.0-pA threshold (Fig. 2.13). The average steady-state signal recorded across the Sigma-bR photosensory bilayer was + 5.3 ± 1.1 pA (mean ± SD, n = 10) (Fig. 2.13); with a maximum steady-state signal of + 7.0 pA.

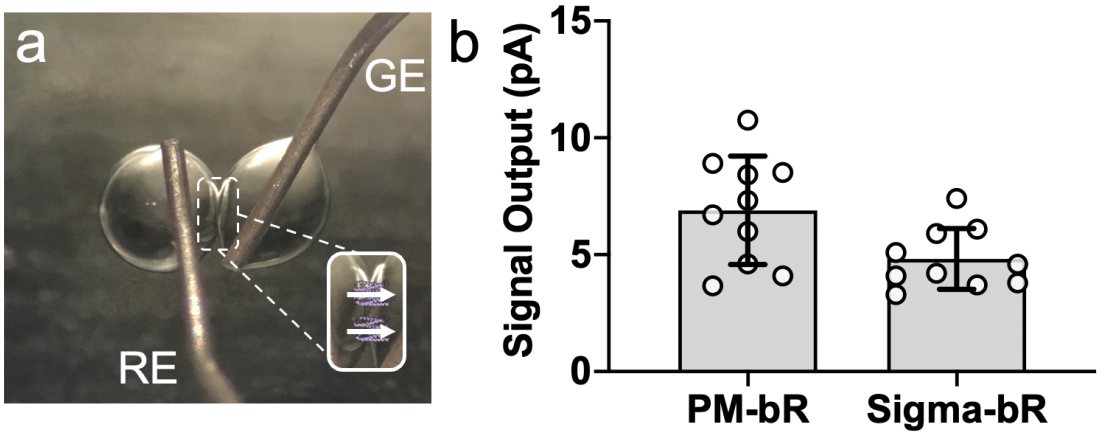


Figure 2.12: Photoactivity of Sigma-bR and PM-bR. a, A photosensory module was made with the recording electrode (RE) in the photosensory droplet (+ bR) and the ground electrode (GE) in the protein-free droplet. Zoom shows the bilayer into which bR inserts, pumping protons across the bilayer upon illumination. **b,** Steady-state signal output recorded across a photosensory bilayer containing Sigma-bR or PM-bR upon illumination (YG light, 490 - 608 nm with peaks at 550 and 592 nm, 15 ± 4.5 mW, mean ± SD, n = 10).

2.2.5.2 PM-bR output

Another source of bR, expressed in its archeal host *Halobacterium salinarum* and purified as purple membrane fragments (PM) by **J.V**, was tested. The time between protein expression and photosensory module formation was significantly shorter for PM-bR than Sigma-bR, making the protein fresher. Further, the protein was kept in solution throughout (i.e., not lyophilised).

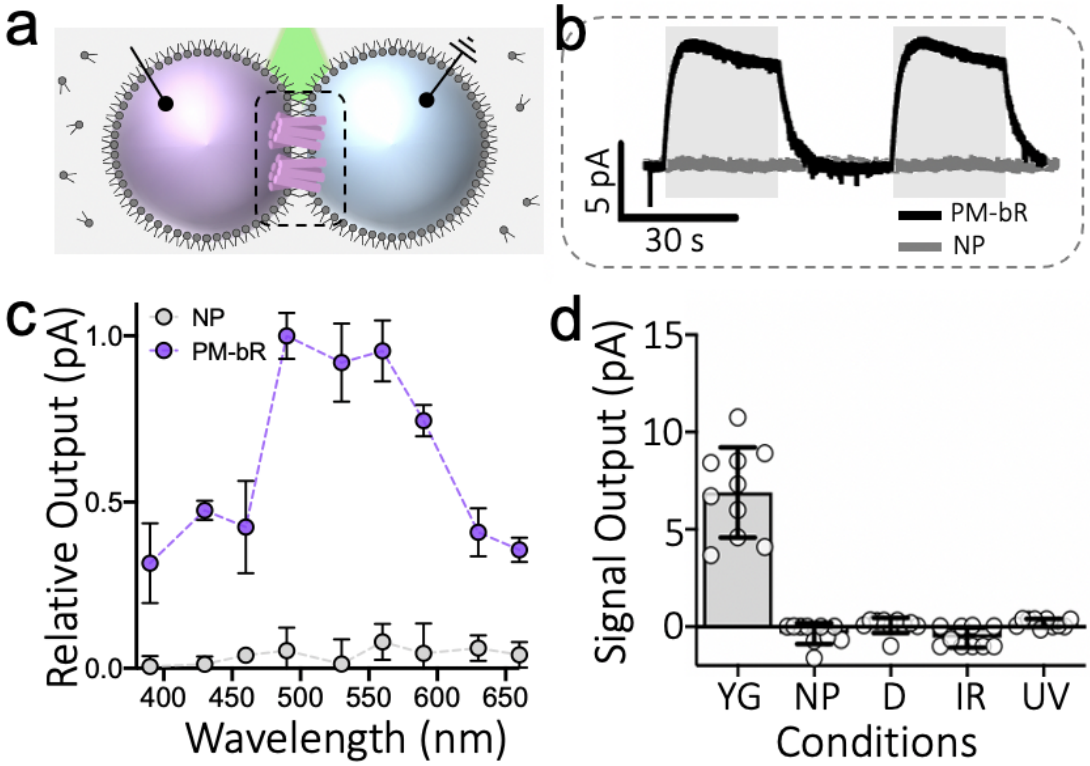


Figure 2.13: Bacteriorhodopsin (bR) photosensory module. **a,** Schematic of the photosensory module. Ag/AgCl electrodes are inserted into the droplets to enable electrical recording. Upon illumination with light (green), protons are pumped across the DIB (as indicated by the arrow). **b,** Signals recorded across a PM-bR photosensory module (black) upon illumination (grey bars indicate when the YG light is on, 15 ± 4.5 mW) and a protein-free DIB (NP, grey). **c,** Action spectra recorded across a DIB in the absence (grey, NP) or presence (purple) of PM-bR (n = 3, mean ± SD, light output is 0.2 ± 0.1 mW at each wavelength). **d,** Steady-state output (mean ± SD, n = 10) when the DIB is illuminated with YG light (490-608 nm, peaks at 550 and 592 nm, 15 ± 4.5 mW) in the presence (YG) or absence (NP) of PM-bR or when a PM-bR-containing DIB is illuminated with infrared (IR, 680-741 nm, peak at 722 nm, 16 ± 5.0 mW), ultraviolet (UV, 355-390 nm, peak at 367 nm, 15 ± 3.9 mW) or no (D) light.

PM-bR photosensory modules generated signals (greater than the 1.0-pA threshold) upon illumination (YG, 490-608 nm with peaks at 550 and 592 nm, 15 ± 4.5 mW) as protons were pumped across the bilayer. The mean steady-state signal recorded was +6.9 ± 2.3 pA (mean ± SD, n = 10) (Fig. 2.13d); with a maximum of +11 pA. For both Sigma-bR and PM-bR positive signals were generated suggesting they insert into the bilayer N-terminal first, pumping proteins into the (protein-free) droplet. However, PM-bR generated larger photosignals than Sigma-bR, likely due to its freshness. Consequently, PM-bR was chosen to form the photosensory module

standard. It should be noted that the signals generated by both Sigma-bR and PM-bR (in this system) are significantly smaller than those reported in the literature[121].

Further, the proton pumping mediated by PM-bR in a photosensory module was dependent on the stimulating light wavelength (Fig 2.13c-d). The action spectrum of the PM-bR photosensory module was determined by monitoring changes in maximal signal generation over a range of light wavelengths (390 nm, 430 nm, 460 nm, 490 nm, 530 nm, 560 nm, 590 nm, 630 nm, and 660 nm, 0.2 ± 0.1 mW, Fig 2.13c). Aligning with literature reports[31,44,115,122,133,195,197], PM-bR retains yellow-green light sensitivity (490-608 nm, peaks at 550 and 592 nm). It was observed that following illumination with IR (680-741 nm, peak at 722 nm, 16 ± 5.0 mW) or UV (355 – 390 nm peaks at 367 nm, 15 ± 3.9 mW) light, signals below the 1.0-pA threshold were generated; + 0.5 ± 0.2 pA and + 0.3 ± 0.3 pA (mean ± SD, n = 10) respectively (Fig 2.13d). Likewise, no signals (< 1.0-pA threshold) were generated in the absence of PM-bR (NP, + 0.2 ± 0.4 pA, mean ± SD, n = 10) or when a PM-bR photosensory module was not illuminated (dark, D, + 0.3 ± 0.2 pA, mean ± SD, n = 10) (Fig 2.13d).

2.2.5.3 Orientation

Whilst the steady-state signals generated by PM-bR photosensory modules varied in magnitude, the signal polarity was consistent indicating that the protein always inserted into the bilayer in the same orientation (Fig. 2.13d). Within its native host, bR pumps protons out of the cell from its C-terminal face to its N-terminal face[115,122,133,197]. As described in Section 2.2.4.2, a positive signal is defined as one in which electrons flow into the ground electrode, i.e. the ground electrode terminal is positive. Therefore, bR must insert with the N-terminal face exposed to the protein-free (ground-electrode containing) droplet, pumping protons into it upon illumination (YG light, 490-608 nm with peaks at 550 and 592 nm, 15 ± 4.5 mW).

By switching the positions of the electrodes across the PM-bR photosensory module, signal polarity was reversed (i.e. became negative) as protons were now pumped into the protein-free (recording-electrode containing) droplet (Fig. 2.14

b2). Since this created a positive terminal at the recording electrode, negative signals were observed (Section 2.2.4.2, see **Chapter 6** for a diagram, Fig. 6.3). Moreover, the signal output was negligible when PM-bR was added to both sides of the DIB, since protein inserted, and pumped protons, in both (opposite) directions (Fig. 2.14 b3). These observations correspond with data previously recorded when Sigma-bR was embedded into artificial droplet bilayers[31,44].

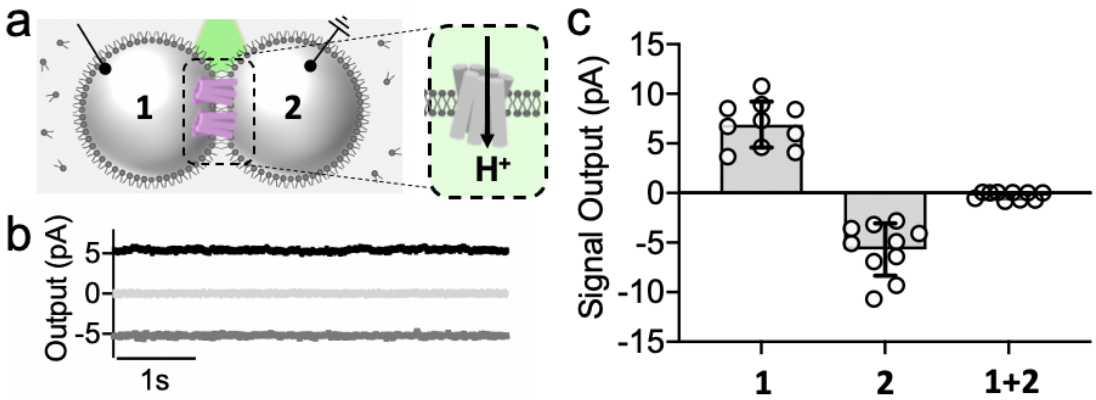


Figure 2.14: PM-bR inserts N-terminus first into DIBs a, Schematic of a PM-bR photosensory module. Ag/AgCl electrodes are added for signal recording; the recording electrode (RE) is added to the left droplet (a1) and the ground electrode (GE) to the right droplet (a2). Upon illumination (YG light, 550 and 592 nm, 15 ± 4.5 mW) protons are pumped across the bilayer. **b,** Steady-state signals recorded across the photosensory bilayer when the PM-bR is added to droplet a1 (+RE, black), droplet a2 (+GE, dark grey) or both droplets (a1+a2, RE+GE, light grey). **c,** The steady-state signal output (mean ± SD, n = 10) recorded across the bilayer when the PM-bR is added to droplet a1 (+RE, black, positive signals), droplet a2 (+GE, dark grey, negative signals) or both droplets (a1+a2, RE+GE, light grey, signals output ≈ 0 pA).

2.2.6 CM-aR3 photosensory modules

Having formed functional photosensory modules using PM-bR, the use of CM-aR3 was explored. CM-aR3 had previously been reported to generate larger photosignals than other known proton pumps: perhaps due to its faster photocycle or more efficient incorporation into membranes[121]. For these reasons, and its novelty, the formation of CM-aR3 photosensory modules was of considerable interest.

2.2.6.1 CM-aR3 output

Whilst aR3 had previously been shown to retain proton pumping activity in cellular membranes[121,173,198,199,200], formation of a CM-aR3 photosensory module was one of the earliest demonstrations of aR3 functionality within an artificial bilayer. CM-aR3 has comparable structure (Fig. 2.5) and size to its homologue PM-bR[121,146,147]. Further, they have similar sequences with the residues involved in proton pumping conserved (Fig. 2.6). Therefore, CM-aR3 photosensory modules were built and characterised in the same manner to those formed using PM-bR.

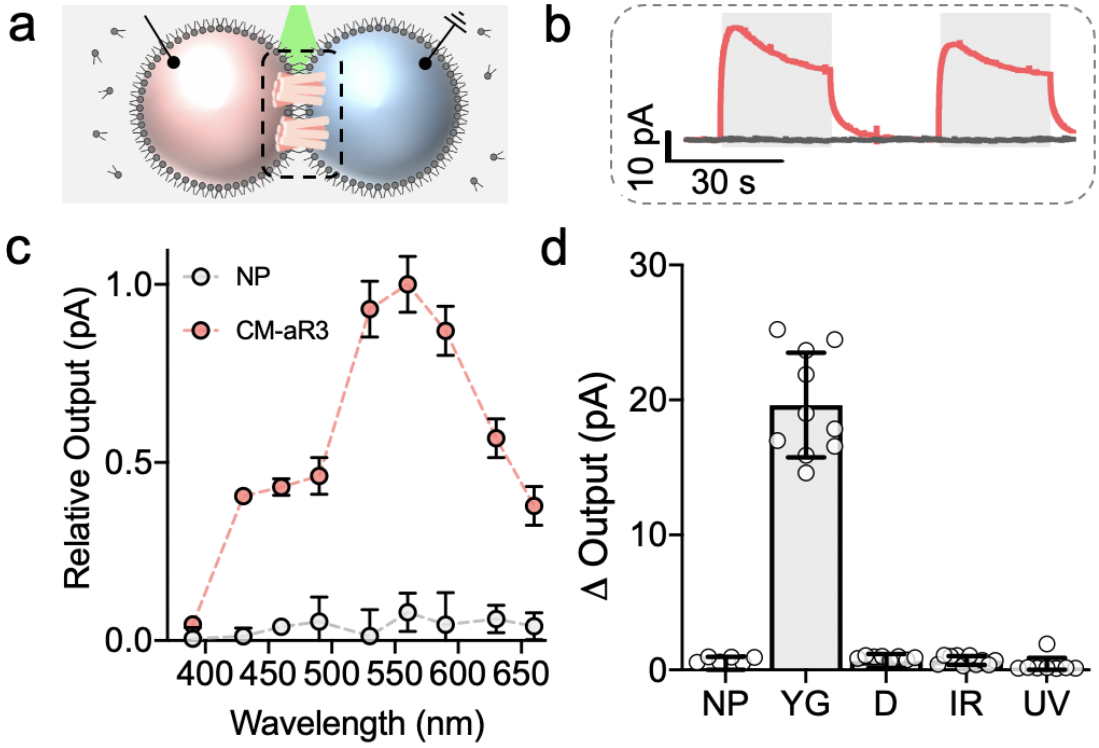


Figure 2.15: CM-aR3 photosensory module. a, Schematic of the photosensory module. Ag/AgCl electrodes are inserted into the droplets to enable electrical recording. Upon illumination with light (green), protons are pumped across the DIB (as indicated by the arrow). b, Signals recorded across a CM-aR3 photosensory module (pink) upon illumination (grey bars indicate when the YG light is on, 15 ± 4.5 mW) or a protein-free bilayer (NP, grey). Grey bars indicate when the light is on. c, Action spectra recorded across a bilayer in the absence (grey) or presence (pink) of CM-aR3 (n = 3, mean ± SD, light output is 0.2 ± 0.1 mW at each wavelength). d, Steady-state output (mean ± SD, n = 10) when the DIB is illuminated with YG light (490-608 nm with peaks at 550 and 592 nm, 15 ± 4.5 mW) in the presence (YG) or absence (NP) of CM-aR3 or when a CM-aR3-containing DIB is illuminated with infrared (IR, 680-741 nm with a peak at 722 nm, 16 ± 5.0 mW), ultraviolet (UV, 355-390 nm with a peak at 367 nm, 15 ± 3.9 mW) or no (D) light. Figure is adapted from the author's manuscript in progree[193].

Upon photoactivation, CM-aR3 pumps protons across a membrane, forming (ionic) signals. For characterisation, responses to light were measured with Ag/AgCl electrodes (Section. 2.2.4.2). First, the action spectrum was determined by recording the changes to signal output across several discrete wavelengths using bandpass filters (390 nm, 430 nm, 460 nm, 490 nm, 530 nm, 560 nm, 590 nm, 630 nm, and 660 nm, 0.2 ± 0.1 mW, Fig 2.15c). Maximal signal generation occurred in response to illumination with yellow-green light (Fig. 2.15c-d) in accordance with reported data[11,121,129], and comparable to PM-bR (Fig. 2.13). Illumination with YG light (490 - 608 nm with peaks at 550 and 592 nm, 15 ± 4.5 mW) generated a maximum steady-state signal of +25 pA with an average of +20 ± 3.7 pA (mean ± SD, n=10). If the CM-aR3 photosensory module was illuminated with either IR (680-741 nm, with a peak at 722 nm, 16 ± 5.0 mW) or UV (355-390 nm, peak at 367 nm, 15 ± 3.9 mW) light, or left in the dark, then no activity was detected (< 1.0-pA threshold): outputs of + 0.7 ± 0.3 pA, + 0.2 ± 0.6 pA and + 0.7 ± 0.5 pA (mean ± SD, n = 10) respectively. Further, illumination (with YG light) of a photosensory module in the absence of protein (NP) did not generate measurable signals (+ 0.1 ± 0.8 pA, mean ± SD, n = 10, < 1.0-pA threshold) since protons weren't pumped across the bilayer.

The signal output of a CM-aR3 photosensory module was typically 2-3 times higher than those generated by PM-bR (Fig. 2.13, 2.15). This difference is in accordance with the literature and may arise due to the intricate water networks within the CM-aR3 channel, the differing pKa values of key residues, a faster photocycle or more efficient protein incorporation into the DIB[129,150,201]. Again, it should be noted that the signals generated by the CM-aR3 photosensory modules described in this thesis are below those reported in the literature[121,129].

2.2.6.2 Orientation

Whilst there was variation in signal magnitude between protein batches, the direction of CM-aR3 insertion was consistent (Fig. 2.15d). In 100 consecutive experiments (using CM-aR3 from over 13 different protein expression batches prepared by **J.V**),

it was observed that CM-aR3 consistently inserted into DIBs N-terminus first; as seen with the proton-pump bR[31,44] (Fig. 3.9).

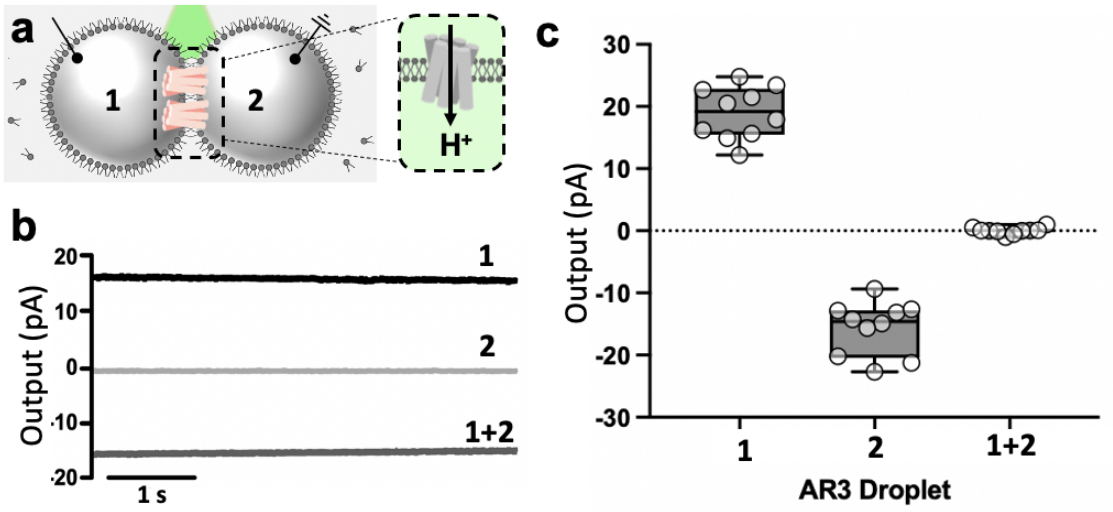


Figure 2.16: CM-aR3 inserts N-terminus first into DIBs a, Schematic of a CM-aR3 photosensory module. Ag/AgCl electrodes are added for signal recording; the recording electrode (RE) is added to the left droplet (a1) and the ground electrode (GE) to the right droplet (a2). Upon illumination (YG light, 550 and 592 nm, 15 ± 4.5 mW) protons are pumped across the bilayer. **b,** Steady-state signals recorded across the photosensory bilayer when the CM-aR3 is added to droplet a1 (+RE, black), droplet a2 (+GE, dark grey) or both droplets (a1+a2, RE+GE, light grey). **c,** The steady-state signal output (mean ± SD, n = 10) recorded across the bilayer when the CM-aR3 is added to droplet a1 (+RE, black, positive signals), droplet a2 (+GE, dark grey, negative signals) or both droplets (a1+a2, RE+GE, light grey, signals output ≈ 0 pA). Figure is adapted from the author's manuscript in progress[193].

Upon illumination (YG light, 490 - 608 nm with peaks at 550 and 592 nm, 15 ± 4.5 mW), CM-aR3 pumped protons out of the photosensory droplet (containing the recording electrode), recurrently generating positive signals (Fig. 2.16, Section. 2.2.4.2). A positive signal is defined as one in which the electrons flow into the ground electrode, here located in the protein-free droplet (Section. 2.2.4.2, see **Chapter 6** for a diagram). Therefore, positively charged ions must move out of the photosensory (recording electrode-containing) droplet. This directionality was confirmed by the negative signals generated when CM-aR3 was added from the ground (instead of recording) electrode-containing droplet (Fig. 2.16). Further, the signal output was negligible when CM-aR3 was added to both droplets as roughly identical numbers of proteins were pumping in both direction (Fig. 2.16).

2.2.6.3 Optimisation

Whilst the signal output of the CM-aR3 photosensory modules was around 2-3 fold higher than their PM-bR counterparts, it remained below those reported in the literature[115,121,173,198,199] (Fig. 2.13, 2.15). Therefore something must be hindering either the protein activity within the DIB or its insertion from the photosensory droplet solution. Literature reports suggest that the protein environment and membrane constituents are known to play important roles in protein activity[149,202,203]. A systematic approach was used to extensively optimise both the photosensory droplet and the bilayer components with the aim of enhancing signal generation; experiments were based on work previously done by **V.R.S** with Sigma-bR.

Detergents

Studies have found that the detergent environment of membrane proteins can affect the photocycle, altering the temporal sequence of the photointermediates[202,203]. Moreover, detergent micelles surround regions of the membrane resulting in their partial dispersal into smaller fragments which is thought to aid insertion.

Previous work using bR in droplet bilayers[31,44], used the detergent DDM (n-Dodecyl-b-D-Maltopyranoside). DDM is a water-soluble non-ionic detergent which is often used in the isolation of hydrophobic membrane proteins as it has amphiphilic properties which facilitate lipid displacement and provide a lipid-like environment for membrane proteins. Whilst detergent is required to aid protein solubilisation, too high concentrations will disrupt bilayer formation leading to leaky membranes or droplet coalescence. As described in 'Protein preparation', CM-aR3 was first buffer exchanged into solution with the detergent above the CMC (0.1 % (w/v) DDM). Then, following sonication, the solution was diluted to lower the detegent concentration to below the CMC. Several concentrations of DDM detergent within the final photosensory module were screened with 0.001 % (w/v) DDM identified as the optimum (Fig. 2.17). The final photosensory droplet solution contained 100 mM MES, 100 mM NaCl, 0.001% DDM, pH 6.5, 0.15 - 0.25 mg mL^{-1} CM-aR3 membrane fragments.

For comparison, two alternative (non-ionic) detergents (widely used for membrane protein solubilisation and not known to denature proteins) were used to form CM-aR3 photosensory modules. The signals of DDM, OG (n-Octyl-β-D-Glucoside) and Triton-X-100-containing CM-aR3 photosensory modules was comparable: outputs were + 13 ± 0.9 pA, + 13 ± 0.6 pA and + 12 ± 1.2 pA respectively (mean ± SD, n = 3). For simplicity, DDM was used in all future photosensory modules.

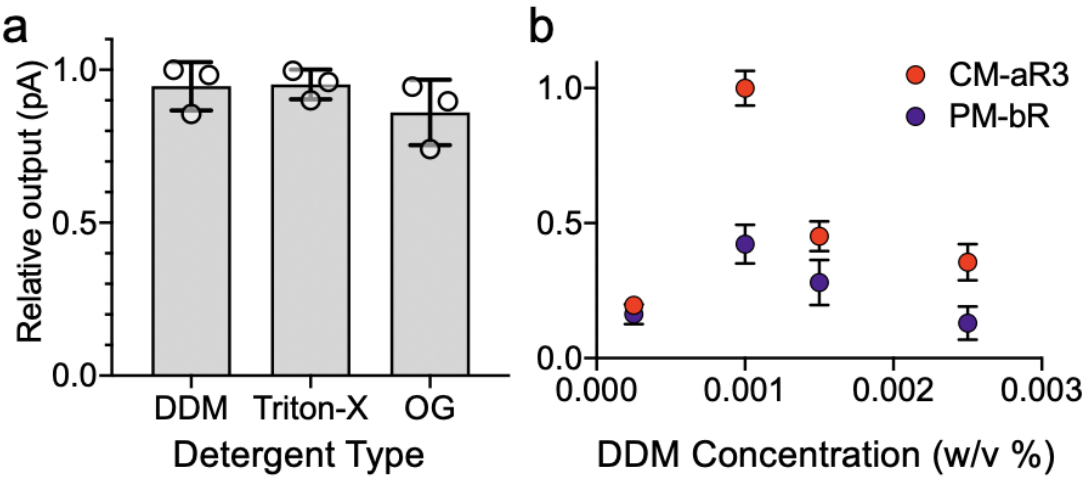


Figure 2.17: Detergent optimisation. **a,** Steady-state signals recorded across a CM-aR3 photosensory bilayer when the protein was reconstituted using n-Dodecyl-β-D-Maltoside (DDM), n-Octyl β-D-glucopyranoside (OG), or Triton X-100 detergents (mean ± SD, n = 3, see **Chapter 6** for the method). Output is plotted relative to the maximum obtained using DDM. **b,** Steady-state output of CM-aR3 (red) and PM-bR (purple) reconstituted into DIBs at different concentrations of DDM weight-per-volume percent (w/v %). Bilayers are illuminated with YG light (550 and 592 nm, 15 ± 4.5 mW, n = 3). Figure is adapted from the author's manuscript in progress[192].

Protein concentration

Within the photosensory module system, CM-aR3 inserted into the bilayer (as CM fragments) from solution. High protein concentrations resulted in increased aggregation of these fragments within the droplet (and a more intense droplet colour, Fig. 2.18a). Further, since the growth of *Halorubrum sodemense* is slow it would be desirable to minimise CM-aR3 use within each photosensory module to prolong supplies. However, the signal output must not be compromised. Since there is excess protein in the photosensory droplet (as determined from electrical recordings, see Section 2.2.9), reducing protein concentration should be feasible

without compromising the signal output. The output of CM-aR3 photosensory modules containing different protein concentrations were compared and the optimal region (when filtering based on output and aggregation frequency) was found to be between 0.1 - 0.3 mg mL^{-1} (measured using nanodrop) (Fig. 2.18c). Throughout this thesis, a CM-aR3 protein concentration of 0.15 - 0.25 mg mL^{-1} is used in the photosensory droplets (measured using nanodrop).

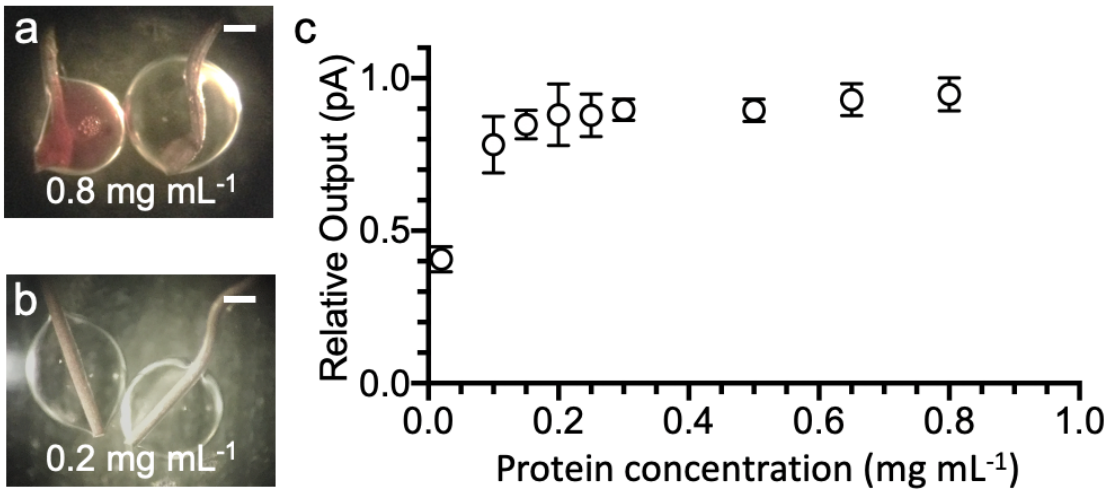


Figure 2.18: Protein concentration optimisation. a-b, Photographs (taken using an iPhone) of a photosensory module containing (a: 0.8 mg mL^{-1}CM-aR3) or (b: 0.2 mg mL^{-1}CM-aR3). Scale bar = 200 μm. At high concentrations the droplet appears visibly pink. **c,** Steady-state output (mean ± SD, n = 3) recorded across the DIB (with different photosenosry droplet protein concentration) upon illumination (YG light, 490-608 nm with peaks at 550 and 592 nm, 15 ± 4.5 mW).

Droplet size

Further, decreasing the size of the droplet pixels would be advantageous since it would enable even lower quantities of CM-aR3 (and in the future other reagents) to be used. In addition, smaller droplets are known to be more stable than larger ones.

Interestingly, halving the droplet volume from 200 nL to 100 nL resulted in the generation of larger bilayers (determined from capacitance measurements) but signal output remained comparable (Fig. 2.19): 21 ± 1.0 pA and 22 ± 1.6 pA respectively. Further, scaling down of CM-aR3 photosensory modules to picolitre (pL) volumes (made by **V.R.S** using the droplet printer[50]) resulted in a reduction

in the signal output; maximum signals generated were close to (and sometimes below) the 1.0-pA threshold[100].

Despite being less stable, 200 nL photosensory droplets continued to be used as they could be readily formed by hand (using a pipette) and generated light-responsive signals which were above the 1.0-pA threshold (Fig. 2.19). Being able to successfully form small but functional photosensory modules (e.g. using the droplet printer) may prove useful in future applications.

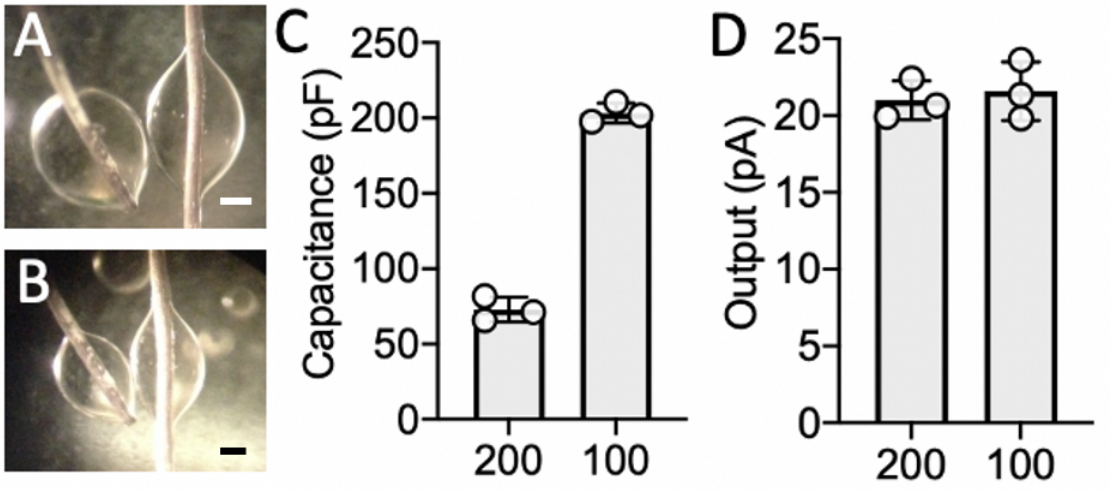


Figure 2.19: Droplet size optimisation. a-b, Photographs (taken using an iPhone) of a 100 nL (a) or 200 nL (b) photosensory module. Scale bar = 200 μm. **c,** Capacitance measurements recorded across the DIB when the droplet size was 100 nL and 200 nL (in the dark, mean ± SD, n = 3). **d,** Steady-state signals recorded across the DIB when the droplet size was 100 nL and 200 nL (YG light, 490-608 nm with 550 and 592 nm, 15 ± 4.5 mW, mean ± SD, n = 3).

Buffer

Another key component of the photosensory droplet is the buffer. Previously it has been shown that bR photosensory droplets containing MES (2-Morpholinoethanesulfonic acid) buffer consistently formed stable droplet bilayers, and that bR retained its functionality in the presence of MES[31]. Further, the inclusion of buffer in the photosensory droplets prolonged the time before CM-aR3 activity was hindered by the build-up of a pH gradient and the time before proton exhaustion occurred (by increasing proton availability)[149,204]. However, the sole use of MES buffer is limiting, for instance it has a pKa of 6.16 (at 20 °C) so the potential pH of the photosensory

droplet is restricted to this region. It would be of interest to explore the effect of droplet pH of pumping since literature studies have shown that the photocycle of a similar protein, archaerhodopsin-4, is sensitive to environmental pH[203].

For this reason, a screening of common buffers was performed: MES, HEPES, Tris, CHES and a phosphate buffer were tested. These different buffers were introduced at the intial buffer exchange stage of protein preparation. Interestingly, bilayers couldn't be formed with HEPES buffer; the high coalescence is likely due to the hydrogen peroxide which forms as a result of the interaction of HEPES and light. However, stable DIBs were formed with droplets containing Tris, CHES and phosphate buffer. In addition, CM-aR3 retained some functionality (when added from these three buffered solutions) but there was an increase in noise making signal detection challenging (this was also seen with bR by **V.R.S**, unpublished observations). Moreover, the noise indicated some bilayer instability and the lifetime of the bilayer was reduced when compared to MES. For these reasons, MES buffer was used to form stable functional photosensory modules (and, for now, the pH was not optimised).

Lipid-in-oil

The use of alternative lipids is of particular interest as literature reports indicate that lipids also play an important role in protein structure and function[135,205,206]. Previously, the exogenous lipid DPhPC (diphytanoyl-sn-glycerol-3-phosphocholine, not native to haloarchea) was used to form the bilayer. Due to its poor solubility in silicone oil, DIBs formed with the lipid DPhPC, solubilised in a oil solution of hexadecane and silicone oil, have been shown to display enhanced kinetic stability[207]. The DPhPC lipids occupy the space at the bilayer interface (not in the oil), fortifying the bilayer as a result. The use of POPC, an alternative exogenous lipid, has previously been shown to increase both bilayer size and stability[40]. Consequently, photosensory modules were made using a combination of DPhPC and POPC. It should be noted that there are some endogenous haloarcheal lipids present as the CM-aR3 inserts as fragments of claret membrane.

Interestingly, it was observed that photosensory modules formed in the presence of POPC all formed opaque droplets almost instantaneously, most likely due to the high lipid concentration crashing out of solution (Fig. 2.20b). Bilayers couldn't be easily formed when the concentration was lowered below 10 mg mL^{-1}, even with long incubation times, and there was a high frequency of droplet coalescence. There is huge potential to delve into the use of alternative lipids in the future but in the interest of time this wasn't explored in this thesis.

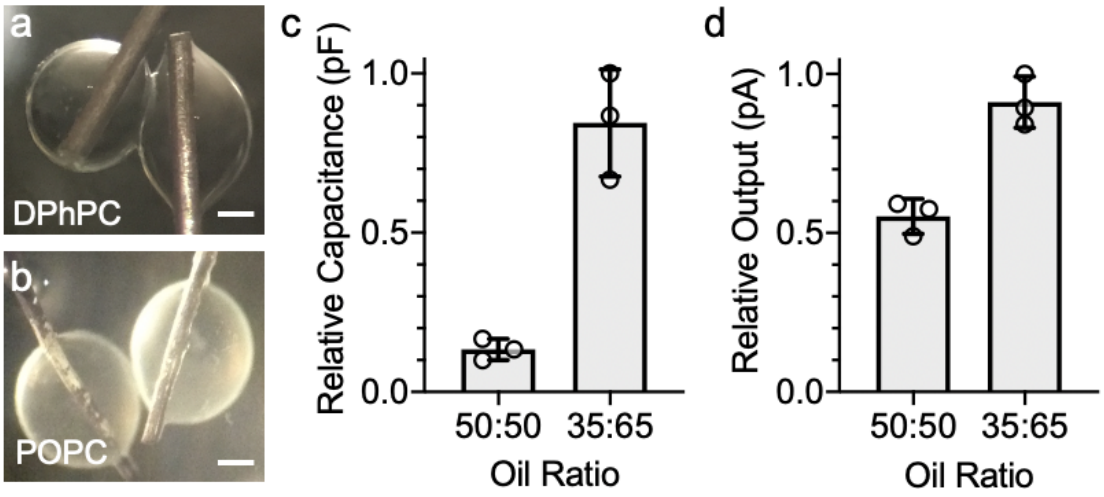


Figure 2.20: Lipid and oil optimisation. a, Photographs (taken using an iPhone) of a photosensory module in a lipid-in-oil solution containing 10 mg mL^{-1} of (a) DPhPC (b) POPC in 50:50 hexadecane, silicone oil. Scale bar = 200 μm. POPC droplets appear white likely due to lipid precipitation. **c,** Capacitance measurements recorded (in the dark) across the DIB when the lipid-in-oil was 10 mg mL^{-1} DPhPC in 50:50 or 35:65 hexadecane, silicone oil (mean ± SD, n = 3). **d,** Steady-state signals recorded across the DIB when the lipid-in-oil was 10 mg mL^{-1} DPhPC in 50:50 or 35:65 hexadecane, silicone oil (YG light, 490-608 nm with peaks at 550 and 592 nm, 15 ± 4.5 mW, mean ± SD, n = 3).

In addition, it has been shown that the oil component can also affect bilayer formation[40]. For instance, increasing the silicone oil component (relative to hexadecane) from 50 % to 65 % altered the contact angle between the two droplets creating larger bilayers; in fact, it was possible to increase the silicone oil concentration so that the bilayer and droplet radii were equal[40]. A larger bilayer would change two key features of the photosensory module DIB: its surface area and its curvature. It seems logical to suggest that a larger bilayer surface area will

permit more protein to insert and consequently lead to greater signal generation; the effect of bilayer curvature on protein insertion is less clear. Based on this work in the literature[40], the silicone oil component was increased. The oil composition was maintained (hexadecane and silicone oil) but the ratio was adjusted from 50:50 to 35:65 (with higher silicone oil). As expected (from the literature[40]), this led to an increase in bilayer size with the capacitance increasing from 40.0 ± 8.1 pF to 213.3 ± 66.0 pF (Fig. 2.20). In addition, the signal output also increased (almost two-fold) from + 7.3 ± 0.3 pA to + 13.1 ± 1.4 pA (Fig. 2.20, n = 3). Future photosensory modules were formed within a lipid-in-oil environment containing DPhPC in 35:65 hexadecane, silicone oil.

Salt

The role of salts within the aqueous photosensory droplet is to permit the formation of (ionic) signals within the droplet and enable such signals to be transferred to the electrodes for recording. There are several attributes of the salt component may be altered. Firstly, the salt type may be considered. However, a comparison between sodium chloride (NaCl) and potassium chloride (KCl, commonly used in planar bilayers) indicated that (in this system) there were negligible differences between ease of bilayer formation or signal output (Fig. 2.21a).

Secondly, the concentration of salt can be considered. This was of particular interest in the photosensory modules because many light-driven proteins (including PM-bR and CM-aR3) are found within halophilic archae and therefore naturally function in high salt conditions. Moreover, it has been suggested that higher salt concentrations enhance bilayer stability. Continuing with sodium chloride in the photosensory droplets, the concentration was increased from 10 mM to 1000 mM (and various concentrations between) and the breaking potential of the bilayers obtained. Breaking potentials determine what voltage a bilayer can withstand before coalescence and provides information about the DIB stability and strength. Here, as sodium chloride concentration increased, the breaking potential also increased, plateauing at ≈ 100 mM NaCl (Fig. 2.21b).

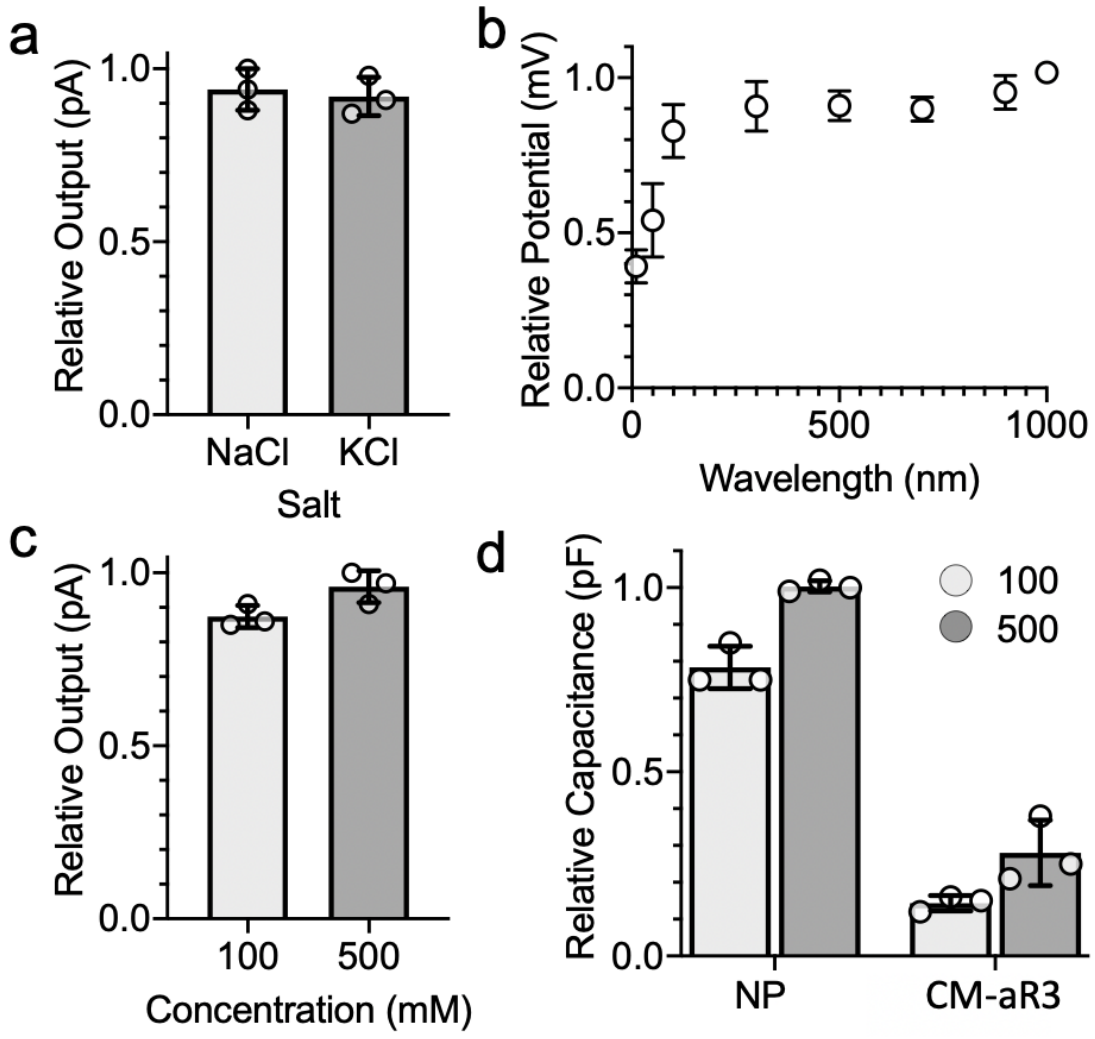


Figure 2.21: Salt content optimisation. a, Steady-state signals recorded across the DIB when the droplets contained 100 mM NaCl or KCl (YG light, 490-608 nm, with peaks at 550 and 592 nm, 15 ± 4.5 mW, mean ± SD, n = 3). **b,** Breaking potential recorded across a DIB with the droplets containing NaCl at different concentrations (mean ± SD, n = 3, in the dark). **c,** Steady-state signals recorded across the DIB (upon illumination) when the droplets contained 100 mM or 500 mM NaCl (490-608 nm, peaks at 550 and 592 nm, 15 ± 4.5 mW, mean ± SD, n = 3). **d,** Capacitance measurements recorded across the DIB when the droplets contained 100 mM or 500 mM NaCl (in the dark, mean ± SD, n = 3). Measurements were taken across bilayers in the absence (NP) or presence of CM-aR3.

Not only did bilayer stability increase at higher salt concentration but also the capacitance measurements (indicative of bilayer size) increased (Section. 2.2.4.2 Fig. 2.21d). Interestingly, it was observed at each salt concentration that the capacitance of a protein-free DIB (NP) was greater than those of a CM-aR3 photosensory module (CM-aR3) (Fig. 2.21d) suggesting the membrane fragments may be interfering

with bilayer formation. The capacitance of a photosensory module DIB was higher at 500 mM sodium chloride (533.3 ± 154.6 pF, mean ± SD, n = 3), compared to 100 mM (213.3 ± 66.0 pF, mean ± SD, n = 3) (Fig. 2.21d); the same trend was observed for DIBs formed in the absence of protein (NP). Further, signals generated upon illumination (YG light, 490-608 nm with peaks at 550 and 592 nm, 15 ± 4.5 mW) were also higher at 500 mM, rising from + 11.1 ± 0.3 pA to + 14.6 ± 1.3 pA (Fig. 2.21c). The main drawback of forming photosensory modules with 500 mM sodium chloride was salt solubility in solution, and salt crystals formed when left overnight (data not shown). Since this would prevent longer experiments from being performed, 100 mM sodium chloride was chosen to form the photosensory modules because it balanced bilayer stability, size, and signal generation with salt solubility in the droplets.

2.2.6.4 Characterisation

Archaerhodopsin-3 (aR3) is poorly characterised and information surrounding its structure and function are still coming to light. In order to maximise the potential of CM-aR3 within photosensory modules, the photophysical characteristics of the protein were explored within this system.

Proton pump

Due to its high sequence similarity with PM-bR (Fig. 2.6), CM-aR3 is thought to function as an outward driven proton pump. From preliminary electrical experiments, it was found that CM-aR3 inserted into DIBs N-terminus first (as with PM-bR), pumping protons out of the photosensory droplet (Fig. 2.16). To confirm that these signals were due to the pumping of protons, and not another ion, droplet pH was monitored optically with pyranine, a fluorescent pH-reporter. First, a CM-aR3 photosensory module was formed between a CM-aR3 photosensory droplet and a pyranine droplet (100 μM dye, in the absence of buffer, Solution C). Here, no electrodes were added to the droplets and pumping was wirelessly monitored.

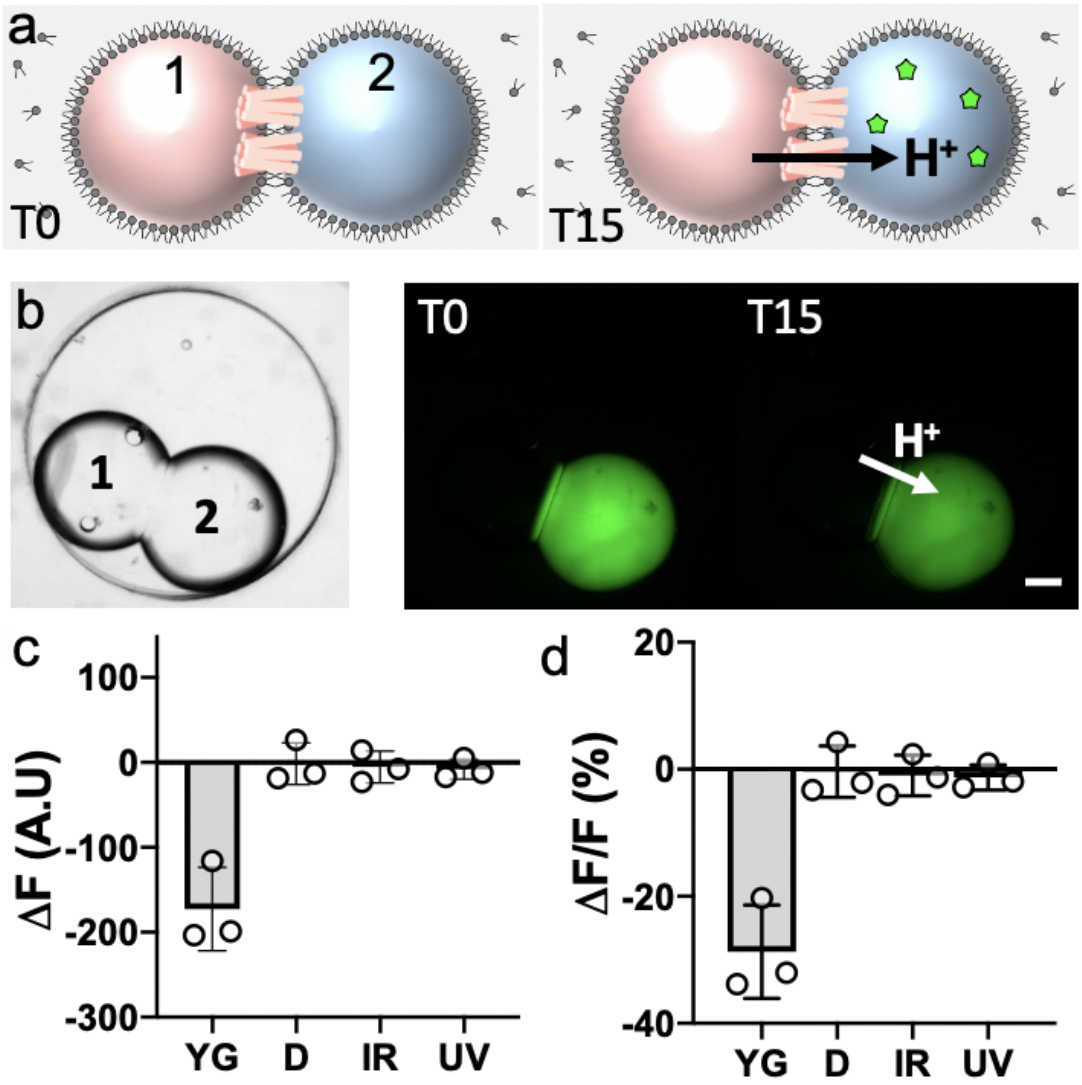


Figure 2.22: CM-aR3 is an outward proton pump **a,** Schematic of a droplet pair with CM-aR3 inserting into the droplet interface bilayer (DIB) from the photosensory droplet (a1). Upon illumination, protons (H+) were pumped out of the photosensory droplet (0.15 – 0.25 mg mL-1 CM-aR3, Solution B, pink, a1) and into the protein-free pyranine-containing droplet (100 μM pyranine, Solution C, blue, a2). **b,** Left: Brightfield image of a DIB composed of a CM-aR3 photosensory droplet (b1) and a protein-free droplet (b2) as in 'a'. Right: Epifluorescent images (minus background) of the DIB before (T0) and after (T15) overnight illumination (15 h, yellow green light, 550 and 592 nm, n = 1). Fluorescence intensity of the pyranine droplet decreased as protons were pumped into it[149]. Scale bar is 200 µm. **c-d,** (c) Absolute and (d) percentage change in fluorescence intensity of the pyranine droplet (b2) following illumination overnight (15 h) with yellow green (YG, 550 and 592 nm, 15 ± 4.5 mW), IR (IR, 722 nm, 16 ± 5.0 mW) or UV (UV, 366 nm, 15 ± 3.9 mW) light or when kept in the dark (D) (n = 3 DIBs with 3 technical replicates). Figure is adapted from the author's manuscript in progress[192]

If protons were pumped directionally out of the photosensory droplet (as

predicted from electrical experiments, Fig. 2.16, Section. 2.2.4.2), then the pyranine droplet fluorescence intensity would decrease (due to the decreased pH); if signals arise due to movement on another ion then no change would be observed. Indeed, following overnight illumination this was observed (YG light, 490 - 608 nm with peaks at 550 and 592 nm, 15 ± 4.5 mW, 15h): pyranine droplet fluorescence intensity decreased by -29 ± 7.4 % (-175 ± 49 A.U, n = 3). Using a calibration curve (Fig. 2.10), the corresponding pH change was quantified: droplet pH decreased by -0.2 ± 0.2 pH (Fig. 2.22, 2.11). The magnitude of this pH change matched both the calculations of the extent and direction of CM-aR3 insertion (as determined from electrical recordings, Section 2.2.9), and the reported kinetics of the CM-aR3 photocycle[129].

Absence of channel activity

Bacteriorhodopsin (PM-bR) functions solely as a photochemically-driven proton pump. In contrast, the related light-driven microbial protein channelrhodopsin-2 (ChR2) displays both proton pumping and ion channel activity. To characterise archaerhodopsin-3 (CM-aR3) photoactivity, responses to light and applied potentials were measured with Ag/AgCl electrodes. Light-driven pumping activity can be observed by changes in the signal output upon illumination (Fig. 2.13, 2.15)[31,44]. Similar changes in signal output were observed when light-driven channels (ChR2) were reconstituted into droplet bilayers and illuminated (unpublished observations by **V.R.S**[196]). However, since channels can move ions across the bilayer at a much higher rate than pumps, the signals generated were much larger. Channel activity was also detected when a potential was applied (in the dark) across the ChR2-containing bilayer[196]. Similar potential-sensitive responses were observed when the bilayer was reconstituted with other types of channel protein: synthetic (BLINK-1)[175,196], mechanosensitive (MscL)[208] and potassium (hERG, KCsA)[42,48] channels. In addition, pore-forming proteins e.g., alpha-hemolysin (αHL) produce large signal responses under an applied potential as they form an (always open) ion-conducting passage through the bilayer (Fig. 2.23e-f)[40,44,50,52].

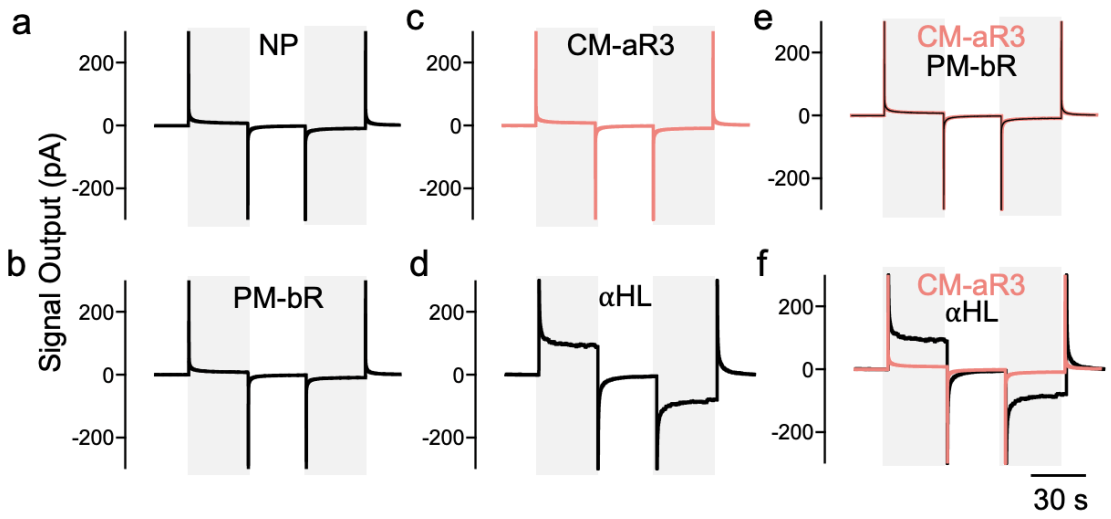


Figure 2.23: Voltage-sensitive responses of protein bilayers. Electrodes were added across a droplet bilayer to apply a potential and record the signal responses. The voltage protocol involved first applying a positive potential (+ 50 mV, 30 s, first grey bar) and then a negative potential (- 50 mV, 30 s, second grey bar). **a-d** Signal responses recorded across a bilayer containing: a - no protein (NP); b - PM-bR (a known proton pump) ; c - CM-aR3 or d - αHL (a protein pore). **e-f,** Overlapping traces of e - CM-aR3 and the proton pump PM-bR and f - CM-aR3 and the protein pore αHL. All recordings were performed in the dark. Figure is adapted from the author's manuscript in progress[192]

In a similar manner, the photoactivity of CM-aR3 was monitored in response to light and/or an applied potential. Previous optical and electrical experiments confirmed that CM-aR3 functioned as a light-driven proton pump (Fig. 2.22, 2.15). Next, a potential was applied across the photosensory bilayer (in the dark) and the signal output recorded; first + 50 mV (30 s) and then - 50 mV (30 s) (grey bars, Fig. 2.23). No large signals (pA $\leqslant$ mV) were observed for a CM-aR3-containing bilayer (under an applied potential, in the dark). This lack of potential-sensitive response suggests that CM-aR3 does not possess channel activity. Moreover, the response was comparable to those of a protein-free bilayer or ones containing the proton pump PM-bR (Fig. 2.23); in contrast αHL generated large signal responses (pA $\geqslant$ mV).

Next, the CM-aR3 containing bilayer was illuminated (YG light, 490 - 608 nm with peaks at 550 and 592 nm, 15 $\pm$ 4.5 mW) simultaneously with an applied potential ($\pm$ 50 mV). Upon illumination CM-aR3 pumped protons across the bilayer regardless of the applied membrane potential (Fig. 2.24). Again, no large signal outputs were observed when a potential was applied across the bilayer even in the

presence of light (pA ⩽ mV, Fig. 2.24). In fact, light-driven proton pumping of CM-aR3 (+ 21 ± 0.6 pA, n = 3) accounted for at least two thirds (67 ± 4.3 %, n = 3) of the signal output recorded across a CM-aR3 photosensory DIB (+ 32 ± 1.2 pA, n = 3) subject to both illumination (YG light, 550 and 592 nm) and a potential (+ 50 mV).

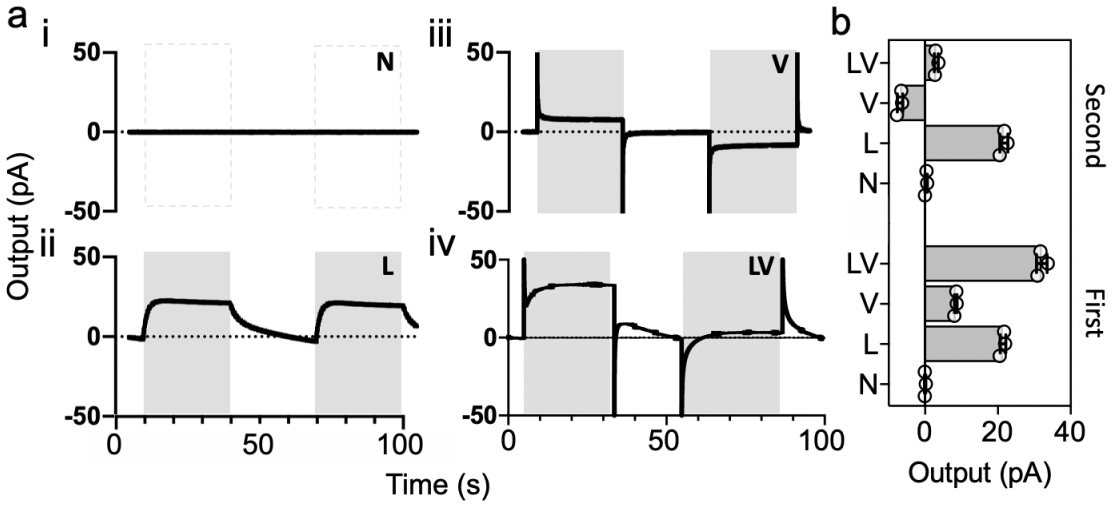


Figure 2.24: CM-aR3 is a light-driven pump. a, Signal traces recorded across a CM-aR3 photosensory DIB (i) in the dark with 0 mV applied potential (N); (ii) with 2 pulses of yellow-green light (30 s in duration, 0.016 Hz, 0 mV, L), grey bars indicate when the light is on; (iii) in the dark with +50 mV (first grey bar) and – 50 mV (second grey bar) applied (V).; (iv) with +50 mV (first grey bar) and – 50 mV (second grey bar) applied simultaneously with yellow-green light (550 and 592 nm, 15 ± 4.5 mW, 30 s in duration, 0.016 Hz, LV). **b,** Steady-state signal (mean SD, n = 3) recorded across a CM-aR3 DIB when: N - in the dark, 0 mV; L - YG light, 0 mV; V - in the dark, ± 50 mV; LV - YG light, ± 50 mV. Figure is adapted from the author's manuscript in progress[192].

Finally the relationship between the voltage applied, and the ions which moved, across a CM-aR3 droplet bilayer was determined. In the dark, only small signal responses (pA < mV) were observed when potentials up to + 100 mV were applied across the bilayer: + 21 ± 3.9 pA (+ 20 ± 1.2 pA in the absence of protein, NP) (Fig. 2.25a). This is in disagreement with channel forming proteins which maintain a large voltage under applied potential (observed by a large increase in signal). Channel-like signal outputs were also not observed when a potential was applied across the CM-aR3 photosensory bilayer under constant illlumination (YG light, 490-608 nm, peaks at 550 and 592 nm, 15 ± 4.5 mW, Fig. 2.25b). Here, the output

recorded at 0 mV was set to zero so that the relationship was more easily observed. As no large signals were generated when a potential was applied across a CM-aR3 photosensory module (unlike protein pores and channels) this suggests that (within this experimental system) CM-aR3 does not display any channel activity. This is in line with literature reports[121,150] and would be predicted from the highly conserved residues located within the pumping pathways of PM-bR and CM-aR3.

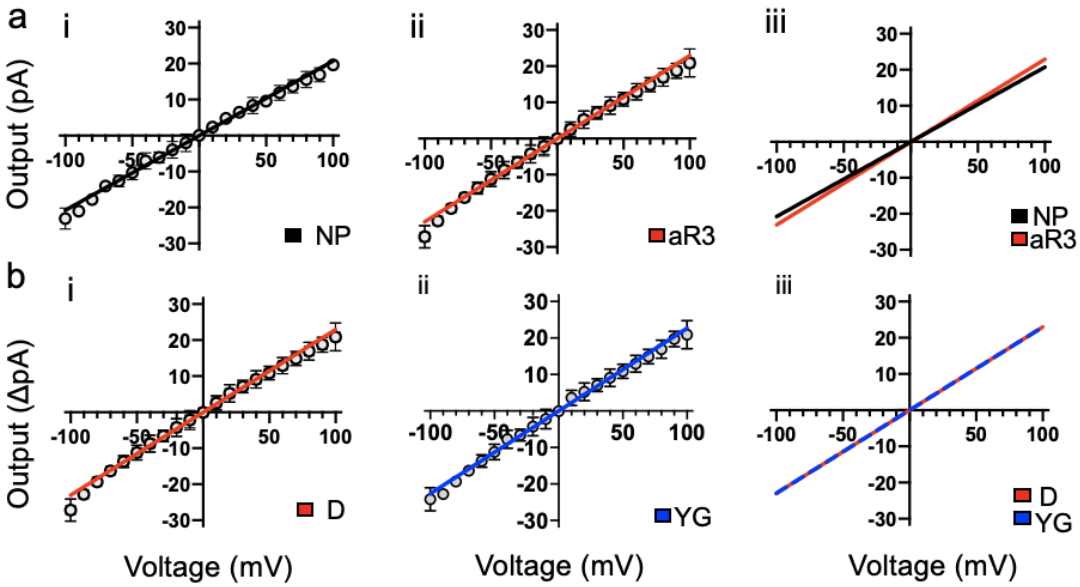


Figure 2.25: IV Curves across a CM-aR3 DIB. a, IV curves recorded across a DIB in the dark when the DIB contains (i) no protein (NP, black), or (ii) CM-aR3 (red) with the line of best fit plotted (n = 3, mean ± SD). (iii) shows the overlapping lines of best fit. **b,** IV curves recorded across a DIB containing CM-aR3 either (i) in the dark (D, red) or (ii) under illumination with YG light (YG, 490 – 608 nm, peaks at 550 and 592 nm, 15 ± 4.5 mW, blue) with the line of best fit plotted. (iii) shows the overlapping lines of best fit. Figure is adapted from the author's manuscript in progress[192].

Photoswitching capabilities

Previous studies on related microbial rhodopsins such as ChR2 have shown that prolonged exposure to light can result in a reduction in protein activity; the protein may be desensitised or become inactivated[129]. To explore whether CM-aR3 underwent these phenomena, the signal generating capability of a CM-aR3 photosensory module was monitored over time. First, it was repeatedly stimulated by 10 successive pulses of yellow-green light (YG, 490 – 608 nm with peaks at 550

and 592 nm, 15 ± 4.5 mW, 0.02 Hz, Fig. 2.26a). Each cycle was composed of two sections: the light pulse (30 s illumination with YG light) and the dark phase (light off, 15 s in duration). CM-aR3 maintained its photoactivity throughout the experiment; signals greater than the 1.0-pA threshold were recorded with each light pulse (i.e. signals were reproducibly generated) (Fig. 2.26). However, there was a slight reduction in the steady-state signal over time with the output reducing from + 18.8 ± 0.3 pA at pulse 2 to + 18.3 ± 0.6 pA at pulse 10 (Fig. 2.26). This is similar to the behaviour of bR when it is repeatedly illuminated and can be restored by increasing the recovery time (in the dark).

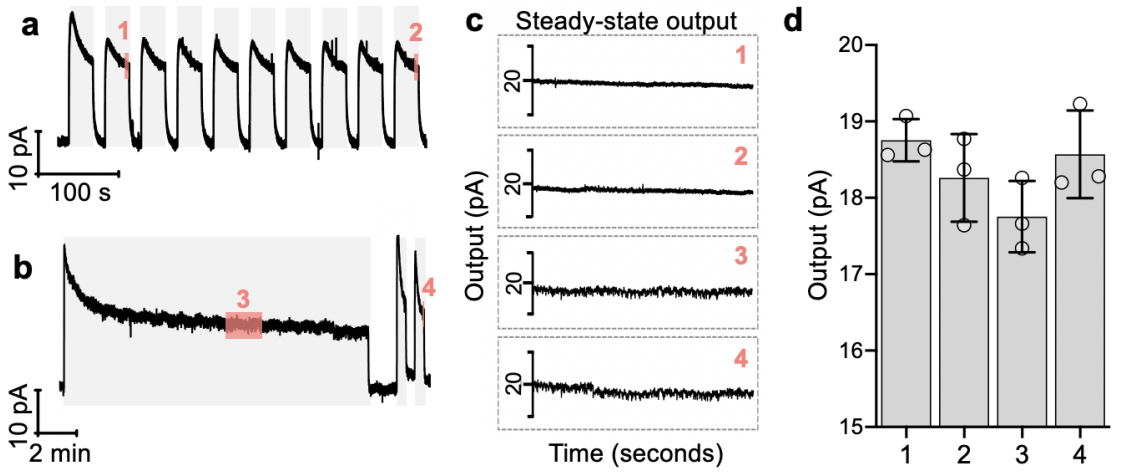


Figure 2.26: Reproducible photoswitching of CM-aR3. a, Signal trace recorded across a DIB containing CM-aR3 upon pulses of illumination (YG light, 490 – 608 nm with peaks at 550 and 592 nm, 15 ± 4.5 mW, light on for 30 s, 0.02 Hz). gGrey bars indicate when the light is on. steady-state level (5 s section) of the second (a1) and final (a2) pulses are indicated by a pink box. **b,** Signal trace recorded across a DIB containing containing CM-aR3 upon continuous illumination (YG light on for 15 min) followed by 5 min in the dark and then two short illumination pulses (30 s, 0.016 Hz). Grey bars indicate when the light is on. steady-state level of the long pulse (b3, 2 min section) and final short pulse (b4, 5 s section) are indicated by a pink box. **c,** Zoom in of the steady-state output levels indicated by the pink boxes in 'a-b'. Output focuses on the 15 – 25 pA section of the trace. For the steady-state levels 1 (a1), 2 (a2) and 4 (b4), the final 5 s of the 30 s illumination pulse is plotted. In the case of the steady-state level 3 (b3), a 2-minute section of the + 15-minute illumination pulse is plotted. **d,** Steady-state signal (mean ± SD, n = 3) of the illumination cycles in 'a-b': 1 = + 18.8 ± 0.3 pA, 2 = + 18.3 ± 0.6 pA, 3 = + 17.8 ± 0.5 pA, 4 = + 18.6 ± 0.6 pA.

Next, the exhaustion point of the photocycle was examined. The signal generating capability of a CM-aR3 photosensory module was monitored over a long

(15 minute) pulse of continuous light (YG, 490 – 608 nm with peaks at 550 and 592 nm, 15 ± 4.5 mW). Once the steady-state output (+ 17.8 ± 0.5 pA, n = 3) was reached, it was maintained until the light was switched off (Fig. 2.26b). After a comparatively short dark phase (LED off, 1 minute), the CM-aR3 photosensory module was illuminated by two pulses (30 s pulses, 0.016 Hz), both generating signals above the 1.0-pA threshold (Fig. 2.26b-d). These experiments indicate that, within the photosensory module system, CM-aR3 doesn't experience protein desensitisation, nor does it become photo-bleached rendering it inactive.

2.2.7 EC-aR3 photosensory modules

As with other microbial rhodopsins[127], aR3 can be heterologously expressed within the bacteria *E.coli*. Using this host, aR3 was rapidly produced by **J.V**).

2.2.7.1 Oligomerisation

The CD spectra of EC-aR3 (performed by **J.V**) confirmed that the protein was correctly folded; the predominately α-helical architecture is characteristic to microbial rhodopsins (Fig. 2.27).

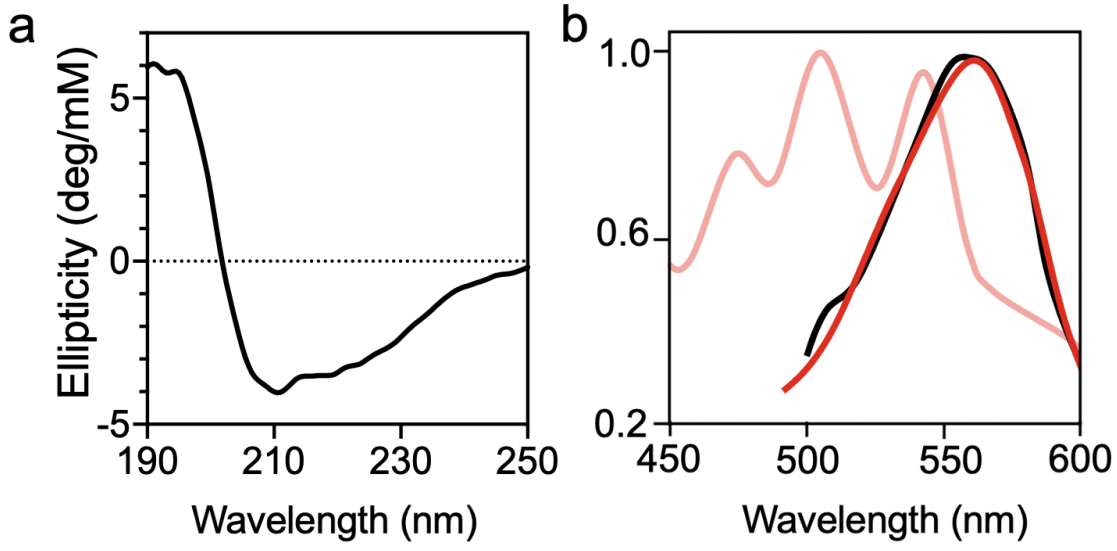


Figure 2.27: Monomeric EC-aR3. a, CD spectrum of EC-aR3 shows a predominantly α-helical structure. **b,** UV-Visible absorption spectra of CM-aR3 (pink, trimeric), EC-aR3 (red, monomeric) and delipidated aR3 (black, monomeric). Figure is adapted from the author's manuscript in progress[192].

Due to the lack of bacterioruberin carotenoid, and the non-native lipid environment, it was hypothesised that EC-aR3 was monomeric. Absorption spectra of CM-aR3 (in membrane fragments containing the bacterioruberin carotenoid), delipidated aR3[204] and EC-aR3 were measured to illustrate their spectral differences (done by **J.V**, see **Chapter 6** for Materials and Methods). For CM-aR3, the protein was within its trimeric organization and its spectrum displays the characteristic three finger-print peaks: due to the presence of retinal and bacterioruberin chromophores (Fig. 2.27). CM-aR3 was then delipidated in order to separate its absorbance from that of bacterioruberin. As predicted, a small hypsochoromic (blue) shift was observed; arising due to the switch to a monomeric organisation (Fig. 2.27). Similar behaviour was observed by **Dr. Javier Vinals** when PM-bR was delipidated, becoming monomeric[186,204]. The presence of only a single peak is also indicative of monomerisation (Fig. 2.27). The absorption spectrum of EC-aR3 was comparable to that of delipidated aR3, and possessed both these traits, indicating its monomeric form (Fig. 2.27).

2.2.7.2 EC-aR3 output

The proton pumping activity of EC-aR3, in response to light, was measured using Ag/AgCl electrodes. The ground electrode was in the protein-free droplet and the recording electrode in the photosensory droplet (see Section. 2.2.4.2). Since EC-aR3 had identical protein sequence to CM-aR3, with residues involved in proton pumping conserved, it was predicted that EC-aR3 would also function as a light-driven proton pump.

Indeed, steady-state signals of -6.1 ± 1.4 pA (mean ± SD, n = 10) were recorded across an EC-aR3 photosensory module upon illumination with yellow-green light (YG, 490 - 608 nm, peaks at 550 and 592 nm, 15 ± 4.5 mW) (Fig. 2.28); no signals were recorded when kept in the dark (< 1.0-pA threshold). The magnitude of this signal was around 2-to-3-fold lower than those generated by CM-aR3 photosensory modules (Fig. 2.28b, 2.15), but comparable in size to those observed using PM-bR (Fig. 2.13). Moreover, the action spectrum of EC-aR3 (determined by recording

maximal signal generation at multiple discrete wavelengths) closely resembled that of CM-aR3 (and PM-bR) with maximal absorption of yellow-green light (Fig. 2.28d).

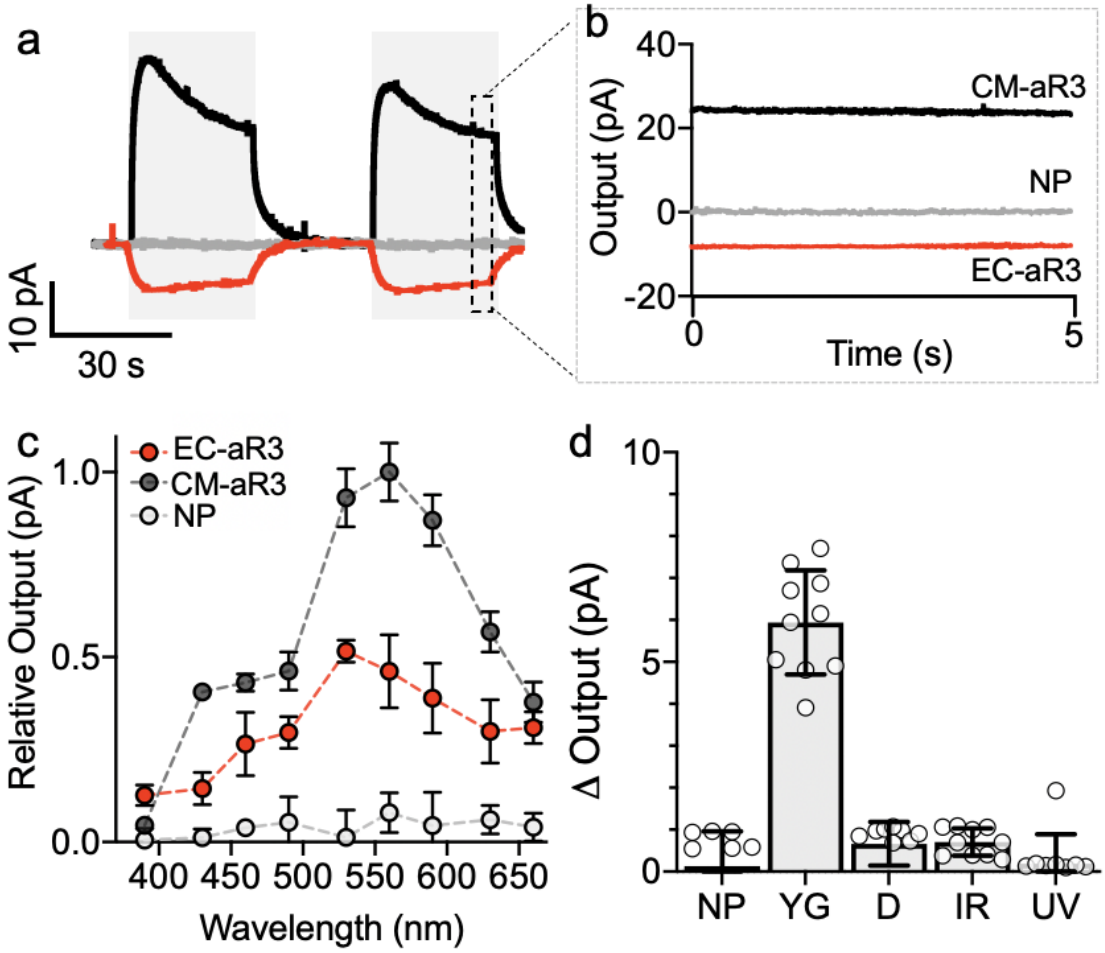


Figure 2.28: EC-aR3 photosensory module. a, Signals recorded across a CM-aR3 (black) or EC-aR3 (red) photosensory module upon illumination (grey bars indicate when the light is on, 490-608 nm with peaks at 550 and 592 nm, 15 ± 4.5 mW) (or in the absence of protein, NP, grey). **b,** Zoom of the steady-state output in 'a'. **c,** Action spectra recorded across a DIB in the absence (grey) of protein or presence of CM-aR3 (black) or EC-aR3 (red) (n = 3, mean ± SD, light output is 0.2 ± 0.1 mW at each wavelength). **d,** Change in output (steady-state level, mean ± SD, n = 10) when the EC-aR3 DIB is illuminated with YG light in the presence (YG) or absence (NP) of EC-aR3 or when an EC-aR3-containing DIB is illuminated with infrared (IR, 680-741 nm with a peak at 722 nm, 16 ± 5.0 mW), ultraviolet (UV, 355-390 nm with a peak at 367 nm, 15 ± 3.9 mW) or no (D) light. Figure adapted from the author's manuscripts in progress[192,193].

2.2.7.3 Orientation

Despite the both EC-aR3 and CM-aR3 being yellow-green light-sensitive pumps, the signal polarity differed as EC-aR3 photosensory module generated negative signals

(Fig. 2.28-b). A negative signal is defined as one in which the electrons (negative) flow out of the ground electrode (see **Chapter 6** for details). Therefore, the protons must move out of the protein-free droplet (which contained the ground electrode) (Section. 2.2.4.2). Consequently, EC-aR3 must insert into the DPhPC bilayer in the opposite orientation to CM-aR3. This difference in topology may reflect its monomeric state (Fig. 2.27), the altered lipid composition (reflecting the two expression systems), the presence of a poly-histidine tag at the C-terminus of the recombinant protein (6-His tag), or the absence of the carotenoid bacterioruberin.

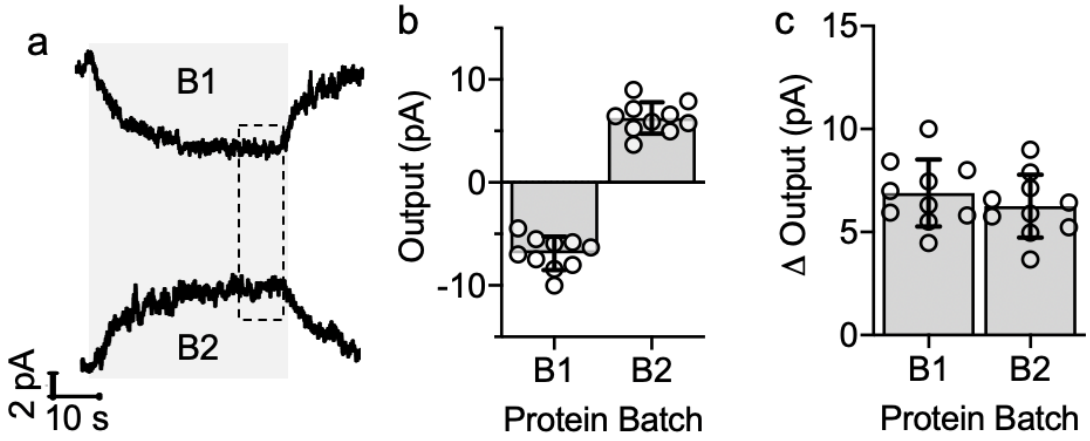


Figure 2.29: EC-aR3 can insert into DIBs in either direction. a, Signal trace recorded across an EC-aR3 DIB upon illumination (YG light, 490-608 nm with peaks at 550 and 592 nm, 15 ± 4.5 mW). For a DIB containing batch 1 (B1) EC-aR3, the signal decreased upon illumination (protons were pumped out of the protein-free droplet) but for a DIB containing batch 2 (B2) EC-aR3, the signal increased upon illumination (protons were pumped into the protein-free droplet). Grey bars indicate when the light is on. **b,** Magnitude and polarity of the steady-state output (mean ± SD, n = 10) recorded across a DIB containing Batch 1 or Batch 2 EC-aR3. **d,** Magnitude of the steady-state output (mean ± SD, n = 10) recorded across a DIB containing Batch 1 or Batch 2 EC-aR3. Figure adapted from the author's manuscript in progress[192].

Interestingly, different protein (expression and purification) batches of wild-type EC-aR3 inserted in different directions. Therefore, some batches generated positive signals upon illumination and some negative signals (see Section 2.2.4.2 and **Chapter 6** for details). Nonetheless, the direction of EC-aR3 insertion was consistent within a single protein (expression and purification) batch (Fig. 2.29).

For this reason, each experiment was performed using only a single protein batch to enable comparisons to be made.

Since protein orientation within the photosensory module is not currently controllable, the direction of insertion was ignored for EC-aR3 experiments. Instead, only the signal magnitude was noted and a change in signal (positive or negative) of $>$ 1.0-pA, was taken to indicate protein functionality (Fig. 2.29).

2.2.7.4 Proton pumping

In addition to electrical recordings, the proton pumping of EC-aR3 was optically monitored by the addition of the pH-sensitive dye pyranine to the protein-free droplet (in the absence of buffer, 100 μM). Here, proton pumping was monitored wirelessly i.e. in the absence of Ag/AgCl electrodes. Droplets with a high pH have a higher fluorescence intensity than those with a lower pH (Fig. 2.10).

Since EC-aR3 pumps protons in the opposite direction to CM-aR3, it would be predicted that the fluorescence of the protein-free (pyranine) droplet would increase over time as protons are pumped out of the pyranine droplet, thereby increasing the pH. Indeed, following overnight illumination (yellow-green light, 550 and 592 nm, 15 $\pm$ 4.5 mW, 15 h) an increase in the protein-free (pyranine) droplet fluorescence of +16 $\pm$1.6 % (+94 $\pm$ 13 A.U, n = 3) was observed (Fig. 2.30). Using the calibration curve (which plots droplet pH against fluorescence intensity) (Fig. 2.10) it was determined that the increase in droplet fluorescence corresponded to a increase in pH of +0.1 $\pm$ 0.0. No significant changes in droplet fluorescence occured when the EC-aR3 photosensory module was illuminated with IR (722 nm , 16 $\pm$ 5.0 mW) or UV (367 nm, 15 $\pm$ 3.9 mW) light or when kept in the dark (D).

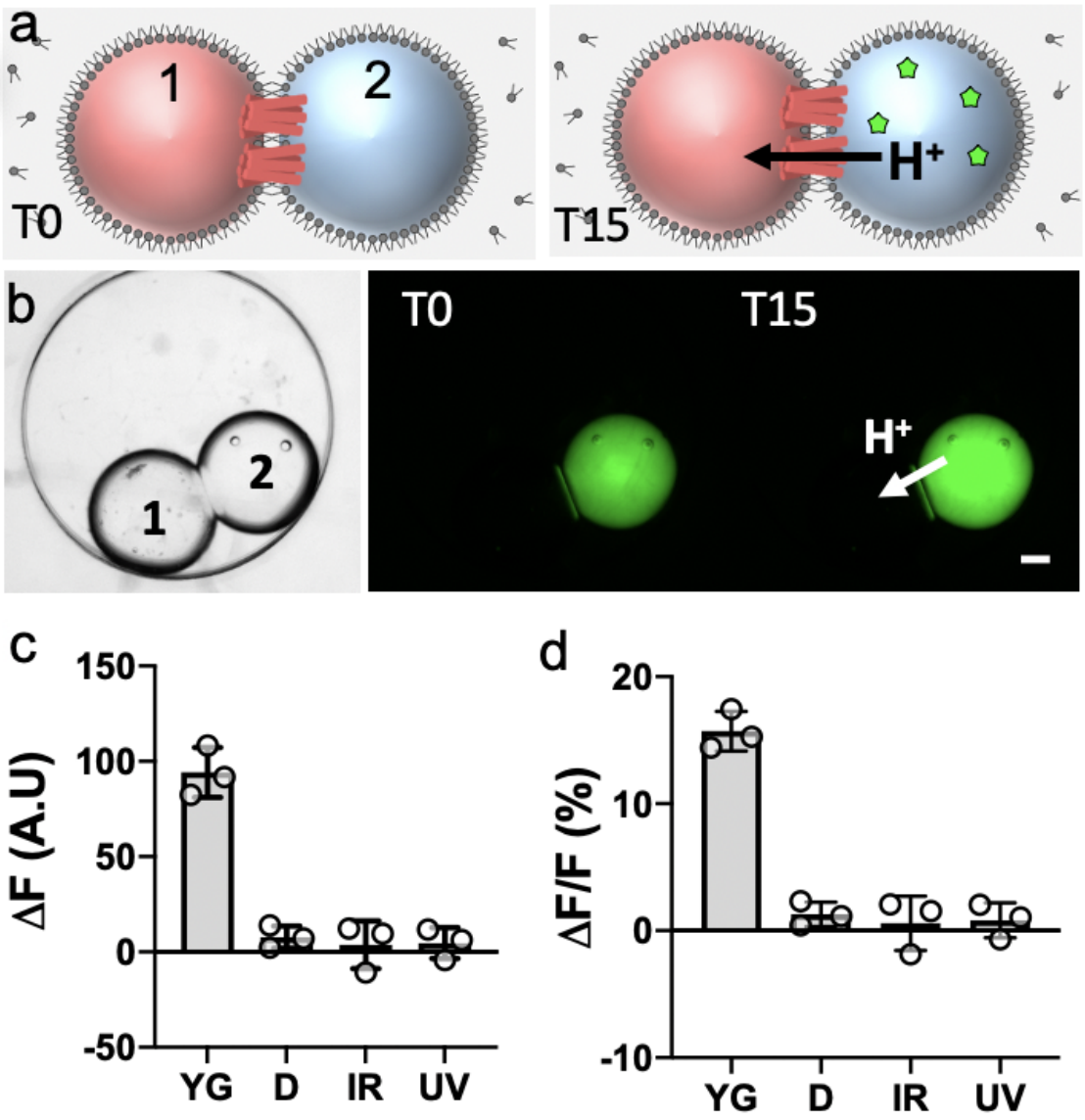


Figure 2.30: EC-aR3 is a light-driven proton pump. a, Schematic of a droplet pair with EC-aR3 inserting into the droplet interface bilayer (DIB) from the photosensory droplet (a1). Upon illumination, protons (H+) were pumped into the photosensory droplet (0.15 – 0.25 mg mL-1 CM-aR3, Solution B, pink, a1) and out of the protein-free pyranine-containing droplet (100 μM pyranine, Solution C, blue, a2). b, Left: Brightfield image of a DIB composed of an EC-aR3 photosensory droplet (b1) and a protein-free droplet (b2) as in 'a'. Right: Epifluorescent images (minus background) of the DIB before (T0) and after (T15) overnight illumination (15 h, YG light, n = 1). Fluorescence intensity of the pyranine droplet increased as protons were pumped out of it[149]. Scale bar is 200 μm. c-d, (c) Absolute and (d) percentage change in fluorescence intensity of the pyranine droplet (b2) following illumination overnight (15 h) with yellow green (YG, 550 and 592 nm, 15 ± 4.5 mW), IR (722 nm, 16 ± 5.0 mW) or UV (367 nm, 15 ± 3.9 mW) light or when kept in the dark (D) (n = 3 DIBs with 3 technical replicates). Figure is adapted from the author's manuscript in progress VinalsCamallongaEnhancedApplication

2.2.8 Photosensory module comparison

Signals generated by photosensory modules containing the photochemically-driven proton pumps, PM-bR, CM-aR3 and EC-aR3 were recorded; below is a table summarising the findings. All three proteins were activated by yellow-green light (YG, 490 - 608 nm with peaks at 550 and 592 nm, n = 10).

Protein	Output (pA)	Orientation	Wavelength	Oligomeric state
PM-bR	+6.9 ± 2.3	N	YG	Trimeric
CM-aR3	+19 ± 3.9	N	YG	Trimeric
EC-aR3	-6.1 ± 1.4	N or C	YG	Monomeric

Table 2.1: Photosensory Module Comparison

2.2.9 Quantitation of CM-aR3 in a photosensory module

The signals generated by microbial rhodopsin-containing droplet bilayers remained significantly smaller than those reported elsewhere[121,129] despite optimisation of the system. Briefly described here are some theoretical considerations related to the photosensory droplets. This section aims to provide information surrounding the insertion of CM-aR3 into the photosensory bilayer. All considerations described in this thesis were adapted in collaboration with **V.R.S** from the similar (bR) droplet system used to make a simple light sensor[31,196].

2.2.9.1 CM-aR3 trimer area

Proteins from the archaerhodopsin family have been found to pack into trimers (in claret membrane patches, CM[129,150]) in a similar manner to the well-characterised proton pump bacteriorhodopsin (bR, which packs into purple membrane patches, PM[121,122,146,147]). Investigations into the structure, properties and proposed mechanism of CM-aR3 are ongoing[129,150] so for the purpose of the following considerations, data is taken from PM-bR.

From their crystal structure (PDB: 2BRD), Grigorieff and colleagues[137] found that the purple membrane contained bR trimers with a hexagonal unit cell that

was 6.2 nm in length (2a, 2 s.f., a = 3.1 nm). Since the recent structure of CM-aR3 (PDB: 6S6C[150]) overlays closely with the structure of bR (Fig. 2.5), it was assumed that CM-aR3 had the same length.

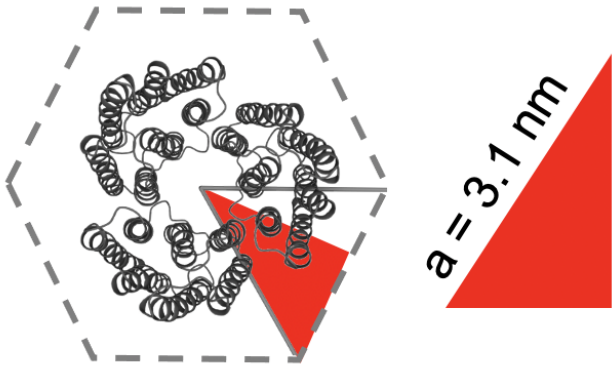


Figure 2.31: A hexagonal unit cell of PM-bR. Structure of a bR trimer in purple membrane (PM) (PDB: 2BRD[137] which forms a hexagonal unit with side length 2a (a = 3.1 nm)

Consequently, the area of an aR3 trimer (A_{aR3}) when packed into the CM can be solved from Equation 2.2. Using the unit cell dimensions of PM-bR, the area of a CM-aR3 trimer area was calculated to be $\approx 25\ nm^2$ ($\approx 10^{-17}\ m^2$).

$$A_{aR3} = (\frac{3\sqrt{3}}{2})a^2 \tag{2.2}$$

2.2.9.2 Number of CM-aR3 trimers in solution

The number of CM-aR3 trimers (N_{pd}) present in a photosensory droplet can be quantified by inserting the relevant variables into Equation 2.3 : Avogadro's constant (N_A, 6.022 $\times 10^{23}\ mol^{-1}$), photosensory droplet volume (V_d, L), protein concentration (C_{pd} g L^{-1}), and molecular mass of the protein (M_P, in units of g mol^{-1}, 27000 g mol^{-1}).

$$N_{pd} = \frac{C_{pd}}{M_p} \times V_d \times N_A \tag{2.3}$$

The photosensory modules constructed in this thesis had a volume of 200 nL (2 $\times 10^{-7}$ L) and contained CM-aR3 at a concentration of 0.15 - 0.25 mg mL^{-1} (0.15 - 0.25 g L^{-1}). Using Equation 2.3, it was estimated that there were approximately

10^{11} - 10^{12} CM-aR3 trimers within the photosensory droplet solution. In addition, Equation 2.3 enables the number of CM-aR3 trimers to be calculated in future photosensory droplets where the variables (e.g. droplet volume) may change.

2.2.9.3 Protein packing into the bilayer

CM-aR3 is a transmembrane protein and inserts spontaneously into droplet interface bilayers.

Minimum bilayer area to host all available proteins

It was of interest to elucidate whether the droplet interface bilayer was even large enough to host all the available CM-aR3 proteins within the droplet (see Equation 2.3, $\approx$ 10^{11} - 10^{12}).

First, the minimum bilayer surface area required to accommodate all the CM-aR3 proteins (A_{mb}) was calculated. Since the area of a CM-aR3 trimer was $\approx$ 25 nm^2 (A_{aR3}) and a 200 nL droplet contained $\approx$ 10^{11} - 10^{12} trimers (N_{pd}), there was sufficient protein to cover a surface of $\approx$ 10^{-5} - 10^{-6} m^2.

$$A_{mb} = N_{pd} \times A_{aR3} \tag{2.4}$$

Actual bilayer size

Next, the number of CM-aR3 proteins which could fit into the experimental photosensory bilayers was calculated. The diameter of a single 200 nL spherical droplet (d_d) is $\approx$ 700 μm, calculated using Equation 2.5.

$$V_d = \frac{4}{3} \times \pi \times (\frac{d_d}{2})^3 \tag{2.5}$$

Under some conditions, e.g., a high silicone oil fragment[40], the diameter of the droplet and the bilayer might be equal. However, within the experimental set-up used in this thesis the bilayer diameter was only a fraction (f) of the total droplet diameter (d_d). It should be noted that bilayer size has not yet been calculated within the photosensory modules but it was estimated to be between 20 - 80 % of the cross-sectional area of the droplet.

$$A_d = \pi \times (\frac{d_d}{2})^2 \tag{2.6}$$

$$A_b = A_d \times f \tag{2.7}$$

Using Equations 2.6 and 2.7, the cross-sectional area of the droplet (Eq. 2.6) and the bilayer (Eq. 2.7) were determined. The area of the photosensory bilayer (A_b), formed between two 200 nL droplets, was found to be between 10^{-7} m^2 (when the bilayer fraction, f, was 80%) and 10^{-8} m^2 (when the bilayer fraction, f, was 20%).

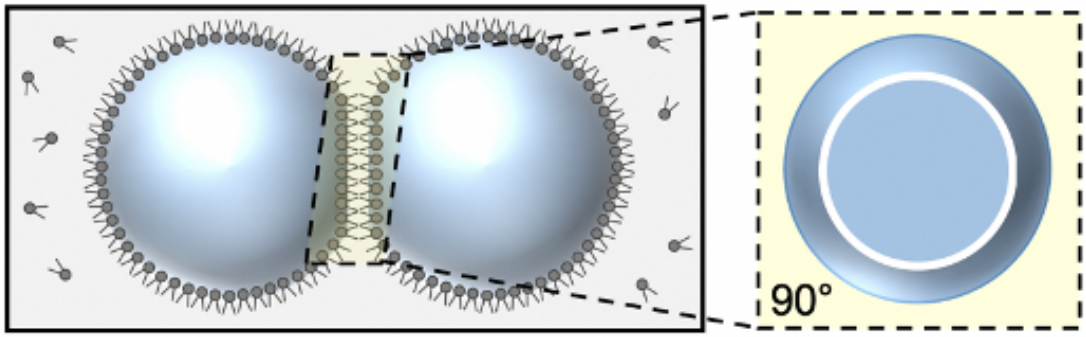


Figure 2.32: DIB surface area. Side view and rotated view (90 of a DIB with a bilayer which has 80% of the cross-sectional area of the droplet. White areola represents the edges of the bilayer. Figure adapted from the author's own paper[193].

Number of CM-aR3 proteins which fit into the bilayer

By knowing the experimental bilayer area (A_b), the maximum number of CM-aR3 trimers which could pack into it (N_{pb}) was calculated by finding the quotient of the bilayer area (A_b) and the CM-aR3 trimer area (A_{aR3}). A maximum of $\approx 10^9$ – 10^{10} (f = 20 - 80 %) CM-aR3 trimers could insert into a photosensory bilayer (formed between 200 nL droplets). Since a 200 nL aqueous droplet has $\approx 10^{11}$ - 10^{12} CM-aR3 trimers within the aqueous solution (Equation 2.3), there is a large excess of CM-aR3 trimers in the photosensory droplet.

$$N_{pb} = \frac{A_b}{A_{aR3}} \tag{2.8}$$

Theoretical maximum signal output

Upon illumination, CM-aR3 proteins pump protons across the bilayer generating a signal output (I_{max}). When the droplets were equipped with Ag/AgCl electrodes, these signals were recorded. Here, the signal is the product of the electron charge (1.6 $\times 10^{-19}$ C), the charge of the species pumped (+1 for protons), the rate of the rate-determining step of the CM-aR3 photocycle (k_p is $\approx$ 20 H^+ s^{-1}[129]) and the number of CM-aR3 trimers in solution (N_{pd}, Equation 2.3).

$$I_{max} = N_{pd} \times (1.6 \times 10^{-19}) \times 1 \times k_p \tag{2.9}$$

In the case of the photosensory droplets described in this thesis, there is sufficient protein in the droplet to generate signals of up to 10^{-6} A (if they fully-packed into the bilayer).

Maximum CM-aR3 inserted into the bilayer

However, the signals recorded across the photosensory bilayers (with saturating light, 550 and 592 nm, 15 $\pm$ 4.5 mW) described in this thesis are much lower: $\approx$ 10^0 - 10^1 pA (I_b instead of I_{max}). Using Equation 2.9, and the reported CM-aR3 photocycle rate (k_p is $\approx$ 20 H^+ s^{-1}[129]), the number of CM-aR3 proteins functionally inserted into the bilayer can be computed (N_{pb} instead of N_{pd}).

A typical signal output for CM-aR3 was approximately + 15 – 25 pA. Therefore, the number of CM-aR3 proteins which functionally insert (N-terminal first) into the bilayer is $\approx 10^6$; a maximum of 10^{11} - 10^{12} CM-aR3 trimers are in solution.

2.2.9.4 Summary of potential limitations

Overall, there are a myriad of reasons why signals lower than those reported in the literature[121,129] are being observed.

1. **Bilayer size**: It is possible that the bilayer is smaller than 20% of the cross-sectional area of the droplets. However, if it is assumed that the bilayer is packed with protein and those proteins are pumping at their maximum rate

(k_p, $\approx$ 20 H^+ s^{-1}[129]), the the bilayer would have to be 0.000001 % of the droplet cross-section. Even with a rate a hundred-fold lower than the reported values, the bilayer would have to be lower than 0.0001% of the droplet cross section. Using optical microscopy, bilayer areas of at least 20% of the droplet cross-section are observed so bilayer size is unlikely to be the limiting factor (e.g., Fig. 2.20, 2.22).

2. **Photokinetics and stability**: Potentially the activity of the aR3 might be reduced or hindered by the reconstitution process. The detergent treatment of CM-aR3 and the use of the exogenous (non-native) DPhPC as the bilayer lipid could disturb the photokinetics and protein stability as they are exogenous lipids. However, for this to be sole cause, the photocycle rate would have to be reduced five-hundred-fold compared to reported values (k_p is $\approx$ 20 H^+ s^{-1}[129]) (the maximum would be expected in these light-saturating experimental conditions).

3. **Orientation**: Within the experimental set-up, CM-aR3 was purified as fragments of the claret membrane. Such fragments might insert into the bilayer randomly or with only a slight preference for a particular orientation. However, photosensitive outputs remained low in other microbial rhodopsins e.g., ChR2-mVenus where a hydrophilic moiety had been added to one side of the protein forcing a single orientation in the bilayer[14] (unpublished experiments by **V.R.S**[196]). Nonetheless, this remains a possible limitation of the current system and should be further investigated.

4. **Inefficient insertion**: The most likely reason for a low output is inefficient protein insertion into the bilayer. It might be that the CM fragments are semi-fusing and form a convex arrangement that alters the bilayer topology and makes it less favourable for additional insertion. A more likely explanation might be that the DPhPC bilayer requires a certain distance between the CM-aR3 trimers and therefore tight packing cannot take place.

There is significant scope for optimisation of protein insertion into the bilayer and some suggestions have been added for future work in **Chapter 5**.

2.2.9.5 Quantitation of proton pumping

To monitor the photoactivity of CM-aR3 in the absence of electrodes pyranine (a pH-sensitive dye) was added to the droplets. Pyranine fluorescence increased with pH (Fig. 2.10[149]). The (200 nL) aqueous droplets used in this thesis have a pH of 6.5. Here, the proton concentration is 3.2 $\times 10^{-7}$ M (Equation 2.10).

$$Moles(n) = Concentration \times Volume \tag{2.10}$$

From overnight experiments (15 h, YG light, 550 and 592 nm, 15 ± 4.5 mW), it was calculated that droplet pH changed by ≈ 0.2 - 0.5 pH; increasing in the photosensory droplet and decreasing in the protein-free droplet (Fig. 2.22, 3.12). For a case in which the photosensory droplet (+ CM-aR3 proteins) increased in pH from 6.5 to 6.8, this would correspond to a loss of approximately 3 $\times 10^{-14}$ moles of protons (which are pumped across the bilayer); the actual number of protons (N_{HP}) can be computed from Equation 2.11.

$$N_{HP} = n \times N_A \tag{2.11}$$

Initially, when the pH is 6.5, the droplets contain ≈ 4 $\times 10^{10}$ protons. An increase in pH (of 0.3 units to pH 6.8) of the photosensory droplet corresponds to the transfer of 2 $\times 10^{10}$ protons across the bilayer.

2.2.10 Chromophores

Bacteriorhodopsin (bR) and archaerhodopsin-3 (aR3) are light-driven proton pumps. Both proteins contain the chromophore retinal; aR3 also has a bacterioruberin carotenoid.

- Retinal is essential for proton pumping; photoisomerisation initiates the protein photocycle and ultimately results in the pumping of one proton across

the bilayer (per photon absorbed)[129]. The bleaching process, in which retinal molecules are removed from the protein, is therefore a major concern in a number of applications (e.g. optogenetics) which rely on light-driven proton pumping[131,132,156].

- The carotenoid bacterioruberin is not known to be involved in proton pumping. Instead, it non-covalently bound at the monomer interface and has been suggested to play an important role in oligomeric protein assembly[144,149,151] and perhaps offer some photoprotection against bleaching[152].

CM-aR3 retinal bleaching

First, the effect of retinal bleaching on CM-aR3 photoactivity was explored. The Schiff base was cleaved, and the retinal bleached, using hydroxylamine (0.2 M) and continuous illumination (white light, > 20 mW output, 20 h). Retinal bleaching was monitored using absorbance spectrophotometry with a decreasing absorption peak at $\approx$ 570 nm indicative of bleaching (Fig. 2.33). The protein bleaching and absorption spectrophotometry were performed by **Dr Javier Vinals**. Interestingly, he observed that the bleaching of CM-aR3 was slower than that of PM-bR, indicating that perhaps bacterioruberin does possess some photoprotective capabilities (unpublished observations [186]).

The bleached proteins (-ret) were then reconstituted into droplet bilayers in order to monitor their proton pumping functionality. As predicted, bleached CM-aR3 (-ret) did not generate signals upon illumination (+0.6 ± 0.3 pA, mean ± SD, n = 3, 490-608 nm, peaks at 550 and 592 nm, 15 ± 4.5 mW) (Fig. 2.33c-d). This was predicted since retinal photoisomerisation is essential for proton pumping activity. However, pumping functionality was recovered following the addition of retinal (all-trans) to the bleached CM-aR3 (-ret) protein with steady-state signals of + 5.0 ± 0.8 pA (+ret)(Fig. 2.33c-d, mean ± SD, n = 3). Despite the presence of retinal, signals remained below those of unbleached CM-aR3 (+20 ± 2.0 pA, mean ± SD, n = 3, Fig. 2.33c-d). Interestingly, the output magnitude was comparable

to those of EC-aR3 (6.2 ± 1.0 ΔpA, mean ± SD, n = 3) in which retinal is added after protein production has been induced (Fig. 2.33c-d, 2.28).

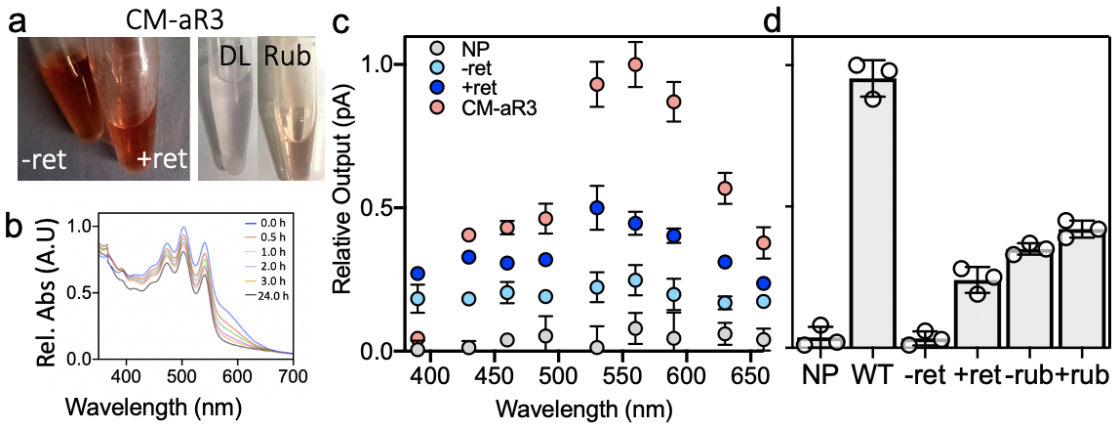


Figure 2.33: Role of CM-aR3 chromophores a, Images of the protein samples. CM-aR3 after bleaching (-ret, no retinal) and after exogeneous retinal is re-added (+ret). Delipidated CM-aRe (DL) and bacterioruberin carotenoid (Rub). **b,** UV-Visible absorption spectrum of CM-aR3 during bleaching with hydroxylamine. Experiment performed by **J.V. c,** Action spectra (mean ± SD, n = 3) of a bilayer containing no protein (NP, grey), CM-aR3 (pink), bleaching CM-aR3 (-ret, pale blue) or CM-aR3 with exogenous retinal (+ret, dark blue). All LEDs were run at an output of 0.2 ± 0.1 mW. **d,** Signal outputs relative to CM-aR3 wild-type upon illumination with YG light (490-608 nm with peaks at 550 and 592 nm, 15 ± 4.5 mW, mean ± SD, n = 3).

Bacterioruberin

Photosensory modules were made using CM-aR3 that had been delipidated (there is no bacterioruberin present, -rub, see **Chapter 6** for details); here, the protein was monomeric (Fig. 2.27). The proton pumping functionality of delipidated CM-aR3 should be retained since the retinal chromophore, critical for pumping, is present. Indeed, steady-state signals of + 7.0 ± 0.8 pA were recorded upon illumination (YG light, 490-608 nm, peaks at 550 and 592 nm, 15 ± 4.5 mW, mean ± SD, n = 3) (Fig. 2.33d). Unsurprisingly, the change in signal following the addition of bacterioruberin to the delipidated protein was negligible; signals of + 8.2 ± 0.7 pA were observed (YG light, mean ± SD, n = 3) (Fig. 2.33d). As the monomer forms the functional unit, it is logical that these two outputs are comparable; bacterioruberin is not essential for pumping.

2.2.11 Spectral mutant library

In nature, each microbial rhodopsin protein is finely tuned to ensure that the maximum light absorbance (λmax) matches that microbe's biological niche thereby enhancing the light-harvesting capability of the organism. However this means that nature may not yet have fully explored all the physiochemical limits of the protein itself. Further, for certain applications some wavelengths may be advantageous, e.g. longer, red-light is desirable in optogenetics since is is less harmful to cells. Protein engineering or synthetic biology techniques might be used to create novel microbial rhodopsins, or shift the absorbance of the current protein tools.

2.2.11.1 Library design

Spectral tuning of the absorbance of microbial rhodopsins is dictated primarily by the electrostatic potential of the retinal environment. It has been shown that subtly altering the amino acid residues located within the retinal binding pocket changes the excitation energy required for photoisomerisation. This corresponds to a different wavelength of light being absorbed (λmax): a spectral shift[178,209,210,211]. Computational studies demonstrate that polar residues in the proximity of the Schiff base alter the λmax of the protein by stabilising the chromophore ground state with respect to the excited state which increases the excitation energy required resulting in a hypsochromic (blue) shift. The excitation energy required decreases when polar residues are located near to the β-ionone ring, resulting in a bathochromic (red) shift. Using molecular dynamics simulations (MD), quantum mechanical and molecular mechanical analysis (QM/MM) and density functional theory (DFT), the mechanism of spectral shifts has been explored in microbial rhodopsins[212,213]. These studies have found that a variety of factors such as retinal orientation, the β-ionone ring electrostatic environment and the distance between the Schiff base and the counterion all influence the spectral absorbance of the protein[212].

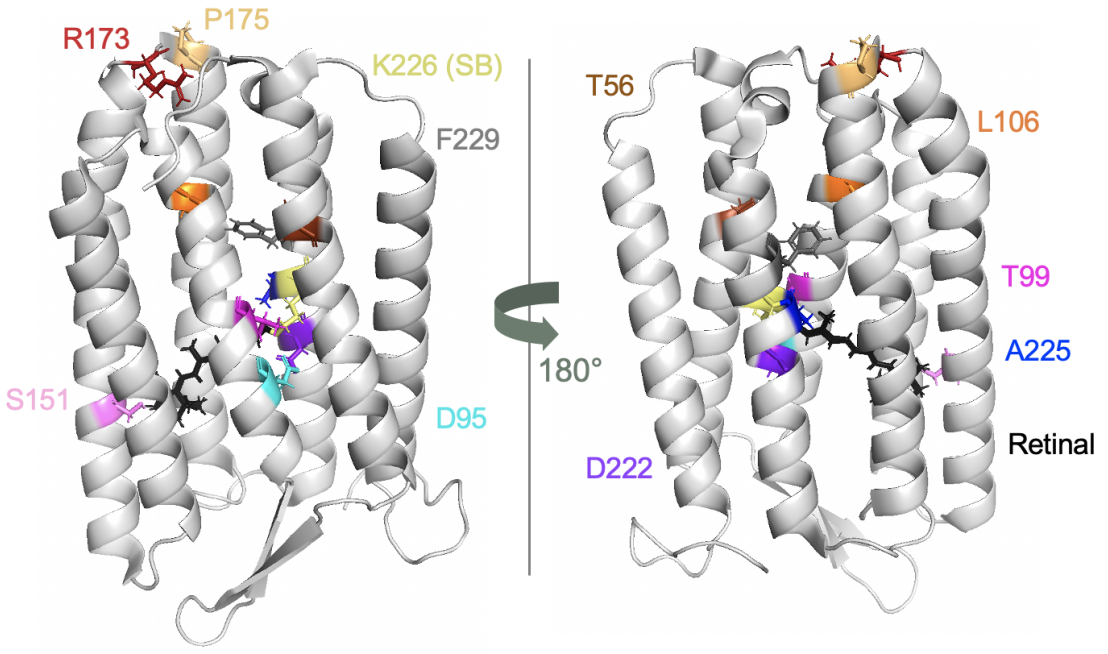


Figure 2.34: Spectral mutants. Structure of CM-aR3 (PDB: 6GUZ[150]) with the residues targeted for mutation shown. The retinal molecule is shown in black and the conserved Schiff base residue (K226), (which was not targeted for mutagenesis) is shown in dark grey. This figure is adapted from the author's manuscript in progress[192].

Spectral aR3 mutants were rationally designed using information obtained from related studies in other microbial rhodopsins[178,209,210,211]. This was possible due to their high sequence homology and structural similarities. The high-resolution CM-aR3 crystal structure (PDB code: 6S6C[150]) was used to identify candidate sites for mutagenesis (Fig. Fig. 2.34) and the resulting mutants were expressed in *E. coli*(E.C). The majority of the residues mutated were located within the retinal binding pocket (RBP) meaning that they are in close proximity (< 5 Å) to the chromophore. An EC-aR3 spectral library, composed of 13 novel mutants and 4 pre-existing ones, was created by **J.V**. The library contained single, (T56R, R173C, A225M, A225T, D95T, D95N, T99C, P175C, S151C, F229S, D222E, L106R), double (T99C/S151C, A225M/S151C, T99C/A225M) and triple (A225M/S151C/T99C, T99C/A225M/P175C, T99C/S151C/P175C) mutants.

Many applications would benefit from the existence of orthogonal microbial rhodopsins whose absorbance maxima are sufficiently far apart that they are not activated by the same region of light. However, it is important for many

applications that the engineered proteins retain their functionality. Therefore, both the spectral properties and pumping activity were investigated since ideal mutants would display a range of maximal absorbance wavelengths without any perturbation to functionality. In addition, the endogenous fluorescence (native to the protein) was recorded for each mutant because enhanced fluorescence would also useful in live-cell imaging, permitting individual action potentials to be reported.

Spectral shifts

Having created a library of colourful EC-aR3 mutants, the absorbance spectra of the proteins was recorded (by **J.V**) to monitor any spectral shifts (Fig. 2.35).

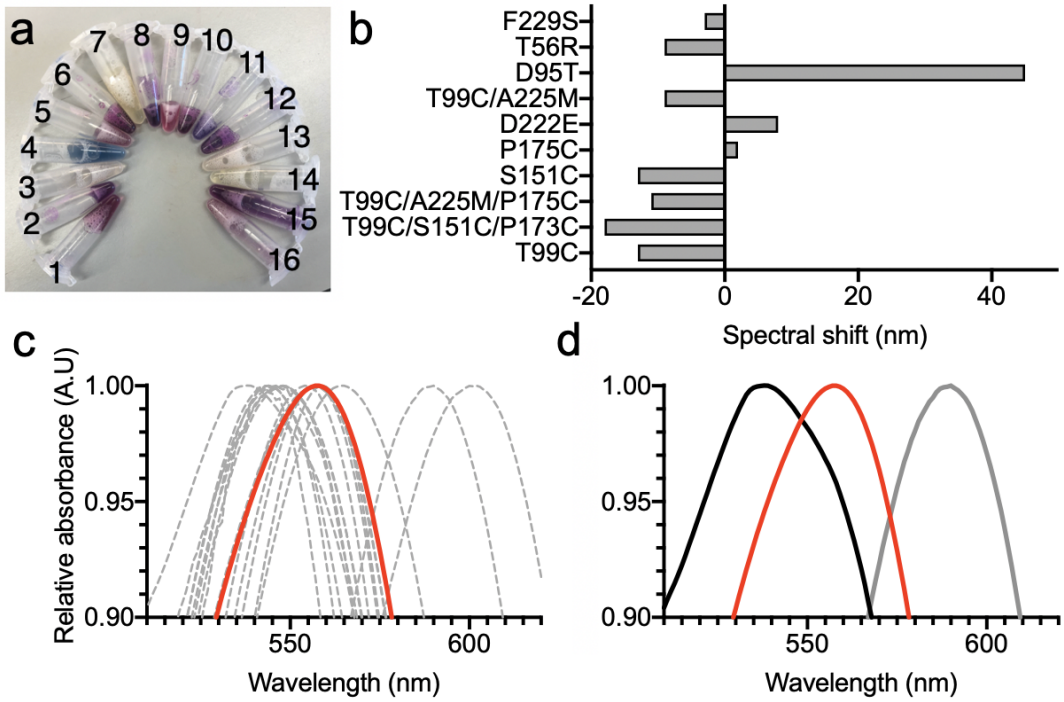


Figure 2.35: Properties of the spectral mutants. a, Colours of the EC-aR3 mutants after purification in 0.003% DDM (see **Chapter 6** for details): 1 - T56R, 2 - R173C, 3 -A225M/S151C/T99C, 4 - D95T, 5 - T99C/A225M/P175C, 6 - T99C, 7 - T99C/S151C, 7 - P175C, 8 - S151C, 9 - F229S, 10 - D212E, 11 - wild-type EC-aR3, 12 - A225M/S151C, 13 - T99C/A225M/P175C, 14 - A225M, 15 - T99C/A225M 16 - A225T. **b,** Bar graph of the spectral shifts (calculated from absorbance spectra in 'c') generated by the EC-aR3 mutants (in 'a') compared to wild-type EC-aR3. All mutants showed a hypsochromic shift except for the residues D95, D222 and P175. **c,** The absorption spectra of the EC-aR3 spectral mutants (grey) relative to WT EC-aR3 (red) reflect the spectral shifts. **d,** Absorption spectra of the largest shifts relative to WT EC-aR3 (red): D95T (grey) and T99C/S151C/P173C (black). Experiment performed by **J.V.** Figure adapted from the author's manuscript in progress[192].

For some mutations, e.g., T99C, a hypsochromic shift would be predicted. By substituting the threonine residue (T) for a cysteine (C) a bulky group was introduced at this position. This restricted the rotational freedom and movement of retinal within the pocket and meant that more energy was required (and therefore more blue-shifted light) for photoactivation. In fact, the absorption spectra of the majority of EC-aR3 mutants had peaks that were blue-shifted relative to the wild-type EC-aR3 (Fig. 2.35 b-d). Of these, the single mutants T56R, T99C, and S151C and the triple mutant T99C/S151C/P173C displayed the greatest hypsochromic (blue) shifts (wild-type EC-aR3 is shown in red, Fig. 2.35d) : -9 nm, -13 nm, -13 nm, and -18 nm respectively (Fig. 2.35 b-d). The triple mutant is the largest blue-shifted protein in the EC-aR3 mutant library (shown in black, Fig. 2.35d). The single mutants D95T, D222E, and P175C were the only bathochromic (red) shifted proteins in the library: +45 nm, +8 nm, +1 nm respectively. The bathochromic shift of D95T is one of the largest reported in the literature for a single mutation (shown in grey, Fig. 2.35d). Within the mutant library, it was found that the double and triple mutants didn't produced spectral shifts equal to the cumulative total of their constituent parts.

Pumping activity

The proton pumping activity of the mutant library was quantified using electrical recordings; Ag/AgCl electrodes were added across the photosensory bilayer. Under illumination (YG light, 550 and 592 nm, 15 ± 4.5 mW), wild-type EC-aR3 generated signals of -6.1 ± 1.4 pA (mean ± SD, n = 3); no signals were generated in the dark, or when illuminated with IR (722 nm, 16 ± 5.0 mW) or UV (367 nm, 15 ± 3.9 mW) light (Fig. 2.28). Since monomeric EC-aR3 might insert into the photosensory bilayer in either direction, for characterisation of the mutant library only signal magnitude (not polarity) was noted; therefore, the EC-aR3 output is 6.1 ± 1.4 ΔpA (Fig. 2.29).

Mutant-containing photosensory modules were then built and the photoactivity recorded: T56R, D95T, T99C, L106R, S151C, R173C, P175C, D222E, A225M,

F229C and T99C/A225M. All of the spectral mutants tested in this thesis produced smaller signals than the wild-type EC-aR3 (Fig. 2.36). For the mutants T99C and S1515C, it was extremely difficult to form stable bilayers and the experiments were eventually abandoned. Droplet coalescence was likely to be due to a high residual concentration of detergent (or some other contaminant) and unlikely to be something to do with the protein itself. However, even after five rounds of buffer exchange it was not possible to form stable bilayers. The mutants D95T, P175C and D222E lacked proton pumping activity (signals $<$ 1.0-pA threshold, n = 3). Both these aspartate residues are known to play a role in proton pumping so it is unsurprising that in their absence no signals were generated. The remaining mutants tested (T56R, L106R, R173C, A225M, F229S and T99C/A225M) generated signals above the 1.0-pA threshold (Fig. 2.36, mean $\pm$ SD, n = 3). The output of the A225M photosensory module was the largest, generating 4.7 $\pm$ 1.3 ΔpA signals upon illumination (YG light, 490 - 608 nm with peaks at 550 and 592 nm, 15 $\pm$ 4.5 mW).

Mutation	**Output (ΔpA)**
WT EC-$aR3^a$	Y (6.9 $\pm$ 2.1)
T56R^a	Y (1.2 $\pm$ 0.2)
D95T^b	N (0.2 $\pm$ 0.2)
T99C^c	Coalesce
L106R^a	Y (2.4 $\pm$ 1.7)
S151C^c	Coalesce
R173C^a	Y (1.3 $\pm$ 0.9)
P175C^b	N (0.1 $\pm$ 0.3)
D222E^b	N (0.0 $\pm$ 0.1)
A225M^a	Y (4.7 $\pm$ 1.3)
F229S^a	Y (2.4 $\pm$ 1.8)
T99C/A225M^a	Y (1.0 $\pm$ 0.1)

Table 2.2: Mutant outputs. Photosensory modules were made of wild-type (WT) EC-aR3 and its mutants, and the outputs in response to yellow-green light recorded (490-608 nm with peaks at 550 and 590 nm, 15 $\pm$ 4.5 mW). a = The mutants T56R, A225M, F229S, R173C, L106R and T99C/A225M generated signals above the 1.0-pA threshold. b = Mutants D95T, D222E, and P175C produced signals below the threshold. c = Photosensory modules could not be formed with the mutants T99C and S151C, most likely due to high detergent or contaminants which couldn't be removed. All experiments were performed using protein from the same batch.

Whilst the absorption spectra indicated that all mutants retained maximal absorption of yellow-green light (490 - 608 nm, Fig. 2.9, 2.35), the action spectra was obtained to confirm this wasn't the reason low (or no) signal outputs were generated by some mutants. The action spectra was determined by measuring the relative signal output at different wavelengths (each LED had an output of 0.2 ± 0.1 mW). Only the mutants A225M and F229S generated signals large enough to detect under the low light intensity; their spectra closely resembled that of wild-type EC-aR3 (Fig. 2.36). A maximal absorption of yellow-green light was expected since they generate shifts of + 0 nm (A225M) and + 3 nm (F229S) respectively (Fig. 2.35).

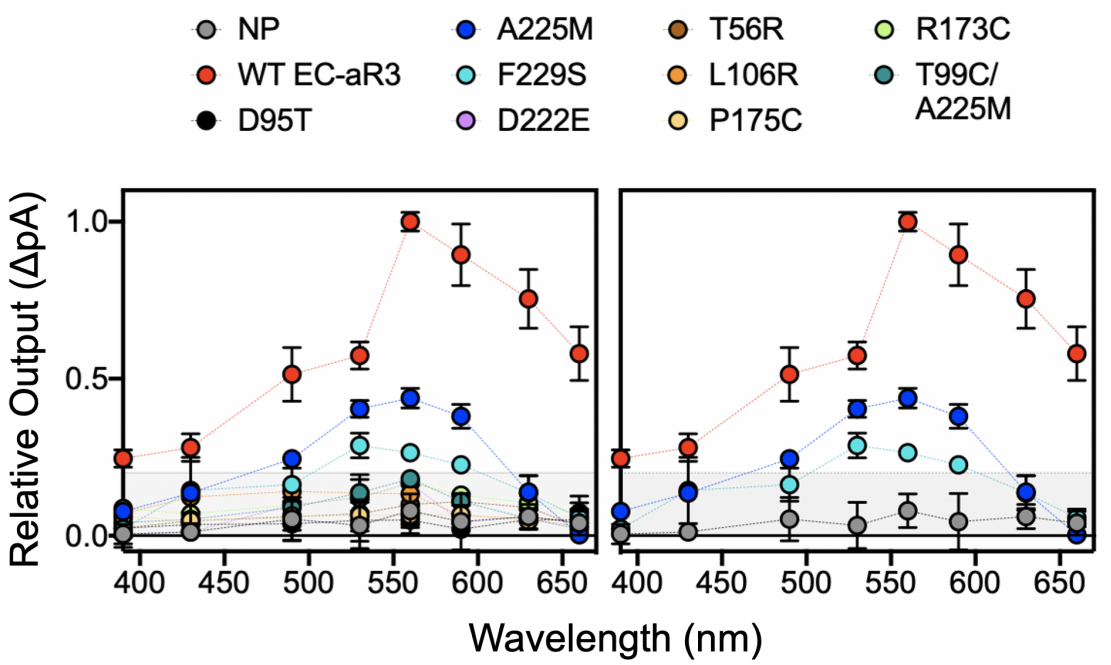


Figure 2.36: Spectral mutant action spectra. Left: Action spectra recorded across a DIB containing wild-type (WT) EC-aR3 (red), no protein (NP, grey) or the spectral mutants: D95T (black); A225M (dark blue); F229S (cyan); D222E (purple); T56R (brown); L106R (orange); P175C (yellow); R173C (light green); T99C/A225M (dark green) (n = 3, mean ± SD, polarity is not noted, ΔpA, each of the 7 LED fibres is run at 0.2 ± 0.1 mW). Grey box indicates signal outputs below the 1.0-pA threshold. Right: Action spectra of WT EC-aR3 and the mutants A225M and F229S (the only proteins to generate outputs above the threshold) under low light conditions (each of the 7 LED fibres is run at 0.2 ± 0.1 mW). All three produce maximal outputs in response to yellow-green light. Figure adapted from the author's manuscript in progress[192].

Fluorescence

Due their endogenous (native) fluorescence, microbial rhodopsins have recently be used as genetically-encoded indicators of membrane potential; the ground state is only weakly fluorescent but this increases upon illumination of the protein. Enhanced protein fluorescence would have utility in optogenetics for improved resolution and sensitivity when studying action potentials. The fluorescence intensity of the EC-aR3 mutants were screened at different excitation/emission wavelength combinations: first in bulk using a plate reader and then in droplets using a epifluorescence microscopy.

In bulk (50 μL in a well plate), fluorescence intensity was monitored at two different excitation/emission wavelength combinations (620/730 nm and 640/710 nm, n = 8). For several mutants (L106R, P173C, R175C, S151C and D222E) fluorescence was suppressed compared to wild-type EC-aR3 (Fig. 2.37). However, the mutants T56R, D95T, A225M, F229S and the double mutant T99C/A225M all exhibited higher fluorescence (under both conditions) than wild-type EC-aR3; this was 2-5-fold higher for D95T, A225M and T99C/A225M. Interestingly, fluorescence of the mutant T99C was suppressed under 620/730 nm conditions but enhanced when 640/710 nm was used (relative to wild-type EC-aR3). Enhanced fluorescence for T99C[178], A225M[178], T99C/A225M[178], and F229S[209] has been previously reported for AR3.

Mutant fluorescence was then acquired in droplets at two different excitation/emission wavelength combinations (540/600 nm and 600/670 nm, n = 3 different droplets with 3 technical replicates taken). The average fluorescence intensity of the droplets (200 nL) was computed in a similar way for those containing pyranine (Fig. 2.11). The background fluorescence (F_B) during imaging was high due to the oil present. However, comparable trends were observed in which the same mutations yielded higher (and lower) fluorescence when compared to the wild-type protein. These mutants might serve as improved genetically-encoded voltage indicators for applications in live cell imaging.

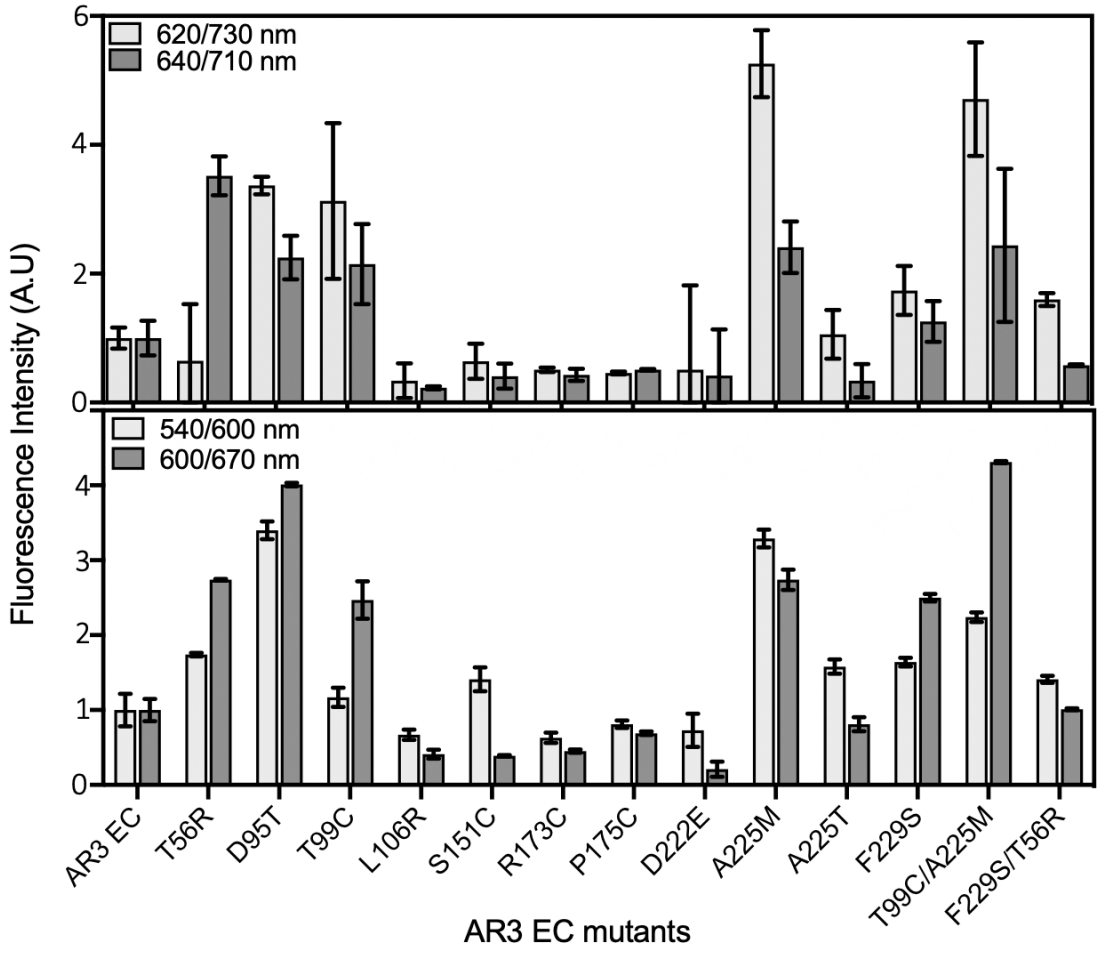


Figure 2.37: Intrinsic protein fluorescence Top: In bulk (50 μL in a well plate), fluorescence intensity was monitored at two different excitation/emission wavelength combinations (620/730 nm and 640/710 nm, n = 8) and the output is plotted relative to wild-type EC-aR3. Bottom: Fluorescence intensity in droplets (200 nL, n = 16) was monitored at two different excitation/emission wavelength combinations (540/600 nm and 600/670 nm) and the output is plotted relative to wild-type EC-aR3. The mean output (± SD) are plotted. Figure is adapted from the author's manuscript in progress[192].

2.2.12 Proton release complex

Differences between the bioelectrical outputs of CM-aR3 and PM-bR is of considerable interest due to the high degree of similarity between their sequences and structures. Whilst the mechanism of CM-aR3 is not yet fully elucidated, differences in proton pumping activity might be a result of the higher pKa of key amino acids located within the CM-aR3 pumping pathway[150]. In addition, CM-aR3 has an intricate water network located in the proton release complex (PRC) which might

enhance photocycle kinetics (PRC)[150]. For this reason, residues located within the PRC were mutated and the effect on their functionality explored.

2.2.12.1 Mutations

Based on studies in other microbial rhodopsins, the amino acids R92 and E214 were mutated; mutants were expressed in *E.coli*. Both residues (R92 and E214) are known to alter the photocycle kinetics, either by trapping the protein in the M-state or delaying the M-state decay time[149]. The positively charged arginine residue (R92) was mutated to either serine (R92S) or threonine (R92T), both of which are uncharged. In addition, the negatively charged glutamate residue (E214) was also mutated to two neutral amino acids: threonine (E214T) and glutamine (E214Q). CD spectrometry confirmed that all four mutants were folded correctly with the predominately α-helical secondary structure maintained ($\approx$ 60% helix, $\approx$ 10% sheet, and $\approx$ 20% random coil) (Fig. 2.38).

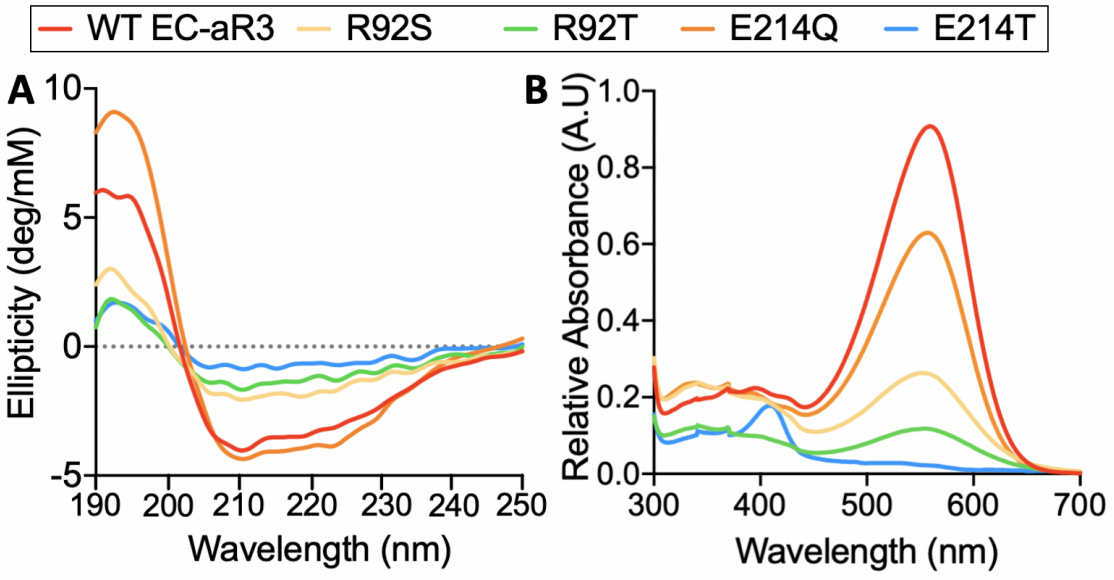


Figure 2.38: CD and UV-Visible spectra of the PRC mutants a, CD absorption spectra of WT EC-aR3 (red) and the PRC mutants: R92S (yellow); R92T (green); E214Q (orange); E214T (blue). All spectra are characteristic of predominantly α-helical structures. **b,** UV-Visible absorption spectra of WT EC-aR3 (red) and the PRC mutants: R92S (yellow); R92T (green); E214Q (orange); E214T (blue). Experiments performed by **J.V.** Figure adapted from the author's manuscript in progress[192].

However, the UV-Visible absorption spectra of the PRC mutants was altered when compared to that of wild-type EC-aR3 (Fig. 2.38). In fact, only the E214Q mutant behaved as predicted. E214Q displayed a single peak at ≈ 560 nm (Fig. 2.38), corresponding to the protein ground state (Fig. 3.10[129]). The spectra of the mutants R92S and R92T had two broad peaks: at ≈ 560 nm and ≈ 410 nm. The latter peak corresponds to the M-state intermediate indicating that the protein population is a mixture of those trapped in the M-state and others in the ground state. This is comparable to the absorption spectra of bR, in which the analogous residue was mutated (R82)[214]. The mutation E214T appeared to trap the protein in the M-state since only one peak at ≈ 410 nm was observed (Fig. 2.38). The introduction of this small neutral residue might disrupt the water network in the proton release complex thereby altering the photocycle kinetics. Interestingly, mutating this amino acid to glutamine (E214Q) doesn't disrupt the PRC to the same extent with the majority of this protein population occupying the ground state (Fig. 2.38, spectra were taken by **J.V**).

2.2.12.2 Proton pumping

To determine the effect these mutations (R92S, R92T, E214Q, E214T) had on proton transport, all mutants were reconstituted into photosensory modules.

Interestingly, only when photosensory modules were formed using R92T was any pumping activity observed, but even here signal output was depleted when compared to wild-type EC-aR3: 3.1 ± 0.8 ΔpA and 6.9 ± 1.6 ΔpA respectively (mean ± SD, n = 3, 490-608 nm, peaks at 560 nm and 590 nm, 15 ± 4.5 mW, Fig. 2.39). Moreover, the action spectra of R92T and wild-type EC-aR3 were comparable; maximal absorption was of yellow-green light. All other mutants (R92S, E214T, E214Q) completely hindered proton transport across droplet bilayers (Fig. 2.39). Contrary to observations in bR, where the equivalent E214T mutant slowed the photocycle, in EC-aR3 the photocycle appeared to be blocked at the M-state (shown by the peak at 410 nm, Fig. 2.38).

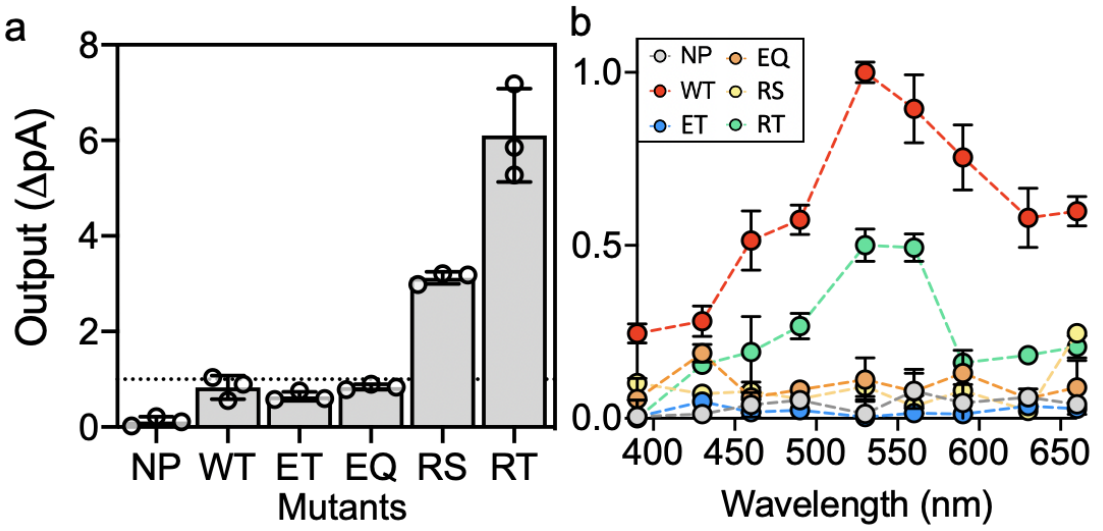


Figure 2.39: Pumping functionality of the PRC mutants. **a,** Steady-state output of the PRC mutants upon illumination with YG light (490 – 608 nm with peaks at 550 and 592 nm, 15 ± 4.5 mW, polarity is not noted, n = 3). R92T exhibits a change in signal (ΔpA) of 3.1 ± 0.6 pA upon illumination with yellow green light; for E214T, E214Q, and R92S the mean signal output is below the 1.0-pA threshold. **b,** Action spectra recorded across a DIB containing WT EC-aR3 (red) and the PRC mutants E214Q (orange), E214T (blue), R92T (green) and R92S (yellow) or no protein (NP, grey). The magnitude of the stable signal is plotted (n = 3, mean ± SD, polarity is not noted), when the bilayer is illuminated with light of different wavelengths (each LED has an output of 0.2 ± 0.1 mW). All signal are plotted relative to the maximum output of WT EC-aR3 (red). Figure is adapted from the author's manuscript in progress[192].

2.2.12.3 Time resolved absorption

Time-resolved absorption was then used to investigate the rapid light-induced absorption changes of wild-type (WT) EC-aR3 and its PRC mutants (Fig. 2.40). These experiments were performed and analysed in collaboration with **V.R.S.** and **C.V**.

The experimental set-up was designed in order to monitor absorption changes at 405 nm (diode Laser 2000, attenuated by a neutral density filter to a power of 8 mW); the samples were excited with a combined pulse of 550 and 590 nm (15 ± 4.5 mW, with pulse lengths between 50 and 400 ms). The laser light (405 nm) passed through the EC-aR3 protein sample which was in turn detected by a photodiode (Thorlabs Det310); this output signal triggered an oscilloscope permitting the visualisation of time-dependent absorption changes.

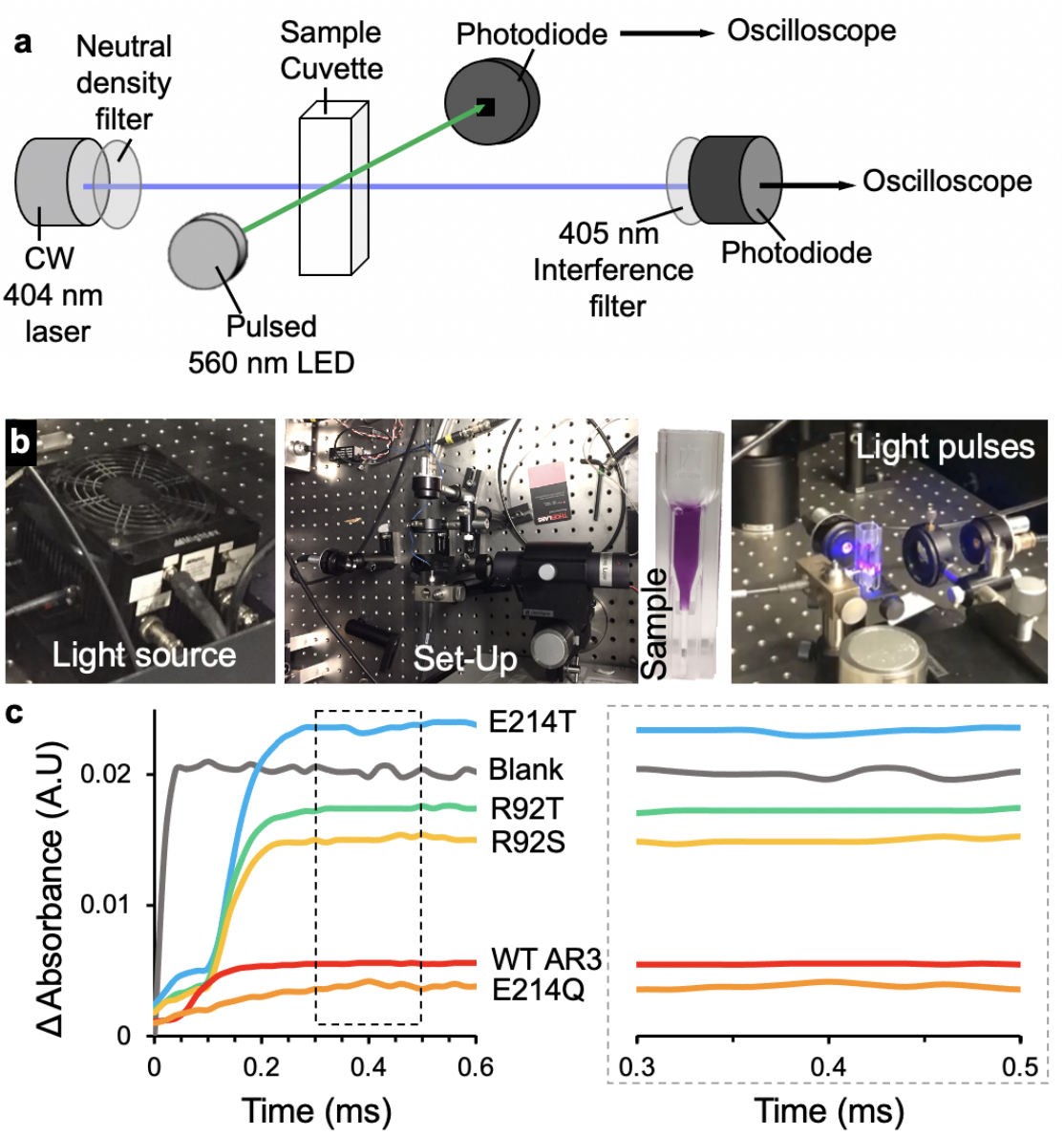


Figure 2.40: Time-resolved absorption of the proteins. **a,** Schematic of the experimental set-up. A 404 nm (blue) light is directed towards the sample, passing through it and on to a photodiode and oscilloscope for detection. Pulses light (≈560 nm, green) passes through the same in the other direction. **b,** Photographs of the experimental set-up shown in 'a'. Left to Right: The light source; Overview of the set-up; Protein sample; Light pulses passing through the protein sample. **c,** Change in absorbance over time for the blank (no protein, grey), WT AR3 (red) and the PRC mutants E214T (blue), E214Q (orange), R92T (green) and R92S (yellow). Dotted box shows a zoom of the plateaued absorbance region. Experiment performed by **C.V** and **V.R.S.** Figure is taken from the author's manuscript in progress[192].

Illuminating wild-type EC-aR3 (550 and 590 nm, 15 ± 4.5 mW) resulted in increased absorption at 405 nm as the protein photocycle was initiated and the

M-state intermediate was formed (peak absorbance at ≈ 410nm) (Fig. 2.40). The PRC mutants (R92S, R92T, E214T and E214Q) were then screened for changes in absorbance over time (Fig. 2.40). The mutant E214Q displayed a lower change in absorbance than wild-type EC-aR3 indicating that the photocycle was hindered (Fig. 2.40).

2.3 Conclusions

Here, power-generating photosensory modules were formed following the successful reconstitution of light-driven proteins into artificial bilayers. Via specialised photochemical and photophysical processes, CM-aR3 transported protons across the droplet bilayer, generating larger signals than its homologue PM-bR. Despite attempts to optimise the system, the photoactivity of these photosensory modules remained below the theoretical maximum with only ≈ 10^5 - 10^6 proteins estimated to functionally incorporated into the bilayer. Consequently, there is scope for this to be improved. A biophysical characterisation of several treated aR3 proteins addressed the different roles of the two chromophores; retinal was critical for photosignal formation whereas bacterioruberin played a role in trimer formation and photo-protection. Moreover, a library of 13 different hypsochromic (blue) and bathochromic (red) shifted mutants was created to provide insights into the spectral properties, endogenous fluorescence and proton pumping behaviour of aR3.

3
A Synthetic Neuron

Here, the photosensory modules developed in **Chapter 2** were elaborated into biomimetic synthetic neurons. The components of these neurons were soft biomaterials: protein-rich lipid membranes connected nanolitre aqueous droplets and hydrogel fibres. Like natural cells, the synthetic neurons communicated using electrochemical events. First, photochemically-driven pumps transduced a physical stimulus (light) into a bioelectrical signal. Mediated by ion-conducting pores, the signal (rapidly and directionally) propagated down centimetre-long axons, and into the synaptic terminals driving neurotransmission. These molecular messengers were capable of initiating functional outputs downstream. By imitating neurobiological architectures and functions, such light-powered synthetic neurons are a significant step towards the development of tetherless bioelectronic devices.

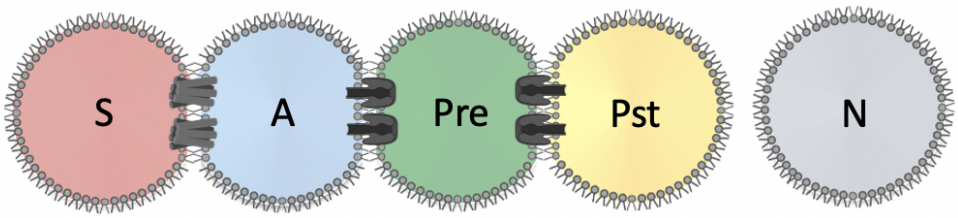


Figure 3.1: A light-powered synthetic neuron. The key components of a light-powered synthetic neuron are: S - photosensory droplet (pink, + CM-aR3 membrane fragments); A - axon (blue); Pre - presynaptic droplet (yellow, + neurotransmitters and monomeric αHL pores); Pst - postsynaptic droplet (yellow) and N - neighbouring cell droplet (grey).

Acknowledgement

The author led the development of the light-powered synthetic neurons described in this thesis, any assistance is indicated in the text. The author would like to acknowledge the practical and intellectual input of Dr Vanessa Restrepo Schild (**V.R.S**) in neuron design and construction. The author also wishes to thank Dr Javier Vinals (**J.V**) for CM-aR3 preparation, Idil Cazimoglu (**I.C**) for αHL preparation, Dr Assala Al Samad (**A.A.S**) for block copolymer preparation and both Dr David Lunn (**D.L**) and Dr Juan Liu (**J.L**) for sharing knowledge.

Publication

The work described in this chapter forms part of a publication currently being written up. Consequently, many of the figures are adapted from this manuscript.

- **Hoskin, C.E.G.**, Restrepo Schild, V., Vinals, J., and Bayley, H. *Parallel transmission in a Synthetic Nerve.*

3.1 Introduction

3.1.1 Bioelectricity

Bioelectricity encompasses all of the biological phenomena arising from the distribution and movement of charge. Research in a variety of systems has identified the important role bioelectricity plays in energy storage, signalling and communication[4,215].

The biophysical properties of the cell are an important modulator for its behaviour and function. Lipid membranes serve as both an insulator and a diffusion barrier to the movement of charge. However, the membrane is rich in proteins which mediate the bioelectrical signals: gap junctions, pumps and channels[4,215]. Transport across biological membranes may be passive or active, depending upon the direction of transport; there is an energy requirement to move molecules against their electrochemical gradient (Fig. 3.2)[4].

- Small, non-polar molecules can simply diffuse across the membrane, but larger polar molecules require assistance. Channel proteins form hydrophilic pores across membranes and are generally ion specific and gated i.e. open in response to a stimulus such as a voltage or ligand. When open, ions can rapidly diffuse downhill through the pore[4] (Fig. 3.2).

- The uphill transport of ions is primarily performed by highly specific protein pumps and carriers (Fig. 3.2). Ion pumps are found throughout nature[411] and consume metabolic energy, usually in the form of ATP. Carrier proteins however utilise the gradients of other molecules, moving different substrates across the membrane either in the same (symporter), or counter (antiporter) direction (Fig. 3.2)[4].

Whilst most ion transport utilises these proteins, other mechanisms exist. Mitochondria use redox proteins to couple electron transfer to the transport of protons across the membrane, and some microorganisms produce small hydrophobic molecules, ionophores, which increase the permeability of the membrane to specific ions[4] (see **Chapter 1** for more details). By controlling transport across the

membrane, cells can dictate the distribution of these charged ions and molecules forming electrochemical gradients.

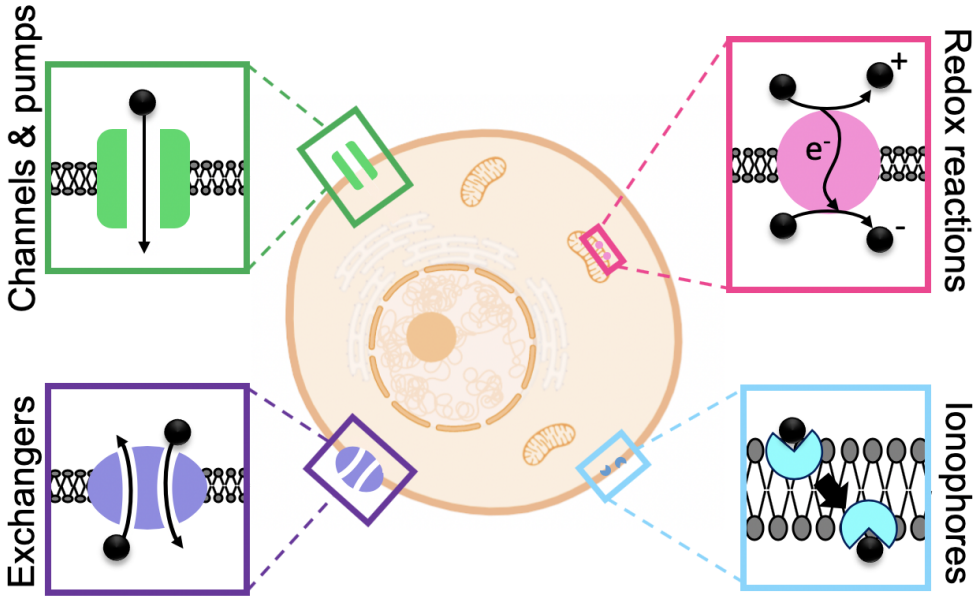


Figure 3.2: Transmembrane proteins. Specialised proteins in the membrane facilitate ion transport. Channels move ions down their concentration gradient and pumps with or against it. Exchangers move ions uphill, alongside the movement of other ions or molecules in the same or opposite direction. Redox reactions transfer charged ions across the membrane via an electron transport chain. Ionophores can be channels or carriers and make the membrane more permeable to ions.

In nature, one use of the electrochemical gradient is in energy storage. By moving charge across the membrane cells generate a transmembrane potential which functions like a battery, providing power to drive metabolic activities[4,215]. A second important role of controlled ion transport is in bioelectrical signalling and cellular communication. The behaviour of cells (in microorganisms, animals and plants) can be dictated by endogenous bioelectrical cues (electric fields, potentials and signals)[215,216,217]. In fact, a cell's behaviour is regulated by the transmembrane potential across both its own membrane and those of its neighbours[4,216,217]. Therefore, bioelectrical signalling is an optimal way for cells (in communities, tissues and organs) to coordinate their responses across anatomically-relevant distances. Spatiotemporal fluctuations in charge distribution, in concert with recognised biochemical pathways, generate trans-tissue potentials. These tissue-wide bioelectrical cues dictate its

behaviour. For instance, such cues can orchestrate pattern formation or serve as signals for a number of cellular outputs including proliferation, differentiation and apoptosis[216]. An example of their utility is in epithelial cells. When cut, these cells generate bioelectrical signals (electric fields and potentials) in the skin. Nearby cells sense these signals, migrating towards the wound which aids healing[216,217,218]. Incredibly, some organisms e.g., salamander are known to use these bioelectrical signals to regenerate entire organs[215,216,217,218]. What is equally as remarkable is that these organisms stop the regeneration once the correct pattern has been achieved. In fact the use of bioelectrical signals to coordinate behaviour is evolutionary ancient, originating in microorganisms. Spatially propagating waves of ionic signals send information over long distances within bacterial biofilm communities[215,219]. By altering the transmembrane potential of nearby bacterial cells, this bioelectrical signal coordinates their metabolic states[219].

3.1.2 Signalling and communication in neurons

Most cells maintain a charge imbalance across their membranes at all times; human photoreceptor cells, erythrocyte and neurons have resting potentials of ≈ -40 mV, ≈ -10 mV and ≈ -70 mV respectively[217]. They also respond to bioelectrical cues. However, only electrically excitable cells posses the intrinsic properties which permit them to generate bioelectrical signals in response to non-bioelectrical stimuli. One of the best studied examples of an electrically excitable cell is the neuron. In 1963, Hodgkin and Huxley won the Nobel Prize after discovering that the transient and rapid fluctuations of the giant squid neuronal membrane, arose from the controlled transport of ions (charge) across it[220]. This defined sequence of transmembrane potentials, at a specific location in the cell, is known as an action potential.

1. The resting potential of human neuronal membranes is negative (≈ -70 mV), as there are more positively charged ions outside the cell. Leaky ion channels embedded within the membrane facilitate ion diffusion: potassium ions leak out and sodium and chloride ions leak in. Therefore, to maintain a negative

resting potential the cell must pump these ions back across the membrane using Na^+ /K^+ pumps[4].

2. When stimulated, the neuronal membrane depolarises, i.e. becomes more positive, as voltage-gated sodium ion channels (VGSC) partially open and sodium enters the cell.

3. If the threshold potential is not reached (≈ -55 mV) then no action potential will be fired[4]. Otherwise, once the transmembrane potential reaches ≈ +30 mV, the VGSCs close and voltage-gated potassium ion channels (VGKC) open. Then, potassium ions diffuse out of the cell which reduces the membrane potential. As the membrane becomes more negative it typically overshoots the resting potential: hyperpolarisation[4].

4. The VGKCs then close and the membrane returns to its resting potential. At this location, the membrane enters a refractory period where inactivated VGSCs mean that no subsequent action potentials can form[4].

This action potential serves as a bioelectrical signal and self-propagates as a wave along the neuronal axon, depolarising the membrane downstream[4]. As membrane sections in the refractory period are unable to be depolarised, the action potential travels directionally along the axon[4]. Eventually, this action potential becomes insufficient to initiate membrane depolarisation. This distance is dependent upon the membrane capacitance (ability to store charge) and its resistance (dictated by its composition). Nature addresses this issue by surrounding the conducting axons in segments of myelin sheath to enable signal transmission over long distances. Glial cells coat axons in this lipid-rich substance, forming an insulating and protective tubular casing; myelination decreases the membrane capacitance and increases its resistance[4]. Located between myelin segments are the Nodes of Ranvier, VGC-rich membranes. Since the internodal membranes contain very few VGCs, the action potential passes directly from one node to the next: saltatory conduction[4]. In

addition to faster conduction, myelinated axons expend less energy maintaining the resting membrane potential as there are fewer ion channels.

Whilst action potentials allow neurons to send bioelectrical signals rapidly, directionally and over large distances, they cannot pass between cells that aren't directly connected. Therefore, nature has developed a sophisticated combination of bioelectrical and chemical signals to transfer information throughout the body. At axon terminals, neurons communicate with one another via synapses[4]. At a chemical synapse the two cells are separated by a small gap called the synaptic cleft. Since electrical signals cannot cross the gap, communication is via chemical neurotransmitters (ions or small molecules), released when an action potential reaches the terminal[4]. Multiple substances may even be simultaneously released following a single neuronal event: co-transmission. After diffusion across the synaptic cleft, neurotransmitters bind to receptors on the postsynaptic cell passing on the information.

As early as the 18^{th} century scientists recognised the importance of bioelectrical phenomena, through their studies of electrically excitable cells[221]. Only more recently has their significant role in physiology (health) and pathophysiology (disease) been recognised[222]. Damage to the myelin sheath of the brain and spinal cord disrupts signal transmission causing multiple sclerosis, and the loss of nerves within the brain is responsible for a range of neurological disorders such as Alzheimer's disease. Channelopathies are disorders resulting from ion channel dysfunction. Consistent with the wide distribution of ion channels throughout the body, channelopathies have been implicated in a variety of diseases: retinitis pigmentosa, cystic fibrosis, epilepsy, asthma, diabetes, and cancer to name a few[222].

3.1.3 Signalling and communication in synthetic cells

Many of the ways in which these functionalities have been emulated in minimal synthetic cells was discussed in **Chapter 1**.

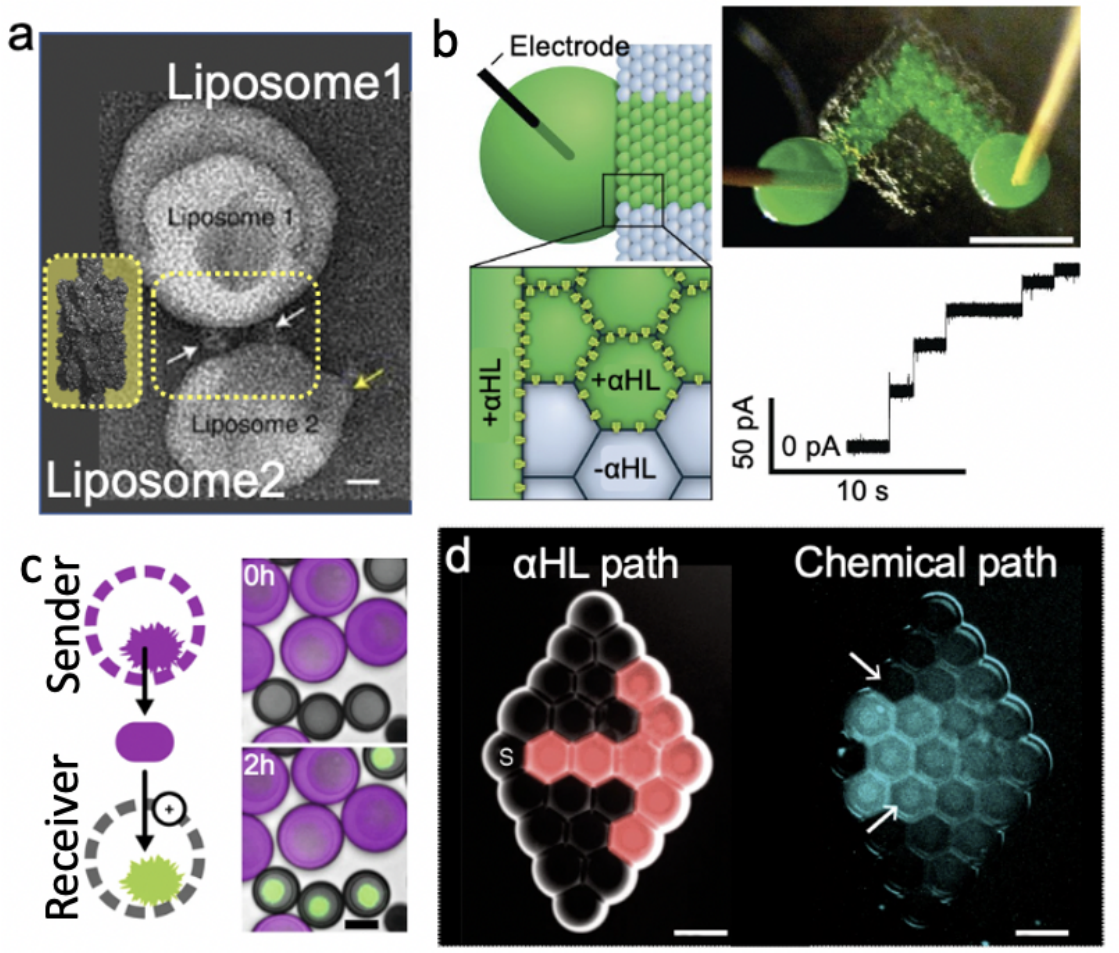


Figure 3.3: Signalling in synthetic cells. **a,** An engineered protein pore (αHL, yellow box) formed a direct (ion-conducting) passage between two liposomes. Scale bar = 20 nm. **b,** A conductive pathway was formed through a printed synthetic tissue. When electrodes were positioned at each end, current flowed through the network as ions moved between the droplet cells via protein pores (αHL, green). Scale bar = 500 μm. **c,** A diffuse signalling molecule, released from the sender cell (purple), initiated expression of a gene in the receiver cell (green). Scale bar = 25 μm. **d,** A chemical signal moved between connected droplet cells. First, a pathway was patterned (red, αHL), then the chemical diffused (blue) along the pathway. Scale bar = 200 μm. Figures are taken from **'a'** Mantri et. al.[223] **'b'** Niederholtmeyer. et. al[70], **'c'** Villar et. al.[50], **'d'** Dupin et. al.[65]. Labels are reproduced.

Briefly, artificial systems have been designed which are capable of transducing environmental stimuli into bioelectrical signals. For instance, work using droplet bilayers rich in light-driven proteins have shown promise as light sensors, moving ions when illuminated[44,196]. Additionally, synthetic sensors have been developed that respond to mechanical stimuli[32,74]. As of yet, transmission of these bioelectrical signals in synthetic cells has not been explored.

Nonetheless, communication between synthetic cells has been demonstrated using tethers to initiate bioelectrical signalling. Imitating nature, the membranes of artificial cells were functionalised by incorporating nanoscale conductors into them. For instance, an engineered protein pore that spanned two bilayers (Fig. 3.3a)[223] mimicked a gap junction, permitting ions to pass directly between two artificial cells. Communication has also been demonstrated in larger structures, composed of thousands of artificial cells. Here, droplet cells were connected via protein-pore containing bilayers through which ions could freely diffuse. By patterning the pore-containing droplets, bioelectrical signals were rapidly and directionally sent through defined pathways in the tissue (Fig. 3.3c)[27,50]. However, these synthetic cells couldn't sense external stimuli instead requiring connection to electrodes and external hardware for communication. Consequently, signals are a combination of electrons and ions.

Wireless synthetic cells have been shown to communicate using chemical signals. For instance, a pathway of protein pore-containing bilayers allowed small molecules to diffuse between synthetic cellular compartments (Fig. 3.3d)[65]. Control over pore opening has also been demonstrated permitting communication on demand[63]. Similar systems have been built in which the molecules diffused directly through the bilayer[224] but even here chemical transmission was slow. Communication between distant synthetic cells has also been demonstrated using chemical signals which diffused between them (Fig. 3.3b)[70]. This example showed a sophisticated level of communication; the protein molecule initiated a response in the receiver cell (Fig. 3.3b)[70].

As with natural cells, bioelectrical phenomena also have roles in energy storage. Since scientists often look to nature for inspiration, soft power sources have been developed which utilise electrochemical gradients and transmembrane potentials. In one example, a simple, disposable bio-battery was developed in which a droplet interface bilayer (DIB) was filled with ion selective pores, and combined with an ionic gradient, to generate energy (Fig. 3.4a)[44]. A more powerful example mimicked the electric organ of a shocking eel. This electric organ generates potentials up to 860

volts through the coordinated depolarisation of specialised cells called electrocytes. By imitiating the morphology of this organ, scientists developed a soft, flexible bio-battery which runs off salt water (Fig. 3.4c)[225]. Using ion gradients formed between hydrogel modules stacks in series, the artificial electric organ generated a transmembrane potential of 110 volts.

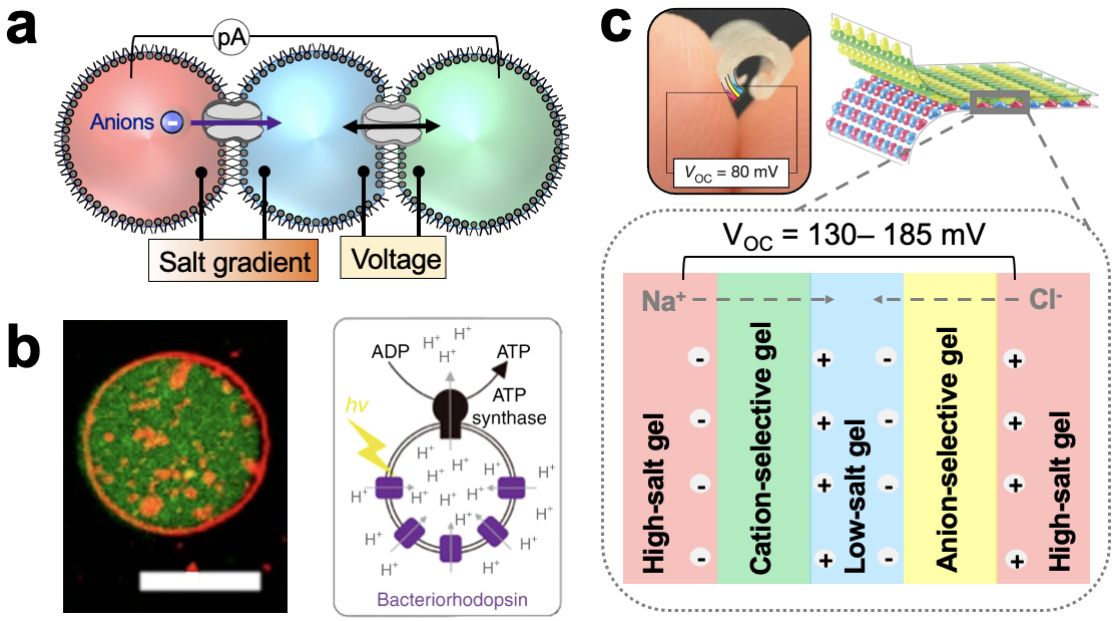


Figure 3.4: Artificial bio-batteries. a, Schematic of a droplet bio-battery based on a concentration cell. A transmembrane potential of + 30 mV was generated across the blue-green droplet interface by incorporating engineered anion-selective pores into the bilayers. **b,** Left: Microscopy image of light-driven protein synthesis (green) in a vesicle. Scale bar 10 μm. Right: Schematic of the light-harvesting vesicle containing a proton pump (bacteriorhodopsin, purple) and ATP synthase (black). **c,** An artificial electric organ composed of a multilayer gel. The open-circuit voltage (Voc) produced was +80 mV. The hydrogels are false-coloured; high-salt (red), low salt (blue), cation-selective (green) and anion-selective (yellow). A combination of ion selectivity and a salt gradient generate the potential. Figures are adapted from **'a'** Holden et. al.[44], **'b'** Behanu et. al.[15] and **'c'** Schroeder et. al.[225]

It would be more advantageous if these transmembrane potentials could be generated in response to a stimulus. Efforts have largely focused on reconstituting natural light-driven proteins e.g., bacteriorhodopsin into synthetic cells. These synthetic chloroplasts use the transmembrane ion gradients generated upon illumination to drive ATP synthesis, generating energy for the synthetic cell to use (Fig. 3.4b)[15,85,87]. Alternatively, entire biological (light-harvesting) membranes[226]

or organelles[227] have been incorporated into synthetic cells. Power-generating functionalities have considerable potential in the formation of biomimetic synthetic tissues and in bioelectronics, replacing the restrictive batteries and tethers. The use of these energy-generating synthetic cells in larger synthetic structures has also been demonstrated. Lee and colleagues first made synthetic chloroplasts by incorporating ATP synthase, a plant photoconverter and a bacterial photoreceptor into a synthetic vesicle. Then, they encapsulated the synthetic chloroplast-like vesicles in a larger vesicle where illumination resulted in energy (ATP) production which was in turn used to power functions e.g. actin polymerization in the larger synthetic cell.

3.1.4 Bioelectronics

Bioelectronics is the branch of science which focuses on the electronic control of physiological function. Whilst most attention has been paid to its medical potential, similar technologies are accelerating progress in soft robotics, prosthetics and computing.

3.1.4.1 Bioelectric medicine

Bioelectric medicine leverages the native, neural signalling pathways to achieve therapeutic effects. Whilst the use of electricity to treat aliments can be traced back to Ancient Egypt, it was Galvani who pioneered this approach when he electrically stimulated a detached frog leg, making it move[221,228]. Today a number of implanted devices are used to electrically stimulate neurons to counteract tissue and organ dysfunction[228]. This novel approach holds real promise as an alternative (or even complementary) therapy for the vast number of conditions not adequately treated using traditional pharmaceuticals. Bioelectric medicine can even stimulate neuronal growth[229] but it is not restricted to electrically excitable cells[217]. The global market for bioelectric medicine is estimated to be ≈ $28bn by 2026 highlighting the enormous potential of the field[230].

For some neurological disorders such as Parkinson's Disease or Essential Tremor, deep brain stimulation (DBS) is the standard treatment of care (Fig. 3.5a). Here,

metal probes are implanted in close proximity to target cells, delivering constant or intermittent electric signals[231,232]. The use of DBS to interrogate the malfunctioning brain circuits of psychiatric disorders (such as depression or anorexia nervosa) is also being explored[233,234]. Unfortunately, even the probes and electrodes used in the most advanced devices, such as cochlear implants and cardiac pacemakers, are too rigid (≈ 1 - 200 GPa) to meet the mechanical requirements of soft (biological) tissues (≈ 1kPa - 1 MPa). This causes a number of adverse effects including tissue scarring, as well as creating a poor tissue-device interface which results in indiscriminate targeting of cells[235,236]. Moreover, the body's immune response to these conventional devices can result in diminished sensitivity and stimulation efficiency over time. Hampered by their stiff materials, traditional devices are yet to reach their full potential. Efforts to address these limitations have focused on device miniaturisation[237,238239] or have added biological (lipid membranes and proteins) or organic coats to the electrodes[238,240237,241] (Fig. 3.5b). Whilst some of these modifications improved device utility e.g. by enhancing flexibility[242,243], they don't alter the inherent mechanical properties of the electrodes. Consequently, these bulky and rigid bioelectronic devices are suboptimal for therapeutic applications due to the significant underlying mismatches between the electronics and soft tissues[238].

Interdisciplinary efforts have been catalysing the rapid development of new bioelectronic materials in order to address some of these drawbacks. Having been used to coat traditional rigid electrodes, the use of organic materials in soft bioelectronics is being explored. These materials offer greater therapeutic potential due to their flexibility, biocompatibility and ability to conduct both electronic and ionic signals. Flexible and stretchable medical sensors have achieved a high level of sophistication using organic electronic materials[242,244,245,246,247] (Fig. 3.5c). Implantable devices have also been developed which modulate neuronal activity. For instance, when a bioinspired organic nerve was connected to the leg muscle of a cockroach, a pressure stimulus triggered muscle flexion (Fig. 3.5d)[248].

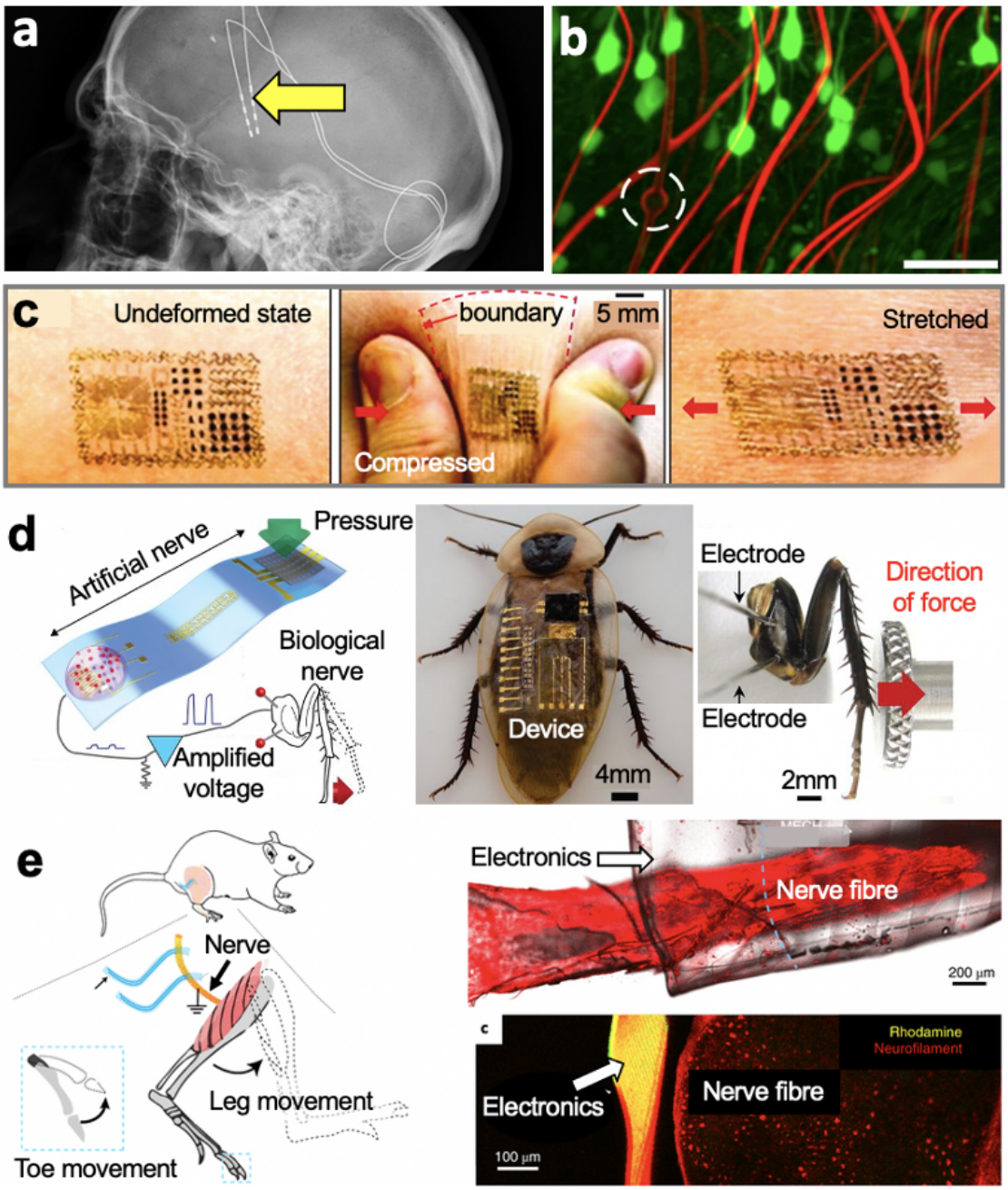


Figure 3.5: Bioelectric medicine. **a,** Deep brain stimulation: a metal neural probe inserts directly into the brain (as indicated by the arrow) to electrically-stimulate neurons. **b,** Flexible, neuron-like electronics have similar morphology to the neurons they mimic. 3D reconstructed interface between neurons (green) and electrodes (red) 6 weeks after implantation. Scale bar, 200 μm. **c,** Electronic skins retained their functionality when compressed and stretched. **d,** An artificial afferent nerve was built from organic electronic materials. It formed part of a hybrid reflex arc that enabled the movement of a cockroach leg upon stimulation of the artificial nerve. Scale bars = 4 mm (centre) and 2 mm (right). **e,** A soft hydrogel-based electronic device activated the leg movement of a mouse. Scale bars = 200 μm (top) and 100 μm (bottom). Figures were taken from **'a'** Jmarchn[249] **'b'** Yang et. al.[238] **'c'** Kim et. al.[242] **'d'** Kim et. al[248] and **'e'** Liu et. al.[19]. Labels were reproduced.

Scientists have also built functional, soft bioelectronic devices using conducting hydrogels[250,251,252]. These materials have vast therapeutic potential due to their flexibility, high water content, and physicochemical similarity to biological tissues[252]. Soft devices have employed hydrogel electrodes in wearable electronics[242,253] and implanted them to stimulate neuronal activity[250,254]. Hydrogel devices have also been made which can release pharmaceuticals in a controlled manner[255]. Whilst devices built using these materials have been promising, they are often compromised by the requirement for connection to external hardware for power or signal amplification (Fig. 3.5e)[250,256,257].

Technologies which rely on physical tethers are limited in their applications. Even the batteries in the best tetherless devices e.g. cardiac pacemakers are restrictive and over time they must be replaced in surgery. The inclusion of power generating modules would enable soft bioelectronics to monitor and treat disease in the long-term. Progress has been made in this area by the inclusion of features capable of transducing internal chemical signals[258] or external stimuli such as ultrasound[259,260] and light[261] into electric signals. In one example, a self-powered pacemaker was found to harvest biomechanical energy to drive cardiac pacing in a pig[262]. However, these wireless devices typically contain rigid, bio-incompatible elements. Interdisciplinary efforts will be required to achieve soft, flexible bioelectronics which effectively interrogate a target cell in a tetherless manner[257,263].

3.1.4.2 Soft robotics

Another application of bioelectronic devices is in the field of robotics. Robots composed from soft, malleable materials offer unique applications in areas where conventional hard robots are not viable: drug delivery, prostheses, and in search and rescue. In addition, the use of stimuli-responsive materials permits tetherless activation, offering the potential for smart, autonomous responses to environmental cues. For these reasons, responsive hydrogels have been widely used in soft robotics. By patterning these materials, the morphology of soft robots can be controlled[109,264,265]. Robots built using stimuli (magnetism, temperature or light)

responsive hydrogels can encapsulate cargo such as cells or drugs[92,266,267] and have even performed *in vivo* biopsies[268].

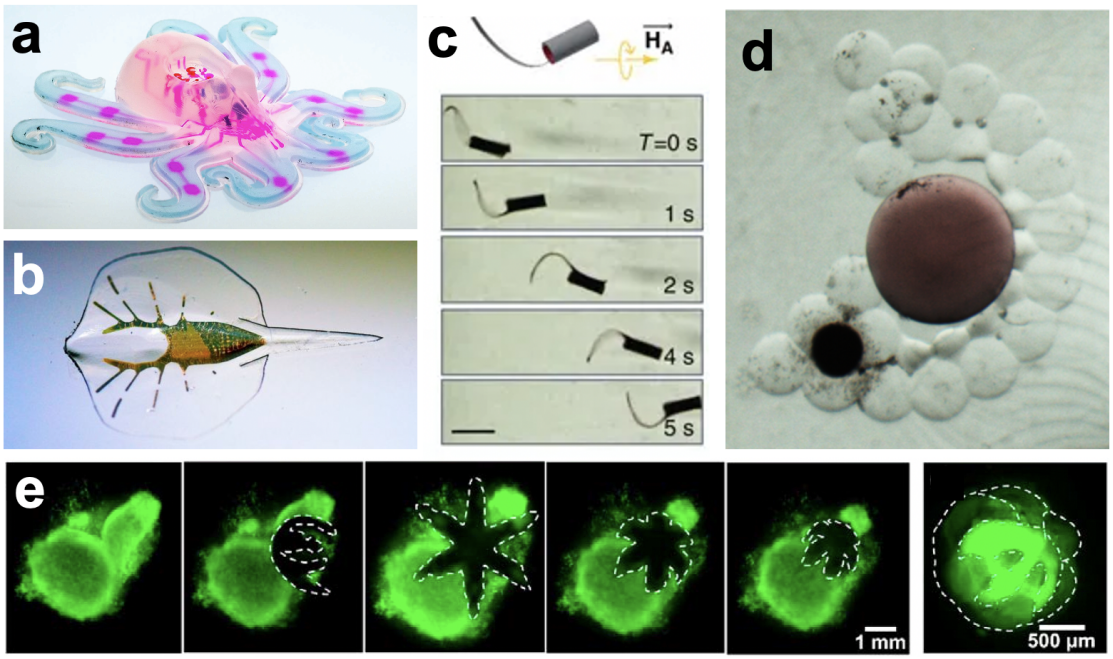


Figure 3.6: Soft robots. a, An octobot, built from entirely soft materials, uses power generated by a chemical reaction to swim. **b,** A robotic stingray performed phototactic swimming powered by rat heart cells. **c,** A mobile microrobotic can be observed moving over time; rotation is driven by a magnetic field. Scale bar = 2 mm. **d,** A patterned, multi-responsive gripper folded upon stimulation with light and heat to transport cargo (brown). **e,** A soft, thermoresponsive gripper, captured and removed cells from a clump of fibroblasts. Scale bars = 1 mm (left) and 500 μm (right). Figures are taken from **'a'** Wehner et. al[269], **'b'** Park et. al.[270], **'c'** Huang et. al.[271], **'d'** Downs et. al.[92] and **'e'** Breger et. al.[268].

Inspired by nature, advances in materials and manufacturing technologies have enabled the fabrication of soft robots with a number of sophisticated capabilities, for instance locomotion[272]. Mimicking the flagella mechanisms used by several microorganisms, motile swimming robots were fabricated which could be remotely controlled using magnetism (Fig. 3.6c)[271]. Another swimming device was built using the musculoskeletal architecture of a stingray as inspiration[270]. Here, the inclusion of optogenetically engineered cardiomyocytes powered the coordinated undulating motion of robotic fins, guided by light cues (Fig. 3.6b).

Whilst flexible devices are predominately composed of soft materials, they often contain integral rigid components. Designing autonomous robots which are

entirely composed of soft materials is a significant challenge because it requires hardware alternatives to control and power the robots. Mimicking the morphological blueprint of an octopus, scientists at Harvard developed an entirely soft-bodied robot (Fig. 3.6a)[269]. Powered by the pneumatic actuation arising from hydrogen peroxide decomposition, and controlled by a microfluidic gate, the octobot could flex its tentacles propelling it through water. Researches are exploring ways in which sensory components might be integrated into the device, but the octobot is the first example of a robot entirely free from rigid hardware.

3.1.4.3 Computing

A third application for soft bioelectronic devices is in computing: biocomputing and chemical computing.

You can think of a living cell as a miniature computing device, processing input information in many different and intricate ways, performing operations and generating outputs[273]. Biocomputers use biological molecules - such as DNA or proteins - to perform these computations. The notion of biocomputing was raised by Feynman in 1959 but it wasn't until 1994 when Adleman constructed the first DNA computer[274] that this feasibility was demonstrated. DNA is an attractive material for data storage[275,276]: it is cheap, stable, compact and ubiquitous throughout nature. Moreover, it can simultaneously process multiple calculations whilst using up minimal energy; a major problem for conventional computers. Exploiting its storage capabilities, scientists have encoded all the information needed to construct a bacterial cell[20] in DNA and even encoded the contents of a book[276] and movie[277]. Theoretically, DNA could store up to 455 exabytes of data per gram[276]. The current costs, and the time required to write and read DNA, make its use in everyday computing impractical for now. Whilst in its infancy, RNA-based computing is also being explored since RNA is more structurally versatile than DNA[278,279,280].

Biomolecules (DNA, RNA and proteins) are also involved in cellular reactions. By exploiting the high precision and programmability of these biomolecules, scientists have constructed simple logic gates and circuits[281,282,283,284] : the workhorse of

conventional computers. Protein-based computers offer more choice in building blocks than their DNA and RNA counterparts: 20 and 4 residues are available respectively. Excitingly, these biocomputers can operate in living prokaryotic[279,285,286] and eukaryotic cells[280,287,288,289]. Scientists have even demonstrated the potential of biocomputers in disease detection and treatment. For example, Xie and colleagues designed an RNA-based genetic circuit which identified cancerous cells and triggered their destruction without affecting the non-diseased cells[290]. Much work is still needed in order for biocomputers to reach their full potential and the metabolic aspect of computation in particular, has not yet been fully exploited.

Since, biochemical reactions are responsible for information processing in living organisms, similar non-living systems could be used to develop chemical computers. A non-living chemical system widely used in chemical computing is the Bolousov-Zhabotinsky reaction; a simple, nonlinear chemical oscillator. Computers utilising this non-living chemical system have demonstrated potential to store and process information, emulate logic gates, perform image processing and even mimic neuromorphic architectures[291,292,293,294]. Other reaction systems have also been employed in chemical computing. For instance, a computational clock was built that operates using the movement of magnetised water droplets[295]. The field requires more exploration, but chemical computers have significant potential.

3.2 Results

3.2.1 Design of a synthetic neuron

Biological afferent neurons transduce specific stimuli into bioelectrical signals[4]. The photosensory modules characterised in **Chapter 2** are capable of phototransduction, a process which converts light into bioelectrical signals. Consequently, the synthetic neurons were designed to be photosensing, exploiting the photochemistry of archaerhodopsin-3 (aR3), a light-driven proton pump found within the claret membrane (CM) patches of *Halorubrum sodomense* (Fig. 3.7b)[11,121,296]. Beneficially, this permits the synthetic neurons to utilise external inputs to drive signalling and power downstream functions. Whilst human photoreceptors work in concert

with other retinal neurons to transmit this visual information to the brain, the photosensory synthetic neurons were designed to perform this function alone i.e. in a single neural structure.

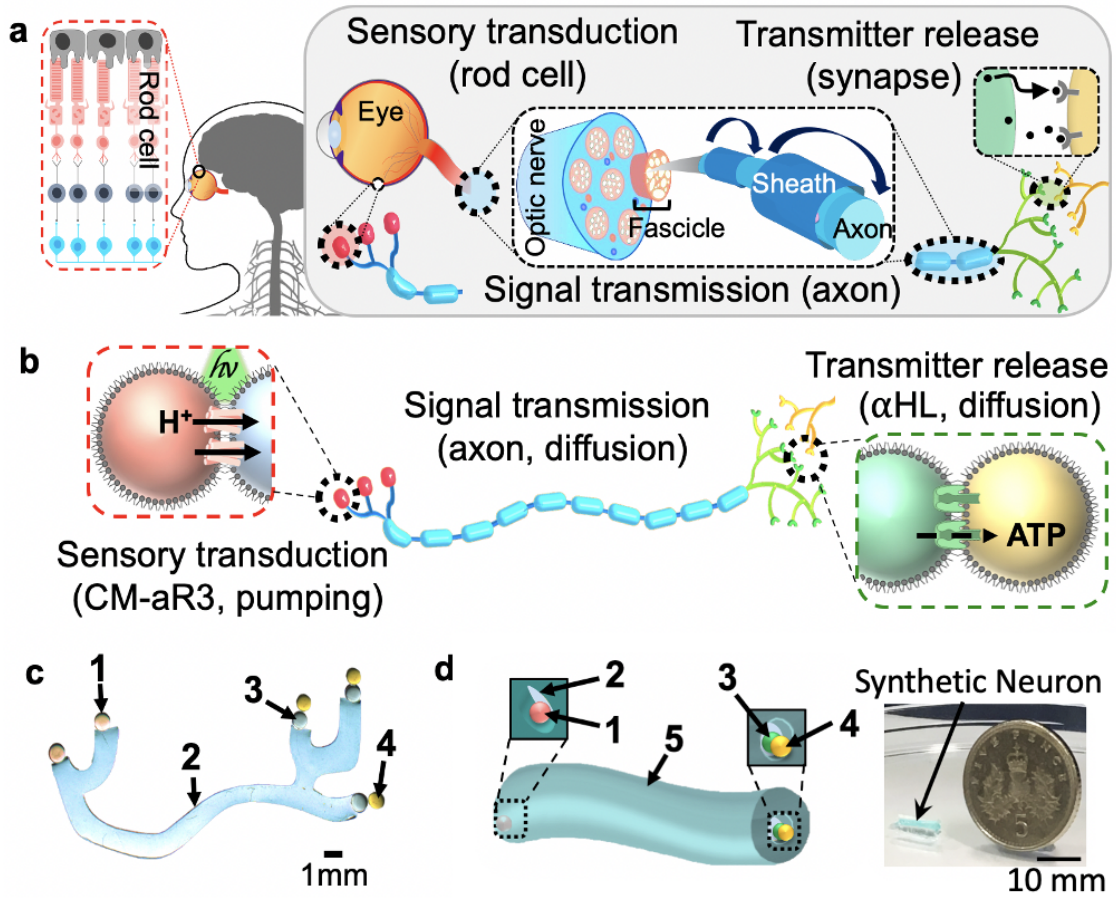


Figure 3.7: Design of a biomimetic neural device. **a,** A biological neuron. Rod cells (in the eye) perform phototransduction. Information is transmitted (through multiple neurons) to the brain as action potentials. Neuronal axons may be coated with a myelin sheath, as displayed here. At synaptic terminals neurotransmitters are release enabling inter-cellular communication. Neurons assemble into fascicles; nerves are typically composed of one or more fascicles. **b,** A synthetic neuron. CM-aR3 performs phototransduction by pumping protons (H+) across a bilayer in response to light ($h\nu$, green) (red box). Ions are carried (via diffusion) directionally along the synthetic axon to the synaptic terminals (green box). Neurotransmitters (ATP) are then released from the presynaptic droplets (green) via diffusion through αHL pores (green box). **c,** Photograph (minus background) of a synthetic neuron. Coloured dyes were included for visualisation - Photosensory droplet (c1, pink), axon (c2, blue), presynaptic droplet (c3, green), postsynaptic droplet (c4, yellow). **d,** Design and photograph (in air, 5p coin for scale) of a synthetic myelinated neuron. The elastomer sheath (d5, teal) surrounds the hydrogel axon (d2, blue). In the design, the sensory (d1, pink), presynaptic (d3, green) and postsynaptic droplets (d4, yellow) are shown. Scale bar = 10 mm. Adapted from the author's manuscript in progress[193].

Despite biological neurons varying in size and shape they share common structural features: a long axon fibre (typically surrounded by an insulating myelin sheath) with sensory receptor cells at one end and the synaptic terminals at the other. The first synthetic axon design used interconnected (nanolitre) aqueous droplets to form the signalling pathway, resembling those used in the literature[50,52,65,67]. However, after brainstorming (with **V.R.S**) and optimisation to improve signal transmission, the design was amended to contain long hydrogel fibres which permitted greater signal transmission and afforded improved structural stability and flexibility (blue, Fig. 3.7c)[252,265]. In the final design, the hydrogel axons were surrounding with a sheath (built from a flexible and biocompatible silicone elastomer) which protected and insulated the synthetic neurons from other electrical impulses (Fig. 3.7d).

The synaptic terminals of the synthetic neurons were built from two aqueous droplets: the presynaptic (green) and postsynaptic (yellow) droplet (Fig. 3.7c). Ion-conducting protein pores (αHL) mediated transmission of the bioelectrical signal into the terminal (as previously done in the literature[27,50]). Like with natural neurons, neurotransmitter molecules were also included within the presynaptic droplet. Arrival of a bioelectrical signal, drove neurotransmission across the synaptic bilayer, mimicking the electrochemical communication used in nature. In the design a nanolitre aqueous droplet was used to represent the neighbouring cell, receiving this molecular signal for functional downstream outputs.

The design used solely soft, biological materials. The final tetherless synthetic neurons were flexible and employed the same communication principles found in nature: conducting ions and translocating molecules[3,4]. Whilst the soft bioelectronic device was designed to imitate both the architecture and function of a biological afferent neuron (Fig. 3.7), it was not intended to be an exact replica of its natural counterpart.

3.2.2 Protein preparation and insertion

More information surrounding protein preparation can be found in **Chapter 2** and **Chapter 6**. But, in summary, all proteins were found to spontaneously insert into the artificial bilayers under experimental conditions.

- CM-aR3 photosensory droplets were used within the synthetic neuron, at a final protein concentration of 0.15 - 0.25 mg ml^{-1} (measured using nanodrop, in Solution B, pH 6.5). The light-activated proton pump CM-aR3 (expressed in *Halorubrum sodomense* by **J.V**) was inserted in the bilayer from purified crystalline membrane fragments in a low concentration of detergent. CM-aR3 protein inserted N-terminus first (Fig. 3.8, 2.16), pumping protons out of the photosensory droplet upon illumination (Fig. 2.22). Consequently, when electrodes were included (for characterisation not function) CM-aR3 generated positive signals (See **Chapter 2**, section. 2.2.4.2); the recording electrode was always added to the photosensory droplet.

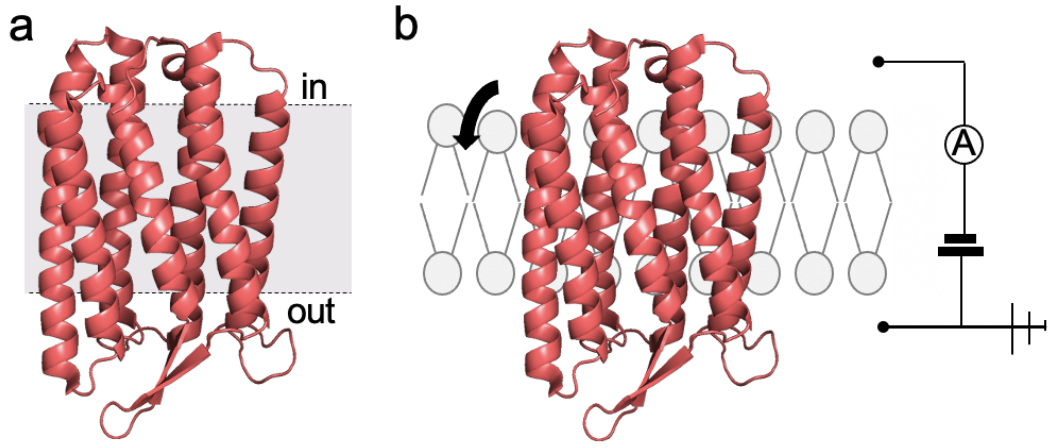


Figure 3.8: Protein insertion into a bilayer. **a,** Schematic of a biological membrane containing CM-aR3 (PDB:6GUZ[150]). CM-aR3 inserts N-terminal first from the intracellular side of the bilayer (in) and pumps protons to the extracellular side (out). **b,** Schematic of a DIB containing CM-aR3, protein inserts N-terminal first from the photosensory droplet (S) and pumps protons to the axon droplet (A). The photosensory droplet contains the recording electrode.

- Alpha hemolysin (αHL) pores (expressed in *Staphylococcus aureus* by **I.C**) were inserted from solution as protein monomers, assembling into heptamers

in the artificial bilayer. All bilayers within the synthetic neuron, with the exception of the photosensory bilayer, contained the protein pore α-hemolysin (αHL) at a concentration of 50 nM. Monomeric αHL functionality decreased when roughly handled so samples were treated with extreme care; a fresh aliquot was defrosted before each experiment and minimal pipetting was performed.

For protein preparation the same four key solutions were used: Solution A (100 mM MES, 100 mM NaCl, 0.1% DDM, pH 6.5); Solution B (100 mM MES, 100 mM NaCl, 0.001% DDM, pH 6.5); Solution C (100 mM NaCl, pH 6.5); Solution D (100 mM MES, 100 mM NaCl, pH 6.5) (see **Chapters 2 and 4** for more details of Materials and Methods).

3.2.3 Photosensory receptors

Microbial rhodopsins are simple, light-sensitive, electrogenic proteins; they are structurally similar to those found in the human eye[11,121]. When incorporated into droplet bilayers, these microbial proteins performed phototransduction (conversion of light stimuli to bioelectrical signals, see **Chapter 2**)[44,196].

3.2.3.1 Rapid pulse generation

For the light-powered synthetic neurons, CM-aR3 was chosen because it generated larger signals than other known proton pumps, perhaps due to its faster photocycle[150,296] or more efficient incorporation into membranes (see **Chapter 2**). The proposed photocycle of CM-aR3[129,154] suggests that it may bypass some of the intermediates found in the homologous rhodopsin bR. This might permit quicker kinetics.

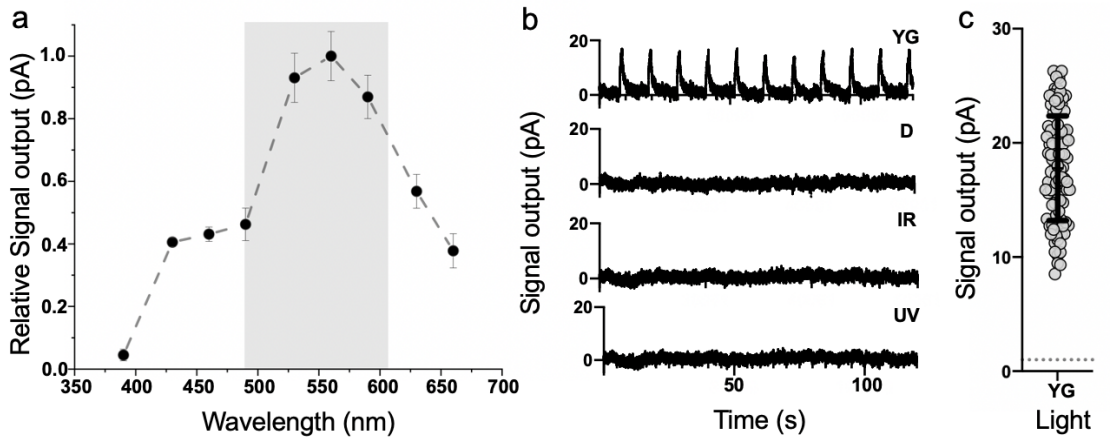


Figure 3.9: CM-aR3 is activated by YG light. a, Action spectra recorded across a CM-aR3-containing DIB (mean ± SD, n = 3, each LED has an 0.2 ± 0.1 mW output). Grey region indicates area covered by the YG light (see Fig. 2.9). **b,** Signals recorded across a CM-aR3-containing DIB upon illumination (1 s pulses, 0.1 Hz) with YG light (550 and 592 nm, 15 ± 4.5 mW), IR light (722 nm, 16 ± 5.0 mW) or UV light (367 nm, 15 ± 3.9 mW) or in the dark (D). **c,** Steady-state output recorded across a CM-aR3-containing DIB upon illumination (YG light, 15 ± 4.5 mW, n = 100, protein is from over 13 different batches). Figure is adapted from the author's manuscript in progress[193].

CM-aR3 photoreceptors were formed (as described in **Chapter 2**) from an aqueous droplet containing claret membrane (CM) fragments of archaerhodopsin-3 (aR3) (200 nL, 0.15 - 0.25 mg mL^{-1} Solution B, pH 6.5). When remotely activated (with yellow-green light, Fig. 3.10a), CM-aR3 proteins pumped protons out of the photosensory bilayer, generating bioelectrical (ionic) signals in a tetherless manner (see **Chapter 2**). The phototransduction activity of CM-aR3 (membrane fragments) was recorded using Ag/AgCl electrodes (Fig. 3.9, as described in **Chapter 2**). In 100 consecutive experiments, signals greater than the 1.0-pA threshold (arbitrarily set to indicate protein activity, dotted line) were recorded upon illumination (YG light, 490 - 608 nm with peaks at 550 and 592 nm, 15 ± 4.5 mW, 13 protein batches Fig. 3.9); within each experiment, protein from a single batch was used. The average steady-state signal recorded was +18 ± 4.5 pA (mean ± SD, n = 100, 13 protein expression and purification batches used), with a maximum of +26 pA. However, when the photosensory bilayer was illuminated with IR (680 - 741 nm peaks at 722 nm, 16 ± 5.0 mW) or UV (355 - 390 nm peaks at 367 nm, 15 ± 3.9 mW) light, photosignals below the threshold were observed (Fig. 2.15, 3.9b, 2.7).

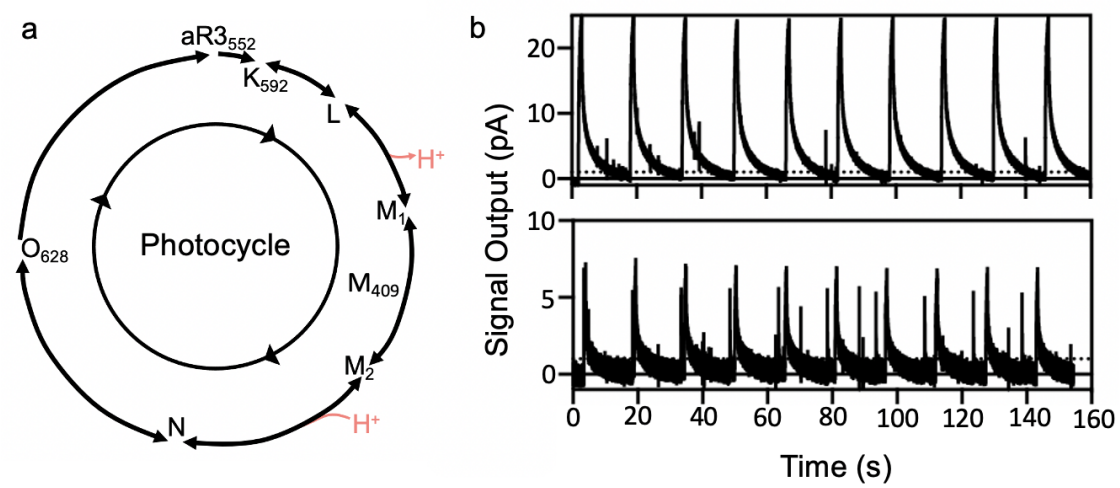


Figure 3.10: CM-aR3 generates rapid signals a, Summary of aR3's photocycle. 1 proton (pink) is pumped per photon absorbed. The reported literature rate is 20 protons per second[129]. **b,** Signals recorded across a CM-aR3 DIB upon brief light pulses: 1 s (top) and 20 ms (bottom) at 0.06 Hz (490-608 nm with peaks at 550 and 592 nm, 15 ± 4.5 mW). Figure **'a'** adapted from Inoue et. al.[129] and **'b'** taken from the author's manuscript in progress[193].

The photochemical reaction which occurs in the human eye is one of the fastest and most efficient biochemical events in nature[11]. This rapid sensory transduction permits signals to be quickly sent to the brain for vision. In order to imitate natural neurons, the synthetic neural mimic demands the ability to quickly perform sensory transduction.

CM-aR3 undergoes a highly ordered sequence of conformational changes (known collectively as the photocycle) after the ground state of the protein ($aR3_{552}$) is stimulated by a photon of appropriate wavelength (YG light, 550 and 592 nm, 15 ± 4.5 mW) (Fig. 3.10a). Fortunately, like animal rhodopsins, this photochemically-driven cycle is expeditious; the reported rates for CM-aR3 are on the milisecond timescale[121,129]. Consequently, signals (greater than the 1.0-pA threshold, dotted line) could be observed following a series of brief light pulses (20 ms and 1 s on at 0.06 Hz, YG light), analogous the firing of successive action potentials along natural neurons[297].

By using electrodes, formation of the electrochemical proton gradient (generated by CM-aR3 proteins pumping protons across the bilayer) could be monitored in real time. However, electrodes were not required for function. Due to its rapid

photocycle, pumping by CM-aR3 generated detectable signals within 6 milliseconds of illumination (YG light, 550 and 592 nm, 15 ± 4.5 mW, Fig. 3.10 3.11). Since CM-aR3 photosensory modules generated rapid signals, they are a good choice for signal initiation in the synthetic neurons.

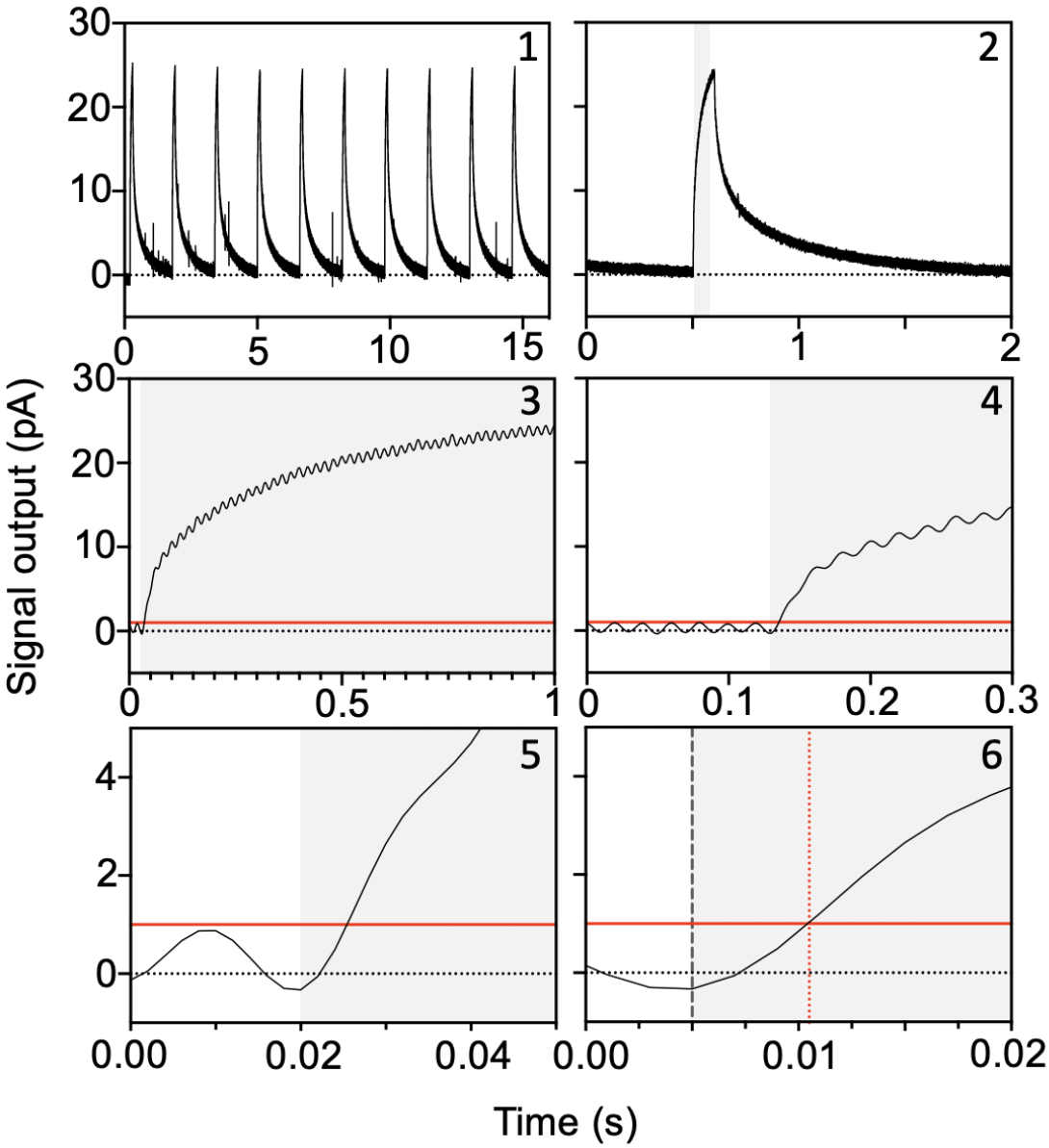


Figure 3.11: Millisecond transduction. Signal recorded across a CM-aR3 DIB upon 10 light pulses of 1s (YG light, 550 and 592 nm, 15 ± 4.5 mW, at 0.06 Hz). **Parts 1-6** become more focused (zoomed) and grey bars indicate when the light is on. A 1.0-pA threshold (red line **3-6**) was chosen as the baseline (light off) is just below this value. **6** shows that when the light is on (0.005 s, black dashed line) signal output increased passing the 1.0-pA threshold (red line) after 5.5 ms (red dotted line).

3.2.3.2 Wireless detection of signal transduction

An additional benefit of using CM-aR3 photosensory modules is that they can be remotely activated. Consequently, the synthetic neurons can function optimally in the absence of tethers or other hard components.

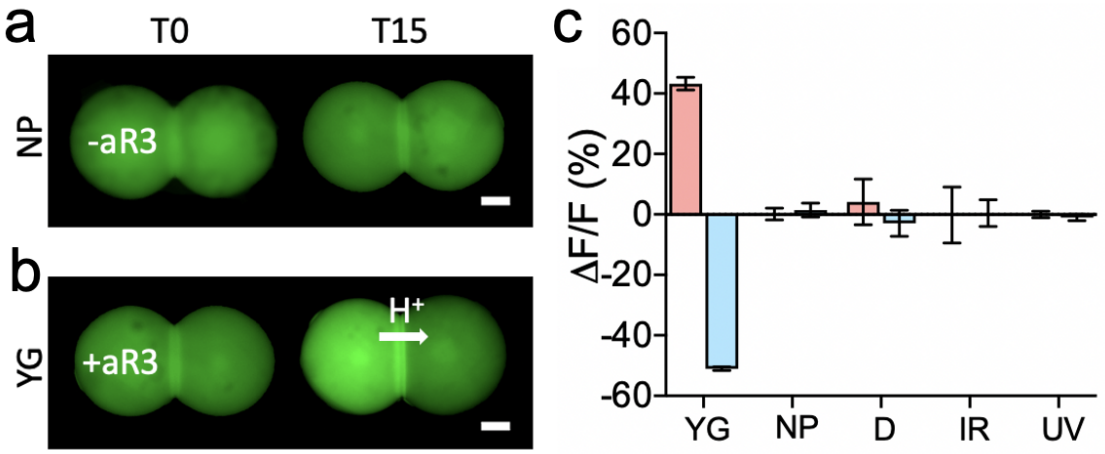


Figure 3.12: CM-aR3 is a proton pump. a-b, Epifluorescent images (minus background) of droplet pairs in the absence (NP, a) or presence (YG, b) of CM-aR3. Images are taken before (T0) and after (T15) illumination (YG light, 490-608 nm with peaks at 550 and 592 nm, 15 ± 4.5 mW). Pyranine fluorescence intensity increases with increasing pH[149]. **c** Percentage change in droplet fluorescence intensity when illuminated with YG (550 and 592 nm), IR (722 nm, 16 ± 5.0 mW) or UV (367 nm, 15 ± 3.9 mW) light, or when kept in the dark (D) or when no CM-aR3 is present (NP) (mean ± SD, n = 3). Figure adapted from the author's manuscript in progress[193].

To demonstrate this, phototransduction was observed in an electrode-free manner by adding the pH-sensitive fluorophore pyranine to the droplets (as described in **Chapter 2**). From the calibration curve (which relates fluorescence intensity to pH, Fig. 2.10), proton movement across the photosensory bilayer was quantified[149]. A photosensory droplet (+ CM-aR3) was interfaced with a second (protein-free) droplet; MES buffer was excluded to enable the detection of small pH changes. Following continuous illumination (15 h, YG light, 490 - 608 nm, with peaks at 550 and 592 nm, 15 ± 4.5 mW), the fluorescence intensity of the photosensory and protein-free droplets changed: increasing and decreasing respectively. The enhanced fluorescence of the (CM-aR3-containing) photosensory droplet corresponded to a pH increase of +0.3 ± 0.0 pH as protons were pumped out of the droplet; the protein-free

droplet decreased by -0.5 ± 0.0 pH (mean ± SD, n = 3, Fig. 3.12). These pH changes matched both the calculations of the extent and orientation of CM-aR3 insertion (as determined from the electrical recordings described in **Chapter 2**, Section. 2.2.9), and the reported kinetics of the CM-aR3 photocycle[121,296]. Whilst detection of the electrochemical gradient using this fluorescence technique was lengthy (requiring hours of stimulation), it demonstrated that no electrodes were required for function.

3.2.4 Signal transmission

The axons of biological neurons conduct impulses directionally and over long distances. The longest synthetic neuron described in this thesis was 25 mm in length (Fig. 3.7c). By comparison the human optic nerve (which inspired these synthetic neurons) is approximately 30 mm in length[298].

3.2.4.1 Biobattery

As discussed, many biological cells utilise transmembrane ion gradients as an energy source, converting them into bioelectricity via membrane-regulated ion transport. Holden and colleagues built a simple droplet bio-battery, and light sensor using the same principles[44]. Inspired by this work, a CM-aR3-containing bio-battery was built to determine whether the bioelectrical signals generated following phototransduction could be transmitted along a droplet chain.

The battery was composed of three interconnected, aqueous droplets: the first droplet contained CM-aR3 (0.15 - 0.25 mg mL^{-1} in Solution B, Fig. 3.13 a1), the second was protein-free (Solution D, Fig. 3.13 a2) and the third contained the monomeric protein pore αHL (50 nM, Fig. 3.13 a3). First, the electrodes were positioned so that signal across the photosensory bilayer was recorded; the recording and ground electrodes were in droplet a1 and a2 respectively (Fig. 3.13). Signals of +12 ± 0.6 pA (mean ± SD, n = 3) were generated upon illumination with YG light (490-608 nm, with peaks at 550 and 592 nm, 15 ± 4.5 mW). The electrodes were then carefully transferred so that signals across the downstream (αHL-containing) bilayer were recorded; here, the recording and ground electrodes

were in droplet a2 and a3 respectively (Fig. 3.13). Excitingly, signals (+11 ± 0.4 pA in size) could be recorded across this downstream bilayer (mean ± SD, n = 3, Fig. 3.13). This simple experiment illustrated the potential for droplet pixels to autonomously power synthetic droplet systems.

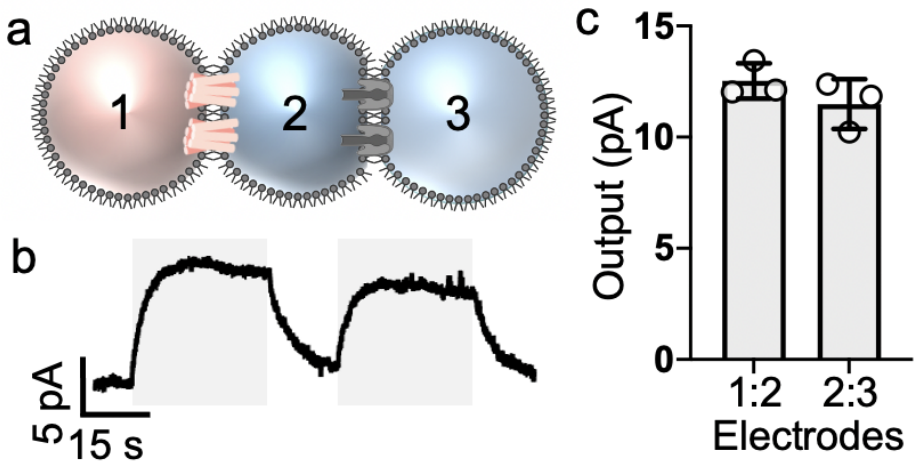


Figure 3.13: Signal transmission in a bionetwork. **a,** Schematic of a three droplet bionetwork (200 nL) formed between a CM-aR3 photosensory droplet (a1, 0.15 - 0.25 mg mL^{-1} CM-aR3, Solution B), a protein-free droplet (a2, Solution D) and an αHL droplet (a3, 50 nM, Solution D). **b,** Signal trace recorded across the 3-droplet bionetwork (with electrodes in droplets a2 and a3) upon illumination (YG light, 490 - 608 nm with peaks at 550 and 592 nm, 15 ± 4.5 mW). Grey bars indicated when the light is on. **c,** Signal output (mean ± SD, n = 3) recorded across the first bilayer (electrodes in droplets 1 and 2) and second bilayer (electrodes in droplets 2 and 3).

3.2.4.2 Directional signalling over centimetre distances

Having demonstrated that signals could be transmitted across a short 3-droplet network, a synthetic neuron was designed in which the artificial axon was composed of a chain of 200 nL aqueous droplets (≈700 μm diameter). Droplets were connected through a series of DIBs and resembled those previously constructed in the literature[27,44,50,65]).

Synthetic neurons of varying axon length (droplet number) were built and signal transmission recorded using electrodes. The photosensory bilayer, was formed between a CM-aR3 droplet (0.15 - 0.25 mg mL^{-1} CM-aR3 in Solution B, pink, S, Fig. 3.14a) and a second, (protein-free) droplet (Solution D, Fig. 3.14a). All

remaining axon droplets contained the monomeric protein pore αHL (50 nM in Solution D) to facilitate signal transmission.

First, the droplets were incubated (in an array chamber) within a lipid-in-oil environment to allow monolayer formation and after a few ($\approx$ 5) minutes carefully transferred (using a pipette) to the bespoke droplet neuron chamber (see **Chapter 6** for Materials and Methods). The photosensory and presynaptic droplets were pipetted directly onto the recording and ground electrodes for movement. Using the micromanipulators to guide the electrode-containing droplets, the photosensory and synaptic bilayers were formed. After a further 10 minutes, the signalling pathway was completed by joining the axon droplets together either by tipping the chamber to one side or by gently pushing the droplets with a piece of silver wire or the micromanipulator.

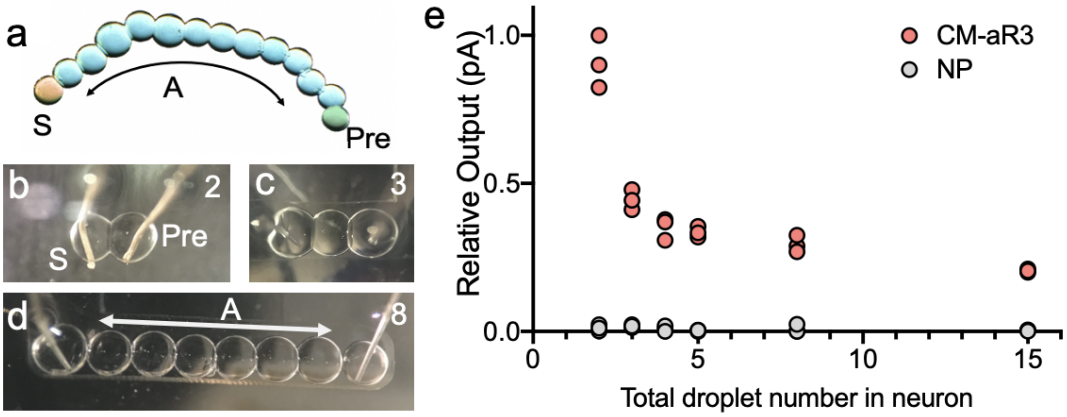


Figure 3.14: Electrical signal transmission a, Photograph (background removed) of a 15-droplet axon. The photosensory droplet (pink, S) contains 0.15 - 0.25 mg mL^{-1} CM-aR3 in Solution B. Axon (except the droplet connected to S, blue, A) and presynaptic droplets (green, Pre) contain 50 nM αHL in Solution D. **b-d** Photographs (taken with an iPhone) of a 2 (b), 3 (c) and 8 (d) droplet axon. **e,** Signal output recorded across synthetic neurons with increasing droplet number in the presence (CM-aR3, pink) or absence (NP, grey) of CM-aR3. The neurons are illuminated with YG light (490 - 608 nm with peaks at 550 and 592 nm, 15 $\pm$ 4.5 mW, n = 3). Figure is adapted from the author's manuscript in progress[193].

Since, droplets are interconnected in series, longer synthetic neurons will have a higher overall resistance (due to the additional DIBs). Inevitably, as axon length increased, signal transmission decreased (at a fixed potential of 0 mV). In

fact, increasing the axon droplet number from 0 to 13 resulted in a reduction in transmission of over 70 %; signals decreased from +22 ± 1.3 pA to +4.4 ± 0.1 pA (mean ± SD, n = 3) (Fig. 3.14). The longest droplet-based synthetic neurons tested were ≈10-mm in length and demonstrated that directional signal transmission (> 1.0-pA threshold) occurred over centimetre distances.

Including the pH-sensitive dye pyranine in the synthetic neuron droplets, enabled the wireless detection of signal transmission along the artificial axons (pKa = 7.31, fluorescence increases with pH, Fig. 2.10[149]). Following phototransduction, the photosensory droplet became brighter as protons were pumped into the axon. The fluorescence of all other droplets decreased over time; the injection of proton into (and along) the axon diminished the pyranine fluorescence intensity (Fig. 3.15). By monitoring changes to this optical output it was also possible to quantify this output[149]. A 5-droplet synthetic neuron was illuminated overnight (YG light, 15 h, 490 - 608 nm, with peaks at 550 and 592 nm, 15 ± 4.5 mW) and, following proton pumping across the bilayer, the pH of the photosensory droplet increased by +0.2 ± 0.1 pH (S, mean ± SD, n = 3, Fig. 3.15). The presynaptic droplet pH decreased by -0.2 ± 0.0 pH (Pre, mean ± SD, n = 3), demonstrating signal transmission along the entire axon (Fig. 3.15). If the photosensory bilayer lacked CM-aR3 (NP), no proton pumping occured meaning that no fluorescence (or pH) changes were observed. This was also seen when the synthetic neuron was not illuminated (D) or when it was illuminated with IR (680 - 741 nm peaks at 722 nm, 16 ± 5.0 mW) or UV (355 - 390 nm peaks at 367 nm, 15 ± 3.9 mW) light. Since αHL mediated signal transmission, its absence (NA) meant that protons could only cross the photosensory bilayer. Consequently, the pH of the first axon droplet (A1) decreased but the remaining droplets remained constant (A2, A3, Pre, Fig. 3.15). All synthetic neurons were stored in a hydrated environment for overnight experiments to avoid dehydration.

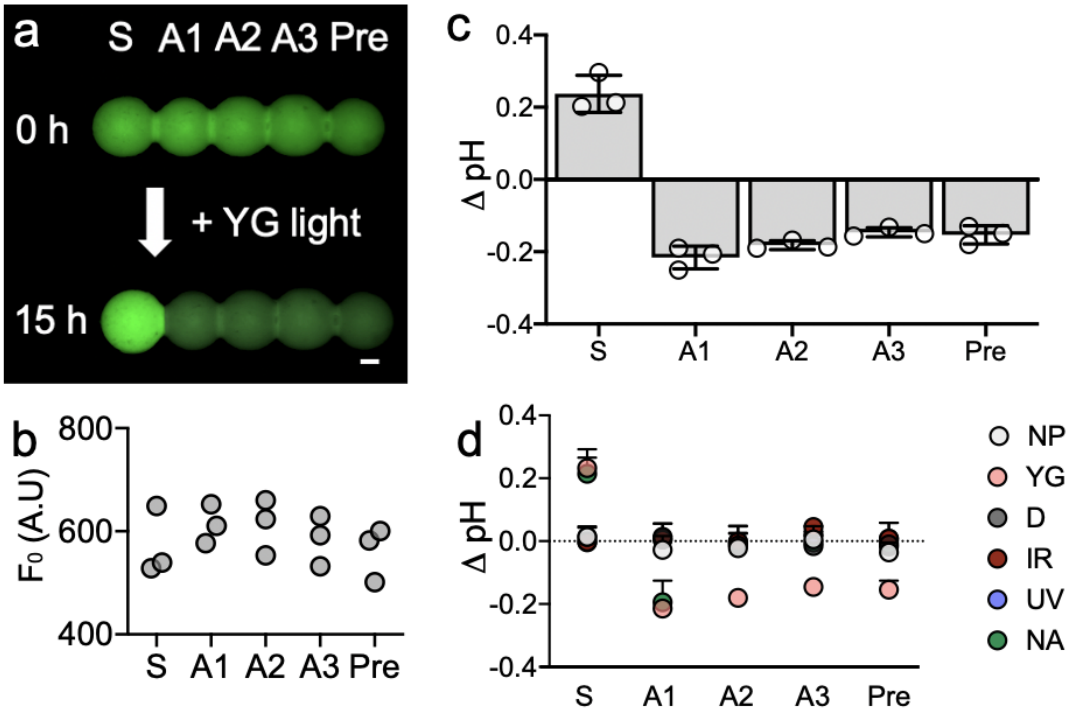


Figure 3.15: Optical detection of signal transmission a, Epifluorescence images of a 5-droplet neuron (images stitched and background removed) composed of a photosensory droplet (S), 3 axon droplets (A1, A2, A3) and a presynaptic droplet (Pre). Images are taken before (0 h) and after (15 h) of illumination with YG light. **b,** Droplet fluorescence oat the start of the experiment (n = 3 neurons with n = 3 technical replicates). **c,** Change in pH of the droplets upon illumination with YG light (mean ± SD, n = 3). pH is calculated from the calibration curve (Fig. 2.10). **d,** Change in pH of the droplets upon illumination with YG light (550 and 592 nm, 15 ± 4.5 mW) in the presence of CM-aR3 (pink), absence of CM-aR3 (NP, grey) and absence of αHL (NA, green) or when illuminated with IR light (burgundy, 722 nm, 16 ± 5.0 mW), UV light (blue, 367 nm, 15 ± 3.9 mW) or in the dark (D, black) (mean ± SD, n = 3). pH is calculated from the calibration curve (Fig. 2.10). Figure is adapted from the author's paper[193].

The long droplet axons had a high resistance which hindered signal transmission. Consequently, the use of a continuous hydrogel fibre was explored since the axon itself would be bilayer-free, reducing the resistance.

Agarose, a natural polysaccharide found in seaweed, was chosen to form the synthetic axon. The linear agarose chains consist of repeating units of agarobiose, a disaccharide composed of 1,3-D-galactose and 3,6-anhydro-L-galactopyranose, which undergo thermal crosslinking[299]. At high temperatures the agarose molecules, in a near-boiling water solution, have a random coil structure which upon cooling

form helical fibres that are held together by hydrogen bonds[299]. This permits the synthetic axon to be shaped into any desired geometry before it cools and solidifies. Between the fibres are water-filled pores enabling agarose to act as a transparent ionic conductor with ions rapidly moving through the pore network[299]. Additionally, agarose gels have a high gel strength which permits low concentrations of agarose to be used enabling good flexibility[299]. By adjusting the agarose concentration used, the mechanical properties of the gel and its pore size can be tuned[299]. In this way, the properties of the synthetic axon, such as conductivity, can be controlled.

First, the photosensory bilayer (formed between a droplet and agarose hydrogel, DHB) was characterised. Capacitance measurements indicated that photosensory DHBs were larger in area than DIBs (Fig. 3.16c-d). As discussed in **Chapter 2**, capacitance values depend on a variety of factors, for instance the content of the droplets, the oil ratio or the lipid type. However, if these factors remain constant then the DHB had a capacitance ≈ 1.6-fold higher than the equivalent DIB (Fig. 3.16). Within the synthetic neuron, a photosensory DIB (0.15 - 0.25 mg mL^{-1} CM-aR3 membrane fragments) had an average capacitance of 508 ± 51 pF; this increased to 819 ± 47 pF when the protein-free droplet was replace by a hydrogel (2% high gelling agarose) (Fig. 3.16). This larger surface area also permitted greater photosignal generation (likely due to more CM-aR3 insertion) (Fig. 3.16).

For this reason, synthetic neurons were then built using a continuous hydrogel axon and signal transmission was compared to its droplet counterpart. To form the axon, the hydrogel (2% high-gelling agarose in Solution D, pH 6.5) was heated (90 °C) and the pipetted into the chamber; homemade stoppers ensured the axon was the desired length. Whilst the hydrogel cooled, the droplets were incubated in a separate chamber for monolayer formation (increased to ≈ 10 minutes as droplet coalescence would require a new axon). Lipid-in-oil was then added to the chamber and the droplets pipetted onto the electrodes and pushed into contact with the axon (using the micromanipulators). As with the synthetic droplet neuron, the effect of increasing axon length on signal transmission was examined. Here, the same trend was observed with increasing axon length (longer hydrogel) resulting

in lower signal transmission; signals decreased from +22 ± 1.3 pA when the axon was 0 mm to +10 ± 1.0 pA when the axon was 10 mm (mean ± SD, n = 3) (Fig. 3.17a). However, larger signals were transmitted over a ≈10-mm distance (> 30%) than by its droplet counterpart (< 30%).

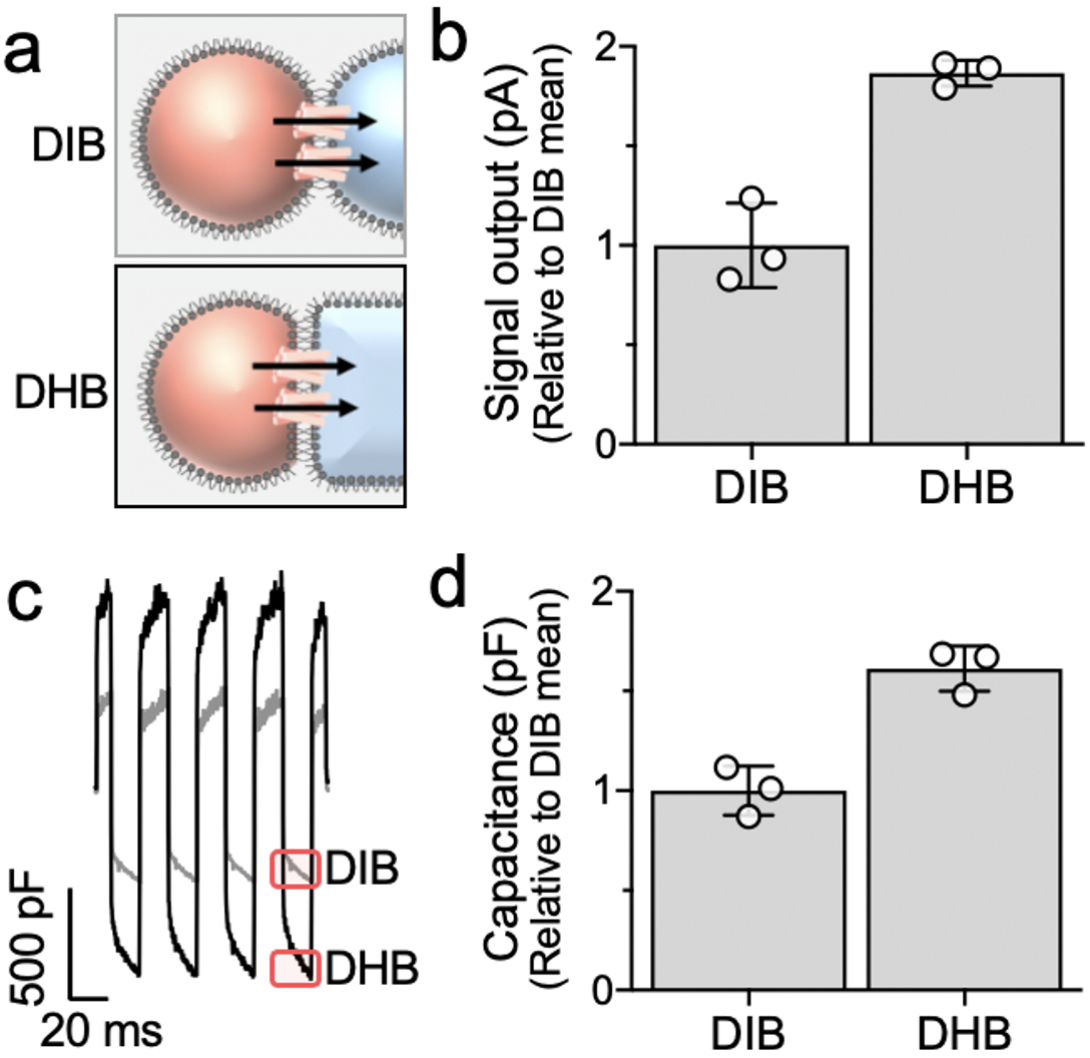


Figure 3.16: DIB and DHB comparison. a, Schematic of a droplet interface bilayer (DIB) and droplet hydrogel bilayer (DHB) containing CM-aR3. Ag/AgCl electrodes are used to record the signal output; the recording electrode is in the CM-aR3-containing sensory droplet (pink) and the ground electrode in the axon droplet (blue, DIB) or hydrogel (blue, DHB). **b,** Signal output recorded across CM-aR3-containing DIBs and DHBs when illuminated with YG light (550 and 592 nm, 15 ± 4.5 mW, n = 3, mean ± SD). The output is plotted relative to the mean of a CM-aR3-containing DIB. **c,** Capacitance trace recorded (in the dark) across a CM-aR3-containing DIB (grey) and DHB (black). **d,** Capacitance of CM-aR3-containing DIBs and DHBs (mean ± SD, n = 3). Capacitance is plotted relative to the mean of a CM-aR3-containing DIB. Figure is taken from the author's manuscript in progress[193].

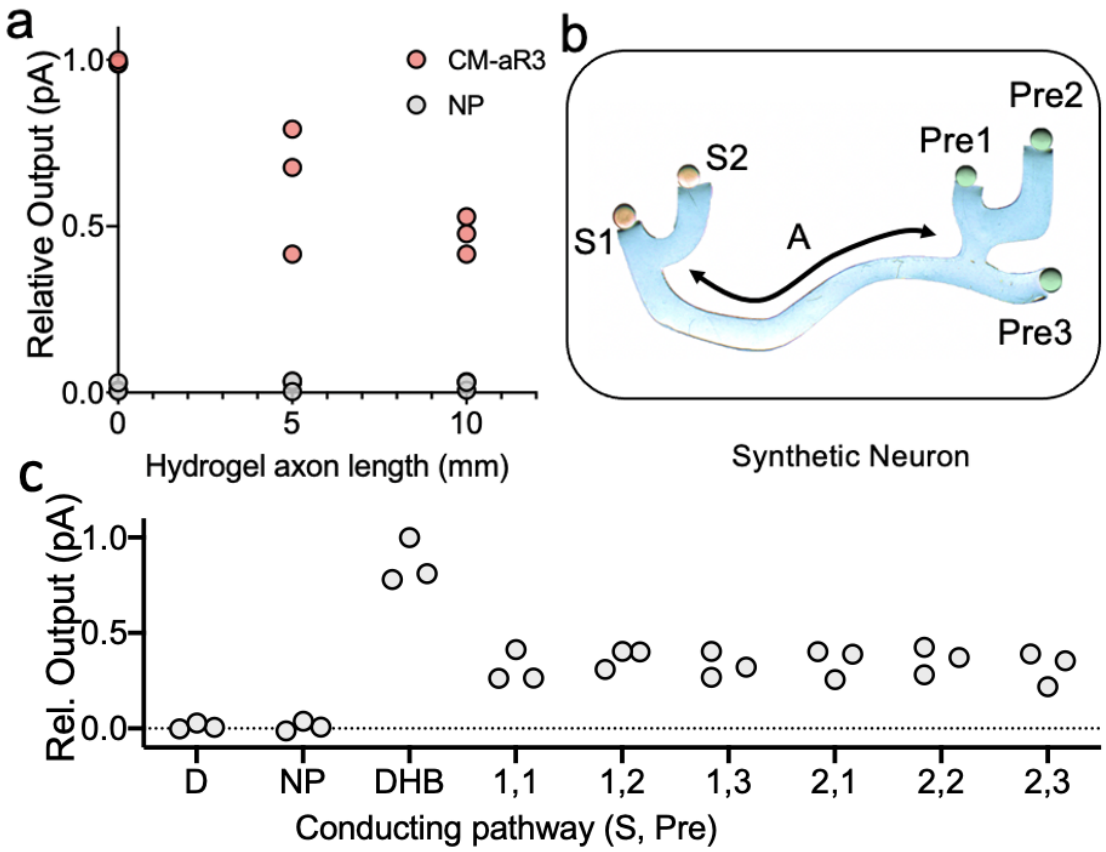


Figure 3.17: Signal transmission in a synthetic hydrogel neuron. **a,** Signal output recorded across a hydrogel axon with increasing length in the presence (CM-aR3, pink) or absence (NP, grey) of CM-aR3 (n = 3). The neurons are illuminated with YG light (550 and 592 nm, 15 ± 4.5 mW). **b,** Left: Photograph (background removed) or a synthetic neuron composed of two photosensory droplets (S1 and S2) and three presynaptic droplets (Pre1, Pre2 and Pre3). Right: Signal output is recorded across the branched hydrogel neuron. D = No light. NP = No CM-aR3. Numbers indicate the signal path (sensory droplet number then presynaptic droplet number, n = 3). Figure is taken from the author's manuscript in progress[193].

Next, a 25-mm long synthetic (hydrogel) neuron was built to determine whether signals could be transmitted over biologically relevant distances; the optic nerve is 30-mm in length[298]. For this, a bespoke chamber was designed to include a branched trench (≈ 1 mm deep and wide) in which the hydrogel could be shaped (see **Chapter 6** for Materials and Methods). The resulting hydrogel axon had a diameter comparable to those found in nature, albeit at the upper end; the giant squid axon is 0.5-1.5 mm wide (*Architeuthis dux*) and human neurons have diameters between 1-20 μm.

In turn, electrodes were positioned so that signals were recorded along each potential conducting pathway in succession (not simultaneously). All branched signalling routes transmitted signals greater than the 1.0-pA threshold when the CM-aR3 photosensory bilayer was illuminated with YG light (Fig. 3.17b). For instance, the conducting pathway between the first photosensory droplet (S1) and the second presynaptic droplet (Pre2) transmitted photosignals of +7.3 ± 1.5 pA (mean ± SD, n = 3, YG light, 490 - 608 nm, with peaks at 550 and 592 nm, 15 ± 4.5 mW) (Fig. 3.17b). However, when kept in the dark (D) no signal transmission was detected (< 1.0-pA threshold); this was also true in the absence of CM-aR3 (NP, Fig. 3.17b).

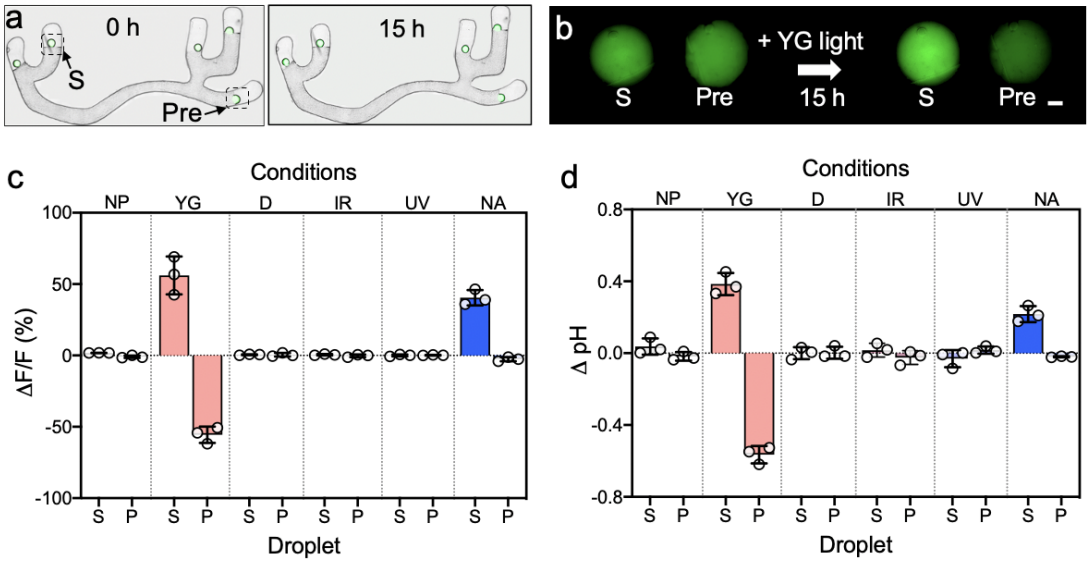


Figure 3.18: Optical detection of transmission in a synthetic neuron a, Composite image of the brightfield and fluorescence images of the hydrogel neuron before (0 h) and after (15 h) illumination. Only the terminal droplets contain the pyranine dye. Images are stitched together (see Materials and Methods). **b,** Epifluorescence microscopy images (minus background) of the sensory (S) and presynaptic (Pre) droplets before and after illumination (YG light, 15 h). Scale bar = 200 μm. **c,** Percentage change in droplet fluorescence (n = 3) when the neuron is illuminated with YG light (550 and 592 nm, 15 ± 4.5 mW) in the presence (YG) or absence (NP) of CM-aR3, or absence of αHL (NA) or illuminated with IR light (722 nm, 16 ± 5.0 mW) , UV light (367 nm, 15 ± 3.9 mW) or kept in the dark (D). **d,** Change in droplet pH (n = 3) when the neuron is illuminated with YG light in the presence (YG) or absence (NP) of CM-aR3 or absence of αHL (NA) or illuminated with IR light, UV light or kept in the dark (D). Figure is adapted from the author's paper[193]

Next, light-driven proton pumping was optically monitored with pyranine, a fluorescent pH reporter. In these experiments, dye was only added to the droplets

and not the hydrogel axon (in the absence of buffer, Fig. 3.18a). The fluorescence intensity of the photosensory droplet increased upon illumination as CM-aR3 transported protons across the bilayer (Fig. 3.18b, 15 h, YG light, 490 - 608 nm, with peaks at 550 and 592 nm, 15 ± 4.5 mW, synthetic neurons were stored in a hydrated environment overnight). At the other end of the hydrogel axon, the fluorescence intensity of the presynaptic droplet decreased as protons were transmitted along the axon and into the terminals (through αHL pores) (Fig. 3.18b). To quantify these observations a calibration curve was used (Fig. 2.10, pKa = 7.3, fluorescence increases with pH)[149]. The photosensory (S) droplet pH increased by +0.4 ± 0.1 pH and the presynaptic (Pre) droplet pH decreased by -0.6 ± 0.1 pH (mean ± SD, n = 3)(Fig. 3.18). Here, directional signal transmission was observed over 2.5-centimetre distances.

In addition to enhanced signal transmission, hydrogel axons also offered greater stability and flexibility; they can be made into almost any size, shape or pattern[265]. Additionally, these optical experiments demonstrated that within a 25-mm branched synthetic neuron, signals converged from multiple photosensory inputs and diverged along separate conducting pathways to multiple terminal droplets.

3.2.4.3 Different signalling mechanism

However, it should be noted that whilst the synthetic neuron architecture and function resembled biology, with signalling remaining rapid and directional, the mechanism of ion conduction differed (Fig. 3.19). Neither the droplet nor hydrogel synthetic neurons generated an action potential.

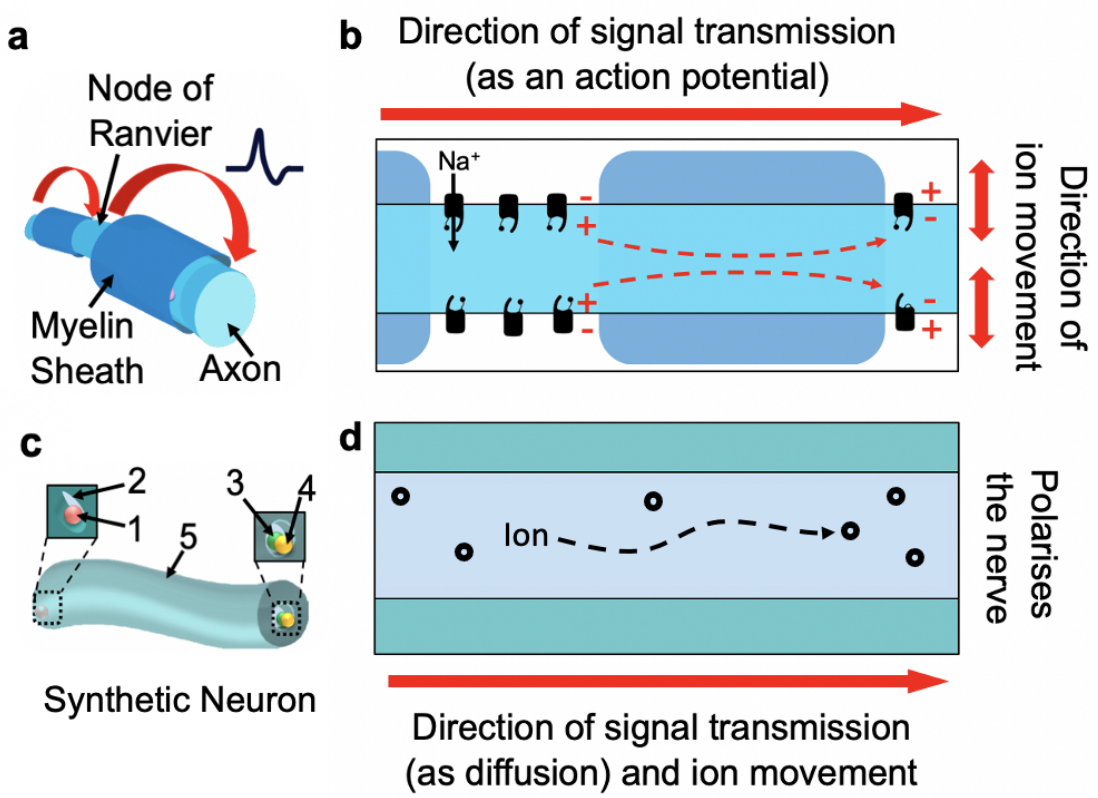


Figure 3.19: Mechanism of signal transmission. Schematic of an afferent biological neuron: the axon is exposed at Nodes of Ranvier (gaps in the myelin sheath), the action potential propagated by one node of Ranvier jumps to and is regenerated at the next node along the axon, thereby enabling the action potential to travel rapidly along the fibre (red arrow). **b,** Schematic of signal transmission along a biological axon in the form of an action potential. Voltage-gated channels (black) facilitate ion transport across the axon membrane and initiate formation of the action potential. Here ion movement is perpendicular to the direction of signal transmission. **c,** Schematic of a synthetic afferent nerve. Zoom highlights key features of a myelinated neuron: 1, sensory droplet, 2, hydrogel axon, 3, presynaptic droplet, 4, postsynaptic droplet and 5, elastomer sheath. **d,** Schematic of signal transmission along a synthetic axon in the form of directional ion diffusion. Here both ion movement and signal transmission are in the same direction. Figure is adapted from the author's manuscript in progress[193]

At the core of the synthetic neurons is the photochemistry of CM-aR3. When illuminated, protons were injected into the axon of the synthetic neuron generating the bioelectrical signal. Here, signal transmission occured as the ionotronic hydrogel carried the protons and other cations along the fibre and into the synaptic terminals (propelled by the electrochemical potential gradient). Ion-conducting protein pores (αHL) facilitated transmission across the interconnecting lipid membranes. Next, anions travelled towards the synaptic terminal. Again, electrochemical (charge and

concentration) potential gradients drove directional ion diffusion (Fig. 3.19). Here, the movement of ions and the direction of signal transmission are parallel; they are perpendicular within biological axons (Fig. 3.19).

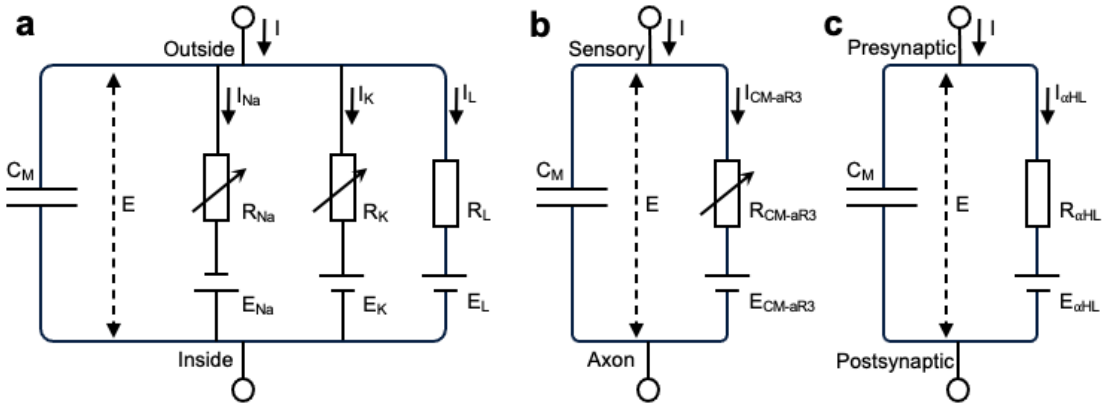


Figure 3.20: Hodgkin-Huxley model of the membrane a, HH model of a biological neuron. The capacitance (Cm) of the membrane describes its ability to store charge. The resistance is determined by the protein components of the membrane (R_L = leaky channels, R_{Na} and R_K are the voltage-dependent sodium and potassium channels respectively). The equilibrium potential of the leaky, sodium and potassium ions are represented by E_L, E_{Na} and E_K respectively. The current contribution of each of these ions is represented by I_L, I_{Na} and I_K. **b,** Conductance-based model of the sensory bilayer. The proton pump contributes to the resistance (R_{CM-aR3}), with the equilibrium potential (E_{CM-aR3}) and current (I_{CM-aR3}) arising due to protons being pumped outwards. **c,** Conductance-based model of the axon and synaptic bilayers. The pore alpha hemolysin contributes to the resistance (R_{aHL}), with the equilibrium potential (E_{aHL}) and current (I_{aHL}) arising due to ion flux through the pore. Figure is taken from the author's paper[193].

Based on their studies in squid nerves, Hodgkin and Huxley developed a mathematical model to described the underlying mechanism for the firing of action potentials (through which information propagates along nerve fibres)[220]. The simple model which they proposed treated each component of the excitable cell membrane as a separate electrical element (Fig. 3.20). The lipid membrane itself was represented via its capacitance (C_m), i.e., its ability to store charge. Their basic model, stated that the membrane contained three independent channels: voltage-gated sodium and potassium channels and a third generic leaky channel. They suggested that these channels were gated and that currents (I_{Na}, I_K and I_L respectively) were carried by the directional movement of ions down their electrochemical potential gradients (E_{Na}, E_K and E_L respectively). The conductance of ions (G_{Na}, G_K

and G_L respectively) through the channels are shown; for sodium and potassium, conductance varies with the membrane potential since the channels are voltage-sensitive (represented by an arrow) (Fig. 3.20).

The equivalent model for the synthetic neuron bilayers are much simpler since they each contain one protein type. Photosensory bilayers contain the proton pump CM-aR3 which generates a current by moving protons directionally into the axon (I_H). Here, large electrochemical potential gradients can hinder pumping[204]. Within the axon or synaptic bilayers, the protein pore αHL acts as a leaky channel, moving a variety of ions across the bilayers (movement can occur in both directions).

3.2.5 Neurotransmission

In biology, interneuronal communication occurs at synaptic junctions through the transmission of chemical or bioelectrical signals[3,300]. Typically, synaptic communication is mediated by neurotransmitters which are released when an action potential reaches the synapse[3,300] (Fig. 3.7a). Multiple substances may even be simultaneously released following a single neuronal event: co-transmission[4,301,302].

3.2.5.1 A synthetic synapse

Biological synapses occur at the junction between a neuron and a neighbouring electrically excitable cell. Typically, communication between these two cells is by diffusion of neurotransmitters. Neurotransmission (chemical communication, a3) is triggered by the arrival of an action potential (electrical signal, a1) at the terminal of the presynaptic neuron. The synapse of the synthetic neuron was designed to imitate this electrochemical signalling used in nature. The synapse mimic is composed of two aqueous droplets (200 nL) connected via a lipid 'synaptic' bilayer: the presynaptic and postsynaptic droplets. Presynaptic droplets contained the neurotransmitters and monomeric α-hemolysin pores (αHL). Chemical transmission in the synthetic neurons occurred via neurotransmitter diffusion through αHL pores located in the $\approx$5 nanometre-thick synaptic bilayer[48]; movement is down the electrochemical potential gradient generated by the photoactive pumps (Fig. 3.21

b2, b3). For comparison, at biological synapses neurotransmitters are packaged into vesicles before release into the ≈ 20 - 40 nanometre-wide[303] synaptic cleft (Fig. 3.21). The lack of a bio-mimetic re-uptake system within the synthetic neurons means that (for now) neurotransmitter availability is finite.

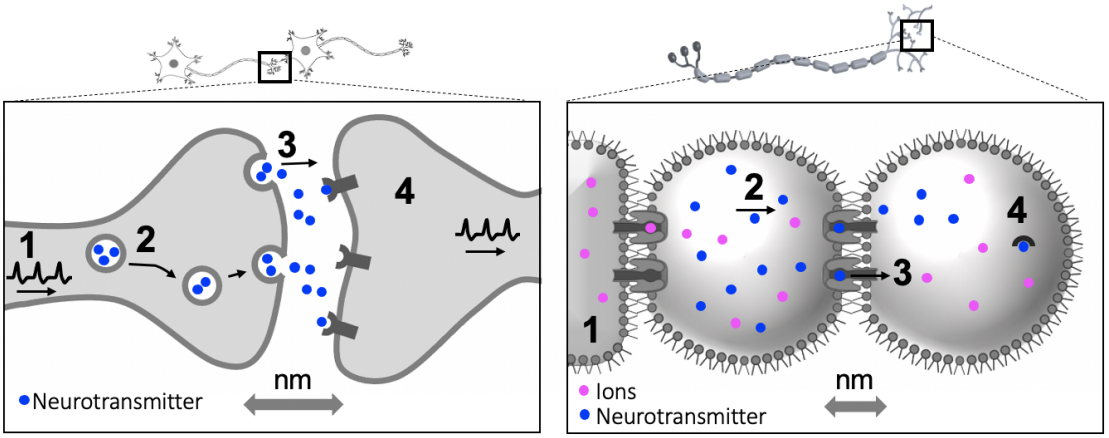


Figure 3.21: Synaptic transmission. a-b, Schematic of neurotransmission in a biological (a) and synthetic (b) neuron. In biology, a signals arrived at the terminal of the presynaptic neuron (as action potentials, a1), then vesicles packed with neurotransmitters move towards (a2) and fuse with (a3) the presynaptic membrane. Transmitters diffuse across the synaptic cleft, binding to receptors on the postsynaptic membrane, triggering a response (a4). In a synthetic neuron, signals arrive at the terminal of the synthetic neuron (as ion flux, b1), triggering neurotransmitter release (via diffusion from the presynaptic to postsynaptic droplet (b2-b3)) and triggering a response in the postsynaptic droplet (b4).

3.2.5.2 Protons as transmitters

One class of biological neurotransmitter are ions e.g., protons[301,304,305]. Since protons are co-released alongside classical (molecular) neurotransmitters, it it wasn't until 2008 that the first conclusive evidence of their role in synaptic communication came to light[305]. Since then, protons have been found to serve as important neurotransmitters throughout the nervous system, highlighted by the involvement of their receptors in a number of pathological conditions[301,304].

Electrical and optical experiments have already demonstrated that synthetic neurons can drive the directional movement of ionic neurotransmitters. Here, protons were injected into the synthetic axon by CM-aR3 proteins, directionally carried along the ionotronic hydrogel fibre and into the synaptic terminals (Fig. 3.15, 3.18).

3.2.5.3 MANT-dATP as a neurotransmitter

More typically, interneuronal communication is mediated by small molecules e.g. ATP, dopamine and glutamate.

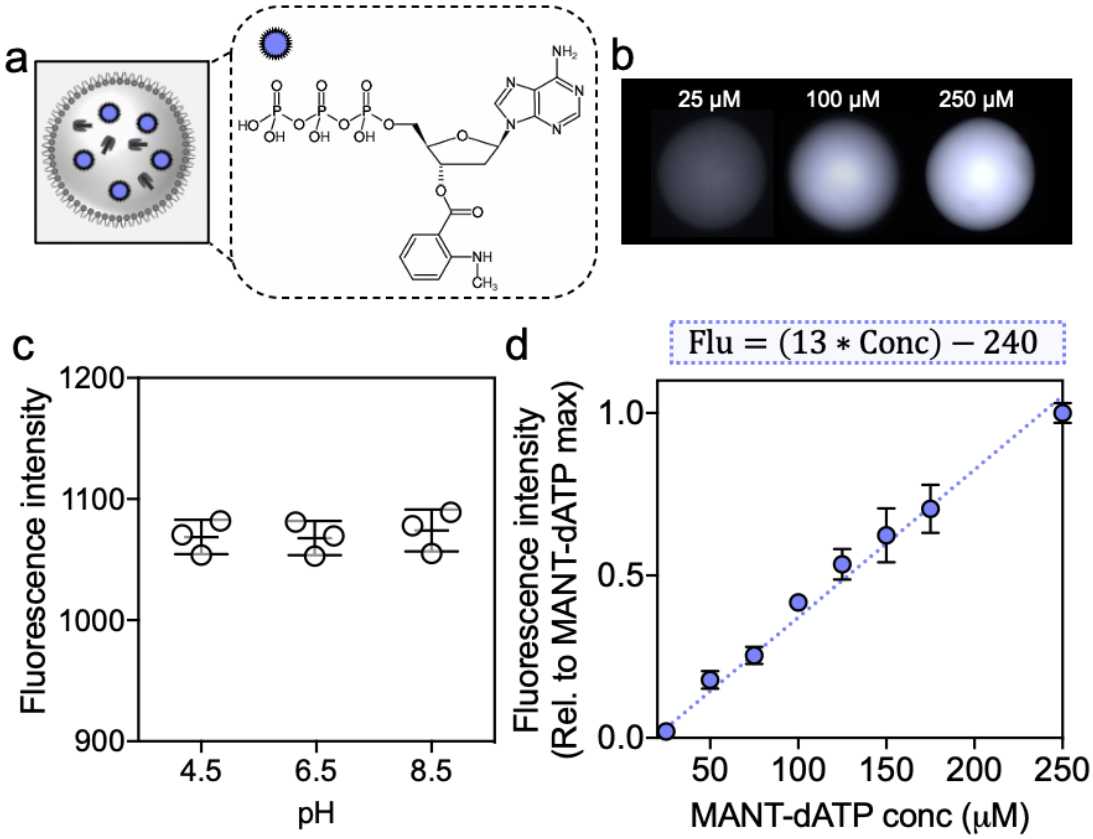


Figure 3.22: MANT-dATP calibration curve. **a,** Schematic of a presynaptic droplet containing αHL (black) and MANT-dATP (purple stars, zoom shows the structure drawn with ChemDraw). **b,** Epifluorescence images of droplets containing 50 nM αHL in Solution D and MANT-dATP at 25 μM, 100 μM, and 250 μM. **c,** Fluorescence of MANT-dATP at different droplet pH values; pH has no effect on fluorescence intensity (n = 8, mean ± SD). **d,** Calibration curve of fluorescence intensity against MANT-dATP concentration (n = 8, mean ± SD). A straight-line fit (dotted line, integer values to 2 significant figures) with equation F = (13 × C) - 240 describes their relationship; fluorescence intensity increases with concentration. MANT-dATP concentrations below 18 μM (2 significant figures) were not detectable using this experimental set-up (Fluorescence < 0). Figure taken from the author's manuscript in progress[193].

ATP has important functions in both intracellular and extracellular signalling. It has been identified as a key signalling molecule and is released at almost every central and peripheral synapse; it is also used in neuroglial transmission (e.g. released from astrocytes in response to pH fluctuations)[306]. ATP is typically released alongside

other signalling molecules: co-transmission. Extracellular ATP plays important signalling roles by binding to and activating a number of widely-distributed cell surface receptors called purinoreceptors. This triggers a diverse range of physiological actions such as smooth muscle contraction and cell proliferation[302]. For this reason, ATP was chosen as a model chemical neurotransmitter.

In the synthetic neuron, a fluorescent ATP analogue (MANT-dATP) was used to enable neurotransmission to be visualised (using epifluorescence microscopy). Aqueous droplets containing different MANT-dATP concentrations were imaged and their fluorescence intensity plotted (n=16, Fig. 3.22). MANT-dATP fluorescence intensity increased linearly with respect to concentration; the detection threshold was 18 μM (n = 16, fluorescence = 0) (Fig. 3.22).

3.2.5.4 Chemical neurotransmission

Next, a synthetic synapse was made from two aqueous droplets. Presynaptic droplets (Fig. 3.23) contained MANT-dATP neurotransmitters (100 μM) and αHL pores (50 nM).

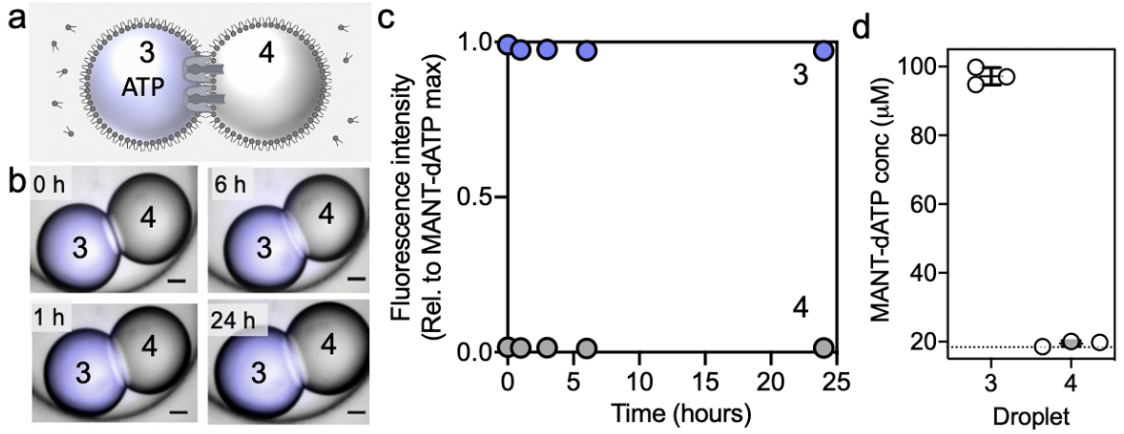


Figure 3.23: Slow neurotransmission in the absence of an electrochemical gradient. a, Schematic of synaptic bilayer formed between the presynaptic (a3, + MANT-dATP, + αHL) and postsynaptic (a4) droplets. **b,** Overlapping images in bright-field and fluorescence mode of the synapse over time (0, 1, 6 and 24 h) with no applied potential (in the dark). **c,** Fluorescence intensity plotted over time (F_T, mean ± SD, n = 3) of the presynaptic (3) and postsynaptic (4) droplets. **d,** ATP (MANT-dATP) concentration in the presynaptic (3) and postsynaptic (4) droplets after 24 h (no applied potential, in the dark, n = 3). The x-axis is at the threshold for fluorescence detection (Fig. 3.22). Figure is taken from the author's manuscript in progress[193].

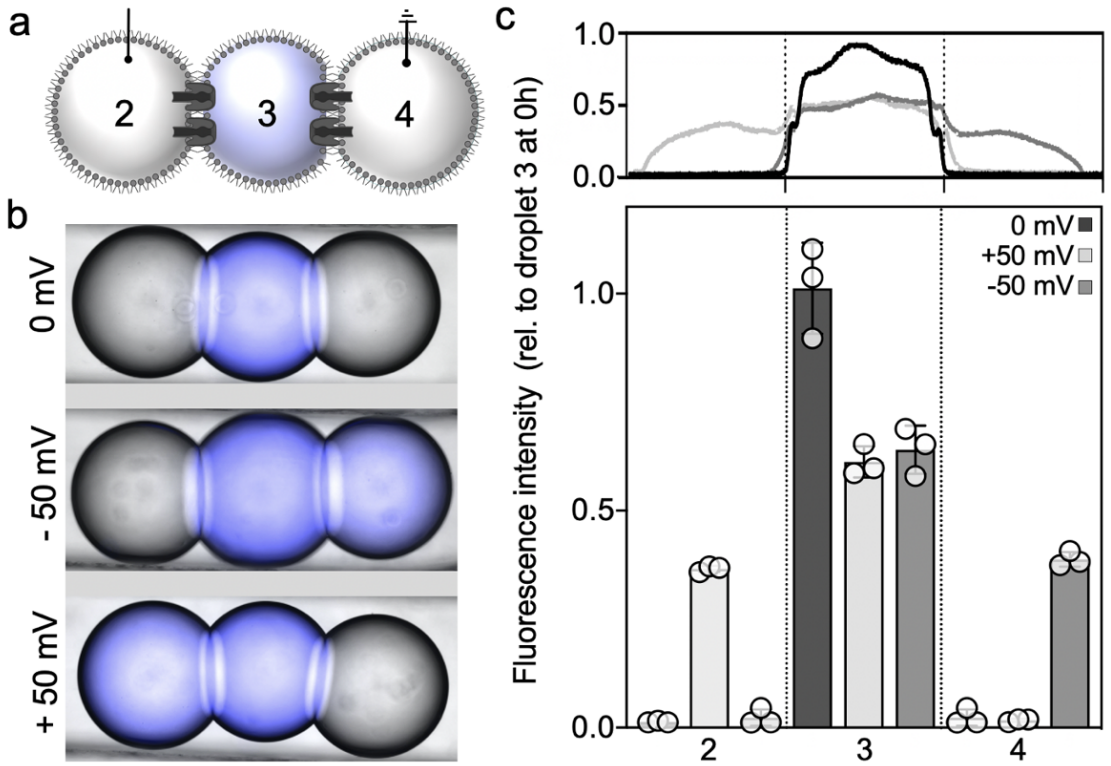


Figure 3.24: An electrochemical potential drives neurotransmitter release. a, Schematic of a 3-droplet chain formed from an axon droplet (a2), presynaptic droplet (a3) and postsynaptic droplet (a4). The presynaptic droplet (a3) contains 50 nM αHL and 100 μM MANT-dATP. Ag/AgCl electrodes are inserted into the terminal droplets (a2, a4); the ground electrode is in the postsynaptic droplet (a4). **b,** Composite image (stitched together, see **Chapter 6**) with bright-field and epifluorescence images overlayed of the 3-droplet chain after 1h with 0 mV, - 50 mV or + 50 mV applied (upon illumination, 550 and 592 nm, 15 ± 4.5 mW). **c,** Fluorescence intensity of the 3-droplet chains shown in 'b' after 1h (T_1) with 0 mV (black), - 50 mV (light grey) or + 50 mV (dark grey) applied. **d,** MANT-dATP concentration (mean ± SD, n = 3) of the axon droplet (d2), presynaptic droplet (d3) and postsynaptic droplet (d4) after 1 h with 0 mV (black), - 50 mV (light grey) or + 50 mV (dark grey) applied. Application of an electrochemical potential gradient drives MANT-dATP transfer by diffusion through αHL. The x-axis is at the threshold for fluorescence detection (Fig. 3.22). Figure taken from the author's paper[193].

To confirm that MANT-dATP did not simply diffuse through the αHL pores at a high rate (and in all directions), transfer was monitored in the dark (at a fixed potential of 0 mV) (Fig. 3.22). Within the synthetic neuron experimental set-up (50 nM αHL, continuous illumination with YG light, 550 and 592 nm, 15 ± 4.5 mW) spontaneous diffusion alone did not release a significant concentration of MANT-dATP (Fig. 3.23); after 24 h the concentration transferred remained

below the threshold (< 18 μM, 1.3 ± 1.4 A.U, n = 3, Fig. 3.23 3.22). However, spontaneous transfer of MANT-dATP did occur within a few hours at higher concentrations of αHL (unpublished observations).

In nature, one use of electrochemical transmembrane gradients is to provide energy for molecule transport. To confirm that MANT-dATP neurotransmission could be driven by such gradients, a potential was applied across a 3-droplet chain. A presynaptic droplet (a3, 100 μM MANT-dATP, 50 nM αHL) was interfaced with two (protein-free) aqueous droplets; the axon droplet (a2) contained the recording electrode and the postsynaptic droplet (a4) contained the ground electrode (Fig. 3.24). The continuous application of a negative potential (-50 mV, 1 h) resulted in the transfer of 44 ± 0.9 μM MANT-dATP into the postsynaptic droplet (mean ± SD, n = 3) (Fig. 3.24). Transmitter release was directional as confirmed by the movement of MANT-dATP into the axon droplet when a positive potential (+ 50 mV) was applied (Fig. 3.24).

3.2.5.5 Electrochemical communication

Finally, neurotransmission was demonstrated in the tetherless synthetic neurons using an electrochemical gradient, formed by illuminating CM-aR3 pumps, to drive release.

As a first demonstration, a short synthetic (droplet) neuron was built (4-droplets long, 2.8 mm). The droplet neuron was composed of a series of interconnected aqueous droplets (200 nL, 700 μm diameter): a photosensory droplet (0.15 - 0.25 mg mL^{-1} CM-aR3, pink, b1); a (protein-free) axon droplet (blue, b2); a presynaptic droplet (100 μM MANT-dATP, 50 nM αHL, green, b3) and a (protein-free) postsynaptic droplet (b4) (Fig. 3.25). As previously described, synthetic neurons were constructed within a bespoke neuronal chamber (see **Chapter 6** for details) in a lipid-in-oil environment (10 mg mL^{-1} DPhPC in 35:65 hexadecane, silicone oil). All droplets were incubated for ≈ 5 minutes to establish the lipid monolayer before they were brought into contact (by tipping the chamber); first

the photosensory (b1:b2) and synaptic bilayers (b3:b4) were formed and then, after a further 10 minutes, the neuron was completed (b2:b3, Fig. 3.25).

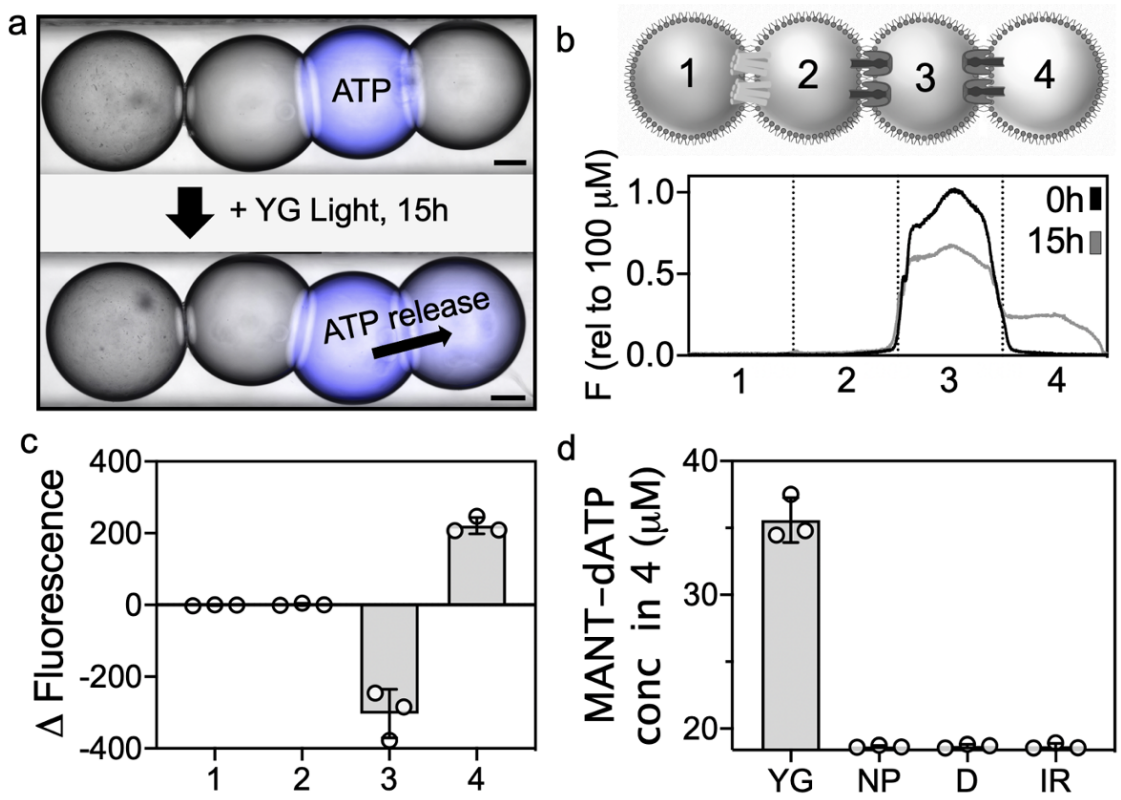


Figure 3.25: Neurotransmission from a droplet neuron. **a,** Composite images (bright-field and epifluorescence images stitched and overlayed) of the 4-droplet synthetic neuron before and after illumination (15 h, YG light, 15 ± 4.5 mW). MANT-dATP is released across the synaptic bilayer. **b,** Top: Schematic of a droplet synthetic neuron composed of a sensory (b1, pink), axon (b2, blue), presynaptic (b3, green) and postsynaptic (b4, yellow) droplet. Sensory droplets contain 0.15 - 0.25 mg mL^{-1} CM-aR3 and presynaptic droplets contain 100 μM MANT-dATP and 50 nM αHL. Bottom: Fluorescence intensity (% of the mean fluorescence at the start) of the synthetic neuron before (grey dotted line) and after (black solid line) illumination. **c,** Change in fluorescence intensity of each droplet (as shown in 'a'). (mean ± SD, n = 3 neurons with 3 technical replicates). **d,** ATP (MANT-dATP) concentration transferred to the postsynaptic droplet (b4, yellow, n = 3, mean ± SD) when the synthetic neuron was illuminated with YG light (550 and 592 nm, 15 ± 4.5 mW) in the presence (YG) or absence (NP) of CM-aR3 or left in the dark (D) or illuminated with IR (722 nm, 16 ± 5.0 mW) or UV (367 nm, 15 ± 3.9 mW). The x-axis is at the threshold for fluorescence detection (Fig. 3.22). Figure taken from the author's paper[193].

Following overnight illumination (YG light, 15 h, 490 - 608 nm, with peaks at 550 and 592 nm, 15 ± 4.5 mW), MANT-dATP release was observed by an increase in fluorescence of the postsynaptic droplet. Quantification of this was

carried out using a calibration curve (Fig. 3.22); 35 ± 1.4 µM MANT-dATP was transferred in the postsynaptic bilayer (mean ± SD, n = 3 neurons, Fig. 3.25). The lack of MANT-dATP in the axon droplet (fluorescence measurements were below the 18 μM threshold) indicated that neurotransmission was directional. Moreover, MANT-dATP release was not observed when the synthetic neuron was illuminated in the absence of CM-aR3 (NP, YG light) or if the photosensory bilayer was illuminated with UV (355 – 390 nm peaks at 367 nm, 15 ± 3.9 mW) or IR (680 – 741 nm peaks at 722 nm, 16 ± 5.0 mW) light or when kept in the dark (D, Fig. 3.25). For all overnight experiments, synthetic neurons were kept in a hydrated environment and only removed for imaging.

Having demonstrated that the synthetic neurons could perform photochemically-powered electrochemical communication, a long synthetic hydrogel neuron (25 mm) was then built. This long neuron was constructed as previously described with the photosensory and synaptic bilayers formed first. Within the synthetic (hydrogel) neurons, chemical transmission was directional with MANT-dATP being propelled into the postsynaptic droplet. In fact, 28 ± 2.6 μM of MANT-dATP was translocated across the synaptic bilayer during prolonged stimulation (YG light, 15 h, mean ± SD, n = 3 neurons, 490 - 608 nm, with peaks at 550 and 592 nm, 15 ± 4.5 mW, neurons were kept in a hydrated environment overnight, Fig. 3.26, 3.22). Again, neurotransmission was only observed when the CM-aR3 photosensory bilayer was illuminated with its activating wavelength (yellow-green light). It is worth noting that no change in MANT-dATP fluorescence intensity was observed when the droplet pH became either more acidic or more basic (Fig. 3.22) indicating that the altered fluorescent output was due to neurotransmission (and not proton pumping itself).

When activated, the photochemically-powered CM-aR3 proteins pumped protons into the synthetic axon, generating a bioelectrical signal. This signal propagated down the centimetre-long synthetic neuron leading to an output at the terminus. First, the (ion-conducting) hydrogel axon transported the protons (and other cations e.g., Na^+) along the fibre and into the synaptic terminals. Then, anions travelled (in a similar manner) along the axon and into the synaptic terminals. Ion

diffusion was propelled by electrochemical (charge and concentration) potential gradients generated following phototransduction. Finally, the energy stored in these electrochemical potential gradients propelled MANT-dATP (a negatively charged molecule) across the synaptic bilayer. This sequence of events mimics the electrochemical signalling used in nature (albeit using a different mechanism).

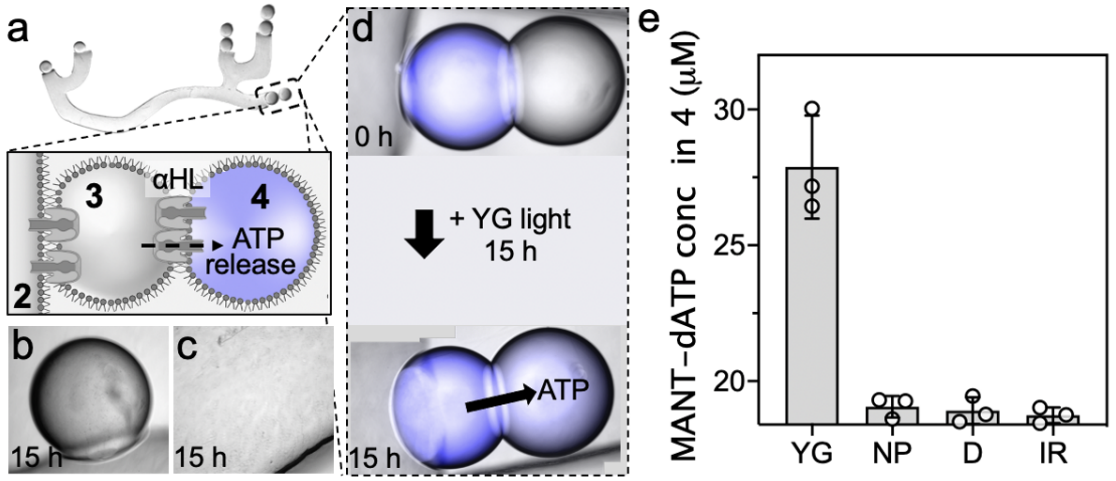


Figure 3.26: Neurotransmitter release from a hydrogel neuron. a, Photograph (background removed) of a synthetic hydrogel (a2) neuron (in black and white). Zoom: Synaptic terminal schematic, a DIB formed between a presynaptic (a3) and postsynaptic (a4) droplet. ATP (MANT-dATP, 100 μM) is released by diffusing through αHL pores (50 nM) in the synaptic bilayer. **b-c,** Bright-field and epifluorescence microscopy overlays of the sensory droplet (b) and hydrogel axon (c) after illumination (15 h, YG light). **c-d** Bright-field and epifluorescence microscopy overlays of the synaptic terminal before and after illumination (15 h, YG light). Overlapping images are stitched together (see **Chapter 6**). **e,** MANT-dATP concentration transferred to the postsynaptic droplet (a4, mean ± SD, n = 3) when the synthetic neuron was illuminated with YG light (550 and 592 nm, 15 ± 4.5 mW) in the presence (YG) or absence (NP) of CM-aR3 or left in the dark (D) or illuminated with IR light (722 nm, 16 ± 5.0 mW). The x-axis is at the threshold for fluorescence detection (Fig. 3.22). Figure adapted from the author's paper[193].

3.2.6 Downstream signalling

In nature, these chemical messengers transmit a signal, passing information to a target cell and triggering postsynaptic events.

3.2.6.1 A neighbouring cell

By releasing chemical molecules and ions in a controlled manner, the synthetic neurons have the ability to dictate downstream responses. To illustrate the potential application of the synthetic neurons in a biotechnological context, a pilot was performed using a well-characterised ATP-dependent reaction cascade. The assay kit (containing all the precursors and enzymes required) was included in a neighbouring cell droplet. Glycerol phosphorylation, using ATP, initiated the biochemical reaction sequence (Fig. 3.27). The product was then involved in a series of successive reactions to generate first a (biologically-relevant) glycoytic intermediate and later a fluorescent product (resorufin) (Fig. 3.27).

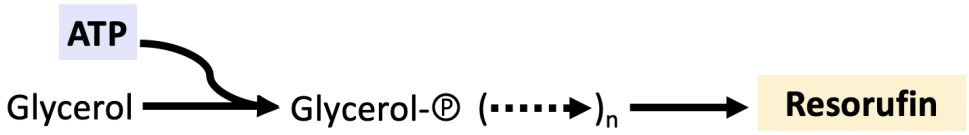


Figure 3.27: Downstream reaction. a, ATP (purple) is released across the synaptic bilayer and is involves in glycerol phosphorylation. This initiates a sequence of reactions which generate a functional output and then fluorescent resorufin (yellow).

To ensure that the reaction cascade functioned within the experimental set-up, two (200 nL) neighbouring cell droplets were made within a single well and ATP (not-fluorescent, 100 μM) was added to one of the droplets. After 30 minutes in the dark (to allow for the biochemical reaction to occur), the droplets were imaged (using epifluorescence microscopy) to monitor resourfin formation. A fluorescent output was only observed in the droplet which contained ATP (1880 $\pm$ 165 A.U, n = 3) (Fig. 3.28); in the absence of ATP, fluorescence was 16 $\pm$ 2.5 A.U, (n = 3). It should be noted that imaging was immediately after 30 minutes since the droplets were unstable due to the presence of glycerol within the neighbouring cell droplet (coalescence typically occurred within 60 minutes). Further, since resorufin is partially hydrophobic in character it leaked across droplet bilayers over time.

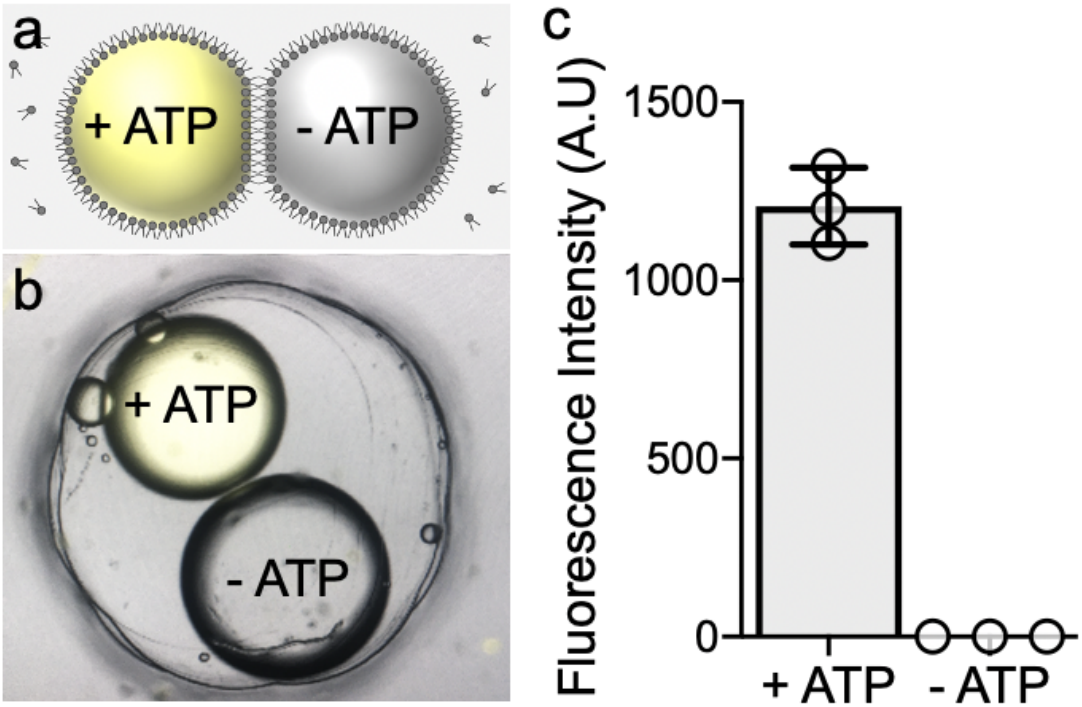


Figure 3.28: ATP is required for downstream signalling. **a,** Schematic of a droplet pair containing all the enzymes and substrates required for downstream signalling (except ATP). ATP is added to one of the droplets (yellow). **b,** Addition of ATP (100 μM) initates the reaction resulting in production of fluorescent resorufin. No fluroescence is seen in the absence of ATP. **c,** Fluorescence intensity (mean ± SD, n = 3 droplet with 3 technical replicates) of droplets in the presence (+ATP) or absence (-ATP) of ATP.

3.2.6.2 Triggering a downstream response

Short (200 nL droplets, ≈ 2.8 mm) and long (hydrogel, 25 mm) synthetic neurons were built as described above; here ATP (not MANT-dATP) was added to the presynaptic droplets.

First the synthetic neurons were continuously illuminated overnight (15 h, YG light, 490 - 608 nm, with peaks at 550 and 592 nm, 15 ± 4.5 mW, in a hydrated environment), releasing neurotransmitters into the postsynaptic droplet. Subsequently, a neighbouring cell droplet (200 nL, aN, containing the biochemical assay reagents) was pipetted at the synaptic terminus. The postsynaptic droplet (a4) was carefully (to avoid coalescence) separated from the presynaptic droplet using a piece of silver wire and mechanically fused with the neighbouring cell droplet (a4+N); this happens readily since the neighbouring droplet contains glycerol

which destabilises the bilayer (Fig. 3.29). The synthetic neuron was incubated for 30 minutes in the dark (allowing the biochemical reactions to occur) before the fused droplets (now 400 nL) were gently brought back into contact with the presynaptic droplet (a3) for visualisation.

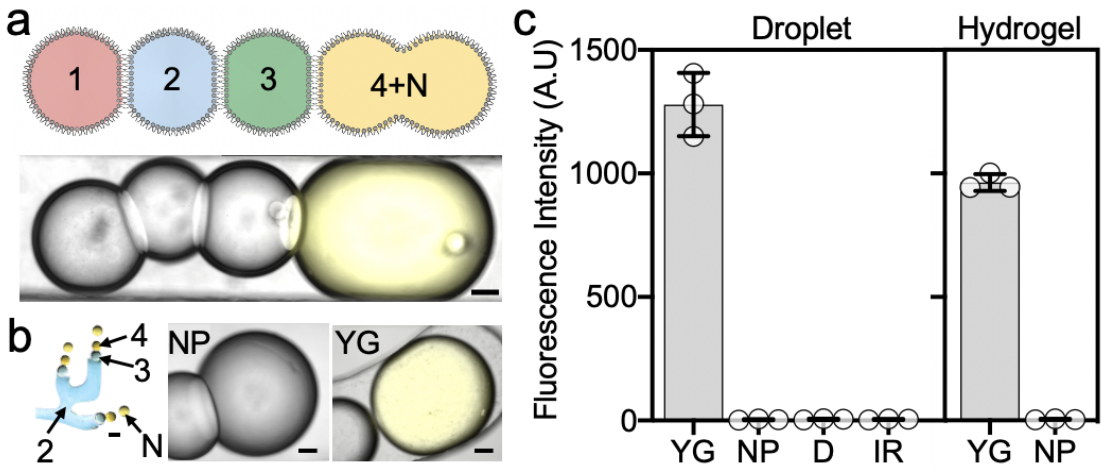


Figure 3.29: Downstream signalling in a synthetic neuron. a, Top: Schematic of a droplet synthetic neuron composed of 200 nL sensory (a1, pink), axon (a2, blue) and presynaptic (a3, green) droplets and a fused (400 nL) postsynaptic-neighbouring (a4+N yellow) droplet. Sensory droplets contain CM-aR3, presynaptic droplets contain MANT-dATP and αHL and neighbouring droplets contain a reaction mixture (all the precursors and enzymes of a biochemical ATP-dependent reaction). Bottom: Bright-field and epifluorescence microscopy overlays of the (stitched) droplet neuron (as in 'a') after downstream signalling. First, the neuron is illuminated (15 h, YG light), then following fusion left for 0.5 h for the reaction to occur. Scale bar 200 μm. **b,** Left: Photograph (minus background, dyed for visualisation) of the synaptic-end of a hydrogel neuron. Right: Bright-field and epifluorescence microscopy overlays of the (stitched) hydrogel neuron after downstream signalling (as described above) in the presence (YG) or absence (NP) of CM-aR3. Only when ATP is released from the synthetic neuron can a fluorescent output be produced. Scale bar 200 μm. **c,** Change in fluorescence intensity of the fused postsynaptic and neighbouring droplets (4+N, yellow) after left: the droplet neuron was illuminated with YG light (550 and 592 nm, 15 $\pm$ 4.5 mW), IR light (722 nm, 16 $\pm$ 5.0 mW) or kept in the dark (D) or right: the hydrogel neuron was illuminated with YG light in the absence (NP) or presence (YG) of CM-aR3 (mean $\pm$ SD, n = 3 neurons with 3 technical replicates). Figure taken from the author's paper[193].

Downstream signalling in the neighbouring cell droplet was only observed when the synthetic neuron was illuminated with yellow-green light (15 h, 490 - 608 nm with peaks at 550 and 592 nm, 15 $\pm$ 4.5 mW). Indeed, a fluorescent output of +1280 $\pm$ 104 A.U and +963 $\pm$ 27.6 A.U was recorded within the short (droplet) and long

(hydrogel) neurons respectively (mean ± SD, n = 3, Fig. 3.29). This is due to the requirement of ATP to initiate the signal cascade and produce a fluorescent resorufin output. No neurotransmission (ATP release) occurred if CM-aR3 proteins were not illuminated with their activating wavelength (YG light).

3.2.7 Synthetic myelination

Many biological axons are coated in a lipid-rich substance: myelin. Alongside protecting the neuron, the myelin sheath serves as an insulator and allows electrical impulses to transmit quickly and efficiently along the axon (Fig. 3.19). Inspired by nature, the synthetic neurons were then surrounded by a biomimetic sheath. It was important that the sheath was an insulator to help prevent interference from other electrical sources and that it was built from soft, biocompatible materials. Brainstorming of potential sheath materials was carried out in collaboration with **V.R.S** and **D.L** and a silicone elastomer (Sylgard-184) was chosen. The Young's moduli of this elastomer (and the hydrogel axons) are comparable to biological tissues indicating similar mechanical properties[235,307]. This is desirable as devices need to be flexible to accommodate deformations arising from movements in the body.

To illustrate the flexibility of these materials, a simple flexion experiment was conducted (Fig. 3.30). Cuboid sections of material (20 mm in length, 5 mm in width) were sequentially placed on various plastic shapes, designed to mimic organ-curvatures: hydrogel (2% high-gelling agarose), elastomer (Sylgard-184) and a myelinated synthetic neuron (the cylindrical axon was 1 mm across). To fabricate the myelinated synthetic neurons the tubular sheath was first formed. A glass rod (length 10 mm, diameter 1 mm) was glued into the centre of a plastic cuvette (length 10 mm, diameter 5 mm). Silicone elastomer monomer (Sylgard 184) and curing agent (Sigma, 761036) were mixed (10:1 ratio), degassed (30 min) and poured into the cuvette. After curing overnight (60° C, see **Chapter 6** for details), the sheath was removed and the hot hydrogel (containing blue food dye for visualisation) pipetted into the central channel.

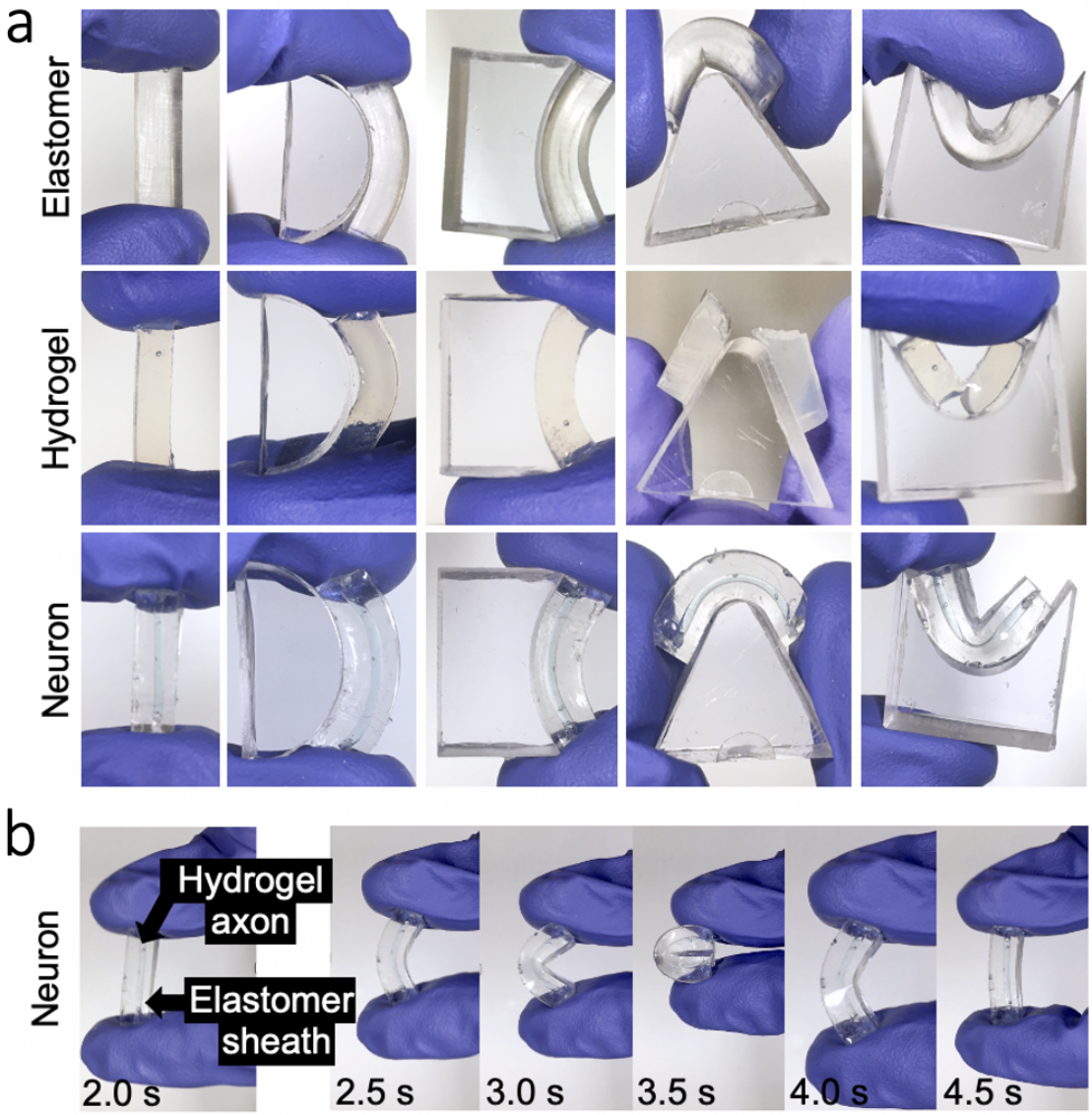


Figure 3.30: Synthetic neurons are flexible. a, Cuboids of the biomaterials (length = 20 mm, width = 5 mm, height 5 mm) were shaped over various curved plastic structures. An elastomeric structure is flexible and can be positioned over all structures without any permanent effect to its structural integrity. A hydrogel structure is less flexible. It can be positioned over structures with a shallow curvature without any permanent effect to its structural integrity but will fracture when forced over structures with a higher (sharper) curvature. A synthetic neuron (formed as above) is flexible and can be positioned over all structures without any permanent effect to its structural integrity; here the hydrogel axon remains intact. **b,** Snapshots of the synthetic neuron being repeatedly bent between two fingers. Figure adapted from the author's manuscript in progress[193].

The elastomer was flexible and could be positioned over all structures without any permanent effect to its structural integrity. However, the hydrogel was less resistant to bending. Whilst it could be positioned over structures with a shallow

curvature without any permanent effect to its structural integrity, fractures occured when forced over structures with a higher (sharper) curvature (Fig. 3.30).

To demonstrate the flexibility of a synthetic myelinated neuron in real-time, a video was taken of the material being bent in half between two fingers. The synthetic myelinated neuron was mechanically folded in two repeatedly and no structural damage occured i.e. it did not undergo any fractures (Fig. 3.30). In fact, the synthetic myelinated neuron returned to its original shape Fig. 3.30).

Alongside its flexibility, the insulating properties of the silicone elastomer made it a desirable material for construction of the synthetic myelinated neuron. In order to characterise the conductivity of the myelin sheath imitation, Ag/AgCl electrodes were used. First, the myelin sheath was formed (as described above except plastic tubing replaced the cuvette to give a cylindrical neuron, see **Chapter 6** for details). Then the hydrogel axon was injected into the central channel to form the conducting pathway. It should be noted, that unlike its biological counterpart, the synthetic axon and sheath were structurally independent, meaning that whilst snugly fitting within the elastomer, it was possible to remove the hydrogel axon if damaged and replace it. The completed synthetic myelinated neuron was then placed into a lipid-in-oil solution and aqueous droplets (200 nL, containing the electrodes) were positioned (using the micromanipulator) at each end of the axon forming the photosensory and synaptic bilayers. Here, the recording electrode was in the CM-aR3 photosensory droplet (S, 0.15 - 0.25 mg mL^{-1}) and the ground electrode was in the presynaptic droplet (Pre, 50 nM αHL) (Fig. 3.31). Upon illumination (YG light, 490 - 608 nm, with peaks at 550 and 592 nm, 15 ± 4.5 mW, 0 mV applied potential) the 10-mm central axon of the synthetic myelinated neuron conducted signals of +14 ± 0.5 pA (mean ± SD, n = 3, Fig. 3.31). However, transferring the ground electrode from the (αHL-containing) presynaptic droplet (Pre), into the elastomeric sheath (E, the recording electrode remained within the photosensory (S) droplet), resulted in no signal transmission upon illumination (+0.2 ± 0.3 pA, below 1.0-pA threshold, mean ± SD, n = 3) (Fig. 3.31). This was because the elastomeric sheath is an insulator.

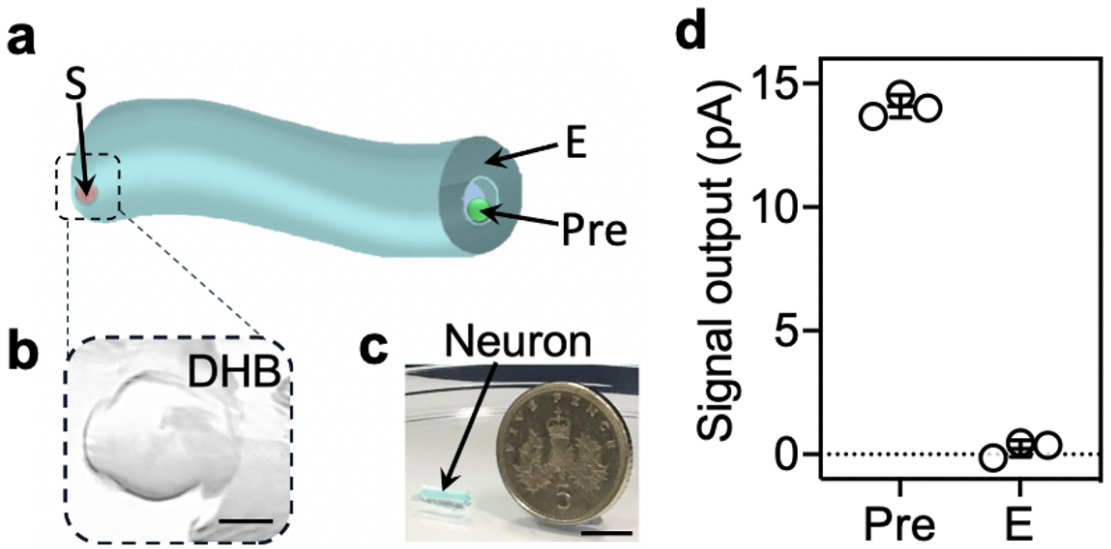


Figure 3.31: A synthetic myelinated neuron. a, Schematic of a myelinated neuron. The recording electrode is inserted into the CM-aR3 sensory droplet (S, pink). The ground electrode is inserted into the presynaptic droplet at the other end of the hydrogel axon (Pre, green) or into the elastomer sheath (E, teal). **b**, Zoom shows brightfield image of the sensory droplet hydrogel bilayer (DHB, in oil). Scale bar = 200 µm. **c,** Photograph of the myelinated synthetic neuron (in air). Central hydrogel neuron contains blue food dye for visualisation. Scale bar = 10 mm. **d,** Signal output detected when the ground electrode is inserted in the presynaptic droplet (Pre) or the elastomer sheath (E) (from 'a') and the synthetic neuron illuminated (YG light, 490-608 nm, peaks at 550 and 592 nm, 15 ± 4.5 mW, n = 3, mean ± SD). A signal is transmitted along the synthetic axon to the presynaptic droplet (Pre) but not through the insulating sheath (E). Figure taken from the author's manuscript in progress[193].

3.2.8 Device lifetime

The ultimate goal of this thesis is to incorporate the synthetic neurons into soft bioelectronic devices for applications in chemical computing, soft robotics and medicine. For many of these applications it is desirable for the device to have a long operational lifetime.

3.2.8.1 Photobleaching

The synthetic neurons described in this thesis bypass the stiff components and powering units that were previously needed in conventional devices. Instead they implement the principles of chemiosmosis, using electrochemical gradients to drive the movement of ions across membranes. Within the tetherless synthetic neurons, formation of such gradients were driven by the photochemistry of CM-aR3.

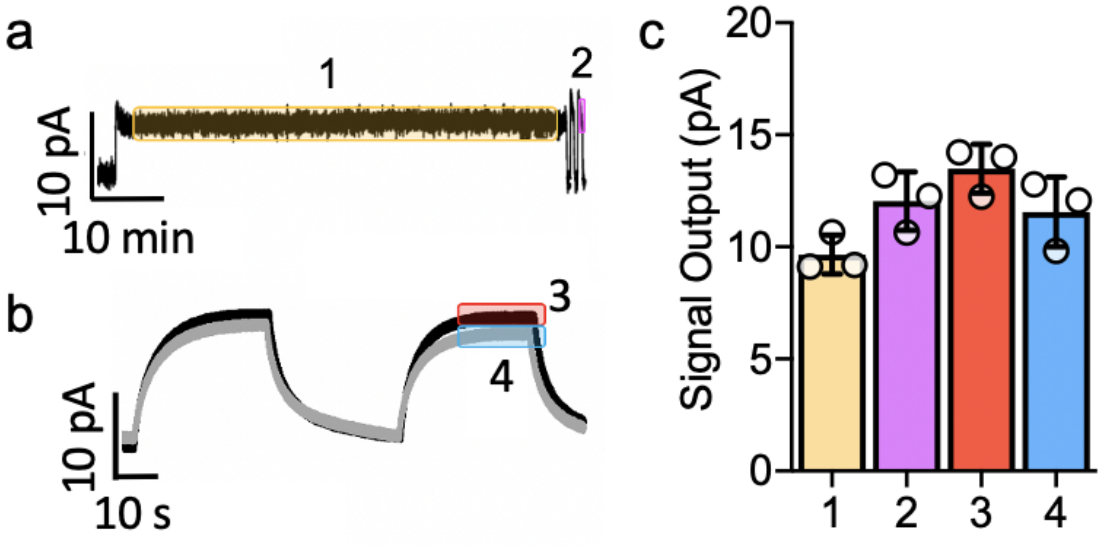


Figure 3.32: CM-aR3 photoactivity is retained under prolonged illumination. **a-b,** Trace recorded across a CM-aR3 photosensory droplet upon prolonged illumination with YG light (490 - 608 nm with peaks at 550 and 592 nm, 15 ± 4.5 mW). a: 1 h continuous illumination followed by two 30s light pulses (0.016 Hz), b: two 30 s light pulses (0.016 Hz) before (black) and after (grey) 20 h illumination at a high light intensity (550 and 592 nm, 32.1 ± 1.6 mW, in the absence of electrodes). **c,** Mean output recorded from the boxes in 'a-b' (n = 3, mean ±SD). Figure adapted from the author's manuscript in progress[193].

The main drawback of light powered devices is that overexposure might damage the system. Indeed, rod rhodopsin (found within the human eye) becomes bleached each time a photon is absorbed. Some microbial rhodopsins, e.g., ChR2 [120], show a decrease in signal generation or becomes less responsive after long periods of continuous illumination in a phenomenon known as desensitisation.

In **Chapter 2**, the effect of illumination intensity and duration on CM-aR3 activity was investigated. It was observed that the photoactivity of CM-aR3 was maintained during prolonged illumination (15 min, electrical recording was continuous, YG light) and when repeatedly subjected to a series of rapid pulses (10 pulses of 30 s, 0.016 Hz, 490 - 608 nm, with peaks at 550 and 592 nm, 15 ± 4.5 mW) (Fig. 3.32a). Further, CM-aR3 signal output was maintained when continuously illuminated for 1 h (Fig. 3.32). These results indicated that within the experimental system, no desensitisation or photobleaching of CM-aR3 occured. In fact, CM-aR3 even retained its photoactivity after continuous illumination (20 h,

in the absence of electrodes, YG light, 550 and 592 nm) with a high light intensity (32.1 ± 1.6 mW, twice that used in this thesis). Photosensory droplets were made using this CM-aR3 (post illumination) and steady-state signals of + 14 ± 4.5 pA were recorded (Fig. 3.32b); before illumination the output was + 15 ± 2.6 pA (n = 3, mean ± SD). Should bleaching be a concern, a very low light intensity could be used; signals above the 1.0-pA threshold were generated with a light output of 0.1 mW (unpublished observations, 0.1 mW was the detection limit of the sensor).

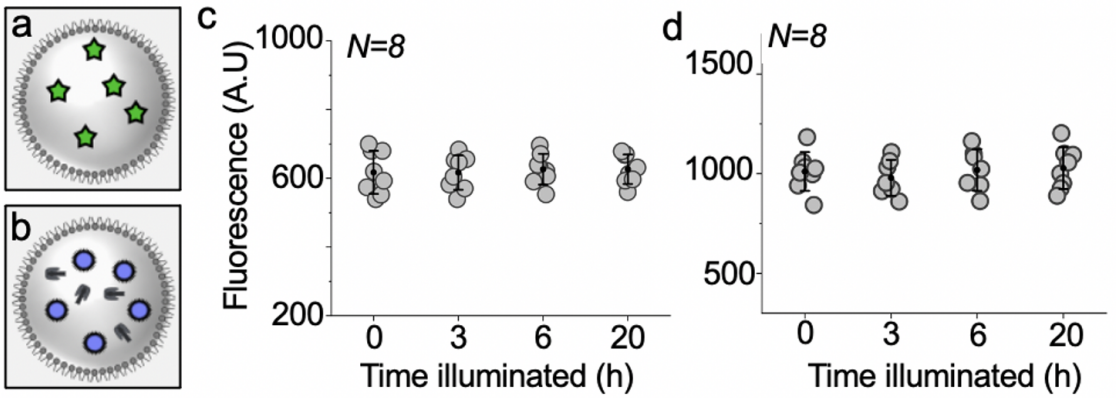


Figure 3.33: The dyes aren't bleached under high light intensity. a-b, Schematic of a droplet containing, a: pyranine (green stars) or b: MANT-dATP (purple stars) and αHL (black). **c-d,** Fluorescence output of the, c: pyranine dye or d: MANT-dATP dye at different time points after illumination (continuous illumination, 550 and 592 nm, 15 ± 4.5 mW, 31.2 ± 6.3 mW, higher than used in this thesis, n = 8). Figure adapted from the author's manuscript in progress[193].

The fluorescent dyes (pyranine and MANT-dATP) used in the synthetic neuron construction were only included for visualisation and will not be a part of the final bioelectronic device. However, the photosensitivity of these molecules was also tested (under more intense light than the experimental conditions used) to confirm the validity of the data. Droplets containing dye were illuminated at a high light intensity (32.1 ± 1.6 mW, YG light) and changes in fluorescence intensity was monitored by epifluorescence imaging (measurements were taken at 0 h, 3 h, 6 h and 20 h, n = 8). For both dyes, no reduction in fluorescence output was observed over 20 hours (Fig. 3.33) indicating no photochemical alteration to the molecules under prolonged illumination.

3.2.8.2 Synthetic neuron storage

Next, a synthetic (hydrogel) neuron was constructed and kept in the dark (in a hydrated chamber) at room temperature. If left in open air, the synthetic neuron dried up and the device was no longer operational. The synthetic neurons remained functional after being stored for 7 days (the longest time tested here); signals of + 17 ± 0.8 pA and + 15 ± 1.1 pA were recorded on day 0 and 7 respectively (mean ± SD, n = 3, Fig. 3.34).

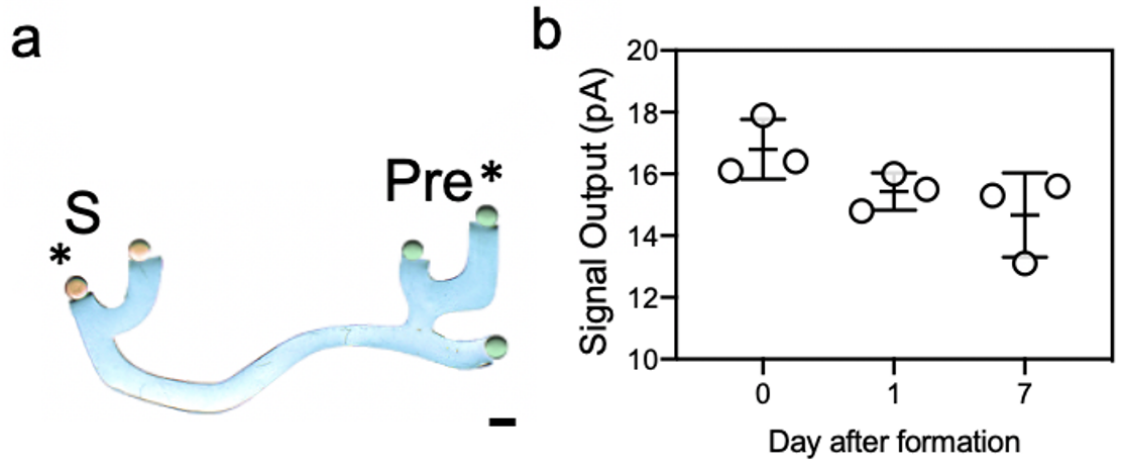


Figure 3.34: Synthetic neuron lifetime in the dark. a, Photograph (+ food dye for visualisation, background removed) of a synthetic neuron. Sensory droplet (pink, 0.25 mg mL -1 CM-aR3, Solution B), axon (blue, 2% agarose, Solution D) and the presynaptic droplet (green, 50 nM αHL, Solution D). Scale bar = 1 mm. **b,** Ag/AgCl electrodes were inserted into the droplets (*) and the signal recorded upon illumination (YG light, 490-608 nm, peaks at 550 nm and 592 nm) on Day 0, Day 1 and Day 7 (mean ±SD, n=3). The synthetic neuron is stored in the dark at room temperature (in a hydrated environment) between recordings. Figure taken from the author's manucript in progress[193]

Previously, CM-aR3 proteins were stored at 4 °C between experiments. However, here the synthetic neurons were kept at room temperature since condensation would build up if the hydrated chamber was stored at low temperatures. It was assumed that the CM-aR3 used in the synthetic neurons retained its photoactivity after weeks-months at room temperature; bR (a homologous protein) is stable for 7–12 years[130]. Indeed this was observed, CM-aR3 proteins kept at room temperature during the first national lockdown (19^{th} March - 7^{th} July 2020, 110 days) remained

active when tested afterwards (data not shown). This suggests that CM-aR3 might also remain stable for a long time, making it an attractive option in bioelectronics.

However, the synthetic neurons must be stored in the dark since the device is powered by light. Photosensory droplets (200 nL, 100 mM MES, 100 mM NaCl, 0.001 % DDM, 0.15 - 0.25 mg mL^{-1} CM-aR3, pH 6.5) have a finite number of protons available for pumping and eventually this will be depleted, restricting the device's ability to function continuously for long periods of time. Including MES buffer in the droplets prolongs the time before proton exhaustion occurs (by increasing proton availability) and the time before CM-aR3 activity is hindered by the build-up of a pH gradient[149,204]. However, eventually the protons will be exhausted or phototransduction will be impeded by the pH gradient. In addition, neurotransmitter stocks will also be depleted over time. The modular approach to the fabrication of the synthetic neurons means that its elements and properties can be easily tuned. One way to enhance device longevity would be to add modules which contain a re-uptake system, enabling ion and neurotransmitter stocks to be restored. More information about potential ways in which these challenges might be addressed are discussed in **Chapter 5**.

3.2.8.3 Improving stability using a copolymer

Most synthetic neural devices failed due to fusion of the droplet and hydrogel elements. This instability was aggravated by fluctuations in the environmental conditions arising due to poor control in the building: temperatures ranged from 20 - 29 °C and humidity from 20 - 50%. Extremes in conditions led to difficulties in forming stable bilayers and the frequency of droplet coalescence increased. At sub-optimal environmental conditions, monolayer incubation times were increased (from $\approx$ 5 minutes to $\approx$ 30 minutes) to improve stability but for future applications a more permanent solution is needed.

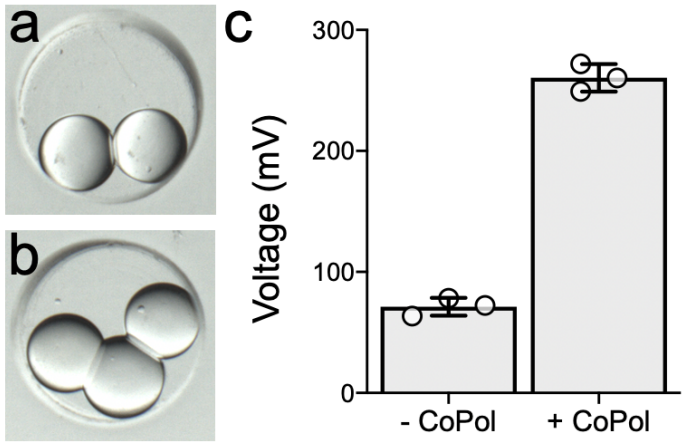


Figure 3.35: Copolymer increases bilayer stability. a-b, Photograph of a droplet pair (a) and 3-droplet chain (b) in a lipid-in-oil containing both lipid (DPhPC) and copolymer (PE-PEG) (see **Chapter 6** for methods). **c,** Breaking potential recorded across the in the absence (-) or presence (+) of the copolymer (mean ± SD, n = 3, in the dark). A higher voltage is required to break a bilayer when copolymer is present (+CoPol).

Polymersomes are artificial compartments in which the membrane is made from amphiphilic synthetic block co-polymers; they are considered more stable due to their thicker membranes. For this reason the use of copolymers to stabilise the membranes of the synthetic neuron was explored. PEG (poly(ethylene glycol)) has widespread use in biomedical applications since it is a biocompatible polymer; this is a desirable trait in the development of a bioelectronic device. Moreover, it has been already been used in droplet networks to strengthen them[31,52]. Polyethylene-block- Poly(ethylene glycol) (PE-PEG) was chosen for this feasibility study due to its immediate availability and was prepared in collaboration with **A.A.S**. First, the copolymer was dissolved (by heating to 50 °C and gentle sonication), at a concentration of 1 mg mL^{-1} in mineral oil. It was not possible to dissolve the copolymer directly into other oils e.g., HFE-7000, nor at concentrations $\geq$ 5 mg mL^{-1}. Next, the copolymer-mineral oil mixture was mixed (at a ratio of 1:10) with the standard lipid-in-oil solution (10 mg mL^{-1} DPhPC in 35:65 hexadecane, silicone oil).

Copolymer (in mineral oil) only droplets adhered to the chamber walls but when blended with DPhPC (in hexadecane and silicone oil) construction of droplet

pairs and small networks was unproblematic (Fig. 3.35a-b). After formation, the copolymer was reduced (forming PE-PEG-SH) by irradiating with UV light (1 min, 367 nm, 10 ± 3.1 mW), generating strong disulphide bonds. All droplet pairs and (3-droplet) networks survived irradiation (n = 16).

To demonstrate that the addition of block copolymers enhanced bilayer stability, the potential at which the bilayer fractured was recorded. After irradiation of a (protein-free) droplet pair, Ag/AgCl electrodes were brought into direct contact with the droplets and a voltage ramp protocol run. The breaking potential was higher when the bilayer contained copolymer, rising from +70 ± 17 mV (DPhPC only) to +260 ± 19 mV (1:10 PE-PEG-SH:DPhPC) (mean ± SD, n = 3, Fig. 3.35). This suggests that even low quantities of copolymer strengthen droplet bilayers.

However, the use of PE-PEG in synthetic neurons has two potential limitations: (possibly damaging) UV irradiation is required for copolymer formation, and the incorporation of CM-aR3 (membrane fragments) into the bilayers may be hampered by the bulky polymer groups. To discern whether the photoactivity of CM-aR3 was impaired, outputs were recorded across the photosensory bilayer (using Ag/AgCl electrodes). For this, the recording electrode was in contact with the CM-aR3 photosensory droplet (0.15 - 0.25 mg mL^{-1} as CM fragments in Solution C (0.001% DDM, 100 mM MES, 100 mM NaCl, pH 6.5)). Whilst there was a small decrease is signal output following PE-PEG inclusion (+ 18 ± 1.4 pA without and + 16 ± 1.5 pA with the copolymer), illumination of a copolymer-containing photosensory bilayer generated signals above the 1.0-pA threshold confirming that CM-aR3 proteins functionally inserted into the membrane (YG light, 550 and 592 nm, 15 ± 4.5 mW, Fig. 3.36b-c).

These preliminary investigations demonstrate the potential use of block-copolymers in stabilising the synthetic neuron without compromising light-powering. Further work might be done to find the optimum concentration of PE-PEG and perhaps explore the use of other copolymers.

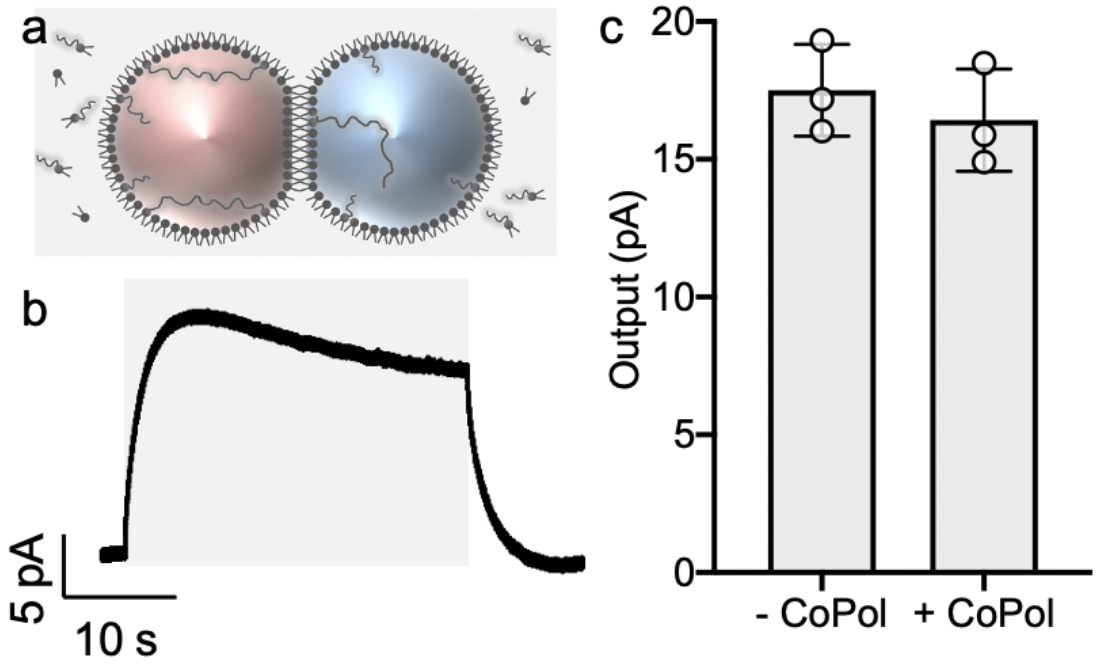


Figure 3.36: CM-aR3 pumps protons across a copolymer-containing bilayer. **a,** Schematic of photosensory module containing lipid (DPhPC) and copolymer (PE-PEG) (see **Chapter 6** for methods). **b,** Signal trace recorded across a photosensory bilayer upon illumination (YG light, 490 - 608 nm with peaks at 550 and 592 nm, 15 ± 4.5 mW). Grey bars indicate when the light is on. **c,** Steady-state signal output recorded across a photosensory bilayer in the presence (+) or absence (-) or copolymer (mean ± SD, n = 3).

3.3 Conclusion

To enable the potential of bioelectronics to be realised, in particular for therapeutic applications, the stiff components of current devices must be replaced with more biocompatible alternatives. The synthetic neurons described in **Chapter 3** are a significant step in this direction. They are composed of soft biological materials (proteins, ionotronic hydrogels and aqueous droplets) and display comparable mechanical characteristics to living tissues. Inspired by nature, these synthetic neurons integrate several functions into a single device: rapid phototransduction, directional ion conduction (over biologically-relevant distances), synaptic neurotransmission and generation of functional outputs downstream. Whilst the mechanisms used in this electrochemical signalling differ from nature, the biomimicry is apparent. The experiments described here demonstrate the exciting potential light-powered synthetic neurons have in next-generation soft bioelectronics.

4

A Synthetic Nerve

Here, parallel transmission of discrete signals is achieved by bundling multiple photosensory synthetic neurons into a bioinspired synthetic nerve. First, patterned sensory information is propagated along neighbouring axons with spatiotemporal resolution. Then, the use of three photosensory pumps for varied signal initiation is demonstrated. Powered by light, these patterned synthetic nerves are a valuable contribution to the development of next generation soft bioelectronics. For instance, a single neural device has the potential to locally and precisely deliver a combination of electric, ionic and molecular therapeutics to cells upon remote activation (Fig. 4.1). Accordingly, this chapter also includes a rudimentary demonstration of how similar synthetic nerves might be interfaced with living tissues to manipulate the bioelectric signals that underlie many cellular behaviours.

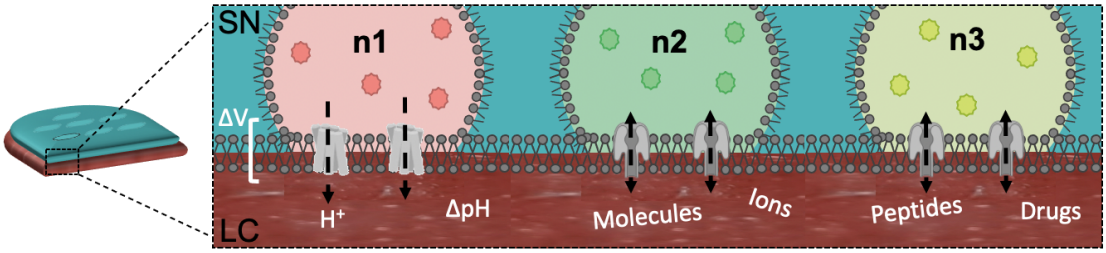


Figure 4.1: Hybrid tissue. A patterned synthetic nerve (SN) sends multiple (electrical, ionic or molecular) signals to living cells (LC): either through protein pumps (n1) or pores (n2,n3). Signals might even move both ways enabling the synthetic nerve to sense and respond to cellular demands.

Acknowledgement

Design and construction of the synthetic nerve was led by the author and any assistance is indicated in the text. The author would like to thank Dr Vanessa Restrepo Schild (**V.R.S**) for helpful discussions and assistance with the manufacture of the nerve cast and set-up of the multi-channel recordings. The author would again like to acknowledge Dr Javier Vinals (**J.V**) and Idil Cazimoglu (**I.C**) for protein preparation. The preliminary experiments presented on hybrid tissue formation were done in collaboration. Dr Vanessa Restrepo Schild (**V.R.S**) led the work involving interfacing CM-aR3 with living cells, performing and analysing the calcium fluctuation experiment; the cells were grown by Dr Linna Zhou (**L.Z**, Bayley Group, University of Oxford).

Publication

The work described in this chapter forms part of a publication currently being written up.

- **Hoskin, C.E.G.**, Restrepo Schild, V., Vinals, J., and Bayley, H. *Parallel transmission in a Synthetic Nerve.*

4.1 Introduction

4.1.1 Patterning

In biological tissues, patterning plays an important role in function. The 3D spatial arrangement of the cells within each tissue reflect its specific role. Accordingly, the construction of biomimetic systems must employ patternable materials in order to recapitulate these functions.

One approach used to fabricate biomimetic structures is patterned droplet networks (as discussed in **Chapter 1**). Here, aqueous compartments ("synthetic cells") are connected via functionalised lipid bilayers and assembled into networks ("synthetic tissues"). There are several attributes of droplet networks which make them a good soft material for the construction of bioinspired structures. Firstly, the versatility of the internal compartments permits a single structure to include multiple types of aqueous droplet, patterning for function. For instance, by spatially arranging droplets based on their internal contents, networks were capable of gripper-like functions and could perform defined shape changes after formation[50,92]. Moreover, living (eukaryotic and prokayotic) cells have been encapsulated within droplets[103,308,309]. The organisation of biological systems was emulated by patterning these cell-containing droplets into predetermined three-dimensional (3D) architectures. Alternatively, droplet compartments might include a myriad of proteins (pumps, channels and pores) which can insert into the (single) interconnecting lipid bilayers and facilitate inter-droplet communication. Typically proteins are incorporated into the interface directly from solution[31,40,44,50], but droplets can include the biomolcular machinery required for *in situ* protein synthesis[27,53]. Patterned networks have even been shown to function in an aqueous environments[50,63,102,103]. The incorporation of membrane proteins within these droplet networks enabled communication between internal compartments, and with the external environment. Within droplet networks, patterning can be achieved with single droplet resolution[40,53], enabling sophisticated structures to be fabricated. A number of functionalities have been achieved in networks following

the precise placement of communicating droplets: power generation, light sensing, wave rectification and biocomputation[44,49,310]. Another useful feature of droplet systems is their scalability; the size of the individual droplets and the overall structure can be adjusted. Technological advances have enabled functional networks to be formed at high throughput by using microfluidics or 3D printing. In this way thousands of droplet compartments might be patterned enabling highly sophisticated synthetic structures to be built.

A number of other techniques e.g., optofluidics[311], 4D biomimetic printing[264] and photolithography[108,271] have also been successfully used in material patterning, forming functional (bioinspired) structures.

4.1.2 Synthetic nerves

The primary function of the nervous system is communication; it gathers, processes and conveys information in a rapid, directional manner. Bioinspired synthetic nerves have been developed to facilitate communication in synthetic systems.

Droplet networks have been used to emulate nerves in their simplest form. As discussed above, patterned aqueous compartments can communicate with one another via membrane proteins embedded within the interconnecting lipid bilayers. Bioelectrical communication was demonstrated in 3D droplet networks, taking advantage of the patterning capabilities of the droplet printer. By positioning protein pore-containing droplets in a line, an ion-conducting pathway was introduced into the (otherwise insulating) network. Bioelectrical signals were carried along the defined pathway (via ion flux through the pores) upon the application of a potential (by external hardware)[40,50]. A method for temporal control over formation of the conducting pathway was also developed[52]. Remote activation (with light) initiated pore expression within patterned droplets which then incorporate into specific bilayer interfaces and mediated rapid, directional communication within the (tethered) droplet network[52]. In addition, chemical signalling across neural-like pathways has also be achieved. Chemical messengers (slowly) diffused either directly through the lipid bilayers[64] or via transmembrane protein-pores[65,93]. Imitating biological

neural networks, these chemical messengers then initiated outputs in the receiver compartments (Fig. 3.3). Internal communication through droplet networks has also been demonstrated using chemical waves (Fig. 1.7)[66,67]; this is faster than relying on molecular diffusion. To some extent, droplet networks have successfully been used to emulate biological nerves. However, as of yet no droplet-based synthetic nerves have been built which communicate via electrochemical events. In addition, opportunities exist to expand methods for controlling signal initiation and for coupling the propagated signals to notable outputs within a single structure.

Biomimetic synthetic nerves have also been made using flexible electronics. One artificial nerve was built which sensed pressure stimuli, transmitting this information to a biological (cockroach) nerve, triggering a response (Fig. 3.5)[248]. This example demonstrated effective communication between a synthetic structure and living tissue. However, applications of this artificial nerve are restricted by the material mismatch with soft living tissue and its inability to send chemical transmitters[312].

4.1.3 Hybrid Tissues

An exciting application of soft synthetic structures is in the formation of hybrid tissues; a patterned system containing communicating synthetic and living components. Previously, living cells have been incorporated into individual compartments and patterned in 3D[103,308,309,313,314]. In the future, functional hybrid structures might be constructed by including living cells in selected compartments and synthetic elements in others: imitating, or even elaborating upon, nature. Of considerable interest is the prospect of integrating synthetic materials and biological tissues, with potentially important applications in medicine. Progress has been made in this area with synthetic cells releasing therapeutic agents directly at the disease site[315]. Efforts have also been made in developing soft materials to send patterned electrical signals for targeted stimulation of living cells[31]. However, there are concerns surrounding the lifetime of synthetic materials in living organisms and more work into their possible interactions with the immune system is needed in order for the potential of hybrid tissues to be realised.

4.2 Results

4.2.1 Design of a synthetic nerve

In biology, a small bundle of patterned nerve fibers (enclosed in a tubular layer of connective tissue) is called a fascicle; assemblies of fascicles form larger nerve bundles (Fig. 3.7, 4.2). A bioinspired synthetic nerve (composed of a single fascicle) was designed which imitated neurobiological architectures and was biomimetic in its function.

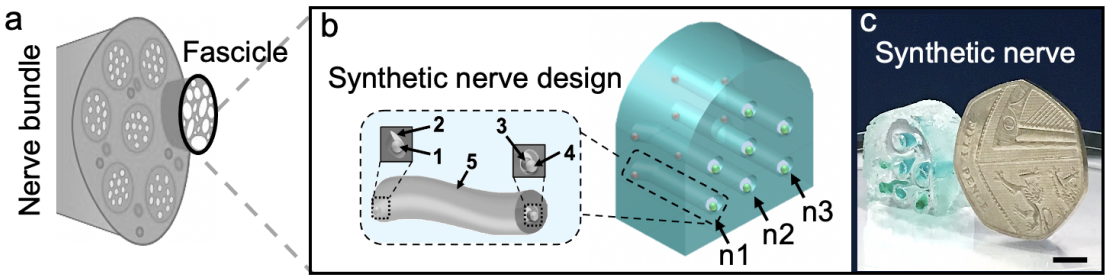


Figure 4.2: Synthetic Nerve Design. **a,** Schematic of a biological nerve bundle composed of multiple fasicles. **b,** AutoCAD design of a synthetic nerve (teal). The nerve is composed of seven hydrogel axons (dotted box, b2) enclosed within an elastomer scaffold (b5). The three neurons which will be later patterned at indicated n1, n2 and n3. At each end are aqueous droplets (200 nL, b2-4) **c,** Photograph (taken with an iPhone) of the synthetic nerve (in air). A 50 pence coin is added for comparison, scale bar = 10 mm. Figure is adapted from the author's manuscript in progress[193].

Seven (hydrogel) axons (characterised in **Chapter 3**) were patterned (in 3D) into an elastomeric nerve scaffold. The diameter of each synthetic hydrogel axon was 1 mm; comparable in size to those of the giant squid (up to 1.5 mm) but larger than human axons (the widest (Betz cells) are up to 0.1 mm)[303]. Importantly, the elastomeric material electrically insulated the conducting hydrogel axons without compromising their flexibility (see **Chapter 3**, Fig. 3.31, 3.30). Consequently, it was possible to transmit distinct bioelectrical signals along parallel axons without any cross-talk. Transmission was powered (at one end of the axon) by photochemically-driven proton pumps and mediated (at the other end) by ion-conducting protein pores (see **Chapter 2 and 3**). Whilst signalling was rapid and directional, and carried by ions, the mechanism of transmission differed from nature (no action potential was generated, Fig. 3.19). Remotely powered by a light stimulus, the

synthetic nerve was tetherless, flexile and composed of entirely soft materials (Fig. 4.2). Further, the synthetic nerve was highly patternable due to its modularity. In future nerves, each element might be readily interchanged for any natural or unnatural component.

4.2.2 Constructing a synthetic nerve

The synthetic nerve was built systematically using a bottom-up synthetic biology approach. First, the elastomeric scaffold (which formed the bulk of the structure) was made. The silicone-based material was prepared as described in **Chapter 3**: the monomer and curing agent were mixed (10:1 ratio), degassed (30 min) and poured into the bespoke cast (see **Chapter 6** for Materials and Methods). This (resin) cast (constructed with assistance from **V.R.S**) contained three straight and four bent pillars; however future casts could be designed to have pillars of any size, shape or number (Fig. 6.1f). Once cured and cooled the elastomeric scaffold was removed from the cast. Next, the hydrogel axons were added to the structure by pipetting hot agarose (2% high gelling in Solution D) into the seven tubular cavities. The synthetic axons were made from hydrogel because it was flexible, easily shaped and enabled greater signal transmission than droplet-based axons (see **Chapter 3**, Fig. 3.14, 3.17). Then, the synthetic nerve (elastomer scaffold with 7 conducting axons) was placed in a (lipid-in-oil filled) chamber; for now, the synthetic nerves can only function in a lipid-containing oil environment. Finally, protein-containing aqueous droplets (200 nL) were interfaced with the synthetic axons forming a functional lipid bilayer into which protein inserted vectorially. Photochemistry of light-driven proton pumps (expressed by **J.V**) initiated bioelectrical (ionic) signals at one end of the synthetic axons; at the other end of each hydrogel fibre, the interface contained ion-conducting protein pores (monomeric αHL, expressed by **I.C**). For patterning in 3D, the aqueous droplets must be located within the elastomeric scaffold. A lid was designed (Fig. 6.1f) to prevent the hydrogel from filling the cavities completely, leaving a 1-mm gap for the droplet to be positioned. Using

this systematic approach for synthetic nerve assembly means that any damaged components can be easily replaced during formation.

4.2.3 Stimulus patterning

The synthetic nerves described in this thesis used an external (light) input to initiate signalling. The simplest way in which signalling might be patterned was to expose each photosensory axon terminal to a distinct periodicity of the light stimulus.

A synthetic nerve was built in which each 10-mm hydrogel axon could be separately addressed, and the outputs individually measured. For simplicity, only the three bottom neurons were used (n1-3, Fig. 4.2); the droplets were positioned outside of the elastomeric scaffold to facilitate electrode attachment. It should be noted that these external tethers were not required for function.

Details on the experimental set-up can be found in **Chapter 6** (Fig. 6.2). Briefly, the synthetic nerve-containing chamber was filled with lipid-in-oil and placed in the centre of the stage directly under the LED bundle, inside a Faraday cage. The photosensory end of the nerve was then surrounded with light-blocking sheets (made from waterproof black card) to permit discrete stimulation of neighbouring axons without interference. Responses to light were measured (independently) using Ag/AgCl electrodes connected (via a Terrapin probe holder) to a multichannel amplifier (Triton+, Tecella LLC, positioned in an adjacent Faraday cage). With the aid of a stereomicroscope, electrodes were carefully positioned at the hydrogel axon terminals. Droplets (200 nL) were then pipetted directly onto the electrodes (following a 5 - 30 minutes incubation in a separate chamber) forming bilayers with the hydrogel axons. Each photosensory bilayer was illuminated using a distinct fibre-coupled LED (490 - 608 nm, peaking at 550 and 592 nm, 15 $\pm$ 4.5 mW output, Mightex, WFC-H7-0560). The LED of axon 1 (n1, Fig. 4.2) was controlled from a computer with the manufacture's software (Mightex) using the strobe setting with 15 s light pulses (at 0.05 Hz). The LEDs of axons 2 (n2) and 3 (n3) were controlled from separate waveform generators (Rigol, DG822) with light pulses of length 1 s and 20 ms at 0.1 and 0.06 Hz respectively.

By using a multi-channel amplifier for recording, the signals transmitted along the parallel axons were detected simultaneously. Following the concurrent application of different stimulatory (YG light) patterns to three parallel axons, distinct signals (which mirrored the patterns applied) were recorded (Fig. 4.3). Light pulses of 15 s, 5 s, and 1 s (at 0.05, 0.1 and 0.06 Hz, respectively) were observed (in parallel axons) with steady-state outputs above the 1.0-pA threshold: + 25 ± 1.2 pA, + 20 ± 0.8 pA and + 13 ± 0.5 respectively (mean ± SD, n = 3, Fig. 4.3). Whilst simple, this experiment neatly demonstrated that parallel transmission (of distinct signals) can be achieved in a single synthetic nerve.

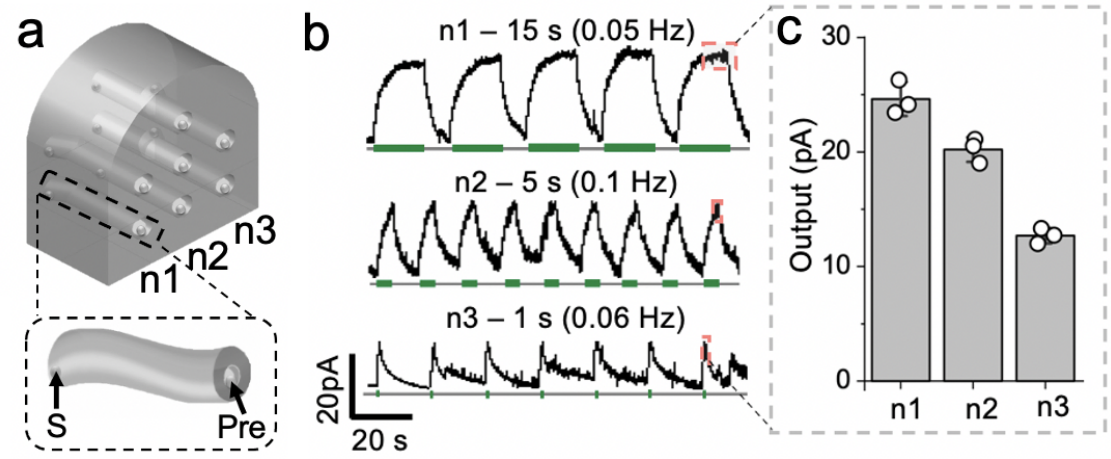


Figure 4.3: Light-patterned signal transmission. **a,** Design of a synthetic nerve: seven hydrogel axons are encased within an elastomer sheath. The three axons that will be stimulated in patterns are labelled (n1-3). Zoom shows an elastomer-encased synthetic hydrogel axon with a sensory droplet (S) and presynaptic droplet (Pre) at either end. Ag/AgCl electrodes (not shown) enable signal detection (recording electrodes in the sensory droplets and a common ground electrode in the presynaptic droplets, see **Chapter 6** for details). **b,** Traces recorded along three neurons n1-3 stimulated with different light pulses (15 s (0.05 Hz), 5 s (0.1 Hz) and 1 s (0.06 Hz), respectively (490-608 nm with peaks at 550 and 592 nm, 15 ± 4.5 mW). Steady-state signal indicated by dotted box (pink). **c,** Steady-state output (n = 3, mean ± SD) recorded simultaneously in a synthetic nerve. Experiment was performed with assistance from **V.R.S**. Figure adapted from the author's manuscript in progress[193].

4.2.4 Photosensory droplet patterning

At the core of the synthetic nerve was the photochemistry of microbial proton pumps: simple, electrogenic proteins. Embedded within the photosensory bilayer,

they transduce a physical stimulus (light) into a bioelectrical (ionic) signal, powering the synthetic nerve in a tetherless manner.

Photosensory modules

Chapter 2 explored the proton pumping activity of two photoactive membrane proteins: bacteriorhodopsin (bR) and archaerhodopsin-3 (aR3). Both proteins were expressed in their native archaeal hosts and purified (purple (PM) or claret (CM)) membrane fragments (confirmed by AFM[186,196]) were then incorporated into the bilayers. The action spectra of CM-aR3 and PM-bR show that the largest signals were generated in response to yellow-green light (Fig. 4.4). Both CM-aR3 and PM-bR generated positive signals (i.e. protons flowed out of the recording-electrode-containing photosensory droplets) upon illumination (490 - 608 nm, with peaks at 550 and 592 nm, 15 ± 4.5 mW) suggesting that they inserted N-terminus first (with their extracellular faces exposed to the axon). The average steady-state signal observed across a CM-aR3-containing bilayer was +19 ± 3.9 pA (mean ± SD, n = 10 DIBs using protein from the same batch); with a maximum of +25 pA (Fig. 2.15). The output of a CM-aR3 photosensory bilayer was ≈ 2-to-3 fold higher than those containing PM-bR (+6.9 ± 2.3 pA, n = 10 DIBs using protein from the same batch, Fig. 2.13), potentially reflecting the faster photocycle of CM-aR3[296], but might also indicate enhanced incorporation into the membrane. It should be noted that the signals recorded within the synthetic nerve, are significantly smaller than those reported following transfection into animal neurons[121].

Interestingly, when archaerhodopsin-3 (aR3) was heterogeneously expressed in *Escherichia coli* (EC) negative signals were observed upon illumination (i.e. protons flowed into the recording-electrode-containing photosensory droplets). EC-aR3 must insert into the (DPhPC) bilayer in the opposite orientation to CM-aR3, perhaps due to its monomeric state, altered lipid composition, the lack of the bacterioruberin carotenoid (found in the CM) or the presence of a His-tag (see **Chapter 2**). The magnitude of this signal (-6.1 ± 1.4 pA) was ≈ 2-to-3-fold lower than those generated by CM-aR3, but comparable to those observed using PM-bR (Fig. 2.28). Moreover,

the action spectrum of wild-type EC-aR3 closely resembled those of CM-aR3 and PM-bR, peaking in response to yellow-green light (Fig. 4.4).

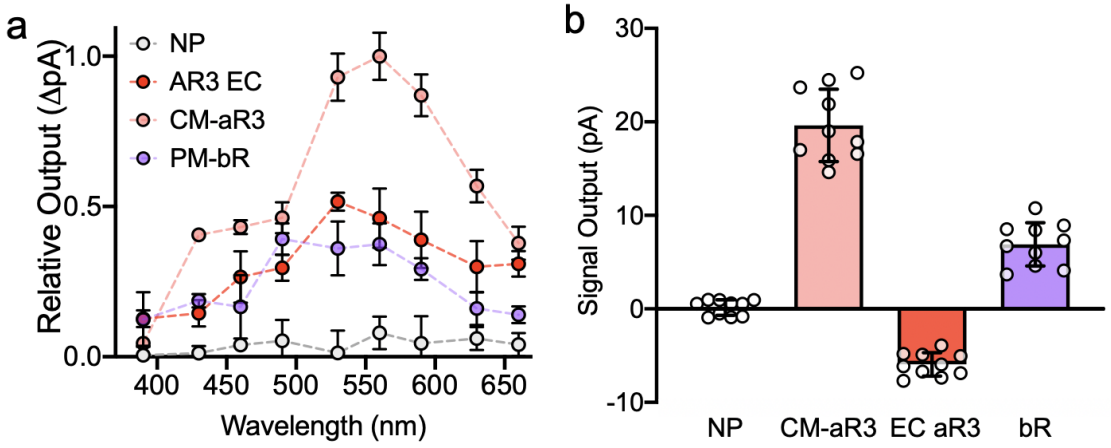


Figure 4.4: Photoactivity of three proton pumps. **a,** Action spectra recorded across a DIB containing no protein (NP, grey), CM-aR3 (pink), EC-aR3 (red) or PM-bR (purple). Steady-state signals are plotted relative to the maximum output of a CM-aR3 DIB (mean ± SD, n = 3 DIBs, LED output is 2.0 ± 0.4 mW at each wavelength). **b,** Steady-state signals recorded across a DIB containing no protein (NP, grey), CM-aR3 (pink), EC-aR3 (red) or PM-bR (purple) upon illumination with YG light (490 - 608 nm, with peaks at 550 and 592 nm, 15 ± 4.5 mW, mean ± SD, n = 3). Figure adapted from the author's manuscript in progress[193].

In addition, directional (light-driven) proton pumping was observed in an electrode-free manner using the fluorescent pH-reporter pyranine (100 μM, in the absence of buffer); at higher pH values pyranine fluorescence intensifies (2.10). Photosensory modules (with dye in both droplets) were first imaged with an epifluorescence microscope to obtain the value of the initial fluorescence intensity. The module was then continually illuminated overnight (YG light, 490-608 nm with peaks at 550 and 592 nm, 15 ± 4.5 mW). For CM-aR3 and PM-bR, pyranine dye present in the photosensory droplets (S) increased in fluorescence as protons were pumped across the bilayer (upon illumination with YG light). These changes in fluorescence intensity (after overnight illumination) were analysed and the pH difference quantified from a calibration curve (Fig. 2.10). The output for the CM-aR3 and PM-bR modules reflected the differences in pumping activity: +0.3 ± 0.0 pH and +0.1 ± 0.0 pH respectively (mean ± SD, n = 3). In contrast, EC-aR3

photosensory droplets decreased in fluorescence (corresponding to a reduction in pH of -0.1 ± 0.0) when the bilayer was continuously illuminated overnight (and protons were pumped in). For the interfacing (axon) droplets, the inverse pattern was observed: outputs of -0.3 ± 0.0 pH (CM-aR3), -0.1 ± 0.0 pH (PM-bR) and +0.1 ± 0.0 pH (EC-aR3) were detected (mean ± SD, n = 3).

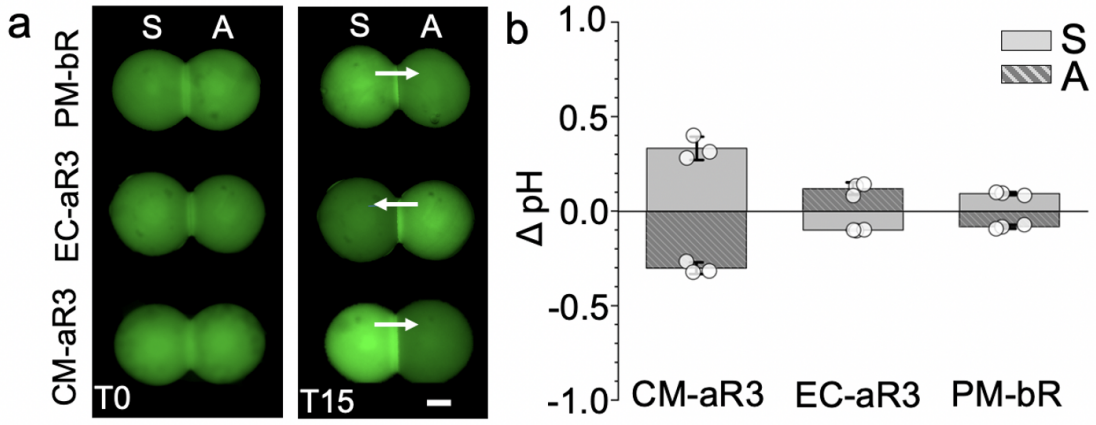


Figure 4.5: Photoactivity of three proton pumps. a, Photosensory modules were made with the photosensory droplets (S) containing either CM-aR3, EC-aR3 or PM-bR. Epifluorescence microscopy images were taken before (T0) and after (T15) illumination (YG light, 15 ± 4.5 mW). Scale bar = 200 μm/ **b,** Bar chart of change in fluorescence of each droplet after illumination (mean ± SD, n = 3). Figure adapted from the author's manuscript in progress[193].

Since the photoinduced signal generated across a droplet bilayer is dependent upon the microbial protein embedded within it, patterning the photosensory bilayers will enable a single stimulus (YG light) to generate heterogeneous signals within a synthetic nerve.

Photosensory droplet patterning

To demonstrate this patterning, a synthetic nerve was then designed and built in which each photosensory bilayer was packed with different proton pump: CM-aR3, EC-aR3 or PM-bR. Pyranine dye (100 μM) was added to the photosensory and presynaptic droplets (in the absence of buffer) at both terminals of three bottom 10-mm hydrogel axons.

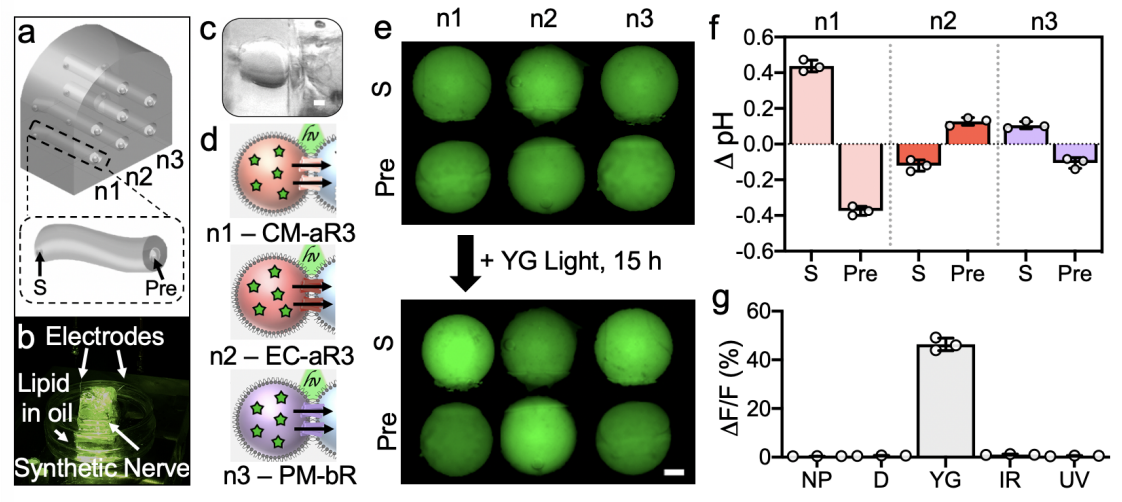


Figure 4.6: Photoreceptor patterning enabled transmission of diverse signals. **a,** Design of a synthetic nerve: seven hydrogel axons are encased within an elastomer sheath. The three axons that will be stimulated are labelled (n1-3). Zoom-in shows an elastomer-encased synthetic hydrogel axon with a sensory droplet (S) and presynaptic droplet (Pre) at either end. **b,** Photograph of a synthetic nerve in lipid-in-oil (oil covers neurons 1-3). Electrodes are added to the droplet for signal recording. **c,** Photograph of a sensory bilayer in lipid-in-oil. Scale bar = 200 μm. **d,** Schematic of the patterned photoreceptors containing CM-aR3 (n1), EC-aR3 (n2) or PM-bR (n3). **e,** Epifluorescent images (minus background) of the droplets before (top) and after (bottom) illumination (15 h, YG light, 490 - 608 nm with peaks at 550 and 592 nm, 15 ± 4.5 mW). All droplets contain 100 µM pyranine (Solution C, in the absence of buffer) with the photosensory droplets (S) also containing 0.15-0.25 mg mL-1 of light-sensitive protein (CM-aR3, EC-aR3 or PM-bR) and the presynaptic droplets (Pre) containing 50 nM αHL. **f,** Changes in droplet pH (calculated from the calibration curve, Fig. 2.10) of each neuronal pathway (see 'a', n = 3 nerves with 3 technical replicates). **g,** Percentage change in fluorescence intensity of the CM-aR3 photosensory droplet when illuminated with YG, IR (722 nm, 16 ± 5.0 mW) or UV (367 nm, 15 ± 3.9 mW) light or kept in the dark (D) or in the absence of CM-aR3 (NP) (n = 3). No electrodes were used. Figure adapted from the author's paper[193].

Powered by light (490-608 nm with peaks at 550 and 592 nm, 15 ± 4.5 mW), the patterned synthetic nerve functioned continuously overnight (15 h). Three distinct outputs were simultaneously observed by changes in droplet fluorescence intensity; the corresponding pH values were computed using the calibration curve (Fig. 2.10). Photosensory droplet pH (S, 0.15 - 0.25 mg mL^{-1} rhodopsin) increased in the cases of CM-aR3 (n1) and PM-bR (n3), by +0.4 ± 0.0 and +0.1 ± 0.0 pH respectively; however, pH decreased in the case of EC-aR3 (n2) by -0.1 ± 0.0 pH (mean ± SD, n = 3) (Fig. 4.6). At the other end of hydrogel axons, the inverse pattern was

observed. For the CM-aR3 (n1) and PM-bR (n3) photosensory synthetic neurons, the presynaptic droplet pH decreased by -0.4 ± 0.0 and -0.1 ± 0.0 pH respectively, whilst it increased by +0.1 ± 0.0 pH in the presynaptic droplet of the EC-aR3 (n2) synthetic neuron (mean ± SD, n = 3) (Fig. 4.6). By using different sensory proteins to initiate signalling, it was possible to transmit different signals along the parallel axons of a wireless synthetic nerve.

4.2.5 A hybrid tissue

Built from soft, patternable biomaterials, light-powered synthetic nerves might lead to a new generation of medical implant, delivering a number of therapeutic agents to cells in response to external signals: in the form of molecules, ions or electric fields. For this reason, their potential is not restricted to interactions with electrically excitable cells.

Interface design

In theory, either end of the synthetic nerve (SN) could be interfaced with living cells (LC) (Fig. 4.7). Firstly, the photosensory droplet might form the synthetic-biological junction in which photoactive proton pumps insert. Remote activation (with light) of the synthetic nerve would pump protons across the interface and by doing so send multiple biological cues: as ionic signals, pH changes, local fields and electrochemical membrane potentials (Fig. 4.7). A patterned synthetic nerve could send these cues with spatiotemporal resolution, regulating a number of key phenomena in living systems e.g., cell differentiation or tissue regeneration. Alternatively, the presynaptic droplets might communicate with living cells via (αHL) protein pores embedded in the interface (Fig. 4.7). These transmembrane pores can facilitate the delivery of a number of ions (not just protons) sending bioelectrical cues (e.g., signals and potentials) to cells. Further, small molecules can be released from presynaptic droplets (Fig. 3.26). The droplets of a synthetic nerve might be patterned (in 3-dimensions) to include any therapeutic agent of

interest (e.g., pharmaceuticals, transcription factors, neurotransmitters) forming a multifaceted neural device.

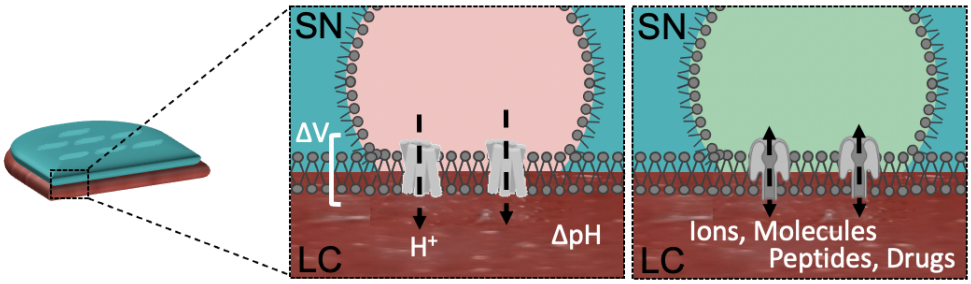


Figure 4.7: Hybrid tissue design. Schematic of a potential hybrid tissue formed between a synthetic nerve (SN, teal) and living cells (LC, red/brown). Zoom shows the interface of the photosensory (left, pink) and presynaptic (right, green) droplets with the living cells (LC, red/brown). Protein inserts into the bilayer formed at the interface. Photosensory droplets pump ions (protons) across the bilayer meaning they can send signals as potentials (ΔV), currents or pH changes (ΔpH). Presynaptic droplets can send signals as ions or a number of molecules e.g. pharmaceuticals (drugs).

In its simplest form, a hybrid tissue could be formed (in a laboratory environment) by placing the synthetic tissue directly on top of the living cells (cultured in a dish). For the initial hybrid tissue experiments (led by **V.R.S**) a second soft, synthetic tissue (henceforth known as a photoreceptor array) was built which was tetherless and powered by light (analogously to the synthetic nerve). This synthetic tissue was based on a droplet-based light sensor previously constructed[31]. Here, a (100 μm thick) hydrogel scaffold was populated with patterned CM-aR3 photosensory droplets (144 droplets, 150 pL, characterised in **Chapter 2**)[31,193]. Astrocytes were chosen for the hybrid tissue since pH and bioelectrical cues are known to initiate observable astrocytic calcium events[306,316].

Proton pumping across a hybrid tissue interface

First, the photoactivity of CM-aR3 was monitored at a hybrid tissue interface. A photosensory droplet (200 nL, 0.15 – 0.25 mg mL^{-1} CM-aR3, Solution B, Fig. 4.8a2) was encapsulated in a lipid monolayer by pipetting it into a lipid-in-oil solution (10 mg mL^{-1} DPhPC in 35:65 hexadecane, silicone oil). An astrocyte-containing droplet (200 nL, human cortical astrocytes in 50:50 matrigel, cell media, Fig. 4.8a1)

was formed in the same manner (cells were trypsinised (by **L.Z**) from a 2D culture that had achieved 90% confluency). After ≈ 15 minutes the droplets were brought into contact; DIB formation was confirmed by measurement of the capacitance (>20 pF, application of a triangular voltage waveform, ±15 mV, 30 s peak-to-peak).

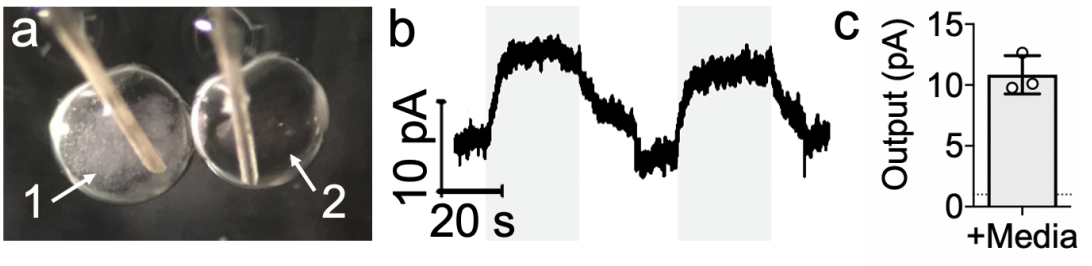


Figure 4.8: CM-aR3 sends photosignals to astrocyte-containing droplets. a, A DIB formed between a photosensory droplet (a1, 0.15 - 0.25 mg mL^{-1} CM-aR3, Solution B) and a cell droplet (a2, corticol astrocytic cells in 50:50 cell media, matrigel). Ag/AgCl electrodes are inserted inside each droplet; the ground electrode is in the cell droplet (a2). **b,** Signal trace recorded across the DIB in 'a' upon illumination (YG light, 490 - 608 nm with peaks at 550 and 592 nm, 15 ± 4.5 mW). Grey bars indicate when the light is on. **c,** Stable signal output (mean ± SD, n = 3) recorded across a photosensory bilayer when interfaced with cells.

Positive signals (> 1.0-pA theshold, set to indicate protein activity) were recorded across the hybrid tissue interface upon illumination (Fig. 4.8 b, YG light, 15 ± 4.5 mW) confirming functional protein insertion into the bilayer. In these experiments the recording electrode was always inserted into the photosensory droplet and the ground electrode in the astrocyte droplet (Fig. 4.8).

Proton-sensitive response in astrocytes

Having established that CM-aR3 functionally inserted at the hybrid tissue interface, the effect of proton pumping on the (human cortical) astrocytes was then explored. Astrocytes are known to respond to physiological decreases in pH with transient elevations in intracellular calcium[306,316]. A 2D layer of human cortical astrocytes (in cell media, grown by **L.Z**) was loaded with a calcium detection reagent (Fluo-4 Direct). Acid (1 μL of HCl, calculated to change the pH by 1) was then added (using a pipette) to the cell media (with an initial pH of 7.35), initiating a calcium

elevation wave which propagated across the cell culture (Fig. 4.9). This experiment demonstrated that when signals (protons) were delivered to cells (human astrocytes), an output was produced (the cells increased calcium signalling). However the response was neither localised nor patterned, instead a wave passed across the entire tissue (Fig. 4.9).

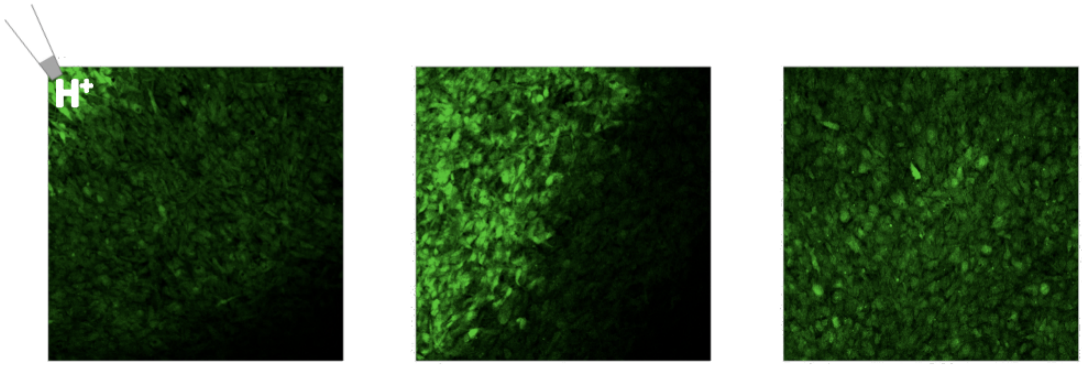


Figure 4.9: Effect of acidifying the cell environment of astrocytes. a, 1 μL of HCl (calculated to decrease the pH by 1) was added (from a pipette) to a well containing a 2D layer of cortical astrocytes in cell media. A calcium elevation wave propagated across the field-of-vision. Here, calcium elevation was not localised or patterned. Experiment was performed in collaboration with **L.Z** and **V.R.S**. The figure is adapted from a manuscript in progress[100].

CM-aR3 modulates astrocyte activity in a hybrid tissue

The final step involved modulating the activity of human astrocytic cells using the synthetic photoreceptor array (Fig. 4.10c). Here, CM-aR3 photosensory droplets were interfaces with astrocytic cells. Upon illumination, protons would be pumped across the interface bilayer and into the cell environment.

The synthetic tissues described in this thesis required a lipid-in-oil environment for function. However, in order to form a hybrid tissue, the synthetic tissues must be transferred to a physiological (aqueous) environment. For this, **Dr Vanessa Restrepo Schild** developed a slow condensation method (unpublished). The photoreceptor array was made in a bespoke container and a coverslip was then (partially) placed over the top. The container was then sealed in a petri dish containing the biofluid and kept at 4 °C overnight (15 h); as biofluid vapour condensed on the coverslip it (slowly) fell onto the synthetic photoreceptor array

displacing (almost all) the oil. Some components of the biofluid were added (using a pipette) after the condensation process to minimise droplet coalescence (from instability). In this way, the CM-aR3 droplets formed two bilayers: one with the hydrogel scaffold and another with the biofluid.

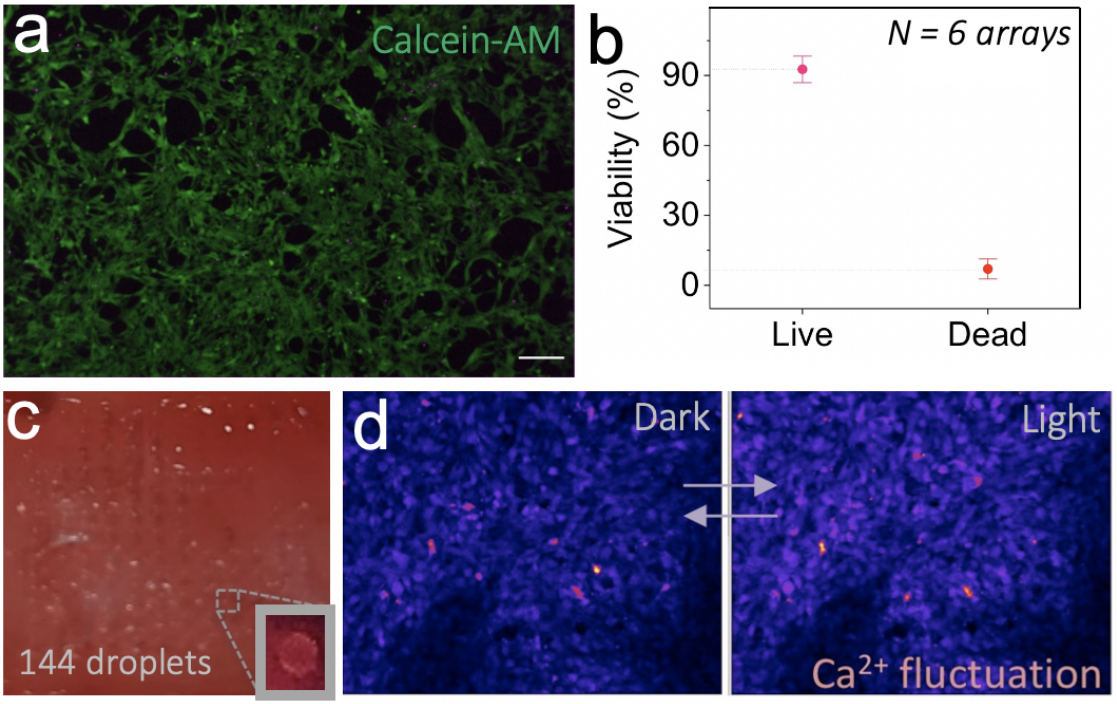


Figure 4.10: Light-driven proton pumping modulates astrocyte behaviour a, Micrograph of a 2D culture of human cortical astrocytes labelled with calcein-AM (live cells) and propidium iodine (dead cells). **b,** Interval plot of cell viability at 20 minutes showing 94% of the cells are labelled with Calcein-AM (2898 cells, n = 6). **c,** Photographs of an array on top of the cell culture. Zoom-in shows a single photosensory droplet. **d,** An array of aR3 photosensory droplets is placed on top of a confluent culture of primary cortical astrocytes loaded with Fluo4 Direct for calcium detection. Photographs of the Z-projection of the standard deviation (of a live-imaging stack) show that the light-driven proton pumping by CM-aR3 modulated the cell activity: increasing calcium signalling (brighter). Illuminated with yellow-green light (490-608 nm with peaks at 550 and 592 nm, 15 ± 4.5 mW). Experiments were performed by **V.R.S** and **L.Z** and the figure adapted from a manuscript in progress[100].

Dr Vanessa Restrepo Schild then (carefully) transferred the synthetic photoreceptor array to the astrocyte cells (confluent 2D culture grown by **L.Z**); live/dead staining confirmed that most (≈94%) of the cells survived the interfacing process (Fig. 4.10a,b). Next, the hybrid tissue was stimulated with pulses of green light (561 nm light at 15% output) and CM-aR3 pumps (in the synthetic tissue) delivered

protons to the living cells. Proton modulation of astrocyte activity was observed by increases in calcium signals (Fig. 4.10d). **Dr Vanessa Restrepo Schild** observed no changes in calcium fluctuations when the hybrid tissue was illuminated with blue (488nm, not CM-aR3 activating) light demonstrating that photochemically-driven proton pumping (from the synthetic tissue) was responsible for the output seen in the living cells (data not shown). Ongoing experiments and data analysis of the astrocytic response to pH are being carried out in collaboration with **Dr Vanessa Restrepo Schild** since preliminary results were varied and depended upon factors such as the cell batch or passage number. Nonetheless, this hybrid tissue experiment demonstrated photoinduced communication between a synthetic and living tissue; the ion flux generated by CM-aR3 photosensory droplets was sufficient to induce a response in human astrocytic cells. Whilst significant work is still needed to optimise signalling in hybrid tissues, this preliminary experiment highlights the potential of soft bioelectronic devices (such the synthetic nerve) in medicine. For such applications, the ability of patterned synthetic tissues to locally and precisely administer treatment (in the form of electric, ionic and molecular signals) will be extremely advantageous.

4.3 Conclusion

To enable the potential of soft bioelectronics to be realised, there is demand for devices capable of tetherless powering. The bioinspired synthetic nerves detailed in this thesis could have a notable impact in this area. Built using soft biomaterials, they employ external (light) inputs to drive signalling with spatiotemporal resolution. The parallel transmission of discrete signals was achieved by patterning multiple conducting fibres in 3-dimensions. Motivated by their potential in medicine, a simple hybrid tissue was built capable of photoinduced communication. Following remote stimulation of the hybrid tissue, (ionic) signals were sent, from the synthetic tissue, to the living (human) cells which reacted to the signals with a functional response. Similar synthetic nerves have the potential to deliver on the promise of bioelectronic medicine: locally and precisely delivering therapeutics to cells.

Interestingly, since each element can be patterned a plethora of potential inputs and outputs might be included. Moreover, future synthetic nerves need not be restricted by attempts to strictly mimic nature.

5
Future work

Soft, bioelectronic devices are at the forefront of medicine, computing and robotics. However, current technologies are restricted by their demand for stiff external hardware for signal amplification and powering. The synthetic neurons and nerves developed in this thesis are a noteworthy step in this direction. These synthetic tissues were tetherlessly powered by light due to the inclusion of photochemically-reactive proteins (**Chapter 2**). Accordingly, remote stimulation initiated the rapid, directional transmission of electrochemical signals over centimetre distances (**Chapter 3**). By patterning multiple conducting pathways into a single device, parallel transmission of discrete signals was achieved (**Chapter 4**). Finally, a simple hybrid tissue was built in which the synthetic tissue sent signals to living cells initiating a response. These wireless, synthetic tissues are the first of their kind; using external inputs to transmit ionic, electrical and molecular signals. However, beyond the progress already described in this thesis, the current version of the device will need to be improved in order to successfully achieve the goals of soft bioelectronics. Prospective modifications to the light-powered, bioinspired synthetic nerve are now discussed.

5.1 Sensory transduction in a synthetic tissue

Sensory transduction is the process by which a neuronal cell converts a physical stimulus into a bioelectrical signal.

5.1.1 Enhancing photosensory module functionality

The synthetic tissues described in this thesis are powered by photochemically-driven proton pumps. They transduce light stimuli into bioelectrical signals.

5.1.1.1 Strategies to increase protein insertion

Since CM-aR3 photochemistry initiates signal formation, it is logical to suggest that higher number of proteins embedded within the bilayer will increase the output. A photosensory bilayer, formed between two 200 nL aqueous droplets, has an area of $\approx 10^{-7}$ - 10^{-8} m^2; large enough to host $\approx 10^9$ - 10^{10} proteins and generate signals of up to $\approx 10^6$ pA (See 'Theoretical considerations' in **Chapter 2**)[193]. However, the output of the photosensory bilayer (determined from electrical recordings) was orders of magnitude lower ($\approx 10^1$ pA) with approximately $\approx 10^5$ - 10^6 proteins functionally inserting[193]. Whilst the reasons behind the low protein insertion remain unclear, and could benefit from molecular simulations and computational modelling, there are several avenues which might be explored to enhance signal generation in the meantime.

- **Bilayer surface area** - Even if the sensory bilayer were tightly packed with protein, the total surface area remains too small to fit all the available protein in the photosensory droplet ($\approx$ 0.1 - 1.0 % can insert) (See 'Theoretical considerations' in **Chapter 2**)[193]. Consistent with the literature[40], in **Chapter 2** it was shown that a higher silicone oil content resulted in a larger interface area and, consequently, a greater signal output; however this was still insufficient to pack all available protein. Perhaps future devices might take inspiration from nature, imitating the highly folded membranes of the mitochondria or chloroplast[4]. Some attempts have been made to increase the surface area of

droplet interfaces, for instance creating a system where the bilayer can buckle and bend[59], but there still remains significant room for improvement.

- **Bilayer lipids** - One possible explanation for the low protein incorporation into the bilayer is that protein reconstitution is hampering insertion. The synthetic tissues described in this thesis use the exogenous (non-native) lipid DPhPC (1,2-Diphytanoyl-sn-Glycero-3-Phosphatidylcholine Phosphatidylcholine); using endogenous (native to the claret membrane) lipids might improve protein inclusion, photokinetics and oligomeric stability. Alternatively, the use of charged lipids might also improve insertion. This fusion technique[317] involves combining protein-loaded vesicles, containing charged lipids, with oppositely charged bilayers. Since these cationic and anionic lipids attract, it is possible that they may improve insertion efficiency as well as impart more control over protein orientation.

- **Bilayer curvature** - Another limitation may be that the protein micelle membranes semi-fuse to the bilayer and form a convex arrangement which modify its topology and hinder further protein insertion. Screening different bilayer curvatures may shed light on how best to address packing limitations in future synthetic tissues.

- **Protein orientation** - Perhaps protein insertion isn't restricted. It could be that CM-aR3 only has a slight preferential orientation; the signal detected would therefore be the difference between two almost equal but opposite signals. However, strategies used to control protein orientation of other microbial rhodopsins, e.g. fusing the hydrophilic moiety mVenus to ChR2 (unpublished experiments performed by **VRS**) didn't improve the output. Further, since positive signals were consistently generated when CM-aR3 was inserted from the recording-electrode side of the membrane (Fig. 2.16) this seems an unlikely cause. However, further investigation is required before it could be completely ruled out.

5.1.1.2 Alternative photosensory systems

A second strategy to increase power generation would be to replace CM-aR3 with light-driven proteins capable of generating greater bioelectric signals.

- **Photochemically-driven channels** - Light-driven proton pumps directionally translocate ions against large electrochemical gradients, making them a useful tool in light-powered synthetic tissues. However, CM-aR3 can only transport one proton across the bilayer per photon absorbed. One potential way in which the insertion challenges might be addressed is to substitute CM-aR3 for proteins which can transport greater numbers of ions. For instance, another class of microbial rhodopsin are the light-driven channels which, whilst dependent upon the electrochemical ion gradient, can flux numerous ions per photon absorbed[11]. Moreover, by replacing CM-aR3 with a photochemically-driven channel, fewer proteins would be required to insert into the sensory bilayer to generate signals sufficient for function ($\geq$ pA). Previous work in the Bayley Group (unpublished experiments performed by **VRS**) has explored the potential use of the algal protein channelrhodopsin-2 (ChR2)[131] and the engineered protein BLINK-1 (blue-light-induced potassium channel 1)[175] in droplet interface bilayers (DIB). Unfortunately, the reversible control of these light-driven channels in DIBs is yet to be achieved as the channels get stuck in the open-state. Whilst further optimisation will be required, these preliminary studies demonstrated that channel-based photosensory modules might be constructed in the future.

- **Databases** - Delving into protein libraries to find alternative light-powered proteins could also prove fruitful since databases such as the Microbial Rhodopsin database for Diversity and Evolution studies (MicRhoDE)[318] are rich with information. In addition to activity data, these databases also highlight predicted protein spectral tuning which might prove useful for future synthetic tissues. Further, it is likely than many more microbial rhodopsins

are yet to be discovered with the potential to significantly advance the energy-generating capability of synthetic tissues, and permit the introduction of novel functions.

- **Directed evolution** - Alongside the possible discovery of new photochemically active membrane proteins, the activity of CM-aR3 might be tuned using synthetic biology techniques such as directed evolution. In this way the activity could be selected for based on a variety of characteristics such as signal magnitude, fluorescence or activating wavelength. Directed evolution might even generate proteins with novel functionality.

- **Nanoparticles** - Future bioelectronic devices would benefit from being activated by more penetrating (bathochromic (red) shifted) wavelengths, especially for medical applications. Alongside exploring the use of natural, engineered or synthetic alternatives to CM-aR3 as discussed above, infrared (IR) nanoparticles could be incorporated into the photosensory droplet. IR is the region where light has its maximum depth of penetration in biological tissues and, at low intensities, is not thought to be damaging. Whilst, nanoparticles like these wouldn't directly transport ions, they could be coupled to proteins which can generate bioelectrical signals. For instance, illuminating a droplet containing IR nanoparticles generates heat, thereby triggering the droplet to change in size. This might activate mechanosensitive or thermosensitive proteins embedded in the bilayer which in turn transport ions across the droplet interface.

5.1.2 Alternative modules for neuronal stimulation

Alternatively, the use of light to remotely control synthetic tissue functionality could be abandoned. Replacing the sensory droplets with modules that respond to different stimuli e.g., magnetism would produce another type of sensory module. Magnetoreceptors have been expressed and activated in biological neurons[319]. Therefore, their incorporation into synthetic tissues should be feasible, enabling remote

activation using magnetism. In addition, ligand-gated and mechanoactivated ion channels have been successfully reconstituted into lipid bilayers demonstrating their potential uses as alternative methods to remotely activate synthetic tissues[32,43,111,320]. In theory, the sensory modules could be replaced with any stimuli-responsive component: natural or synthetic.

5.1.3 Multi-responsive synthetic tissues

The modular approach used to fabricate the synthetic nerve facilitates formation of multifaceted devices. By patterning the water-soluble elements encapsulated within each sensory droplet, parallel axons might respond to alternative wavelengths or stimuli (e.g. small membrane-permeable molecules, temperature or magnetic fields): the possibilities are endless. A future synthetic nerve could be bifunctional, for instance containing some neuronal axons (activated by stimulus A) which electrically activate living cells and some (activated by stimulus B) which inhibit their activity.

5.2 Synthetic Tissue functionality

5.2.1 Miniaturisation of the synthetic nerve

The synthetic neurons and nerves constructed in this thesis have dimensions of up to a few centimetres. The hydrogel axons have a diameter of 1 mm, on the upper end of those found in nature. For comparison, a giant squid axon is up to 1.5 mm across and human neurons have a diameter of $\leq$ 0.1 mm. Therefore, it is of interest to built smaller synthetic nerves, in particular for implanted medical applications. Miniaturisation of the hydrogel axons (and the elastomeric sheath) should be feasible since the pre-cured materials are fluid. However, the technique for synthetic nerve formation might need to be optimised to accommodate the liquid material viscosity. In addition, scaling down of the aqueous droplets (to biologically-relevant dimensions) might be achieved using the 3D droplet printer[40,50]. The main limitation for fabricating smaller synthetic nerves is the challenges in forming the cast using lithography. Optimisation of this step will be required.

Another way in which formation of smaller synthetic neurons and nerves might be realised is using a microfabrication techniques e.g., photomicrolithography. A novel class of miniaturised bioelectronic implants have previously been built using a combination of these techniques and similar biomimetic materials e.g., hydrogels[261,321]. In fact, hydrogel structures have been built using photomicrolithography with micrometre resolution[322]. Such devices can achieve high precision and selectivity but they can be expensive and their use in long-term studies is yet to be demonstrated.

An additional benefit of using these alternative strategies to make the synthetic neurons and nerves is that they permit a higher throughput of tissue production than is possible by hand. However, it is important to ensure that device functionality is not lost as the size is reduced.

5.2.2 Bio-mimetic mechanism of signal transmission

Whilst the function of the synthetic neurons and nerves outlined in this thesis resembles their biological counterparts, with signalling remaining fast and directional, the mechanism of ion conduction differs. Namely, no action potential is generated (Fig. 3.19). Voltage-gated channels have been successfully reconstituted into artificial bilayers and their use in droplet-hydrogel systems should also be feasible[26,323,324]. By lining the surface of the hydrogel axon with these voltage-gated proteins, a more biomimetic mechanism of signal transmission might be achieved. Since transmission would only be reliant on ion diffusion across the thin (nanometre-thick) interface bilayer (and not along centimetre axons) it is likely to be faster as well as more biomimetic.

5.2.3 Synthetic nerves for *in situ* biosynthesis

The modular approach to the fabrication of the synthetic nerves means that future devices might include a vast range of physiologically relevant and endogenous neurotransmitters, gene inducers, enzyme substrates or pharmaceuticals within the pre-synaptic droplet, creating a multifaceted device. **Chapter 3** described how a small chemical molecule (ATP) could be released from synaptic terminals,

generating functional outputs downstream (Fig. 3.29). This serves as a proof of concept for future synthetic nerves which might, for instance, transfer pro-drug molecules that could then be activated in situ.

5.2.4 Synthetic Organs

Whilst remarkable progress has been achieved with non-living synthetic cells built from the bottom-up, the construction of synthetic tissues and organs from such cells is limited. Previous work in the Bayley Group has shown how printed droplet networks can exhibit tissue-like behaviours[50], and as such, there is the potential to print a diversity of structures which mimic biological tissue functionalities. Energy generation and communication are requisite for the fabrication of sophisticated synthetic structures. Since the synthetic nerves fabricated in this thesis can generate, transmit and utilise energy, they could have a significant impact in this area. Acting as a light-powered battery, inclusion of neuronal pathways in a (printed) synthetic organ would allow directional signal transmission to a number of regions, driving a myriad of processes for function.

5.2.5 Transfer to an aqueous environment

The development of soft bioelectronic devices has primarily been with potential medical applications in mind. An inherent feature of droplet networks is that they exist in a lipid-in-oil environment; this restricts their use in a number of potentially powerful applications e.g., in drug delivery. In order to maximise the potential therapeutic applications of droplet networks, they must first be transferred to an aqueous (biological) external environment.

One way in which this issue has been addressed previously was by creating multisomes: functional multi-compartment structures formed from lipid-stabilised water droplets in a larger oil-in-water droplet. These internal droplet compartments have been shown to undergo controlled fusion[103] and communicate with one another (and the external environment) via ionic or molecular signals[27,50,57,61]. Multisomes might be built using microfluidics[57], by manually pipetting[103] or using a droplet

printer[50]. Perhaps a similar approach might be used to transfer the synthetic nerve to an aqueous environment.

More complex networks, composed of cell-containing printed droplets, have also been successfully transferred to aqueous environments; surviving transfer to cell media. Within this previous example, the pattern was conserved[103] so a similar approach might be employed for the synthetic nerve as it is essential that patterning is not lost. However, the network required a thin layer of non-aqueous solution (oils or gels) to maintain its structure and functionality following the phase transfer. This might prove problematic within the synthetic nerve since the elastomeric sheath was added to function as an insulator and prevent cross-talk between the hydrogel elements.

Therefore, one way in which this might be realised within the synthetic nerve is by incorporating the lipids directly into the elastomeric sheath itself. Instead of dissolving the lipid in the oil phase (as with current synthetic nerves), the lipid would be located within vesicles inside the elastomeric sheath. **Dr David Lunn** (Bayley Group) did some preliminary work in which he diluted the lipid (2 mg ml^{-1} DPhPC in 100 % hexadecane) with the elastomeric mix (eliminating the need for silicone oil). The addition of lipids and hexadecane made the elastomeric sheath more jelly-like and flexible (unpublished work) but protein functionality in this environment wasn't tested. Consequently, significant work is needed to explore whether a nerve constructed in this way would be sufficiently stable to survive transfer and remain functional.

5.2.6 Using synthetic nerves in hybrid tissues

Hybrid tissues are formed when synthetic and living tissues are connected; integrating these materials *in vivo* is of considerable interest. The synthetic nerve has the potential to interact with living cells in a number of different ways, using:

- **Potentials** - Endogenous voltage gradients act as cues for a vast number of cellular behaviours including cell migration, orientation and differentiation. Using the synthetic nerve to apply a potential to a living tissue is an intriguing

avenue to explore since it impacts tissue development and regeneration. Since the synthetic nerve generates patterned signals, forming electrochemical potential gradients across the different membranes, it could have a significant impact in this area. A great deal of work will need to be carried out to improve the synthetic nerve's ability to generate potentials sufficient in both size and duration to drive these behaviours.

- **Local pH changes** - Similarly, the synthetic nerve can release protons with high spaciotemporal resolution. pH homeostasis is critical for normal cell physiology and many processes e.g., migration are exquisitely sensitive to fluctuations in the environment. In **Chapter 4** we showed that protons released by CM-aR3-rich bilayers could initiate calcium signalling responses in human cortical astrocytes (experiments performed by **VRS** and **L.Z**)[100], demonstrating its potential.

- **Ions** - Future tissues might generate bioelectric signals using any number of endogenous ions. The behaviours of excitable cells are particularly susceptible to changes in the local concentration of such ions as they generate electrochemical gradients.

- **Endogenous molecules** - Each synapse may be patterned with any number or type of endogenous chemical molecules with their release from the synthetic nerve tightly controlled. As each neuron is distinct, in terms of both input and output, the nerve could be a notable advance in this area.

- **Pharmaceuticals** - Alternatively, molecules known to have therapeutic effects could be included. Due to the minimised side effects and negated blood brain barrier, the direct release of such molecules to target cells would be of considerable interest.

Moreover, hybrid tissues capable of bidirectional communication could also be built with the capacity to sense analytes and generate logic-based outputs. For

instance, the synthetic neural tissue could release substances dependent upon the endogenous biological cues detected.

To minimize rejection by the immune system, the synthetic nerve materials should be biocompatible and unrecognisable by immune cells. This might be achieved by coating the synthetic nerve in a material designed to do this, perhaps even containing pharmaceuticals. Additionally, this coat might prevent any degradation within the body which would reduce its chance of triggering an immune response.

5.3 Synthetic tissue longevity

Future synthetic tissues must remain both stable and functional for a prolonged period of time (days to years) in order to be used in applications such as medicine, robotics and computing.

5.3.1 Methods to enhance synthetic tissue stability

The choice of soft biomaterials used to construct the synthetic neurons and nerves, ensures that such devices have structures and mechanics comparable to living tissues, including high flexibility to accommodate deformations arising from movements in the human body or from soft robots (Fig. 3.30). In the majority of failed synthetic nerve experiments, the reason was coalescence of the droplet and hydrogel components. In particular, the sizeable fluctuations in environmental conditions (temperature and humidity) were problematic. Future devices would therefore benefit from enhanced stability.

5.3.1.1 Adding PEGylated lipids

Poly(ethylene glycol) (PEG) hydrogels are extensively utilised in biomedicine due to their established biocompatibilty, low toxicity and highly tunable properties. Previously, PEGylated lipids have been employed to stabilise liposomes and the use of them to improve droplet bilayer strength has also been demonstrated[100]. Further, work from the Bayley Group[100] has shown that microbial rhodopsins retain their activity when inserted into bilayers containing some PEGylated lipids. These combined

properties make PEGylated lipids an attractive method to enhance the long-term robustness of the synthetic nerve without compromising device functionality.

5.3.1.2 Using block copolymers

In order for the bio-pixels to survive any future implantation, the bilayer must resist a significant amount of mechanical stress. Since a key advantage of polymer-based vesicles (compared to lipid-based ones) is their enhanced membrane stability[325], another possibility is the creation of a hybrid system in which a lipid - block-copolymer mixture is used. In **Chapter 4**, the use of a DPhPC - PE-PEG-SH mixture was explored; strengthened sensory bilayers were formed in which CM-aR3 could functionally insert (Fig. 3.36). However, there remains significant scope for further exploration of lipid-copolymer mixtures (in particular their ratios and components).

5.3.1.3 Including an emulsion stabiliser

An additional strategy might be to include a water-in-oil emulsion stabiliser in the system to enhance lipid bilayer stability. For example, literature studies have shown that the use of the stabiliser SPAN-80 greatly enhanced the robustness of a freestanding lipid bilayer[326]. Preliminary experiments performed in the Bayley Group (unpublished experiments performed in conjunction with **VRS**) found that whilst bilayer stability was improved, protein incorporation was compromised which reduced device functionality. In the future, alternative emulsion stabilizers might be explored in which protein insertion wasn't hindered.

5.3.2 Bioresorbable devices

The long-term presence of bioelectronic devices is not required for some functions e.g., for wound healing[263]. For applications such as this, the synthetic nerve would benefit from the use of bioresorbable materials which can degrade into non-toxic products under physiological conditions. These materials exist and have been used in medicine for applications such as drug delivery and stitches. Simple electronic devices have even been built which are degraded and reabsored over time[327,328].

The idea is that eventually, the synthetic nerve implant would degrade without any requirement for further intervention.

5.3.3 Methods to increase the lifetime of a synthetic nerve

Whilst the synthetic neurons described in this thesis remained functional when kept in the dark (in a hydrated chamber) for at least a week after formation (Fig. 3.34), prolonged illumination will eventually lead to ion and molecule depletion limiting the device lifetime.

5.3.3.1 Addition of an uncoupler

In order for the synthetic neuron to sustain functionality over a long period, the protons within the sensory droplet must be replenished. One potential method would be the inclusion of an uncoupling agent: a controllable ion channel or transporter which modulates the gradient by redistributing the ions. The presence of an uncoupler within the sensory droplet pixels would permit the neuron to perform for a longer time as the protons available for pumping could be continuously recycled. This uncoupler might be a small molecule such as 2,4-Dinitrophenol (DNP), shuttling protons back across the sensory bilayer. Alternatively, this could be performed by proteins activated by the electrochemical gradient which arises following proton pumping. Once a sufficient potential had built-up, the voltage-sensitive proteins would open restoring ion stocks. Proteins, activated by a second stimulus (e.g. an alternative wavelength, magnetism or a small membrane-permeable molecule) might also facilitate the restoration of ion stocks, transporting ions in the opposite direction upon activation. This system has the added benefit of being easily controlled; the direction of ion movement could be remotely dictated depending on the device requirements.

5.3.3.2 Incorporating ATP synthesis machinery into the structure

The current synthetic neural device uses electrochemical gradients as an energy source. However, in the mitochondria, the proton gradient is used to drive ATP synthase and generate the major energy storage molecule ATP. This principle has

previously been performed in artificial cells[15,85] and its inclusion in the synthetic nerves would permit the device to produce proteins *in situ*, for instance using *in vitro* transcription and translation (IVTT) machinery. Such molecular machinery has previously been shown to function in aqueous droplets[52]. A synthetic nerve which, when remotely stimulated, not only sends electrochemical signals but also generates ATP to power protein synthesis, would be of interest.

6 Materials and Methods

This chapter provides all the information and details relevant to the construction and characterisation of a photosensory synthetic neuron and nerve.

6.1 Materials

2- mercaptoethanol - (Sigma, M6250); **Agarose** - High-gelling agarose (Sigma, A9045); Low-gelling agarose (Sigma, A9414); **Astrocytes** - Human primary astrocytes (ScienCellTM research laboratories, 1800); **ATP** - Adenosine 5-triphosphate (Sigma, A2383); **ATP Assay kit** - (Abcam, ab83355); **ATR** - All trans retinal (Sigma, R2500); **B-27** - (Gibco, 17504044); **Bacteriological peptone** - (LP72, Oxoid); **BL21 Cells** - (Thermo Scientific, EC0114); **$CaCl_2$** - calcium chloride (Sigma, C1016); **Chloroform** - (Sigma, 288306); **DDM** - n-dodecyl-β-D-maltopyranoside (Sigma, D4641); **DMEM/F12** - (Gibco, 11320033); **DNAse** - (Sigma, DN25); **DPBS** - Dulbecco's phosphate buffered saline (Sigma, T3924); **DPhPC** - 1,2-Diphytanoyl-sn-glycero-phosphatidyl choline (Avanti, 850356P); **EDTA** - Ethylenediaminetetraacetic acid (Sigma, E6758); **Elastomer monomer** - Sylgard 184 (Sigma, 761036); **Elastomer curing agent** - (Sigma, 761036); **Ethanol** - (Sigma, 51976); **FBS** - (Gibco, 10270-106); **FGF2** - (Gibco, 13256029); **Fluo-4** - (Invitrogen, F10471); **GlutaMax** - (Gibco, 35050-038); **Hexadecane**

- (Sigma, H0255); **Hydroxylamine** - (Sigma, 159417); **Imidazole** - (Sigma, I2399); **IPTG** - Isopropyl β-D-1-thiogalactopyranoside (Sigma, I6758); $\mathbf{K_2SO_4}$ - potassium sulphate (Sigma, P0772); **Kanamycin** - (Sigma, B5264); **KCl** - potassium chloride (Sigma, P9541); **LB** - Luria Bertani agar (Supelco, L3027); **Leupeptin** - (Sigma, EI8); **Lysozyme** - (Sigma, 10837059001); **MANT-dATP** - 3'-O-(N-methylanthraniloyl)-2'-deoxyadenosine 5'-triphosphate tri-ethyl ammonium salt (Sigma, 69258); **MES** - 2-(N-morpholino)ethanesulfonic acid (Sigma, M3671); $\mathbf{MgCl_2}$- magnesium chloride (Sigma, M8266); $\mathbf{MgSO_4}$ - magnesium sulphate (Sigma, M7506); **Mineral oil** - (Sigma, M5904); **N-2** - (Gibco, 17502048); **NaCl** - sodium chloride (Sigma, S7653); **NaClO** - sodium hypochlorite (10% active chlorine, Sigma, 28-3100); $\mathbf{Na_2HPO_4}$ - (Sigma, S976); $\mathbf{NaH_2OH}$ - hydroxylamine (Sigma, 438227); $\mathbf{NaH_2PO_4}$ - Monosodiumphosphate (Sigma, S0751); **NEAA** - (Gibco, 1605380); **OG** - n-Octyl-β-D-glucopyranoside (Sigma, 494459); **PE-PEG** - (Sigma, 24869357); **Pepstatin** - (Sigma, P5318); **Poly-L-lysine** - (Sigma, P4707); **POPC** - 1-palmitoyl-2-oleoyl-glycero-3-phosphocholine (Avanti, 16:0-18:1 PC, 850457C); **Pyranine** - 8-hydroxypyrene-1,3,6-trisulfonic acid (HPTS) (H1529, ThermoFisher); **Resin** - Clear resin (FormLabs); **Sigma-bR** - (Sigma, B0184); **Silicone oil** - AR20 (Sigma, 10836); **Sodium citrate** - (Sigma, 71497); **Soluble starch** - (Sigma, S9765); ***Staphyloccocus aureus*** - (ATCC, 25923); **Sucrose** - (Sigma, S0389); **Tris-HCl** - (Sigma, 10812846001); **Triton-X-100** - (Sigma, X100) ; **Trypsin** - (Sigma T3924); **Yeast extract** - (Sigma, Y1625);

6.2 Aqueous solutions

There were 4 major aqueous solutions used throughout this thesis. Double-distilled 'ultrapure' water (ddH_2O, Millipore, Milli-Q: 18.2 MΩ cm) was used throughout.

Solution	Buffer	Salt	Detergent (% w/v)	pH
A	100 mM MES	100 mM NaCl	0.1% DDM	pH 6.5
B	100 mM MES	100 mM NaCl	0.001% DDM	pH 6.5
C	-	100 mM NaCl	-	pH 6.5
D	100 mM MES	100 mM NaCl	-	pH 6.5

A number of additional solutions were made for optimisation experiments.

Solution	Buffer	Salt	Detergent	pH
E	100 mM MES	100 mM NaCl	0.001% OG	pH 6.5
F	100 mM MES	100 mM NaCl	0.001% Triton-X-100	pH 6.5
G	100 mM HEPES	100 mM NaCl	0.001% DDM	pH 6.5
H	100 mM Tris	100 mM NaCl	0.001% DDM	pH 6.5
I	100 mM CHES	100 mM NaCl	0.001% DDM	pH 6.5
J	100 mM PBS	100 mM NaCl	0.001% DDM	pH 6.5
K	100 mM MES	100 mM NaCl	0.00025% DDM	pH 6.5
L	100 mM MES	100 mM NaCl	0.0015% DDM	pH 6.5
M	100 mM MES	100 mM NaCl	0.0025% DDM	pH 6.5
N	100 mM MES	100 mM NaCl	0.001% DDM	pH 6.5
O	100 mM MES	100 mM KCl	0.001% DDM	pH 6.5
P	100 mM MES	10 mM NaCl	0.001% DDM	pH 6.5
Q	100 mM MES	50 mM NaCl	0.001% DDM	pH 6.5
R	100 mM MES	300 mM NaCl	0.001% DDM	pH 6.5
S	100 mM MES	500 mM NaCl	0.001% DDM	pH 6.5
T	100 mM MES	700 mM NaCl	0.001% DDM	pH 6.5
U	100 mM MES	900 mM NaCl	0.001% DDM	pH 6.5
V	100 mM MES	1000 mM NaCl	0.001% DDM	pH 6.5

6.3 Protein preparation

Sigma-bR

Sigma-bR was prepared as described for previous droplet bilayer experiments[31,44]. Lypohilised purple membrane (PM, containing bR) was purchased from Sigma (Strain S9, B0184). The Sigma-bR powder was then dissolved directly into Solution A and sonicated for 30 minutes in a water bath at 20 ° C. Next, the protein was diluted using Solution D so that the final detergent concentration (DDM, Sigma, D4641) was below the CMC (0.001 % (w/v) DDM). Finally, the protein solution was concentrated using centrifugation (Amicon spin column, Millipore) to a final Sigma-bR concentration of 0.15 - 0.25 mg mL^1 (measured using nanodrop). The final Sigma-bR in Solution B was stored at 4 ° C in the dark. Sigma-bR solution is purple in colour. Frequent aggregation was observed for Sigma-bR so between experiments, the protein solution was sonicated (30 minutes) and gently vortexed.

PM-bR

Protocol for the transformation and expression of bacteriorhodopsin was adapted from Cline et. al.[185]. Plasmid pMPK85 (containing the bacteriorhodopsin gene) was transformed into the *Halobacterium salinarum* strain L33 (which does not express wild-type bacteriorhodopsin). Initially, cells were grown in 20-25 mL of liquid culture media at a high salt concentration (250 gL^{-1} sodium chloride (NaCl Sigma, S7653), 20 gL^{-1} magnesium sulphate ($MgSO_4$, Sigma, M7506), 3 gL^{-1} sodium citrate (Sigma, W302600), 2 gL^{-1} potassium chloride (KCl, Sigma, P3911), 10 $gL^{-1}$of bacteriological peptone (LP72, Oxoid), pH 7.4) at 45 ° C and 170 rpm shaking for 5-7 days (until the OD_{600} reached 1.2). Flasks containing 1 L of fresh culture medium were inoculated from the 25 mL cultures and shaken at 170 rpm at 45 ° C for at least 12 days. The cells were harvested by centrifugation (8000 g, 30 minutes, 4° C) and the pellets were resuspended in 4 M NaCl. After being stirred for 2 hours, 5 mg of DNAse (Sigma, DN25) was added and the suspension incubated for 30 min at 4 ° C. Next the suspension was dialysed overnight in 0.1 M NaCl, and centrifuged (50,000 g, 45 min, 4° C). Sucrose density gradient ultracentrifugation was used to isolate the bR-rich purple membrane (PM), using a step gradient of 25%, 35%, 45%, 55% w/v (110,000 g, 15 hours, 15° C). The the purple band was harvested and sucrose remaining in the sample was removed by dialysis against double distilled water (ddH_2O) overnight. The sample was centrifuged again (70,000g ; 45 min; 4° C), and the pellet was resuspended in ddH_2O to a final concentration of 20 mg mL^{-1} and stored at 4° C in the dark. PM-bR protein expression and purification was performed by **Javier Vinals** (Watts Group, University of Oxford). PM-bR protein samples were then buffer exchanged (using a P3 BioSpin column) into Solution A (with the DDM detergent concentration above the CMC, 0.1 % (w/v) DDM) and sonicated (30 minutes, water bath at 20 ° C) for homogenisation. It is worth noting that during buffer exchange some protein was lost, sticking to the column and turning the white resin pale purple in colour. The PM-bR was then diluted (using Solution D) to a final solution in which the detergent (DDM) was below the CMC (Solution B, 0.001 % (w/v) DDM). PM-bR samples (0.15 - 0.25 mg mL^1(measured

using nanodrop) were stored at 4° C in the dark. PM-bR samples required regular agitation as they tended to aggregate: sonication and vortexing were used.

CM-aR3

Halorubrum sodomense strain RD-26 (ATCC-33755) cells were purchased from LGC Standards Ltd (Teddington, UK) and were grown according to the supplier's protocol with minor modifications. Initially, cells were grown in 20-25 mL of liquid culture media at a high salt concentration (125 g sodium chloride (NaCl Sigma, S7653), 160 g magnesium chloride ($MgCl_2$, Sigma, M8266), 0.13 g calcium chloride ($CaCl_2$, Sigma, C1016), 5 g potassium sulphate (K_2SO_4, Sigma, P0772), 1 g of bacteriological peptone (LP72, Oxoid), 1 g yeast extract (Sigma, Y1625), 2 g L^{-1} soluble starch (Sigma, S9765)), pH 7.4) at 45 ° C and 170 rpm shaking for 5-7 days (until the OD_{600} reached 1.2). Flasks containing 1 L of fresh culture medium were inoculated from the 25 mL cultures and shaken at 170 rpm at 45 ° C for at least 12 days. Cells were harvested by centrifugation after the OD_{600} had reached 1.7 - 1.9 (8000 g, 30 min, 4° C) and the pellets were resuspended in 4 M NaCl, and stirred for 2 hours. Then, 5 mg of DNAse (Sigma, DN25) was added. After the suspension had been incubated for 30 min at 4 ° C, it was dialysed overnight in 0.1 M NaCl, and centrifuged (70,000 g, 45 min, 4° C). Sucrose density gradient ultracentrifugation was used to isolate the aR3-rich claret membrane (CM), using a step gradient of 35%, 40%, 45%, 50% w/v (110,000 g, 15 hours, 15° C). The lowest band with a pink/purple colour was collected and dialysed against double distilled water (ddH_2O) overnight to remove the sucrose. The sample was centrifuged again (70,000g, 45 min, 4° C), and the pellet was resuspended in ddH_2O to a final concentration of 20 mg mL^{-1} and stored at 4° C in the dark. CM-aR3 protein expression and purification was performed by **Javier Vinals** (Watts Group, University of Oxford). CM-aR3 protein samples were then buffer exchanged (using a P3 BioSpin column) into Solution A (with the DDM detergent concentration above the CMC) and sonicated for 30 minutes in a water bath at 20 ° C for homogenisation. Again, it is worth noting that during buffer exchange some protein was lost, sticking to the

column and turning the white resin pale pink in colour. The CM-aR3 was then diluted (using Solution D) to a final solution in which the detergent (DDM) was below the CMC (Solution B). CM-aR3 samples (0.15 - 0.25 mgmL^1(measured using nanodrop) were stored at 4° C in the dark. Prior to use, CM-aR3 samples were sonicated (30 minutes in a water bath at 20 ° C) and gently vortexed.

EC-aR3

A plasmid containing the aR3 gene was purchased from Addgene (pET28b, ID: 58487). The plasmid contained a kanamycin resistance gene, a T7 promoter and an aR3 open reading frame with a polyHis tag (His6) at the C-terminal end of the protein. The EC-aR3 was expressed and purified following the previous established protocol[154]. First, the EC-aR3 was incubated with shaking overnight (170 rpm) in 50 mL LB (Supelco, L3027) with 100 μg ml^{-1} kanamycin (Sigma, B5264) at 37 ° C. The cultures were then added to 500 mL of LB (Supelco, L3027) with 100 μg ml^{-1} kanamycin (Sigma, B5264) at 37 ° C and shaken (170 rpm) until an OD_{600} of 0.6 was reached. Next, the cultures were induced with 0.5 mM IPTG (Isopropyl β-D-1-thiogalactopyranoside , Sigma, I6758) and 5 μM all-trans retinal (ATR, Sigma, R2500) solubilised in ethanol (Sigma, 51976). The sample was then centrifuged (70,000 g, 60 min, 4 ° C) and the pellet resuspended in 75 mL of 150 mM NaH_2PO_4 (Monosodiumphosphate, Sigma, S0751), 20 mM sodium chloride (NaCl Sigma, S7653) and 5 mM magnesium chloride (MgCl_2, Sigma, M8266) at pH 7. Lysozyme (0.2 g, Sigma, L3790), aprotinin (Roche, ROAPRO) , DNAse (Sigma, DN25), leupeptin (Sigma, L2884), pepstatin A (Sigma, P5318) and magnesium chloride (MgCl_2, Sigma, M8266) were added to the solution and mixed (150 rpm, 2 h, 4 ° C). After sonication (tip sonicator, 10 s on/off pulses, 5 minutes, 50% amplitude), the sample was homogenized (using glass/Teflon tissue homogeniser 5 to 10 times) and then centrifuged (70,000 g, 1 h, 4 ° C). The pellet was resuspended overnight at 4 ° C in 20 mM NaH_2PO_4 (Monosodiumphosphate, Sigma, S0751), 30 mM Na_2HPO_4 (di-Sodium hydrogen phosphate, Sigma, S9763), 300 mM sodium chloride (NaCl Sigma, S7653) and 1% (w/v) DDM (n-dodecyl-β-D-maltopyranoside, Sigma, D4641)

at pH 7). Once solubilisation was completed, the samples were centrifuged (70,000 g, 60 min, 4° C), the supernatant collected and incubated with Ni/NTA beads. The beads were washed with 50 mM NaH_2PO_4 (Monosodiumphosphate, Sigma, S0751), 100 mM sodium chloride (NaCl Sigma, S7653), 10 mM imidazole (Sigma, I2399), 0.03% DDM (n-dodecyl-β-D-maltopyranoside, Sigma, D4641), pH 7.0. The protein was then eluted with 50 mM NaH_2PO_4 (Monosodiumphosphate, Sigma, S0751), 100 mM sodium chloride (NaCl Sigma, S7653), 300 mM imidazole (Sigma, I2399) and 0.03% DDM (n-dodecyl-β-D-maltopyranoside, Sigma, D4641) at pH 7.0. Following elution, the samples were concentrated using Amicon Vivaspin concentrators with 100,000 MWCO and applied onto a Superdex 200 10/300 GL column attached to an AKTA pure (GE Healthcare). The protein was then eluted with 50 mM NaH_2PO_4 (Monosodiumphosphate, Sigma, S0751), 100 mM sodium chloride (NaCl Sigma, S7653), 0.03% DDM (n-dodecyl-β-D-maltopyranoside, Sigma, D4641) at pH 7.0, and the coloured fractions were pooled, concentrated (to 20 $mgmL^{-1}$) and kept at 4 ° C in the dark. EC-aR3 protein expression and purification was performed by **Javier Vinals** (Watts Group, University of Oxford). EC-aR3 protein samples were then buffer exchanged (using a P3 BioSpin column) into Solution A (with the DDM detergent concentration above the CMC) and sonicated for 30 minutes in a water bath at 20 ° C for homogenisation. During buffer exchange some protein was lost as it stuck to the column; this was observed by a change in colour from white to red/pink. The EC-aR3 was then diluted (using Solution D) to a final solution in which the detergent (DDM) was below the CMC (Solution B). EC-aR3 samples (0.15 - 0.25 mg mL^1 (measured using nanodrop) were stored at 4° C in the dark. Prior to use, EC-aR3 samples were sonicated (30 minutes in a water bath at 20 ° C) and gently vortexed before use.

Bleached protein

Retinal was removed from the microbial rhodopsins following the previously reported method. Bleaching was achieved by incubating the protein sample (0.15 - 0.25 mg mL^{-1} protein in Solution B) in 0.2 M hydroxylamine (NH_2OH.HCl, Sigma,

159417), pH 7.5 and continuous illumination (white halogen light, 20 cm from the sample, 25 W output) at 4 ° C. To monitor the bleaching of the protein, absorbance measurements were taken to assess the decrease of the protein absorption at 560 nm and an increase of the retinaloxime at 360 nm. Once bleached, the sample was washed four times by centrifugation (40,000 g, 30 minutes, 4 ° C) with double distilled water (ddH_2O) to remove any remaining hydroxylamine or retinaloxime present. For regeneration of the Schiff base after bleaching, the protein sample was incubated (3 hours at room temperature) with an excess of all-trans retinal (ATR, dissolved in ethanol at a concentration of 5 mM, Sigma, R2500). Several wash cycles in double-distilled water using centrifugation were performed in order to remove any free retinal (40,000 g, 30 minutes, 4 ° C). PM-bR protein expression and purification was performed by **Javier Vinals** (Watts Group, University of Oxford).

Delipidated protein

The protocol for protein delipidation was adapted by **J.V** from one developed by Huang and colleagues[204]. Protein was expressed in the native archaeal host *H. sodomense* and the claret membrane harvested by centrifugation (40000g for 30 minutes, 4 ° C) as described in 'CM-aR3 preparation'. The pellet was then resuspended, using a glass rod, in 2 mL of 10% (v/v) octylglucoside (OG, Sigma, 10634425001) and 25mM NaH_2PO_4 (Monosodiumphosphate, Sigma, S0751), pH 6.5. The solution was sonicated in a bath sonicator for 1 minute before being left to stand overnight (without stirring) at room temperature and in the dark. The pH was then adjusted to pH 5.5 and centrifuged (100000g for 45 minutes, 15 ° C) to remove all aggregated and non-solubilised material. The supernatant was applied to a GE column (Hi-Load 16/600, Superdex 200 pg) with 1.2% OG (octylglucoside, Sigma, 10634425001) in 25 mM NaH_2PO_4 (Monosodiumphosphate, Sigma, S0751) at pH 5.5. The column was eluted in the dark at 4 °C. All coloured fractions were pooled and stored (in the dark) at -20 °C.

Alpha hemolysin

Protocol for the transformation and expression of alpha hemolysin (αHL) was adapted from Lind et. al.[189]. The protein was expressed in the native Staphylococcus aureus (Wood 46, ATCC). The αHL was purified as monomers, concentrated and stored at -80 ° C. The monomeric protein pores were provided by **I.C**, (Bayley Group, University of Oxford). Alpha hemolysin monomers (293 residues, 33 kDa[329]) assembled into functional heptameric pores upon insertion into the lipid bilayer as previously observed[44,50,53,63]. A fresh aliquot of protein was defrosted for each experiment and discarded afterwards since functionality degraded over time.

6.4 Mutagenesis

Design

The residues mutated were identified through sequence homology and based on previous work done with microbial rhodopsins[209,330].

Site-directed mutagenesis

Primers were designed using using the plasmid map (pET28b, ID: 58487) and the Thermo Fisher primer design tools. Complementary primers were 20-mers with melting temperatures in the range of 65-70 ° C. Mutations were introduced using PCR and a QuickChange II Site-Directed Mutagenesis Kit (Agilent, USA). The PCR programme for competent *E.coli* cell incorporation (DH5α, Sigma) was as follows. First the samples underwent one cycle of a full minute at 95 ° C, followed by a three-step cycles (30 sec at 95 ° C; 1 min at 55 ° C; 10 min at 68 ° C) repeated 20 times overall. After this, the sample was further incubated (68 ° C for 10 min) and then stored at 4 ° C. After PCR, solutions were incubated with DpnI for 1 hour at 37 ° C to remove the template DNA. Site-directed mutagenesis was performed by **Javier Vinals** (Watts group, University of Oxford).

Expression of mutants

The PCR products were transformed into BL21 (DE3, Sigma, CMC0014) *E. coli* cells (for increased protein expression) by heat shock which were then plated onto Luria Bertani agar (LB, Supelco, L3027), supplemented with kanamycin (100 mg mL^{-1}, Sigma, B5264) and incubated overnight (37 ° C). Individual colonies were picked and extracted from the cells using a Qiagen QIAprep Spin Miniprep Kit (Qiagen, Netherlands). After extraction, the DNA was sent for sequencing to Source Bioscience to confirm uptake of the plasmid and the presence of the mutation.

Large scale expression and purification of the mutant proteins was then performed as described for EC-aR3 (see above). Purified protein was kept at 4 ° C in the dark. EC-aR3 mutant protein preparation was performed by **Javier Vinals** (Watts Group, University of Oxford).

6.5 Dye and polymer preparation

Pyranine preparation

Pyranine dye (8-hydroxypyrene-1,3,6-trisulfonic acid (HPTS), H1529, ThermoFisher) was dissolved to a final concentration of 100 μM in Solution C and stored at 4° C in the dark. If protein (0.15 – 0.25 mg mL^{-1} microbial rhodopsin proteins or 50 nM alpha hemolysin pores) was needed within the pyranine droplet to functionalise the bilayers, then this solution (pyranine in Solution C) was used during the protein preparation phase (described above, replacing Solutions A, B and D - 0.001% DDM detergent was also used in CM-aR3 experiments). All pyranine experiments were performed in the absence of MES buffer to facilitate visualisation of small changes to droplet pH.

Carboxyfluorescein preparation

Carboxyfluorescein dye (Sigma, 21877) was prepared as for 'pyranine preparation', with a final concentration of 100 μM. The dye was stored in the dark at 4° C

. All carboxyfluorescein experiments were performed in the absence of buffer to enable small pH changes to be visualised.

MANT-dATP

MANT-dATP (3'-O-(N-methylanthraniloyl)-2'-deoxyadenosine 5'-triphosphate triethylammonium salt, Sigma, 69258) was diluted to a final concentration of 100 μM in Solution D containing monomeric αHL (50 nM) and stored at -20 ° C in the dark.

ATP

ATP (Adenosine 5-triphosphate, Sigma, A2383) was dissolved to a final concentration of 100 μM in Solution D containing monomeric αHL (50 nM) and stored at -20 ° C in the dark.

ATP assay kit reagents

The components (ATP assay buffer, ATP probe in DMSO, ATP Converter, Developer mix) of the ATP assay kit (Abcam, ab83355) were prepared and stored in line with the manufacturer's manual. A more concentrated ATP source (see above) was used instead of the ATP standard. The fluorometric assay was used in accordance with the manufacturer's guidelines (it is more sensitive than the colorimetric assay).

Hydrogel preparation

Agarose (2% high-gelling agarose, Sigma, A9045) was dissolved in Solution D (with vortexing) and stored at room temperature. Prior to use, the hydrogel was heated to 95° C in a dry block heater to enable pipetting.

Elastomer preparation

Silicone elastomer monomer (Sylgard 184) and curing agent (Sigma, 761036) were mixed in a 10:1 ratio and degassed for 30 minutes. The mixture was then carefully poured into a bespoke cast (Fig. 6.1), avoiding the formation of bubbles. The filled cast was placed in an incubator overnight at 60° C. After the elastomer had cooled,

it was cut at the edges of the cast using a scalpel. Silicone oil (AR20, Sigma, 10836) was then pipetted down the interface between elastomer and cast. After 24 h, this elastomer nerve was carefully removed from the cast with a spatula and tweezers.

6.6 Lipid-in-oil solutions

All synthetic neurons and nerves described in this thesis require a lipid-in-oil environment for function.

Mix	Lipid type	Lipid Concentration	Oil
A	DPhPC	10 $mgmL^{-1}$	50:50 Hexadecane, Silicone oil
B	DPhPC	10 $mgmL^{-1}$	35:65 Hexadecane, Silicone oil
C	POPC	10 $mgmL^{-1}$	50:50 Hexadecane, Silicone oil
D	PE-PEG	1 $mgmL^{-1}$	Mineral oil
E	DPhPC PE-PEG	10 $mgmL^{-1}$ 1 $mgmL^{-1}$	35:65 Hexadecane, Silicone oil Mineral oil

Lipid-in-oil preparation

1,2-Diphytanoyl-sn-glycero-phosphatidylcholine (DPhPC, Avanti, 4ME, 16:0 PC, 850356P) was dissolved in chloroform (Sigma, 288306), aliquoted into glass vials (7 mL, Supelco) and dried with a stream of nitrogen gas to form a lipid film. The film was placed in a vacuum for 3 h and then dissolved at the requisite concentration in filtered (0.22 µm Millex GP filters, Millipore) hexadecane (Sigma, H0255) and silicone oil (AR20, Sigma, 10836) (35:65 (Mix B) or 50:50 (Mix A) (v/v)). For the system optimisation POPC lipids (Mix C, 1-palmitoyl-2-oleoyl-glycero-3-phosphocholine, Avanti, 16:0-18:1 PC, 850457C) were also prepared as described for DPhPC. Lipid-in-oil solutions were stored at room temperature in a sealed vial; fresh solution was used for each experiment.

Copolymer preparation

Polyethylene-block-poly(ethylene glycol) (PE-PEG, Sigma, 24869357) was dissolved upon heated sonication (60 minutes, 50° C, Branson 2800,Cleanosonic) in mineral oil to a final concentration of 1 mgmL^{-1} (Mix D). The copolymer was then mixed at a 1:10 ratio with 10 mgmL^{-1} DPhPC (Avanti, 4ME, 16:0 PC, 850356P) in

hexadecane (Sigma, H0255) and silicone oil (AR20, Sigma, 10836) (35:65 (v/v), Mix B) (prepared as described for 'Lipid-in-oil'. The copolymer-lipid-in-oil mixture (Mix E) was stored at 4 ° C in the dark. Preparation was performed in conjunction with **Dr. Assala Al Samad** (Booth Group, University of Oxford).

6.7 Chamber and cast design

The synthetic neurons and nerves were placed in bespoke chambers for characterisation. All chambers were designed using AutoCAD software (SolidWorks, Fig. 6.1a-e). In addition, a cast for moulding the synthetic nerve was also designed (Fig. 6.1f).

Chamber design

All chambers used for the electrical and optical experiments in this thesis were made from poly (methyl methacrylate) (PMMA). The chambers had a 1-mm thick base to facilitate imaging using the microscope.

- **Photosensory module electrophysiology chamber** - The cuboidal chamber (PMMA) had outer dimensions of 10 x 10 x 6 mm and inner dimensions of 8 x 8 x 5 mm (Fig. 6.1a).
- **Photosensory module optical experiments chamber** - The array chamber (PMMA) had outer dimensions of 20 x 20 x 6 mm and inner dimensions of 18 x 18 x 2 mm. The chamber contained 16 wells (1.5 mm diameter, 3 mm deep) (Fig. 6.1b).
- **Synthetic neuron length chamber** - The cuboidal chamber (PMMA) had outer dimensions of 15 x 10 x 6 mm and inner dimensions of 14 x 9 x 2 mm. The chamber contained 4 trenches with dimensions of 10 x 1 x 3 mm (Fig. 6.1c).
- **Branched neuron chamber** - The cuboidal chamber (PMMA) had outer dimensions of 30 x 20 x 5 mm and inner dimensions of 26 x 16 x 3 mm. The

chamber contained a hand-drawn neuron-shaped trench: 1 mm deep, ≈ 1 mm in diameter and 25 mm at the longest point (Fig. 6.1d).

- **Synthetic nerve chamber** - The cuboidal chamber (PMMA) had outer dimensions of 30 x 30 x 30 mm and inner dimensions of 24 x 24 x 29 mm. (Fig. 6.1e).

The chambers were manufactured by micromilling of PMMA with a Roland Modela MDX-40A computerized numerical control (CNC) machine. At the start and end of each experiment all chambers were washed twice with water and ethanol and dried using a nitrogen gas stream.

Cast design

- To fabricate the myelinated synthetic neurons a tubular cast was built. A glass rod (length 10 mm, diameter 1 mm) was glued into the centre of plastic tubing (length 10 mm, diameter 5 mm). A new cast was made for each experiment.

- A bespoke cast for the synthetic nerve was also designed using AutoCAD software (SolidWorks, Fig. 6.1f). The casts were manufactured using Low Force Stereolithography Form 3 (FormLabs) with Clear Resin (FormLabs) and said casts were then washed with Form Wash (FormLabs) before curing with Form Cure (FormLabs). The synthetic nerve cast had outer dimensions of 25 x 25 x 15 mm and inner dimensions of 16.65 x 15 x 10 mm (Fig. 6.1f). The cast contained 7 cylindrical tubes (diameter 1 mm and height 10 mm) spaced with the centres 4 mm apart. In addition, a lid was made for synthetic nerve formation. The lid had outer dimensions of 25 x 25 x 5 mm and contained 7 cylindrical tubes (diameter 1 mm and height 1 mm) spaced with the centres 4 mm apart (Fig. 6.1f). Prior to use, all casts were washed with water and ethanol and dried using a nitrogen gas stream. The cast was designed in collaboration with **Dr Vanessa Restrepo Schild** (Bayley Group, University of Oxford).

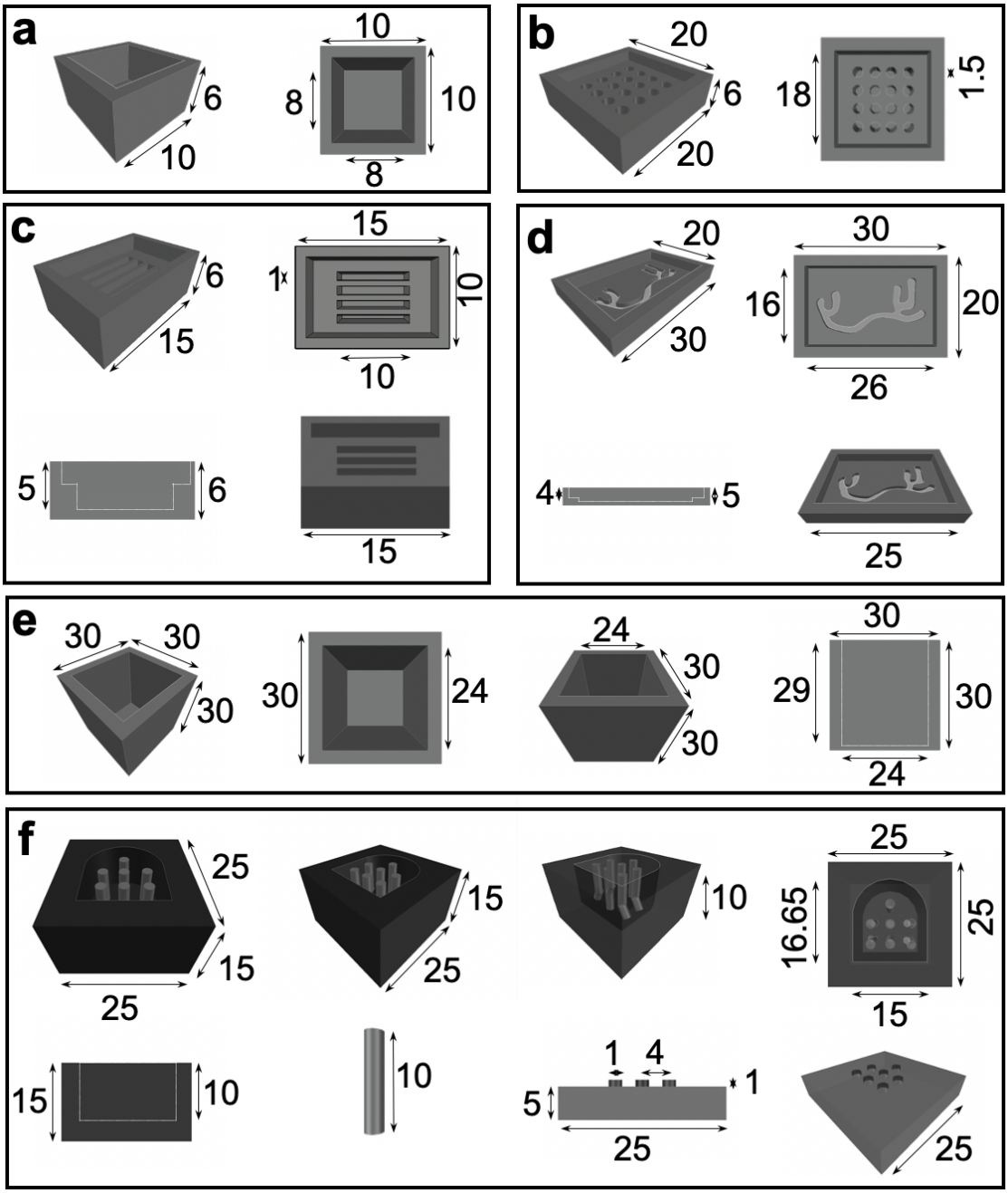


Figure 6.1: Chamber Design. AutoCAD software was used to design the bespoke chambers used: **a,** A droplet pair electrophysiology chamber, **b,** A droplet array chamber for optical experiments, **c,** A neuron length electrophysiology chamber, **d,** A branched (25-mm) neuron chamber for both electrophysiology and optical experiments, **e,** A synthetic nerve electrophysiology chamber, **f,** A synthetic nerve cast (first 6 images left to right) and lid (last 2 images, left to right). All dimensions are in millimetres and the chamber images are taken from the AutoCAD layout in perspective mode.

6.8 Absorbance

Protein concentration using spectrophotometry

The concentration of the proteins was determined photometrically using a NanoDrop 1000 Spectrophotometer (Thermo Scientific), blanked against Solution B (100 mM MES, 100 mM NaCl, 0.001% DDM, pH 6.5).

UV-Visible spectroscopy

UV-Visible absorption spectra were recorded on a Jasco V-630 spectrophotometer fitted with microcell attachment EMC-709. All analyses were corrected against respective solution buffers. Spectra were recorded at room temperature in the range 350 nm - 700 nm, at a scan speed of 100 nm min^{-1} using a 1 cm quartz cuvette. Spectra were recorded by **J.V**.

CD spectroscopy

Purified samples were loaded onto Jasco J-815 CD spectrometer. Spectra were measured at room temperature between 190 nm and 260 nm using a 1 mm cuvette. Protein secondary structure was predicted using the Jasco spectra manager software and calculated from the Dichroweb website using the CDSSTR programme with the membrane protein SMP180 set as the reference. Spectra were recorded by **J.V**.

6.9 Electrical characterisation

The proteins embedded within the bilayers were electrically interrogated and characterised by the addition of electrodes into the droplets.

System layout

Electrical recordings were performed within a Faraday cage containing: A platform (Mechanical workshop, University of Oxford) supporting the headstage of a

conventional patch-clamp amplifier (Axopatch 200B, Axon Instruments); Two micromanipulators (Narishige, NMN-21) to guide the electrodes; and the experimental (PMMA) chamber (Fig. 6.2).

Electrical recording and analysis

Signals were recorded with an amplifier (Axopatch 200B, Axon Instruments), connected to a digitizer (Digidata 1440 A, Axon Instruments), operating in gap-free acquisition mode at a sampling frequency of 10 kHz, with a 2 kHz filter and five-fold gain. Data was analysed with Clampfit (version 10.3, Axon Instruments) after post-filtering with a 25 Hz low-pass filter. Electrical recordings were conducted at 24.5 ± 3.4 ° C and 32.4 ± 8.6% humidity. Temperature (20 - 29 ° C) and humidity (20 - 50 %) fluctuated and extremes led to difficulties in forming stable bilayers and the frequency of droplet coalescence increased (recorded using a USB Temperature and Humidity sensor from ThorLabs). At sub-optimal environmental conditions, monolayer incubation times were increased from 5 minutes to 30 minutes to improve stability.

Illumination source

Fibre-coupled LEDs (run at 15.0 ± 4.5 mW output, PM100A Compact Power Meter Console, Thorlabs) were used as an illumination source (Mightex, WFC-H7-0560). The LED bundle used was composed of 7 distinct LEDs, each of which was controlled by a separate channel using the manufacturer's software (Mightex): LED channel 1 (680 - 741 nm peaks at 722 nm), 2 (634 - 680 nm peaks at 660 nm), 3 (603 - 645 nm peaks at 631 nm), 4 (576 - 608 nm peaks at 592 nm), 5 (490 - 594 nm peaks at 550 nm), 6 (392 - 430 nm peaks at 410 nm), 7 (355 - 390 nm peaks at 367 nm) (Fig. 2.9). The LED bundle was passed through a hole at the top of the Faraday cage (solid metal, Fig. 6.2d) via a bespoke adaptor (Mechanical Workshop, University of Oxford) and aligned to the PMMA chamber at a distance of 5 cm. Spectral information for all LED channels was obtained using an Optical Spectrum Analyser (Thorlabs) with the LEDs run at 10 mA (all LED channels on) and at the maximum intensity for each channel (single LED channel on) (n = 3) (Fig. 2.9).

Electrode preparation

Ag/AgCl electrodes were prepared by soldering silver wire (100-μm diameter, Sigma, 348783) into male crimp-terminals (RS Components) The wire tips were incubated in sodium hypochlorite (NaClO, 10% active chlorine, Sigma, 28-3100) for a few minutes and then their surfaces coated with a hydrogel layer by pipetting hot melted agarose (1% low-melt agarose, Sigma, A9045). Electrodes were stored at room temperature in the dark. The male crimp-terminals of these electrodes were each plugged into a female crimp-terminal (RS Components), which was in turn attached to a micromanipulator (Narishige, NMN-21). The other end of the female crimp-terminal was soldered to a cable terminating in a second male crimp-terminal. These second male crimp-terminals were connected to the amplifier headstage (Axopatch 200B, Axon Instruments), one at the grounding site and one at the recording site.

General experimental set-up

The PMMA chamber was filled with lipid-in-oil and placed at the centre of the stage directly under the LED (Fig. 6.2c). The electrodes were visualized with a stereomicroscope (Nikon, SMZ660, Fig. 6.2a2) and positioned with the micromanipulators so that their terminals were immersed in the lipid-in-oil (Fig. 6.2b6-8). Droplets (200 nL) were pipetted onto each electrode (Finnpipette F1, 0.2-2 µL, ThermoFisher); the droplets hung on the electrode tip, adhering to the hydrogel coating (described above). The photosensory droplets (containing the CM-aR3 protein) were added to the recording electrode, and the ground electrode was within a droplet containing only Solution A. After incubating for 5 min, the two droplets were gently brought into contact and a DIB spontaneously formed (as confirmed by measurement of the capacitance, >20 pF, Section. 2.2.4.2).

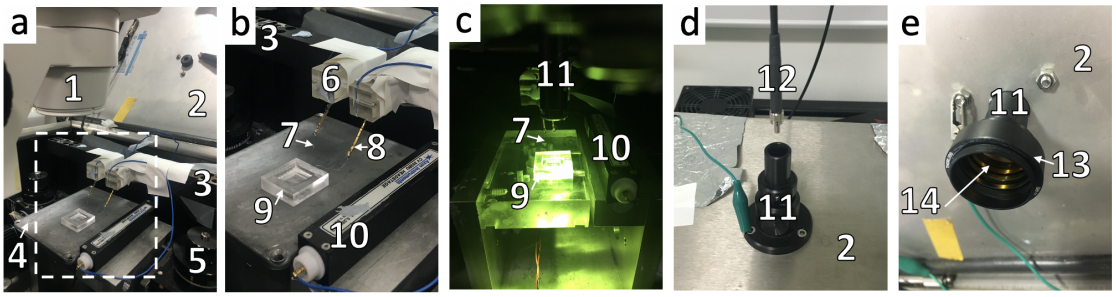


Figure 6.2: Set-up for electrical recordings. Photographs (taken with an iPhone) of the experimental set-up for single channel electrical recordings. **a,** View of inside the Faraday cage: 1 = Stereomicroscope, 2 = Faraday cage, 3 = Micromanipulator arm, 4 = Stage, 5 = Micromanipulator dial. **b,** Zoom of dotted box in 'a': 3 = Micromanipulator arm, 6 = Electrode holder, 7 = Ag/AgCl Electrode, 8 = Male/Female pin connection, 9 = Chamber, 10 = Amplifier headstage. **c,** View inside the Faraday cage with yellow-green light on: 7 = Ag/AgCl Electrode, 9 = Chamber, 10 = Amplifier headstage, 11 = LED adapter. **d,** View from the top of the Faraday cage outside: 2 = Faraday cage, 11 = LED adapter, 12 = LED fibre bundle. **e,** Inside the Faraday cage for action spectra experiments. 2 = Faraday cage, 11 = LED adapter (containing the LED fibre bundle), 13 = Filter adapter, 14 = Bandpass filter

Electrode controls

At the start of each experiment, electrode controls were performed. Two (protein-free) 200 nL droplets (containing Solution D) were pipetted onto the electrodes. After a brief monolayer incubation period (5 minutes), they were brought into contact with each other forming a droplet interface bilayer (DIB). First, a capacitance measurement (recorded by applying a triangular voltage waveform, ± 15 mV, 30 s peak-to-peak) was taken to determine if a DIB has successfully formed. It is assumed that bilayer formation has occurred if the capacitance is > 20 pF. All capacitance measurements were performed in the dark. Then, this droplet pair was illuminated first with IR light (LED Channel 1, 680 - 741 nm peaks at 722 nm, 16 ± 5.0 mW), or with UV light (355 - 390 nm peaks at 367 nm, 15 ± 3.9 mW), and then with YG light (Channels 4 and 5, 490 - 608 nm peaks at 550 and 592 nm, 15 ± 4.5 mW) (Fig. 2.9). Electrodes that generated a signal when illuminated were discarded and fresh electrodes made. Electrode controls were performed at the start and end of an experiment to ensure no artefacts arose from photochemistry at the Ag/AgCl electrode surface.

Protein preparation for electrical recordings

Prior to use, all microbial rhodopsin protein samples were removed from the fridge (4 ° C) and gently vortexed to reduce protein aggregation. Samples were stored on ice (in the dark) between experiments but the experiments were conducted at room temperature. For alpha hemolysin pore (αHL) experiments a fresh sample was defrosted (-80 ° C).

Photosensory module recording

First the (200 nL) aqueous droplets were pipetted onto the electrodes: the photosensory droplet contained the recording electrode and the protein-free (Solution D) droplet contained the ground electrode (Fig. 2.7). After incubating for 5 min, they were gently brought into contact and a DIB spontaneously formed as confirmed by measurement of the capacitance (>20 pF, performed as with 'Electrode controls'). A lower capacitance was consistently observed for protein-containing bilayers than of those which do not contain any protein. The photosensory module was illuminated with IR light (680 - 741 nm, peaks at 722 nm, 16 ± 5.0 mW), or with UV light (355 - 390 nm peaks at 367 nm, 15 ± 3.9 mW). If a signal was observed, then the experiment was abandoned since neither UV nor IR light can activate the microbial rhodopsins used in this thesis. If no signal was observed, then the photosensory module was illuminated with YG light (490 – 608 nm with peaks at 550 and 592 nm, 15 ± 4.5 mW). Control experiments were also performed in the absence of light (D, Dark) or the absence of protein (NP) to confirm that the light-driven proton pumping (under YG illumination) was responsible for the signals observed.

Protein insertion orientation

Photosensory droplets containing active CM-aR3 or PM-bR proteins, generated positive signals greater than 1.0-pA (an arbitrary threshold set to indicate activity); the maximum signal detected was +25 pA for CM-aR3 (Fig. 2.13, 2.15). Several factors influenced the signal output of the photosensory droplets, resulting in variability. Firstly, insertion of the microbial rhodopsin into the bilayer was

stochastic, differing between experiments. Moreover, no two bilayers were of identical size, meaning not only the surface area but also bilayer-curvature varied. Additionally, extremes in environmental conditions (temperature and humidity) lead to some droplet instability and caused them to coalesce. In this case monolayer incubation times were increased to 30 minutes.

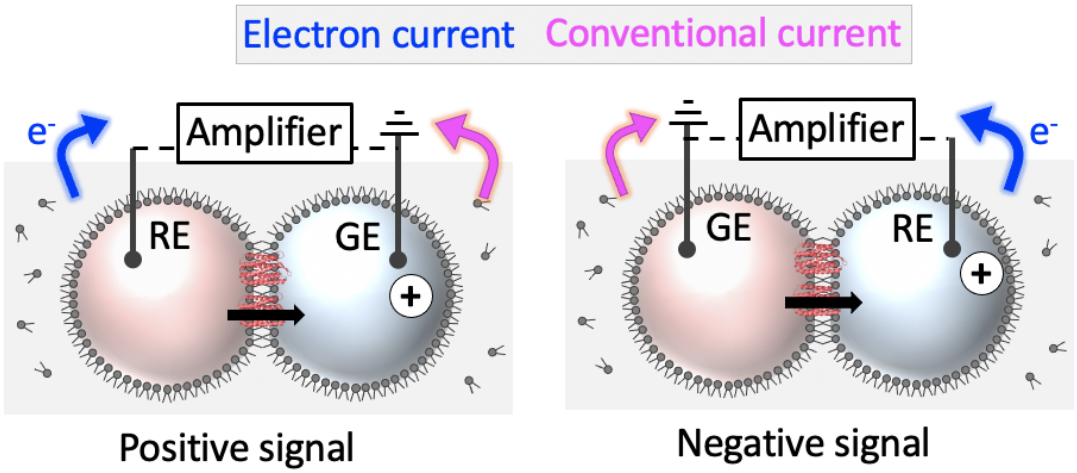


Figure 6.3: Signal polarity. Left: A positive signal is generated in a photosensory module. CM-aR3 is added to the recording electrode (RE) containing photosensory droplet (pink). The ground electrode (GE) is inserted into the protein-free droplet (blue). Upon illumination, CM-aR3 pumps protons into the protein-free droplet creating a positive terminal at the ground electrode. Electrons then flow towards the ground electrode (protein-free droplet) forming the electron current (blue). The conventional current (magenta) moves towards the recording electrode (photosensory droplet) and is recorded by the amplifier. Right: A negative signal is generated in a photosensory module. CM-aR3 is added to the ground electrode (GE) containing photosensory droplet (pink). The recording electrode (RE) is inserted into the protein-free droplet (blue). Upon illumination, CM-aR3 pumps protons into the protein-free droplet creating a positive terminal at the recording electrode. Electrons then flow towards the ground electrode (photosensory droplet) forming the electron current (blue). The conventional current (magenta) moves towards the recording electrode (protein-free droplet) and is recorded by the amplifier.

When electrodes were included in the droplets, proton pumping across the bilayer could be recorded. Since protons are cations (positively charged ions), pumping generates a positive terminal at the ground electrode and a negative terminal at the recording electrode. Within the DIB set-up the recording electrode was embedded within the protein-containing droplet and the ground within the protein-free droplet (unless otherwise specified). Therefore, electrons flowed towards

the positively charged (protein-free) terminal generating the electron current. The conventional current flowed in the opposite direction, towards the negative terminal (protein-containing droplet), and was recorded by the amplifier (Axopatch 200B, Axon Instruments). A positive signal is defined as one in which the conventional current flows into the recording electrode; the electron current flows into the ground electrode (Molecular Devices).

Action spectra

A photosensory module was prepared as described above with the recording Ag/AgCl electrode in a photosensory droplet (+ protein, 200 nL) and the ground electrode in a protein-free droplet (Solution D only, 200 nL). The fibre-coupled LED bundle used was composed of 7 distinct LEDs, each of which was controlled by a separate channel using the manufacturer's software (Mightex): LED channel 1 (680 - 741 nm peaks at 722 nm), 2 (634 - 680 nm peaks at 660 nm), 3 (603 - 645 nm peaks at 631 nm), 4 (576 - 608 nm peaks at 592 nm), 5 (490 - 594 nm peaks at 550 nm), 6 (392 - 430 nm peaks at 410 nm), 7 (355 - 390 nm peaks at 367 nm) (Fig. 2.9). All LED channels used were run at 0.2 ± 0.1 mW output (measured using compact power meter console ThorLabs). Here, the LED fibre bundle was inserted into the Faraday cage through an adaptor (Mechanical workshop, University of Oxford), which was in turn connected to a second adapter (SM1A1, ThorLabs) on the inside of the Faraday cage (Fig. 6.2d-e). Bandpass filters were screwed into the second adapter at a distance of 4 cm from the PMMA chamber containing the DIB. These filters allowed light of only a narrow wavelength band to pass through (± 10 nm). In turn, filters allowing light at 390 nm, 430 nm, 490 nm, 530 nm, 560 nm, 590 nm, 630 nm and 660 nm were fitted. Electrical traces were recorded for each filter as described above, using Clampex and analysed using Clampfit (version 10.3, Axon Instruments). The steady-state signal was then determined for each trace and the mean ± SD plotted (n = 3). The signal output was recorded in response to a higher intensity of YG light (490 - 608 nm, with peaks at 550 and 592 nm, 15 ± 4.5 mW)

at the start and end of each experiment. If there was a significant reduction in signal output then the experiment was discarded and repeated.

Synthetic neuron set-up

Electrical recordings were performed within a Faraday cage, (Fig. 6.2). The bespoke neuron chamber was placed in the centre of the stage.

- For the droplet-based neurons, the chamber was first filled with lipid-in-oil. All droplet neurons were composed of a series of aqueous droplets (200 nL, 700 µm diameter) connected through DIBs. The photosensory bilayer was composed of a DIB formed between a photosensory receptor droplet (0.25 mg mL-1 protein, 0.001% DDM, Solution B) and a protein-free droplet (Solution D). All subsequent droplets in the axon contained the protein pore αHL (50 nM αHL in Solution D). All droplets (200 nL) were made by pipetting into a separate array for incubation (Fig. 6.1b). After 5 - 30 minutes, the droplets were transferred (by pipetting) directly into the trench of the neuron chamber (Fig. 6.1). The recording electrode was inserted into the photosensory droplet and the ground electrode into the terminal synaptic droplet. These droplets were moved using the micromanipulators. All central droplets were positioned by hand using a separate piece of silver wire (100-µm diameter, Sigma, 348783). When two droplets were brought into contact a DIB spontaneously formed.

- The hydrogel neuron was composed of a hydrogel axon connected to aqueous droplets (200 nL, 700 μm diameter) via droplet hydrogel bilayers (DHBs). For the hydrogel-based neurons, handmade 'stoppers' (made from pipette tips) were positioned at the terminals of the trench. The hot hydrogel (prepared as described above) was then pipetted into the desired neuron shape by ejecting into the trench of the bespoke chamber and left to cool. Once cooled, the 'stoppers' were removed and the chamber was filled with lipid-in-oil, coating the hydrogel. The bespoke neuron chamber was then placed in the centre of the stage within the Faraday cage. All droplets were incubated in a separate array

and after 5 - 30 minutes were transferred by pipetting into the appropriate sites of the neuron. They were then gently pushed into contact with the hydrogel axon by tipping the chamber, forming droplet hydrogel bilayers (DHBs).

Once all bilayers had formed the electrical recordings could take place as described above.

Voltage protocol

A DIB was formed (as described above) between two droplets (containing Ag/AgCl electrodes). The signal output was then recorded across the DIB under an applied potential (in the dark).

- For the standard voltage protocol, first a positive potential (+ 50 mV, 30 s) and then (after 30 s at 0 mV) a negative potential (- 50 mV, 30 s) was applied across the bilayer.
- For the IV ramp, a potential was applied across the bilayer increasing (or decreasing) stepwise (10 mV steps) between -100 mV and +100 mV.

Breaking potential protocol

A DIB was formed between two droplets (containing Ag/AgCl electrodes) as described above. First, a capacitance measurement (recorded by applying a triangular voltage waveform, ± 15 mV, 30 s peak-to-peak) was taken to determine if the DIB has successfully formed. Next, a voltage ramp protocol was run (increasing the potential applied across the DIB from 0 mV to 500 mV) in the dark. The voltage at which the bilayer fractured was recorded.

Simultaneous recording in a synthetic nerve

The synthetic nerve-containing chamber was filled with lipid-in-oil and placed in the centre of the stage directly under the LED bundle, inside the first Faraday cage (Fig. 6.4). The sensory end of the nerve was surrounded with light-blocking

sheets (made from waterproof black card) to permit independent stimulation of neighbouring axons without interference. Electrical recordings were conducted with a multichannel amplifier (Triton+, Tecella LLC, MA, Fig. 6.4), located within a Faraday cage (Cage 2, Fig. 6.4). Ag/AgCl electrodes were connected to the amplifier via an 8-channel electrode probe holder (Terrapin, Tecella LLC, TP, Fig. 6.4), with each channel ending in a screw-terminal. The probe holders were contained in a Faraday cage separate Faraday cage (Cage 1, Fig. 6.4) and the screw-terminals were each connected to one of the electrodes for individual recording. Probe holders were placed under a homemade aluminium box to reduce noise (AB, Fig. 6.4). With the aid of a stereomicroscope, each of the three recording electrodes (RE, Fig. 6.4) and ground electrodes (GE, Fig. 6.4) were carefully positioned within 0.5 mm of the hydrogel axons.

Droplets (200 nL) were then pipetted directly onto the electrodes following a 5 - 30 minutes incubation in a separate PMMA chamber, forming DHBs with the hydrogel axons. The synthetic nerve-containing chamber (C, Fig. 6.4) was filled with lipid-in-oil and placed in the centre of the stage directly under the LED bundle, inside the first Faraday cage (Cage 1, Fig. 6.4). The sensory end of the nerve was surrounded with light-blocking sheets (made from waterproof black card, BS, Fig. 6.4) to permit independent stimulation of neighbouring axons without interference. Each axon was illuminated using a distinct fibre-coupled LED (490 - 608 nm, peaking at 550 and 592 nm, run at 15.0 ± 4.5 mW output, Mightex, WFC-H7-0560) (L1, L2, L3, Fig. 6.4). The LEDs (described previously, 2.2.4.2) were positioned within the first Faraday cage using separate clamp-stands. The LED of Axon 1 (L1, Fig. 6.4) was controlled from a computer with the manufacture's software (Mightex) by using the strobe setting with 15 s light pulses (at 0.05 Hz). The LEDs of Axons 2 and 3 (L2 and L3, Fig. 6.4) were controlled from separate waveform generators (Rigol, DG822) with light pulses of length 5 s and 1 s at 0.1 and 0.06 Hz respectively. The signal was obtained by gap-free acquisition with a feedback resistor of 1 GΩ. Data was acquired at 20 kHz with a 5 kHz filter

with the 'TecellaLab v0.90 type 2 software. Data from the multichannel amplifier (Triton+, Tecella LLC) was analysed using Clampfit.

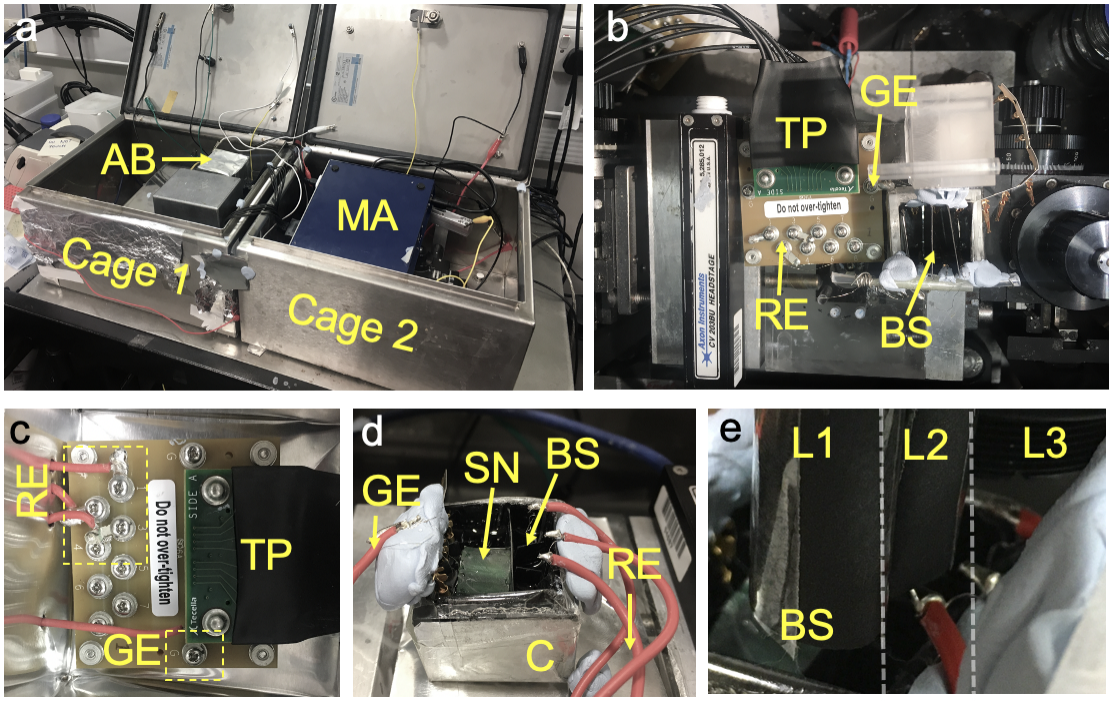


Figure 6.4: Set-up for electrical recordings. Photographs (taken using an iPhone) of the experimental set-up. **a,** Two Faraday cages are required. Cage 1 contains the electrodes within an aluminium box (AB) and the synthetic nerve. Cage 2 contains the multichannel amplifier (MA). **b,** Image of the components in Cage 1: the terrapin (TP), the recording electrodes (RE), the common ground electrode (GE) and the nerve chamber covered with black (light-blocking) sheets (BS). **c,** The terrapin (TP), recording electrodes (RE) and common ground electrode (GE) and contained within an aluminium box (AB). **d,** The synthetic nerve (SN) is added to the bespoke chamber (C) covered in black (light-blocking) sheets (BS). The recording (RE) and ground (GE) electrodes are added to each side of the nerve. **e,** Black (light-blocking) sheets (BS) are added to channel the light from three sources (L1-3) directly to the photosensory bilayers of the synthetic nerve.

6.10 Optical recordings

Microscope

A Leica DMi8 inverted epi-fluorescence microscope was used for imaging in brightfield and fluorescence mode. All samples were placed on a glass coverslip for imaging.

Illumination protocol

For optical experiments, photosensory droplets were illuminated continuously overnight (15 h). Images were taken before (0 h) and after 15 h of illumination. During illumination, the chamber was positioned within a hydration chamber (composed of a petri dish containing multiple water-filled glass vial lids), on the stage and directly below the LED at a distance of 5 cm. The chamber was not compatible with the microscope so the neurons and nerves were removed for imaging. The same fibre-coupled LED was used as with the electrical experiments, controlled using the manufacturer's software (see above).

Pyranine imaging

Images of the aqueous droplets (200 nL) that contained 100 μM of the pH-sensitive dye pyranine (prepared as described above) were imaged. The microscope settings used for imaging were: 5 x magnification, with a lamp of excitation wavelength 450 - 490 nm, emission wavelength 500 - 550 nm, gain 1.0. Fluorescence intensity increases with pH (Fig. 2.10)[149].

MANT-dATP imaging

MANT-dATP is a fluorescent analogue of ATP (Sigma, 100 μM) and was prepared as described above. The microscope settings used were: 10 x magnification, with a lamp of excitation wavelength 350-390 nm, emission wavelength 420-480 nm, gain 1.0. Concentrations of MANT-dATP below <18 μM could not be observed under the experimental set-up (fluorescence intensity = 0 A.U, Fig. 3.22).

Resourfin imaging

In the assay, ATP initiated a signalling cascade which generated a fluorescent resorufin output. The microscope settings used to visualise this were: 10 x magnification, with a lamp of excitation wavelength 540 - 552 nm, emission wavelength 562 - 643 nm, gain 1.0. Since resorufin is partially hydrophobic in character and is known to leak across droplet bilayers, some neurons had higher

background fluorescence (leakage became more visible after longer incubation times). Further, imaging was immediately after the 30 minute reaction since the droplets were unstable due to the presence of glycerol within the assay kit (coalescence typically occurred within 60 minutes).

Protein fluorescence imaging

A 200 nL droplet of each protein was added to a well for visualisation. Protein fluorescence was visualised at 10x magnification under a number of excitation/emission wavelength combinations ($\lambda_{ex}/\lambda_{em}$): 1 = 540/600 nm, 2 = 600/670 nm.

Image analysis

All fluorescent images were analysed using Fiji (ImageJ). Any brightness or contrast changes (for visualisation) made to the images were the same within any image set. Only raw data images were used for analysis. In order to determine the fluorescence of a particular droplet, its cross-section was first plotted. From this the average fluorescence intensity of the droplet was determined (the absolute fluorescence, F_A). Then the background fluorescence (F_B) was then subtracted from this absolute fluorescence value. For each droplet, the mean output of three technical replicates (fluorescence reading from the same droplet) was calculated. Finally, the output from three biological replicates (from different droplets) was plotted.

6.11 Plate reader experiments

Fluorescence measurements were also analysed by a Tecan Infinite M1000 Pro fluorescence plate reader. The protocol was controlled using the i-ControlTM software and data was exported to Microscoft Excel for analysis.

Bulk pH-sensitive dyes

A well plate was filled with 100 μL of dye at a concentration of 100 μM. The fluorescence intensity of both pyranine (H1529, ThermoFisher) and carboxyfluorescein (Sigma, 21877) were monitored (n = 16) at at a number of discrete pH values (pH

6-8 at intervals of 0.1, Fig. 2.10). An excitation wavelength of 454 nm and emission wavelength of 520 nm were used (flash frequency = 100 Hz, room temperature).

Protein fluorescence

A well plate was filled with 50 μL of microbial rhodopsin at a concentration of 1 mg mL^{-1}. The fluorescence intensity of the protein (n = 8) was recorded. Two excitation/emission wavelength combinations were used: 620/730 nm and 640/710 nm (flash frequency = 100 Hz, room temperature).

6.12 Time-resolved absorption

The time-resolves absorption apparatus used to investigate light-induced absorption changes in WT EC-aR3 and its mutants was designed to measure changes in absorption at 405 nm when the sample was illuminated with a combined pulse of yellow-green light (409 - 608 nm, with peaks at 550 and 592 nm). For these measurements, the sample was contained within a UV fused silica cuvette (Sigma, BrandTech 759235, pathlength 10 mm). The excitation light was provided by a pulsed light emitting diode (Mightex, WFC-H7-0560). Excitation light transmitted through the sample was detected by a photodiode (Thorlabs Det310), and the photodiode output signal was used to trigger an oscilloscope (Tektronix 2024) on which the time dependent absorption signals were visualised. The light used to make the continuous absorption measurement was provided by a 405 nm diode laser (Laser 2000), attenuated by a neutral density filter to a power of 8 mW. Light transmitted through the sample was detected by a second photodiode, and the time-dependent signal was visualised on the oscilloscope. A 405 nm interference filter placed in front of the photodiode prevents detection of background light or green light from the pulsed LED. Excitation pulses from the green LED with pulse lengths between 50 and 400 ms were employed to initiate photoisomerisation. Experiments were performed by **Professor Claire Vallance and Dr Vanessa Restrepo Schild**; data was analysed in collaboration.

6.13 Synthetic tissue formation

The synthetic neurons and nerves described in this thesis are modular and the individual elements have to be assembled.

Synthetic neurons

Synthetic neurons were built within the bespoke chambers (Fig. 6.1c-d). All the neurons had a photosensory droplet (0.15 - 0.25 mg mL^{-1} microbial rhodopsin, Solution B) at one end. At the other end of the synthetic axon were two additional aqueous droplets, the presynaptic and postsynaptic droplets (Fig. 3.7). The presynaptic droplet contained the protein pore α-hemolysin (50 nM αHL in Solution D), and the neurotransmitter.

- **Droplet neuron** - Here, the synthetic axon was composed of a series of aqueous droplets (200 nL, 700 μm diameter) connected through DIBs. First, all the aqueous droplets were pipetted into an array chamber (Fig. 6.1b) and incubated for up to 5 minutes in the lipid-in-oil to allow monolayer formation. Next, the droplets were transferred (by pipetting) directly into the trench of the neuron chamber. Then, the photosensory and synaptic bilayers were formed by gently connecting the photosensory and axon droplets, and the presynaptic and postsynaptic droplets, respectively. Droplets were connected by tipping the chamber or using a piece of silver wire. After a further 10 minutes, the signalling pathway was completed by joining the remaining droplets together (by tipping the chamber).

- **Hydrogel neuron** - Here, hydrogel (2% high-gelling agarose, Solution D) was used to form the synthetic axon. First, the hydrogel was heated in a hot plate (95 ° C). As described for the droplet neuron, all droplets were incubated in a separate chamber for up to 10 minutes. At the same time, the hot hydrogel was then pipetted into the neuron-chamber trench and left to cool. Handmade hydrogel 'stoppers' (made from pipette tips) prevented the hydrogel from filling the trench completely. Once cooled, the 'stoppers' were

removed and the chamber was filled with lipid-in-oil. Finally, the droplets were then added to the gaps left by the 'stoppers' and connected in the same order as described for the droplet neuron (photosensory and synaptic bilayers were formed first). All incubation times were doubled (compared to the droplet neuron) to avoid coalescence.

- **Myelinated neuron** - First, a myelin cast was made: a glass rod (length 10 mm, diameter 1 mm) and a cylindrical piece of PVC plastic tubing (length 15 mm, diameter 5 mm) were glued onto a sheet of PMMA with the glass rod in the centre of the tube. Next, the silicone elastomer monomer (SYLGARD 184, Sigma, 761036) and curing agent (Sigma, 761036) were mixed in a 10:1 ratio and degassed for 30 minutes. The elastomeric mixture was carefully poured into the cast to avoid the formation of bubbles. After overnight incubation (15 h, 60 ° C), the cast was left to cool before the plastic tubing was cut with a scalpel and the elastomeric sheath removed. The glass rod was then removed using tweezers, and cut (using a scalpel) to 10 mm to form the synthetic myelin sheath. Subsequently, this central channel was filled with hot hydrogel (2% high-gelling agarose) forming the synthetic axon. After the hydrogel had cooled the myelinated axon was transferred into the (lipid-in-oil filled) synthetic nerve chamber (Fig. 6.1d). Finally, the droplets (having been incubated in a separate chamber) were pipetted into the nerve chamber and gently pushed into contact with the hydrogel axon.

- **Downstream (neighbouring) cell** - First the synthetic neurons were built as described above. After overnight illumination (YG light, 15h, in a hydrated environment), a neighbouring cell droplet (200 nL, containing the contained the enzymes and substrates (Abcam, ab83355) was pipetted into the chamber at the synaptic terminal. This neighbouring cell droplet was not initially in contact with the synthetic neuron. Next, the postsynaptic droplet was mechanically separated from the presynaptic droplet using a piece of silver wire (Sigma, 348783). The neighbouring cell and postsynaptic droplets were

mechanically fused. The fused droplets (now 400 nL) were incubated in the dark (in a hydrated environment) for 0.5 h to allow the reaction to occur. The fused droplets were then gently reconnected to the presynaptic droplet for visualisation.

Synthetic nerves.

All synthetic nerves were built within the bespoke chamber (Fig. 6.1f). As described for the myelinated neuron, the silicone elastomer monomer (SYLGARD 184, Sigma, 761036) and curing agent (Sigma, 761036) were mixed in a 10:1 ratio and degassed for 30 minutes. The elastomeric mixture was then carefully poured into the cast to avoid the formation of bubbles. After overnight incubation (15 h, 60 ° C), the cast was left to cool. The edges of the elastomer were then cut with a scalpel and silicone oil was pipetted into the gap to help separate the nerve from the cast. Once the elastomeric nerve had been removed from the cast, the 7 tubular channels (1 mm diameter, 10 mm length) were filled by pipetting hot hydrogel (2% low-melt agarose, Sigma) into them. The hydrogel axons fitted tightly into the elastomer sheath, but they were not fixed to it thereby permitting damaged ones to be carefully removed with tweezers and replaced. The lid was designed so that the droplets could sit inside the sheath. The synthetic nerve was then placed in lipid-in-oil filled chamber. Finally, droplets were added at each end of the hydrogel axons as described for the 'myelinated' neuron.

6.14 Flexibility experiments

Cuboid sections of material (prepared as described above) were cut from a larger structure for testing (length of 20 mm, height of 5 mm). The materials tested were hydrogel (2% high gelling agarose), elastomer (Sylgard-184) and a square neuron (20 mm long cuboid of elastomer with a central cylindrical hydrogel axon, diameter 1 mm, length 20 mm). Each cuboid was sequentially placed on a variety of plastic shapes with convex or concave curvature and imaged using an iPhone (n = 3). In the case of the hydrogel cuboid, new structures were used (taken from

the same larger original structure) following formation of hydrogel fractures. The elastomer and nerve both returned to their original shape after bending. The (cuboidal) synthetic neuron was then placed between the thumb and forefinger and a video of the material bending was taken.

6.15 Cell experiments

The hybrid tissue experiments formed part of a project led by **Dr Vanessa Restrepo Schild** (Bayley Group, University of Oxford). Cell culture and staining was performed in collaboration with **Dr Vanessa Restrepo Schild** and **Dr Linna Zhou** (Bayley Group, University of Oxford).

Cell culture

Human primary astrocytes isolated from cerebral cortex were purchased from ScienCellTM Research Laboratories (catalogue # 1800). The cells were thawed and cultured according to the manufacturer's instructions. Briefly, the culture containers were coated with poly-L-lysine (Sigma, P4707) for 1 hour before seeding the cells in astrocyte medium, which contained: DMEM/F12 (Gibco, 11320033), 1 × N- 2 (Gibco, 17502048), 1 × B-27 (Gibco, 17504044), 100 μM NEAA (Gibco, 1605380), 100 μM 2- mercaptoethanol (Gibco, 31350-010), 10 ng mL^{-1} FGF2 (Gibco, 13256029), 10% FBS (Gibco, 10270-106), and 1 mM GlutaMax (Gibco, 35050-038). Half of the culture medium was exchanged with fresh medium every second day. Once the culture reached over 90% confluency, the cells were washed once with DPBS (Dulbecco's Phosphate Buffered Saline, Sigma Aldrich, D8537) and passaged by incubation with 1 × trypsin- EDTA solution (0.5 gL^{-1} trypsin, Sigma Aldrich, T3924) for 3 minutes according to the manufacturer's instructions. Cell culture was carried out by **Dr Linna Zhou** (Bayley Group, University of Oxford).

Cell electrophysiology

The electrical recordings were performed within a Faraday cage as described for the above. Here, a CM-aR3 (0.15 - 0.25 mgmL^{-1} protein in Solution B) droplet and an

astrocyte-containing droplet (50:50 matrigel:astrocyte media) were added to the recording and ground electrodes respectively. The astrocytes had been trypsinised from a 2D culture that had achieved 90% confluency. After 10 minutes, the droplets were brought into contact forming a droplet interface bilayer (DIB): confirmed by measurement of the capacitance (>20 pF) by the application of a triangular voltage waveform (±15 mV, 30 s peak-to-peak). The DIB was then illuminated with YG light (490 - 608 nm with peaks at 550 and 592 nm, 15 ± 4.5 mW). All signals were recorded with an amplifier (Axopatch 200B, Axon Instruments), connected to a digitizer (Digidata 1440 A, Axon Instruments), operating in gap-free acquisition mode at a sampling frequency of 10 kHz, with a 2 kHz filter and five-fold gain. Data was analysed using Clampfit (version 10.3, Axon Instruments) after post-filtering with a 25 Hz low-pass filter. Controls were performed in the absence of protein (NP) and light (D) as previously described.

Cell viability

Live and dead cells were labelled with calcein-AM and propidium iodide respectively. Microscopy images of the 2D culture of (labelled) human cortical astrocytes were taken (laser scanning confocal microscope, Leica SP5) and processed (Fiji/ImageJ). The percentage of cells labelled with calcein-AM was determined as the viability value for a given tissue at that timepoint. Viability was measured in the presence of lipid-in-oil. Experiments were performed by **Dr Linna Zhou** and **Dr Vanessa Restrepo Schild**.

Droplet positioning

All reagents were autoclaved and kept in sterile conditions throughout the experiment. The hydrogel microarray was made using astrocyte media as the aqueous component and incubated for 40 minutes in lipid-in-oil for lipid monolayer formation. Then, the astrocyte media (present in the 2D cell culture) was carefully removed (care was taken to avoid touching the cells). The microarray was then gently placed over the 2D culture and photosensory droplets (incubated in a separate

chamber for lipid monolayer formation) were then pipetted into the holes of the microarray and into direct contact with the cells. Experiments were performed by **Dr Vanessa Restrepo Schild.**

Calcium signalling: staining and imaging

A Fluo-4 DirectTM calcium assay kit (Invitrogen, F10471) was used according to the manufacturer's instructions to measure calcium activities. Briefly, astrocytes were incubated with astrocyte medium and Fluo-4 calcium imaging reagents (v:v, 1:1) for 1 hour at 37 °C. A laser scanning confocal microscope (Leica SP5) was used to monitor the calcium oscillations over time (37 °C, timelapse at 1 frame per 10 seconds for 10 min, imaged with a 488 nm laser after illumination (YG light, 490 - 608 nm with peaks at 550 and 592 nm, 15 ± 4.5 mW) for 4 seconds between imaging frames). Data was analysed using ImageJ (Fiji) with all brightness and contrast setting kept the same for each data set. The timelapse was transformed into a single image using the Z- project of the standard deviation (Image>Stack>Zproject>StDeviation). Calcium imaging and data analysis was carried out by **Dr Vanessa Restrepo Schild** (Bayley Group, University of Oxford).

6.16 Replicates

For electrical recordings, (a minimum of three) independent synthetic neurons/nerves were built. All sensory droplets were formed using the same aliquot of CM-aR3 protein. Each trace was analysed using Clampfit (version 10.3, Axon Instruments) and the mean steady-state output was plotted as a single data point. All repeats were performed using the same light source (wavelength, intensity etc..) and experimental set-up.

For all optical experiments, (a minimum of) three independent synthetic neurons/nerves were built. Each structure was imaged three times and the fluorescence of the three images (analysed using Fiji (ImageJ)) averaged to form a single datapoint. At the start of each experiment, an aliquot of each solution was placed on ice and each independent repeat was composed of droplets (200 nL) formed using

a single solution aliquot. All repeats were built and illuminated simultaneously, and under the same conditions (e.g., same temperature, humidity, light intensity).

For the hybrid tissue experiments in which the photosensory array was interfaced with living cells, six biological replicates were made.

6.17 Display figure preparation

For all experiments detailed in this thesis, the raw images were used for data analysis. In order to determine the fluorescence of a particular droplet, its cross-section was first plotted. From this the average fluorescence intensity of the droplet was determined (the absolute fluorescence, F_A). Then the background fluorescence (F_B) was then subtracted from this absolute fluorescence value.

However, for display the images were modified in order to aid visualisation; they were not used for data analysis.

- Brightfield photographs - For display only, brightfield photographs of the neurons and nerves (taken with an iPhone) were background-removed (for clarity). During construction, food dye was added to the droplet and hydrogel components to aid visualisation. After imaging, the background was removed using the Microsoft background removal feature (Fig. 6.5a). Dyed synthetic tissues were not used for data collection.

- Pyranine fluorescent images - All pyranine experiments were also background-removed for display purposes only (Fig. 6.5b). Using Fiji (ImageJ) a mask was formed highlighting the background (BG, Fig. 6.5b, red). The background (red, BG) was then removed, leaving only the droplet region (grey). The resulting image (minus background) may be rotated or moved for display. Raw data images were used for image analysis and not the display images (Fig. 6.5b).

- Stitching - For display purposes only, images of the synthetic neurons were stitched together using ImageJ Fiji pairwise stitching software[331] (Fig. 6.5c).

The synthetic tissues were too large to fit within the microscope field of view so multiple overlapping images were taken. First, the brightfield images were stitched together to form the final structure. Using the same parameters, the fluorescence images were stitched together before being overlayed with the brightfield channel for display (Fig. 6.5c).

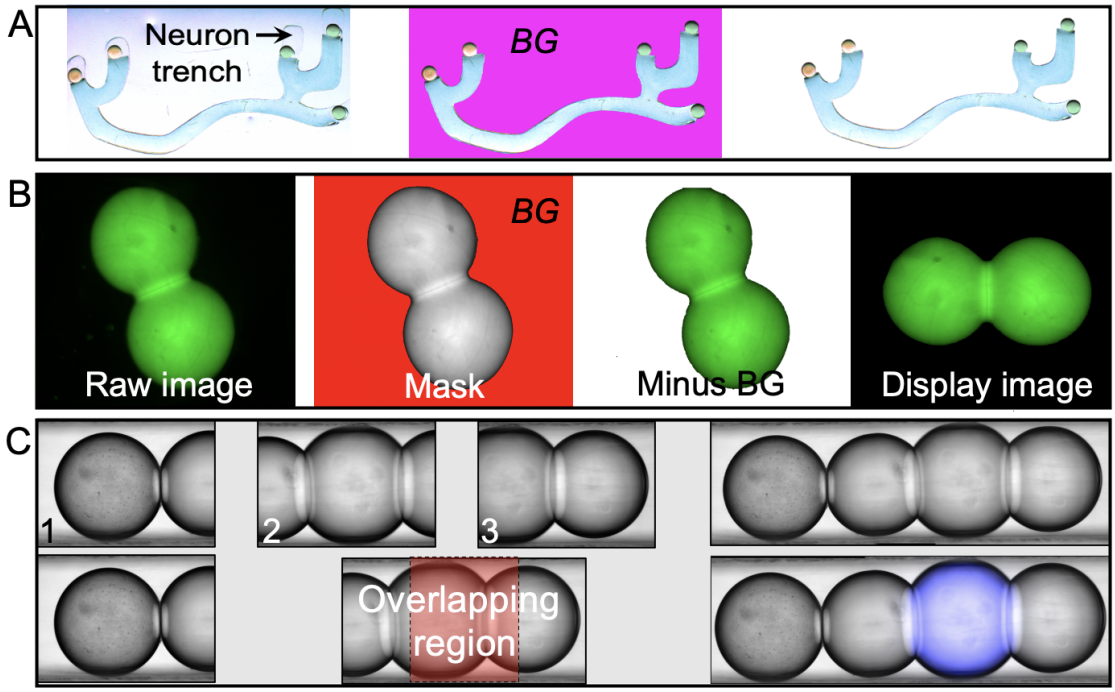


Figure 6.5: Display figure preparation. **a,** Processing of a brightfield image. The background (BG, pink) is removed to aid visualisation. No data is taken from brightfield images. **b,** Processing of a pyranine dye image. The background (BG, red) is removed to aid visualisation and enable the image to be rotated. All data analysis is performed using the raw images. **c,** Stitching of images. For all fluorescence experiments, overlapping images of the structure are taken and then stitched together for visualisation. Composite images are made by overlaying the brightfield and fluorescence channels. No display images are used for data analysis.

References

[1] S J Singer and Garth L Nicolson. "The Fluid Mosaic Model of the Structure of Cell Membranes". In: *Science* 175.4023 (Feb. 1972), p. 720. URL: http://science.sciencemag.org/content/175/4023/720.abstract.

[2] Olaf S Andersen and Roger E Koeppe. "Bilayer Thickness and Membrane Protein Function: An Energetic Perspective". In: *Annual Review of Biophysics and Biomolecular Structure* 36.1 (May 2007), pp. 107–130. URL: https://doi.org/10.1146/annurev.biophys.36.040306.132643.

[3] Lodish et al. *Molecular Cell Biology.*

[4] Bruce Alberts et al. *Molecular Biology of the Cell.* 6th ed. Garland Science, 2015, p. 1464.

[5] Takeshi Harayama and Howard Riezman. "Understanding the diversity of membrane lipid composition". In: *Nature Reviews Molecular Cell Biology* 19.5 (2018), pp. 281–296. URL: https://doi.org/10.1038/nrm.2017.138.

[6] Erdinc Sezgin et al. "The mystery of membrane organization: composition, regulation and roles of lipid rafts". eng. In: *Nature reviews. Molecular cell biology* 18.6 (June 2017), pp. 361–374. URL: https://pubmed.ncbi.nlm.nih.gov/28356571%20https://www.ncbi.nlm.nih.gov/pmc/articles/PMC5500228/.

[7] Rob Phillips et al. "Emerging roles for lipids in shaping membrane-protein function". In: *Nature* 459.7245 (2009), pp. 379–385. URL: https://doi.org/10.1038/nature08147.

[8] Anthony G Lee. "How lipids affect the activities of integral membrane proteins". In: *Biochimica et Biophysica Acta (BBA) - Biomembranes* 1666.1 (2004), pp. 62–87. URL: https://www.sciencedirect.com/science/article/pii/S0005273604001592.

[9] H Ronald Kaback, Miklós Sahin-Tóth, and Adam B Weinglass. "The kamikaze approach to membrane transport". In: *Nature Reviews Molecular Cell Biology* 2.8 (2001), pp. 610–620. URL: https://doi.org/10.1038/35085077.

[10] Benjamin C.-K. Tee et al. "A skin-inspired organic digital mechanoreceptor". In: *Science* 350.6258 (Oct. 2015), p. 313. URL: http://science.sciencemag.org/content/350/6258/313.abstract.

[11] Oliver P Ernst et al. "Microbial and Animal Rhodopsins: Structures, Functions, and Molecular Mechanisms". In: *Chemical Reviews* 114.1 (Jan. 2014), pp. 126–163. URL: https://doi.org/10.1021/cr4003769.

[12] PETER MITCHELL. "Coupling of Phosphorylation to Electron and Hydrogen Transfer by a Chemi-Osmotic type of Mechanism". In: *Nature* 191.4784 (1961), pp. 144–148. URL: https://doi.org/10.1038/191144a0.

[13] Alessandro Maria Morelli et al. “An update of the chemiosmotic theory as suggested by possible proton currents inside the coupling membrane”. In: *Open Biology* 9.4 (Mar. 2021), p. 180221. URL: https://doi.org/10.1098/rsob.180221.

[14] Noah Ritzmann et al. “Fusion Domains Guide the Oriented Insertion of Light-Driven Proton Pumps into Liposomes”. eng. In: *Biophysical journal* 113.6 (Sept. 2017), pp. 1181–1186. URL: https://pubmed.ncbi.nlm.nih.gov/28697898%20https://www.ncbi.nlm.nih.gov/pmc/articles/PMC5607040/.

[15] Samuel Berhanu, Takuya Ueda, and Yutetsu Kuruma. “Artificial photosynthetic cell producing energy for protein synthesis”. In: *Nature Communications* 10.1 (2019), p. 1325. URL: https://doi.org/10.1038/s41467-019-09147-4.

[16] Lynn E Heasley. “Autocrine and paracrine signaling through neuropeptide receptors in human cancer”. In: *Oncogene* 20.13 (2001), pp. 1563–1569. URL: https://doi.org/10.1038/sj.onc.1204183.

[17] Haiyang Jia and Petra Schwille. “Bottom-up synthetic biology: reconstitution in space and time”. In: *Current Opinion in Biotechnology* 60 (2019), pp. 179–187. URL: https://www.sciencedirect.com/science/article/pii/S0958166918302015.

[18] Bastiaan C Buddingh’ and Jan C M van Hest. “Artificial Cells: Synthetic Compartments with Life-like Functionality and Adaptivity”. In: *Accounts of Chemical Research* 50.4 (Apr. 2017), pp. 769–777. URL: https://doi.org/10.1021/acs.accounts.6b00512.

[19] Allen P Liu and Daniel A Fletcher. “Biology under construction: in vitro reconstitution of cellular function”. eng. In: *Nature reviews. Molecular cell biology* 10.9 (Sept. 2009), pp. 644–650. URL: https://pubmed.ncbi.nlm.nih.gov/19672276%20https://www.ncbi.nlm.nih.gov/pmc/articles/PMC2937256/.

[20] Daniel G Gibson et al. “Creation of a Bacterial Cell Controlled by a Chemically Synthesized Genome”. In: *Science* 329.5987 (July 2010), p. 52. URL: http://science.sciencemag.org/content/329/5987/52.abstract.

[21] Clyde A Hutchison et al. “Design and synthesis of a minimal bacterial genome”. In: *Science* 351.6280 (Mar. 2016), aad6253. URL: http://science.sciencemag.org/content/351/6280/aad6253.abstract.

[22] Noël Yeh Martín, Luca Valer, and Sheref S Mansy. “Toward long-lasting artificial cells that better mimic natural living cells”. In: *Emerging Topics in Life Sciences* 3.5 (Sept. 2019), pp. 597–607. URL: https://doi.org/10.1042/ETLS20190026.

[23] Petra Schwille. “Division in synthetic cells”. In: *Emerging Topics in Life Sciences* 3.5 (Sept. 2019), pp. 551–558. URL: https://doi.org/10.1042/ETLS20190023.

[24] Lukas Aufinger and Friedrich C Simmel. “Establishing Communication Between Artificial Cells”. In: *Chemistry – A European Journal* 25.55 (Oct. 2019), pp. 12659–12670. URL: https://doi.org/10.1002/chem.201901726.

[25] Yan Qiao et al. “Predatory behaviour in synthetic protocell communities”. In: *Nature Chemistry* 9.2 (2017), pp. 110–119. URL: https://doi.org/10.1038/nchem.2617.

[26] William L Hwang et al. “Asymmetric Droplet Interface Bilayers”. In: *Journal of the American Chemical Society* 130.18 (May 2008), pp. 5878–5879. URL: https://doi.org/10.1021/ja802089s.

[27] Michael J Booth et al. “Functional aqueous droplet networks”. In: *Molecular BioSystems* 13.9 (2017), pp. 1658–1691. URL: http://dx.doi.org/10.1039/C7MB00192D.

[28] Guru A Venkatesan et al. “Adsorption Kinetics Dictate Monolayer Self-Assembly for Both Lipid-In and Lipid-Out Approaches to Droplet Interface Bilayer Formation”. In: *Langmuir* 31.47 (Dec. 2015), pp. 12883–12893. URL: https://doi.org/10.1021/acs.langmuir.5b02293.

[29] Lingbing Kong et al. “Chemical polyglycosylation and nanolitre detection enables single-molecule recapitulation of bacterial sugar export”. In: *Nature Chemistry* 8.5 (2016), pp. 461–469. URL: https://doi.org/10.1038/nchem.2487.

[30] Stephen A Sarles and Donald J Leo. “Physical encapsulation of droplet interface bilayers for durable, portable biomolecular networks”. In: *Lab on a Chip* 10.6 (2010), pp. 710–717. URL: http://dx.doi.org/10.1039/B916736F.

[31] Vanessa Restrepo Schild et al. “Light-Patterned Current Generation in a Droplet Bilayer Array”. In: *Scientific Reports* 7.1 (2017), p. 46585. URL: https://doi.org/10.1038/srep46585.

[32] Nima Tamaddoni et al. “Reversible, voltage-activated formation of biomimetic membranes between triblock copolymer-coated aqueous droplets in good solvents”. In: *Soft Matter* 12.23 (2016), pp. 5096–5109. URL: http://dx.doi.org/10.1039/C6SM00400H.

[33] Divesh K Baxani et al. “Bilayer Networks within a Hydrogel Shell: A Robust Chassis for Artificial Cells and a Platform for Membrane Studies”. In: *Angewandte Chemie International Edition* 55.46 (Nov. 2016), pp. 14240–14245. URL: https://doi.org/10.1002/anie.201607571.

[34] Mariam Bayoumi et al. “Multi-compartment encapsulation of communicating droplets and droplet networks in hydrogel as a model for artificial cells”. In: *Scientific Reports* 7.1 (2017), p. 45167. URL: https://doi.org/10.1038/srep45167.

[35] Jonathan B Boreyko et al. “Air-stable droplet interface bilayers on oil-infused surfaces”. In: *Proceedings of the National Academy of Sciences* 111.21 (May 2014), p. 7588. URL: http://www.pnas.org/content/111/21/7588.abstract.

[36] Guru A Venkatesan and Stephen A Sarles. “Droplet immobilization within a polymeric organogel improves lipid bilayer durability and portability”. In: *Lab on a Chip* 16.11 (2016), pp. 2116–2125. URL: http://dx.doi.org/10.1039/C6LC00391E.

[37] Ryuji Kawano et al. “A Portable Lipid Bilayer System for Environmental Sensing with a Transmembrane Protein”. In: *PLOS ONE* 9.7 (July 2014), e102427–. URL: https://doi.org/10.1371/journal.pone.0102427.

[38] Andrew J Heron et al. “Direct Detection of Membrane Channels from Gels Using Water-in-Oil Droplet Bilayers”. In: *Journal of the American Chemical Society* 129.51 (Dec. 2007), pp. 16042–16047. URL: https://doi.org/10.1021/ja075715h.

[39] K Tanuj Sapra and Hagan Bayley. “Lipid-coated hydrogel shapes as components of electrical circuits and mechanical devices”. In: *Scientific Reports* 2.1 (2012), p. 848. URL: https://doi.org/10.1038/srep00848.

[40] Alessandro Alcinesio et al. “Controlled packing and single-droplet resolution of 3D-printed functional synthetic tissues”. In: *Nature Communications* 11.1 (2020), p. 2105. URL: https://doi.org/10.1038/s41467-020-15953-y.

[41] Ruhma Syeda et al. “Screening Blockers Against a Potassium Channel with a Droplet Interface Bilayer Array”. In: *Journal of the American Chemical Society* 130.46 (Nov. 2008), pp. 15543–15548. URL: https://doi.org/10.1021/ja804968g.

[42] Sebastian Leptihn et al. “In Vitro Reconstitution of Eukaryotic Ion Channels Using Droplet Interface Bilayers”. In: *Journal of the American Chemical Society* 133.24 (June 2011), pp. 9370–9375. URL: https://doi.org/10.1021/ja200128n.

[43] Joseph S Najem et al. “Activation of bacterial channel MscL in mechanically stimulated droplet interface bilayers”. In: *Scientific Reports* 5.1 (2015), p. 13726. URL: https://doi.org/10.1038/srep13726.

[44] Matthew A Holden, David Needham, and Hagan Bayley. “Functional Bionetworks from Nanoliter Water Droplets”. In: *Journal of the American Chemical Society* 129.27 (July 2007), pp. 8650–8655. URL: https://doi.org/10.1021/ja072292a.

[45] Heather E Findlay, Nicola J Harris, and Paula J Booth. “In vitro synthesis of a Major Facilitator Transporter for specific active transport across Droplet Interface Bilayers”. In: *Scientific Reports* 6.1 (2016), p. 39349. URL: https://doi.org/10.1038/srep39349.

[46] Jonathan R Burns et al. “A biomimetic DNA-based channel for the ligand-controlled transport of charged molecular cargo across a biological membrane”. In: *Nature Nanotechnology* 11.2 (2016), pp. 152–156. URL: https://doi.org/10.1038/nnano.2015.279.

[47] Maxwell Allen-Benton, Heather E Findlay, and Paula J Booth. “Probing membrane protein properties using droplet interface bilayers”. In: *Experimental Biology and Medicine* 244.8 (May 2019), pp. 709–720. URL: https://doi.org/10.1177/1535370219847939.

[48] Hagan Bayley et al. “Droplet interface bilayers”. eng. In: *Molecular bioSystems* 4.12 (Dec. 2008), pp. 1191–1208. URL: https://pubmed.ncbi.nlm.nih.gov/19396383%20https://www.ncbi.nlm.nih.gov/pmc/articles/PMC2763081/.

[49] Giovanni Maglia et al. “Droplet networks with incorporated protein diodes show collective properties”. In: *Nature Nanotechnology* 4.7 (2009), pp. 437–440. URL: https://doi.org/10.1038/nnano.2009.121.

[50] Gabriel Villar, Alexander D Graham, and Hagan Bayley. “A Tissue-Like Printed Material”. In: *Science* 340.6128 (Apr. 2013), p. 48. URL: http://science.sciencemag.org/content/340/6128/48.abstract.

[51] Stéphane Renauld et al. “Functional reconstitution of cell-free synthesized purified Kv channels”. In: *Biochimica et Biophysica Acta (BBA) - Biomembranes* 1859.12 (2017), pp. 2373–2380. URL: https://www.sciencedirect.com/science/article/pii/S0005273617302766.

[52] Michael J Booth et al. “Light-activated communication in synthetic tissues”. In: *Science Advances* 2.4 (Apr. 2016), e1600056. URL: http://advances.sciencemag.org/content/2/4/e1600056.abstract.

[53] Michael J Booth et al. “Light-patterning of synthetic tissues with single droplet resolution”. In: *Scientific Reports* 7.1 (2017), p. 9315. URL: https://doi.org/10.1038/s41598-017-09394-9.

[54] Oliver K Castell, James Berridge, and Mark I Wallace. “Quantification of Membrane Protein Inhibition by Optical Ion Flux in a Droplet Interface Bilayer Array”. In: *Angewandte Chemie International Edition* 51.13 (Mar. 2012), pp. 3134–3138. URL: https://doi.org/10.1002/anie.201107343.

[55] Audrey Fischer et al. “Ultrasensitive detection of protein translocated through toxin pores in droplet-interface bilayers”. In: *Proceedings of the National Academy of Sciences* 108.40 (Oct. 2011), p. 16577. URL: http://www.pnas.org/content/108/40/16577.abstract.

[56] Shuo Huang et al. “High-throughput optical sensing of nucleic acids in a nanopore array”. In: *Nature Nanotechnology* 10.11 (2015), pp. 986–991. URL: https://doi.org/10.1038/nnano.2015.189.

[57] Yuval Elani et al. “Microfluidic generation of encapsulated droplet interface bilayer networks (multisomes) and their use as cell-like reactors”. In: *Chemical Communications* 52.35 (2016), pp. 5961–5964. URL: http://dx.doi.org/10.1039/C6CC01434H.

[58] Takeshi Ohya et al. “Reconstitution of Rab- and SNARE-dependent membrane fusion by synthetic endosomes”. In: *Nature* 459.7250 (2009), pp. 1091–1097. URL: https://doi.org/10.1038/nature08107.

[59] Prachya Mruetusatorn et al. “Dynamic morphologies of microscale droplet interface bilayers”. In: *Soft Matter* 10.15 (2014), pp. 2530–2538. URL: http://dx.doi.org/10.1039/C3SM53032A.

[60] David Zwicker et al. “Growth and division of active droplets provides a model for protocells”. In: *Nature Physics* 13.4 (2017), pp. 408–413. URL: https://doi.org/10.1038/nphys3984.

[61] Yuval Elani, Robert V Law, and Oscar Ces. “Protein synthesis in artificial cells: using compartmentalisation for spatial organisation in vesicle bioreactors”. In: *Physical Chemistry Chemical Physics* 17.24 (2015), pp. 15534–15537. URL: http://dx.doi.org/10.1039/C4CP05933F.

[62] Jan Guzowski et al. “Microfluidic platform for reproducible self-assembly of chemically communicating droplet networks with predesigned number and type of the communicating compartments”. In: *Lab on a Chip* 16.4 (2016), pp. 764–772. URL: http://dx.doi.org/10.1039/C5LC01526J.

[63] Michael J Booth, Idil Cazimoglu, and Hagan Bayley. “Controlled deprotection and release of a small molecule from a compartmented synthetic tissue module”. In: *Communications Chemistry* 2.1 (2019), p. 142. URL: https://doi.org/10.1038/s42004-019-0244-y.

[64] P Carreras et al. “A microfluidic platform for size-dependent generation of droplet interface bilayer networks on rails”. In: *Biomicrofluidics* 9.6 (Nov. 2015), p. 064121. URL: https://doi.org/10.1063/1.4938731.

[65] Aurore Dupin and Friedrich C Simmel. “Signalling and differentiation in emulsion-based multi-compartmentalized in vitro gene circuits”. In: *Nature Chemistry* 11.1 (2019), pp. 32–39. URL: https://doi.org/10.1038/s41557-018-0174-9.

[66] Shashi Thutupalli and Stephan Herminghaus. “Tuning active emulsion dynamics via surfactants and topology”. In: *The European Physical Journal E* 36.8 (2013), p. 91. URL: https://doi.org/10.1140/epje/i2013-13091-2.

[67] Gareth Jones et al. “Autonomous Droplet Architectures”. In: *Artificial Life* 21.2 (May 2015), pp. 195–204. URL: https://doi.org/10.1162/ARTL_a_00156.

[68] Abolfazl Akbarzadeh et al. “Liposome: classification, preparation, and applications”. In: *Nanoscale Research Letters* 8.1 (2013), p. 102. URL: https://doi.org/10.1186/1556-276X-8-102.

[69] Manuela Dezi et al. “Detergent-mediated incorporation of transmembrane proteins in giant unilamellar vesicles with controlled physiological contents”. eng. In: *Proceedings of the National Academy of Sciences of the United States of America* 110.18 (Apr. 2013), pp. 7276–7281. URL: https://pubmed.ncbi.nlm.nih.gov/23589883%20https://www.ncbi.nlm.nih.gov/pmc/articles/PMC3645586/.

[70] Henrike Niederholtmeyer, Cynthia Chaggan, and Neal K Devaraj. “Communication and quorum sensing in non-living mimics of eukaryotic cells”. In: *Nature Communications* 9.1 (2018), p. 5027. URL: https://doi.org/10.1038/s41467-018-07473-7.

[71] Thomas Litschel et al. “Beating Vesicles: Encapsulated Protein Oscillations Cause Dynamic Membrane Deformations”. In: *Angewandte Chemie International Edition* 57.50 (Dec. 2018), pp. 16286–16290. URL: https://doi.org/10.1002/anie.201808750.

[72] Daniela A Wilson, Roeland J M Nolte, and Jan C M van Hest. “Autonomous movement of platinum-loaded stomatocytes”. In: *Nature Chemistry* 4.4 (2012), pp. 268–274. URL: https://doi.org/10.1038/nchem.1281.

[73] Nan-Nan Deng et al. “Microfluidic Assembly of Monodisperse Vesosomes as Artificial Cell Models”. In: *Journal of the American Chemical Society* 139.2 (Jan. 2017), pp. 587–590. URL: https://doi.org/10.1021/jacs.6b10977.

[74] James W Hindley et al. “Building a synthetic mechanosensitive signaling pathway in compartmentalized artificial cells”. In: *Proceedings of the National Academy of Sciences* 116.34 (Aug. 2019), p. 16711. URL: http://www.pnas.org/content/116/34/16711.abstract.

[75] Maria Godoy-Gallardo et al. “Multicompartment Artificial Organelles Conducting Enzymatic Cascade Reactions inside Cells”. In: *ACS Applied Materials & Interfaces* 9.19 (May 2017), pp. 15907–15921. URL: https://doi.org/10.1021/acsami.6b16275.

[76] Ruud J R W Peters et al. “Cascade Reactions in Multicompartmentalized Polymersomes”. In: *Angewandte Chemie International Edition* 53.1 (Jan. 2014), pp. 146–150. URL: https://doi.org/10.1002/anie.201308141.

[77] Katarzyna P Adamala et al. “Engineering genetic circuit interactions within and between synthetic minimal cells”. eng. In: *Nature chemistry* 9.5 (May 2017), pp. 431–439. URL: https://pubmed.ncbi.nlm.nih.gov/28430194%20https://www.ncbi.nlm.nih.gov/pmc/articles/PMC5407321/.

[78] Kilian Vogele et al. “Towards synthetic cells using peptide-based reaction compartments”. In: *Nature Communications* 9.1 (2018), p. 3862. URL: https://doi.org/10.1038/s41467-018-06379-8.

[79] Pauline van Nies et al. “Self-replication of DNA by its encoded proteins in liposome-based synthetic cells”. In: *Nature Communications* 9.1 (2018), p. 1583. URL: https://doi.org/10.1038/s41467-018-03926-1.

[80] Eyal Karzbrun et al. “Programmable on-chip DNA compartments as artificial cells”. In: *Science* 345.6198 (Aug. 2014), p. 829. URL: http://science.sciencemag.org/content/345/6198/829.abstract.

[81] Vincent Noireaux and Albert Libchaber. “A vesicle bioreactor as a step toward an artificial cell assembly”. In: *Proceedings of the National Academy of Sciences of the United States of America* 101.51 (Dec. 2004), p. 17669. URL: http://www.pnas.org/content/101/51/17669.abstract.

[82] Rylie A Green et al. “Conducting polymer-hydrogels for medical electrode applications”. In: *Science and Technology of Advanced Materials* 11.1 (2010), p. 014107. URL: http://dx.doi.org/10.1088/1468-6996/11/1/014107.

[83] J Thiele et al. “DNA-functionalized hydrogels for confined membrane-free in vitro transcription/translation”. In: *Lab on a Chip* 14.15 (2014), pp. 2651–2656. URL: http://dx.doi.org/10.1039/C3LC51427G.

[84] Lukas Aufinger and Friedrich C Simmel. “Artificial Gel-Based Organelles for Spatial Organization of Cell-Free Gene Expression Reactions”. In: *Angewandte Chemie International Edition* 57.52 (Dec. 2018), pp. 17245–17248. URL: https://doi.org/10.1002/anie.201809374.

[85] Keel Yong Lee et al. “Photosynthetic artificial organelles sustain and control ATP-dependent reactions in a protocellular system”. In: *Nature Biotechnology* 36.6 (2018), pp. 530–535. URL: https://doi.org/10.1038/nbt.4140.

[86] Tjeerd Pols et al. “A synthetic metabolic network for physicochemical homeostasis”. In: *Nature Communications* 10.1 (2019), p. 4239. URL: https://doi.org/10.1038/s41467-019-12287-2.

[87] Hyo-Jick Choi and Carlo D Montemagno. “Artificial Organelle: ATP Synthesis from Cellular Mimetic Polymersomes”. In: *Nano Letters* 5.12 (Dec. 2005), pp. 2538–2542. URL: https://doi.org/10.1021/nl051896e.

[88] Siddharth Deshpande et al. “Mechanical Division of Cell-Sized Liposomes”. In: *ACS Nano* 12.3 (Mar. 2018), pp. 2560–2568. URL: https://doi.org/10.1021/acsnano.7b08411.

[89] Masaki Osawa, David E Anderson, and Harold P Erickson. “Reconstitution of Contractile FtsZ Rings in Liposomes”. In: *Science* 320.5877 (May 2008), p. 792. URL: http://science.sciencemag.org/content/320/5877/792.abstract.

[90] Rohan Fernandes et al. “Engineered biological nanofactories trigger quorum sensing response in targeted bacteria”. In: *Nature Nanotechnology* 5.3 (2010), pp. 213–217. URL: https://doi.org/10.1038/nnano.2009.457.

[91] Roberta Lentini et al. “Integrating artificial with natural cells to translate chemical messages that direct E. coli behaviour”. In: *Nature Communications* 5.1 (2014), p. 4012. URL: https://doi.org/10.1038/ncomms5012.

[92] Florence G Downs et al. “Multi-responsive hydrogel structures from patterned droplet networks”. eng. In: *Nature chemistry* 12.4 (Apr. 2020), pp. 363–371. URL: https://pubmed.ncbi.nlm.nih.gov/32221498%20https://www.ncbi.nlm.nih.gov/pmc/articles/PMC7117959/.

[93] Tobias Wauer et al. “Construction and Manipulation of Functional Three-Dimensional Droplet Networks”. In: *ACS Nano* 8.1 (Jan. 2014), pp. 771–779. URL: https://doi.org/10.1021/nn405433y.

[94] Mark S Friddin et al. “Optically assembled droplet interface bilayer (OptiDIB) networks from cell-sized microdroplets”. In: *Soft Matter* 12.37 (2016), pp. 7731–7734. URL: http://dx.doi.org/10.1039/C6SM01357K.

[95] Guido Bolognesi et al. “Sculpting and fusing biomimetic vesicle networks using optical tweezers”. In: *Nature Communications* 9.1 (2018), p. 1882. URL: https://doi.org/10.1038/s41467-018-04282-w.

[96] Sanhita S Dixit et al. “Light-Driven Formation and Rupture of Droplet Bilayers”. In: *Langmuir* 26.9 (May 2010), pp. 6193–6200. URL: https://doi.org/10.1021/la1010067.

[97] Yuval Elani et al. “Novel technologies for the formation of 2-D and 3-D droplet interface bilayer networks”. In: *Lab on a Chip* 12.18 (2012), pp. 3514–3520. URL: http://dx.doi.org/10.1039/C2LC40287D.

[98] Luoran Shang, Yao Cheng, and Yuanjin Zhao. “Emerging Droplet Microfluidics”. In: *Chemical Reviews* 117.12 (June 2017), pp. 7964–8040. URL: https://doi.org/10.1021/acs.chemrev.6b00848.

[99] Magdalena A Czekalska et al. “A droplet microfluidic system for sequential generation of lipid bilayers and transmembrane electrical recordings”. In: *Lab on a Chip* 15.2 (2015), pp. 541–548. URL: http://dx.doi.org/10.1039/C4LC00985A.

[100] Vanessa Restrepo Schild et al. “A Soft Bioelectric Implant Modulates Cellular Behaviour”.

[101] Simon Bachler et al. “Microfluidic platform enables tailored translocation and reaction cascades in nanoliter droplet networks”. In: *Communications Biology* 3.1 (2020), p. 769. URL: https://doi.org/10.1038/s42003-020-01489-w.

[102] Gabriel Villar, Andrew J Heron, and Hagan Bayley. “Formation of droplet networks that function in aqueous environments”. In: *Nature Nanotechnology* 6.12 (2011), pp. 803–808. URL: https://doi.org/10.1038/nnano.2011.183.

[103] Alexander D Graham et al. “High-Resolution Patterned Cellular Constructs by Droplet-Based 3D Printing”. In: *Scientific Reports* 7.1 (2017), p. 7004. URL: https://doi.org/10.1038/s41598-017-06358-x.

[104] Christina K Kim, Avishek Adhikari, and Karl Deisseroth. “Integration of optogenetics with complementary methodologies in systems neuroscience”. In: *Nature Reviews Neuroscience* 18.4 (2017), pp. 222–235. URL: https://doi.org/10.1038/nrn.2017.15.

[105] Jon Dobson. “Remote control of cellular behaviour with magnetic nanoparticles”. In: *Nature Nanotechnology* 3.3 (2008), pp. 139–143. URL: https://doi.org/10.1038/nnano.2008.39.

[106] Pierangelo Gobbo et al. “Programmed assembly of synthetic protocells into thermoresponsive prototissues”. In: *Nature Materials* 17.12 (2018), pp. 1145–1153. URL: https://doi.org/10.1038/s41563-018-0183-5.

[107] Ravinash Krishna Kumar et al. “Self-transformation and structural reconfiguration in coacervate-based protocells”. In: *Chemical Science* 7.9 (2016), pp. 5879–5887. URL: http://dx.doi.org/10.1039/C6SC00205F.

[108] Angelo Cangialosi et al. “DNA sequence–directed shape change of photopatterned hydrogels via high-degree swelling”. In: *Science* 357.6356 (Sept. 2017), p. 1126. URL: http://science.sciencemag.org/content/357/6356/1126.abstract.

[109] Amirali Nojoomi et al. “Bioinspired 3D structures with programmable morphologies and motions”. In: *Nature Communications* 9.1 (2018), p. 3705. URL: https://doi.org/10.1038/s41467-018-05569-8.

[110] Ravinash Krishna Kumar et al. “Cytoskeletal-like Supramolecular Assembly and Nanoparticle-Based Motors in a Model Protocell”. In: *Angewandte Chemie International Edition* 50.40 (Sept. 2011), pp. 9343–9347. URL: https://doi.org/10.1002/anie.201102628.

[111] Stephen A Sarles and Donald J Leo. “Membrane-based biomolecular smart materials”. In: *Smart Materials and Structures* 20.9 (2011), p. 094018. URL: http://dx.doi.org/10.1088/0964-1726/20/9/094018.

[112] K Kovalev et al. “High-resolution structural insights into the heliorhodopsin family”. In: *Proceedings of the National Academy of Sciences* 117.8 (Feb. 2020), p. 4131. URL: http://www.pnas.org/content/117/8/4131.abstract.

[113] Alina Pushkarev et al. “A distinct abundant group of microbial rhodopsins discovered using functional metagenomics”. In: *Nature* 558.7711 (2018), pp. 595–599. URL: https://doi.org/10.1038/s41586-018-0225-9.

[114] J L Spudich and R A Bogomolni. “Mechanism of colour discrimination by a bacterial sensory rhodopsin”. eng. In: *Nature* 312.5994 (Dec. 1984), pp. 509–513. URL: https://pubmed.ncbi.nlm.nih.gov/6504161%20https://www.ncbi.nlm.nih.gov/pmc/articles/PMC4996264/.

[115] Dieter Oesterhelt and Walther Stoeckenius. “Functions of a New Photoreceptor Membrane”. In: *Proceedings of the National Academy of Sciences* 70.10 (Oct. 1973), p. 2853. URL: http://www.pnas.org/content/70/10/2853.abstract.

[116] Oded Béjà et al. “Bacterial Rhodopsin: Evidence for a New Type of Phototrophy in the Sea”. In: *Science* 289.5486 (Sept. 2000), p. 1902. URL: http://science.sciencemag.org/content/289/5486/1902.abstract.

[117] X Edward Zhou, Karsten Melcher, and H Eric Xu. “Structure and activation of rhodopsin”. eng. In: *Acta pharmacologica Sinica* 33.3 (Mar. 2012), pp. 291–299. URL: https://pubmed.ncbi.nlm.nih.gov/22266727%20https://www.ncbi.nlm.nih.gov/pmc/articles/PMC3677203/.

[118] Jarone Pinhassi et al. “Marine Bacterial and Archaeal Ion-Pumping Rhodopsins: Genetic Diversity, Physiology, and Ecology”. eng. In: *Microbiology and molecular biology reviews : MMBR* 80.4 (Sept. 2016), pp. 929–954. URL: https://pubmed.ncbi.nlm.nih.gov/27630250%20https://www.ncbi.nlm.nih.gov/pmc/articles/PMC5116876/.

[119] Oren Froy et al. “Illuminating the Circadian Clock in Monarch Butterfly Migration”. In: *Science* 300.5623 (May 2003), p. 1303. URL: http://science.sciencemag.org/content/300/5623/1303.abstract.

[120] Georg Nagel et al. “Channelrhodopsin-2, a directly light-gated cation-selective membrane channel”. eng. In: *Proceedings of the National Academy of Sciences of the United States of America* 100.24 (Nov. 2003), pp. 13940–13945. URL: https://pubmed.ncbi.nlm.nih.gov/14615590%20https://www.ncbi.nlm.nih.gov/pmc/articles/PMC283525/.

[121] Brian Y Chow et al. “High-performance genetically targetable optical neural silencing by light-driven proton pumps”. In: *Nature* 463.7277 (2010), pp. 98–102. URL: https://doi.org/10.1038/nature08652.

[122] R Henderson and P N T Unwin. “Three-dimensional model of purple membrane obtained by electron microscopy”. In: *Nature* 257.5521 (1975), pp. 28–32. URL: https://doi.org/10.1038/257028a0.

[123] Leonid S Brown and Oliver P Ernst. “Recent advances in biophysical studies of rhodopsins – Oligomerization, folding, and structure”. In: *Biochimica et Biophysica Acta (BBA) - Proteins and Proteomics* 1865.11, Part B (2017), pp. 1512–1521. URL: https://www.sciencedirect.com/science/article/pii/S1570963917301875.

[124] Georg Nagel et al. “Channelrhodopsin-1: A Light-Gated Proton Channel in Green Algae”. In: *Science* 296.5577 (June 2002), p. 2395. URL: http://science.sciencemag.org/content/296/5577/2395.abstract.

[125] Ying Fan et al. “Photochemical characterization of a novel fungal rhodopsin from Phaeosphaeria nodorum”. In: *Biochimica et Biophysica Acta (BBA) - Bioenergetics* 1807.11 (2011), pp. 1457–1466. URL: http://www.sciencedirect.com/science/article/pii/S000527281100171X.

[126] David M Needham et al. “A distinct lineage of giant viruses brings a rhodopsin photosystem to unicellular marine predators”. In: *Proceedings of the National Academy of Sciences* 116.41 (Oct. 2019), p. 20574. URL: http://www.pnas.org/content/116/41/20574.abstract.

[127] Dmitry Bratanov et al. “An Approach to Heterologous Expression of Membrane Proteins. The Case of Bacteriorhodopsin”. In: *PLOS ONE* 10.6 (June 2015), e0128390–. URL: https://doi.org/10.1371/journal.pone.0128390.

[128] Elena G Govorunova et al. “Microbial Rhodopsins: Diversity, Mechanisms, and Optogenetic Applications”. eng. In: *Annual review of biochemistry* 86 (2017), pp. 845–872. URL: http://europepmc.org/abstract/MED/28301742%20https://doi.org/10.1146/annurev-biochem-101910-144233%20https://europepmc.org/articles/PMC5747503%20https://europepmc.org/articles/PMC5747503?pdf=render%20https://doi.org/10.1146/annurev-biochem-101910-144233.

[129] Keiichi Inoue et al. “Converting a Light-Driven Proton Pump into a Light-Gated Proton Channel”. In: *Journal of the American Chemical Society* 137.9 (Mar. 2015), pp. 3291–3299. URL: https://doi.org/10.1021/ja511788f.

[130] Yu-Tao Li et al. “A Review on Bacteriorhodopsin-Based Bioelectronic Devices”. eng. In: *Sensors (Basel, Switzerland)* 18.5 (Apr. 2018), p. 1368. URL: https://pubmed.ncbi.nlm.nih.gov/29702621%20https://www.ncbi.nlm.nih.gov/pmc/articles/PMC5982678/.

[131] Karl Deisseroth. “Optogenetics”. In: *Nature Methods* 8.1 (2011), pp. 26–29. URL: https://doi.org/10.1038/nmeth.f.324.

[132] Erika Pastrana. “Optogenetics: controlling cell function with light”. In: *Nature Methods* 8.1 (2011), pp. 24–25. URL: https://doi.org/10.1038/nmeth.f.323.

[133] ALLEN E BLAUROCK and WALTHER STOECKENIUS. “Structure of the Purple Membrane”. In: *Nature New Biology* 233.39 (1971), pp. 152–155. URL: https://doi.org/10.1038/newbio233152a0.

[134] T Renner and N Hampp. “Bacteriorhodopsin-films for dynamic time average interferometry”. In: *Optics Communications* 96.1 (1993), pp. 142–149. URL: https://www.sciencedirect.com/science/article/pii/003040189390537F.

[135] Colin D Heyes and Mostafa A El-Sayed. “The Role of the Native Lipids and Lattice Structure in Bacteriorhodopsin Protein Conformation and Stability as Studied by Temperature-dependent Fourier Transform-Infrared Spectroscopy *”. In: *Journal of Biological Chemistry* 277.33 (Aug. 2002), pp. 29437–29443. URL: https://doi.org/10.1074/jbc.M203435200.

[136] Manoj K Joshi et al. “Importance of Specific Native Lipids in Controlling the Photocycle of Bacteriorhodopsin”. In: *Biochemistry* 37.41 (Oct. 1998), pp. 14463–14470. URL: https://doi.org/10.1021/bi980965j.

[137] N Grigorieff et al. “Electron-crystallographic Refinement of the Structure of Bacteriorhodopsin”. In: *Journal of Molecular Biology* 259.3 (1996), pp. 393–421. URL: https://www.sciencedirect.com/science/article/pii/S0022283696903289.

[138] Cecilia Wickstrand et al. “Bacteriorhodopsin: Would the real structural intermediates please stand up?” In: *Biochimica et Biophysica Acta (BBA) - General Subjects* 1850.3 (2015), pp. 536–553. URL: http://www.sciencedirect.com/science/article/pii/S0304416514002190.

[139] Hartmut Luecke, Hans-Thomas Richter, and Janos K Lanyi. “Proton Transfer Pathways in Bacteriorhodopsin at 2.3 Angstrom Resolution”. In: *Science* 280.5371 (June 1998), p. 1934. URL: http://science.sciencemag.org/content/280/5371/1934.abstract.

[140] H J Butt et al. “Aspartic acids 96 and 85 play a central role in the function of bacteriorhodopsin as a proton pump”. eng. In: *The EMBO journal* 8.6 (June 1989), pp. 1657–1663. URL: https://pubmed.ncbi.nlm.nih.gov/2548851%20https://www.ncbi.nlm.nih.gov/pmc/articles/PMC401006/.

[141] Antoine Royant et al. “Helix deformation is coupled to vectorial proton transport in the photocycle of bacteriorhodopsin”. In: *Nature* 406.6796 (2000), pp. 645–648. URL: https://doi.org/10.1038/35020599.

[142] Hans Jürgen Sass et al. “Structural alterations for proton translocation in the M state of wild-type bacteriorhodopsin”. In: *Nature* 406.6796 (2000), pp. 649–653. URL: https://doi.org/10.1038/35020607.

[143] Eriko Nango et al. “A three-dimensional movie of structural changes in bacteriorhodopsin”. In: *Science* 354.6319 (Dec. 2016), p. 1552. URL: http://science.sciencemag.org/content/354/6319/1552.abstract.

[144] Yasuo Mukohata et al. “An Australian halobacterium contains a novel proton pump retinal protein: Archaerhodopsin”. In: *Biochemical and Biophysical Research Communications* 151.3 (1988), pp. 1339–1345. URL: http://www.sciencedirect.com/science/article/pii/S0006291X88805096.

[145] Koichi Uegaki, Yasuo Sugiyama, and Yasuo Mukohata. “Archaerhodopsin-2, from Halobacterium sp. aus-2 further reveals essential amino acid residues for light-driven proton pumps”. In: *Archives of Biochemistry and Biophysics* 286.1 (1991), pp. 107–110. URL: http://www.sciencedirect.com/science/article/pii/000398619190014A.

[146] Aharon Oren. “Bacteriorhodopsin-mediated CO2 photoassimilation in the Dead Sea1”. In: *Limnology and Oceanography* 28.1 (Jan. 1983), pp. 33–41. URL: https://doi.org/10.4319/lo.1983.28.1.0033.

[147] Kunio Ihara et al. “Evolution of the archaeal rhodopsins: evolution rate changes by gene duplication and functional differentiation11Edited by G. Von Heijnel”. In: *Journal of Molecular Biology* 285.1 (1999), pp. 163–174. URL: http://www.sciencedirect.com/science/article/pii/S0022283698922860.

[148] Qingguo Li et al. “Newly isolated archaerhodopsin from a strain of Chinese halobacteria and its proton pumping behavior”. In: *Biochimica et Biophysica Acta (BBA) - Biomembranes* 1466.1 (2000), pp. 260–266. URL: https://www.sciencedirect.com/science/article/pii/S0005273600001887.

[149] Ming Ming et al. “pH dependence of light-driven proton pumping by an archaerhodopsin from Tibet: comparison with bacteriorhodopsin”. eng. In: *Biophysical journal* 90.9 (May 2006), pp. 3322–3332. URL: https://pubmed.ncbi.nlm.nih.gov/16473896%20https://www.ncbi.nlm.nih.gov/pmc/articles/PMC1432102/.

[150] Juan F Bada Juarez et al. “Structures of the archaerhodopsin-3 transporter reveal that disordering of internal water networks underpins receptor sensitization”. In: *Nature Communications* 12.1 (2021), p. 629. URL: https://doi.org/10.1038/s41467-020-20596-0.

[151] Keiko Yoshimura and Tsutomu Kouyama. “Structural Role of Bacterioruberin in the Trimeric Structure of Archaerhodopsin-2”. In: *Journal of Molecular Biology* 375.5 (2008), pp. 1267–1281. URL: http://www.sciencedirect.com/science/article/pii/S0022283607015100.

[152] Ian D Dundas and Helge Larsen. “The physiological role of the carotenoid pigments of halobacterium salinarium”. In: *Archiv für Mikrobiologie* 44.3 (1962), pp. 233–239. URL: https://doi.org/10.1007/BF00510943.

[153] Vladimir A Boichenko et al. “Functions of carotenoids in xanthorhodopsin and archaerhodopsin, from action spectra of photoinhibition of cell respiration”. eng. In: *Biochimica et biophysica acta* 1757.12 (Dec. 2006), pp. 1649–1656. URL: https://pubmed.ncbi.nlm.nih.gov/17020745%20https://www.ncbi.nlm.nih.gov/pmc/articles/PMC1761948/.

[154] Dougal Maclaurin et al. “Mechanism of voltage-sensitive fluorescence in a microbial rhodopsin”. In: *Proceedings of the National Academy of Sciences* 110.15 (Apr. 2013), p. 5939. URL: http://www.pnas.org/content/110/15/5939.abstract.

[155] Karl Deisseroth and Peter Hegemann. “The form and function of channelrhodopsin”. In: *Science* 357.6356 (Sept. 2017), eaan5544. URL: http://science.sciencemag.org/content/357/6356/eaan5544.abstract.

[156] Elena G Govorunova et al. “NEUROSCIENCE. Natural light-gated anion channels: A family of microbial rhodopsins for advanced optogenetics”. eng. In: *Science (New York, N.Y.)* 349.6248 (Aug. 2015), pp. 647–650. URL: https://pubmed.ncbi.nlm.nih.gov/26113638%20https://www.ncbi.nlm.nih.gov/pmc/articles/PMC4764398/.

[157] Jonas Wietek et al. “Conversion of Channelrhodopsin into a Light-Gated Chloride Channel”. In: *Science* 344.6182 (Apr. 2014), p. 409. URL: http://science.sciencemag.org/content/344/6182/409.abstract.

[158] Oleksandr Volkov et al. “Structural insights into ion conduction by channelrhodopsin 2”. In: *Science* 358.6366 (Nov. 2017), eaan8862. URL: http://science.sciencemag.org/content/358/6366/eaan8862.abstract.

[159] Christian Bamann et al. “Spectral Characteristics of the Photocycle of Channelrhodopsin-2 and Its Implication for Channel Function”. In: *Journal of Molecular Biology* 375.3 (2008), pp. 686–694. URL: http://www.sciencedirect.com/science/article/pii/S0022283607014301.

[160] Katrin Feldbauer et al. “Channelrhodopsin-2 is a leaky proton pump”. In: *Proceedings of the National Academy of Sciences* 106.30 (July 2009), p. 12317. URL: http://www.pnas.org/content/106/30/12317.abstract.

[161] B Schobert and J K Lanyi. “Halorhodopsin is a light-driven chloride pump.” In: *Journal of Biological Chemistry* 257.17 (Sept. 1982), pp. 10306–10313. URL: https://doi.org/10.1016/S0021-9258(18)34020-1.

[162] Keiichi Inoue et al. “Schizorhodopsins: A family of rhodopsins from Asgard archaea that function as light-driven inward H⁺ pumps”. In: *Science Advances* 6.15 (Apr. 2020), eaaz2441. URL: http://advances.sciencemag.org/content/6/15/eaaz2441.abstract.

[163] Sergei P Balashov et al. “Xanthorhodopsin: A Proton Pump with a Light-Harvesting Carotenoid Antenna”. In: *Science* 309.5743 (Sept. 2005), p. 2061. URL: http://science.sciencemag.org/content/309/5743/2061.abstract.

[164] Kirill Kovalev et al. “Structure and mechanisms of sodium-pumping KR2 rhodopsin”. In: *Science Advances* 5.4 (Apr. 2019), eaav2671. URL: http://advances.sciencemag.org/content/5/4/eaav2671.abstract.

[165] I Lutz et al. “Primary reactions of sensory rhodopsins”. In: *Proceedings of the National Academy of Sciences* 98.3 (Jan. 2001), p. 962. URL: http://www.pnas.org/content/98/3/962.abstract.

[166] Shatanik Mukherjee, Peter Hegemann, and Matthias Broser. “Enzymerhodopsins: novel photoregulated catalysts for optogenetics”. In: *Current Opinion in Structural Biology* 57 (2019), pp. 118–126. URL: https://www.sciencedirect.com/science/article/pii/S0959440X18301775.

[167] Leonid S Brown. “Fungal rhodopsins and opsin-related proteins: eukaryotic homologues of bacteriorhodopsin with unknown functions”. In: *Photochemical & Photobiological Sciences* 3.6 (2004), pp. 555–565. URL: http://dx.doi.org/10.1039/B315527G.

[168] Dmitry Bratanov et al. “Unique structure and function of viral rhodopsins”. In: *Nature Communications* 10.1 (2019), p. 4939. URL: https://doi.org/10.1038/s41467-019-12718-0.

[169] Vitaly Shevchenko et al. “Inward H⁺ pump xenorhodopsin: Mechanism and alternative optogenetic approach”. In: *Science Advances* 3.9 (Sept. 2017), e1603187. URL: http://advances.sciencemag.org/content/3/9/e1603187.abstract.

[170] Juan A Ugalde et al. “Xenorhodopsins, an enigmatic new class of microbial rhodopsins horizontally transferred between archaea and bacteria”. In: *Biology Direct* 6.1 (2011), p. 52. URL: https://doi.org/10.1186/1745-6150-6-52.

[171] F Crick. “The impact of molecular biology on neuroscience”. eng. In: *Philosophical transactions of the Royal Society of London. Series B, Biological sciences* 354.1392 (Dec. 1999), pp. 2021–2025. URL: https://pubmed.ncbi.nlm.nih.gov/10670022%20https://www.ncbi.nlm.nih.gov/pmc/articles/PMC1692710/.

[172] Edward S Boyden et al. “Millisecond-timescale, genetically targeted optical control of neural activity”. In: *Nature Neuroscience* 8.9 (2005), pp. 1263–1268. URL: https://doi.org/10.1038/nn1525.

[173] Joel M Kralj et al. “Optical recording of action potentials in mammalian neurons using a microbial rhodopsin”. In: *Nature Methods* 9.1 (2012), pp. 90–95. URL: https://doi.org/10.1038/nmeth.1782.

[174] Elena G Govorunova et al. “Extending the Time Domain of Neuronal Silencing with Cryptophyte Anion Channelrhodopsins”. eng. In: *eNeuro* 5.3 (July 2018), pp. 0174–18. URL: https://pubmed.ncbi.nlm.nih.gov/30027111%20https://www.ncbi.nlm.nih.gov/pmc/articles/PMC6051594/.

[175] Cristian Cosentino et al. “Engineering of a light-gated potassium channel”. In: *Science* 348.6235 (May 2015), p. 707. URL: http://science.sciencemag.org/content/348/6235/707.abstract.

[176] M Papanatsiou et al. “Optogenetic manipulation of stomatal kinetics improves carbon assimilation, water use, and growth”. In: *Science* 363.6434 (Mar. 2019), p. 1456. URL: http://science.sciencemag.org/content/363/6434/1456.abstract.

[177] Joel M Kralj et al. “Electrical Spiking in Escherichia coli Probed with a Fluorescent Voltage-Indicating Protein”. In: *Science* 333.6040 (July 2011), p. 345. URL: http://science.sciencemag.org/content/333/6040/345.abstract.

[178] R Scott McIsaac et al. “Directed evolution of a far-red fluorescent rhodopsin”. In: *Proceedings of the National Academy of Sciences* 111.36 (Sept. 2014), p. 13034. URL: http://www.pnas.org/content/111/36/13034.abstract.

[179] Negin Azimi Hashemi et al. “Rhodopsin-based voltage imaging tools for use in muscles and neurons of Caenorhabditis elegans” in: *Proceedings of the National Academy of Sciences* 116.34 (Aug. 2019), p. 17051. URL: http://www.pnas.org/content/116/34/17051.abstract.

[180] Michael Z Lin and Mark J Schnitzer. “Genetically encoded indicators of neuronal activity”. In: *Nature Neuroscience* 19.9 (2016), pp. 1142–1153. URL: https://doi.org/10.1038/nn.4359.

[181] Yiyang Gong et al. “High-speed recording of neural spikes in awake mice and flies with a fluorescent voltage sensor”. In: *Science* 350.6266 (Dec. 2015), p. 1361. URL: http://science.sciencemag.org/content/350/6266/1361.abstract.

[182] Raheleh Mohammadpour and Sajad Janfaza. “Efficient Nanostructured Biophotovoltaic Cell Based on Bacteriorhodopsin as Biophotosensitizer”. In: *ACS Sustainable Chemistry & Engineering* 3.5 (May 2015), pp. 809–813. URL: https://doi.org/10.1021/sc500617w.

[183] Norbert Hampp. “Bacteriorhodopsin as a Photochromic Retinal Protein for Optical Memories”. In: *Chemical Reviews* 100.5 (May 2000), pp. 1755–1776. URL: https://doi.org/10.1021/cr980072x.

[184] Pardis Saeedi et al. “Bacteriorhodopsin and its Mutants allude a breakthrough impending to artificial retina construction and strategies for curing blindness”. In: 2 (Jan. 2011).

[185] S W Cline and W F Doolittle. “Efficient transfection of the archaebacterium Halobacterium halobium”. eng. In: *Journal of bacteriology* 169.3 (Mar. 1987), pp. 1341–1344. URL: https://pubmed.ncbi.nlm.nih.gov/3818549%20https://www.ncbi.nlm.nih.gov/pmc/articles/PMC211943/.

[186] Javier Vinals Camallonga. “Biophysical studies on the structure and function of Archaerhodopsin-3”. PhD thesis. Oxford: University of Oxford, 2019.

[187] Zhen Cao et al. “Novel expression and characterization of a light driven proton pump archaerhodopsin 4 in a Halobacterium salinarum strain”. In: *Biochimica et Biophysica Acta (BBA) - Bioenergetics* 1847.4 (2015), pp. 390–398. URL: https://www.sciencedirect.com/science/article/pii/S0005272814006744.

[188] Marcella Orwick-Rydmark et al. “Detergent-Free Incorporation of a Seven-Transmembrane Receptor Protein into Nanosized Bilayer Lipodisq Particles for Functional and Biophysical Studies”. In: *Nano Letters* 12.9 (Sept. 2012), pp. 4687–4692. URL: https://doi.org/10.1021/nl3020395.

[189] Inge Lind et al. “Purification of alpha-toxin from Staphylococcus aureus and application to cell permeabilization”. In: *Analytical Biochemistry* 164.1 (1987), pp. 84–89. URL: https://www.sciencedirect.com/science/article/pii/000326978790371X.

[190] Christian Horn and Claudia Steinem. “Photocurrents generated by bacteriorhodopsin adsorbed on nano-black lipid membranes”. eng. In: *Biophysical journal* 89.2 (Aug. 2005), pp. 1046–1054. URL: https://pubmed.ncbi.nlm.nih.gov/15908580%20https://www.ncbi.nlm.nih.gov/pmc/articles/PMC1366590/.

[191] G Nagel et al. “Voltage Dependence of Proton Pumping by Bacteriorhodopsin Is Regulated by the Voltage-Sensitive Ratio of M1 to M2”. In: *Biophysical Journal* 74.1 (1998), pp. 403–412. URL: https://www.sciencedirect.com/science/article/pii/S0006349598777975.

[192] Javier Vinals Camallonga et al. “Enhanced versatility and spectral tuning of Archaerhodopsin-3 through targeted mutation for biotechnological application”.

[193] Charlotte Hoskin et al. “Parallel Transmission in a Synthetic Nerve”.

[194] Michel Seigneuret and Jean-Louis Rigaud. “Use of the fluorescent pH probe pyranine to detect heterogeneous directions of proton movement in bacteriorhodopsin reconstituted large liposomes”. In: *FEBS Letters* 188.1 (Aug. 1985), pp. 101–106. URL: https://doi.org/10.1016/0014-5793(85)80883-8.

[195] E Bamberg et al. “Photocurrents generated by bacteriorhodopsin on planar bilayer membranes”. In: *Biophysics of structure and mechanism* 5.4 (1979), pp. 277–292. URL: https://doi.org/10.1007/BF02426663.

[196] Vanessa Restrepo Schild. “Light-Activated Synthetic Tissues”. PhD thesis. Oxford: University of Oxford, 2020.

[197] DIETER OESTERHELT and WALTHER STOECKENIUS. “Rhodopsin-like Protein from the Purple Membrane of Halobacterium halobium”. In: *Nature New Biology* 233.39 (1971), pp. 149–152. URL: https://doi.org/10.1038/newbio233149a0.

[198] Srividya Ganapathy et al. “Redshifted and Near-infrared Active Analog Pigments Based upon Archaerhodopsin-3”. In: *Photochemistry and Photobiology* 95.4 (July 2019), pp. 959–968. URL: https://doi.org/10.1111/php.13093.

[199] Mohamady El-Gaby et al. “Archaerhodopsin Selectively and Reversibly Silences Synaptic Transmission through Altered pH”. In: *Cell Reports* 16.8 (Aug. 2016), pp. 2259–2268. URL: https://doi.org/10.1016/j.celrep.2016.07.057.

[200] Xue Han et al. “A High-Light Sensitivity Optical Neural Silencer: Development and Application to Optogenetic Control of Non-Human Primate Cortex”. In: *Frontiers in Systems Neuroscience* 5 (2011), p. 18. URL: https://www.frontiersin.org/article/10.3389/fnsys.2011.00018.

[201] Erica C Saint Clair et al. “Near-IR Resonance Raman Spectroscopy of Archaerhodopsin 3: Effects of Transmembrane Potential”. In: *The Journal of Physical Chemistry B* 116.50 (Dec. 2012), pp. 14592–14601. URL: https://doi.org/10.1021/jp309996a.

[202] Steven J Milder et al. “Effects of detergent environments on the photocycle of purified monomeric bacteriorhodopsin”. In: *Biochemistry* 30.7 (Feb. 1991), pp. 1751–1761. URL: https://doi.org/10.1021/bi00221a004.

[203] Ming Ming et al. “Triton X-100 can alter the temporal sequence of the light-driven proton pump of archaerhodopsin 4”. In: *FEBS Letters* 580.28 (2006), pp. 6749–6753. URL: https://www.sciencedirect.com/science/article/pii/S0014579306013627.

[204] K S Huang, H Bayley, and H G Khorana. “Delipidation of bacteriorhodopsin and reconstitution with exogenous phospholipid”. eng. In: *Proceedings of the National Academy of Sciences of the United States of America* 77.1 (1980), pp. 323–327. URL: http://europepmc.org/abstract/MED/6928624%20https://doi.org/10.1073/pnas.77.1.323%20https://europepmc.org/articles/PMC348262%20https://europepmc.org/articles/PMC348262?pdf=render.

[205] Ramya Tunuguntla et al. “Lipid bilayer composition can influence the orientation of proteorhodopsin in artificial membranes”. eng. In: *Biophysical journal* 105.6 (Sept. 2013), pp. 1388–1396. URL: https://pubmed.ncbi.nlm.nih.gov/24047990%20https://www.ncbi.nlm.nih.gov/pmc/articles/PMC3785883/.

[206] Christian Renner, Brigitte Kessler, and Dieter Oesterhelt. “Lipid composition of integral purple membrane by ¹H and ³¹P NMR”. In: *Journal of Lipid Research* 46.8 (Aug. 2005), pp. 1755–1764. URL: https://doi.org/10.1194/jlr.M500138-JLR200.

[207] P Poulin and J Bibette. “Adhesion of Water Droplets in Organic Solvent”. In: *Langmuir* 14.22 (Oct. 1998), pp. 6341–6343. URL: https://doi.org/10.1021/la9801413.

[208] Robert Strutt et al. “Activating mechanosensitive channels embedded in droplet interface bilayers using membrane asymmetry”. In: *Chemical Science* 12.6 (2021), pp. 2138–2145. URL: http://dx.doi.org/10.1039/D0SC03889J.

[209] Martin K M Engqvist et al. “Directed Evolution of Gloeobacter violaceus Rhodopsin Spectral Properties”. In: *Journal of Molecular Biology* 427.1 (2015), pp. 205–220. URL: https://www.sciencedirect.com/science/article/pii/S0022283614003088.

[210] Nicholas C Flytzanis et al. “Archaerhodopsin variants with enhanced voltage-sensitive fluorescence in mammalian and Caenorhabditis elegans neurons”. In: *Nature Communications* 5.1 (2014), p. 4894. URL: https://doi.org/10.1038/ncomms5894.

[211] Hideaki E Kato et al. “Atomistic design of microbial opsin-based blue-shifted optogenetics tools”. In: *Nature Communications* 6.1 (2015), p. 7177. URL: https://doi.org/10.1038/ncomms8177.

[212] Federico Melaccio, Nicolas Ferré, and Massimo Olivucci. “Quantum chemical modeling of rhodopsin mutants displaying switchable colors”. In: *Physical Chemistry Chemical Physics* 14.36 (2012), pp. 12485–12495. URL: http://dx.doi.org/10.1039/C2CP40940B.

[213] Hirohiko Houjou, Yoshio Inoue, and Minoru Sakurai. “Study of the Opsin Shift of Bacteriorhodopsin: Insight from QM/MM Calculations with Electronic Polarization Effects of the Protein Environment”. In: *The Journal of Physical Chemistry B* 105.4 (Feb. 2001), pp. 867–879. URL: https://doi.org/10.1021/jp0032863.

[214] R Govindjee, S P Balashov, and T G Ebrey. “Quantum efficiency of the photochemical cycle of bacteriorhodopsin”. eng. In: *Biophysical journal* 58.3 (Sept. 1990), pp. 597–608. URL: https://pubmed.ncbi.nlm.nih.gov/19431766%20https://www.ncbi.nlm.nih.gov/pmc/articles/PMC1281001/.

[215] Zoe Schofield et al. “Bioelectrical understanding and engineering of cell biology”. In: *Journal of The Royal Society Interface* 17.166 (May 2020), p. 20200013. URL: https://doi.org/10.1098/rsif.2020.0013.

[216] Michael Levin. “Molecular bioelectricity: how endogenous voltage potentials control cell behavior and instruct pattern regulation in vivo”. eng. In: *Molecular biology of the cell* 25.24 (Dec. 2014), pp. 3835–3850. URL: https://pubmed.ncbi.nlm.nih.gov/25425556%20https://www.ncbi.nlm.nih.gov/pmc/articles/PMC4244194/.

[217] Michael Levin, John Selberg, and Marco Rolandi. “Endogenous Bioelectrics in Development, Cancer, and Regeneration: Drugs and Bioelectronic Devices as Electroceuticals for Regenerative Medicine”. In: *iScience* 22 (2019), pp. 519–533. URL: https://www.sciencedirect.com/science/article/pii/S2589004219304730.

[218] Sheena E B Tyler. “Nature’s Electric Potential: A Systematic Review of the Role of Bioelectricity in Wound Healing and Regenerative Processes in Animals, Humans, and Plants”. eng. In: *Frontiers in physiology* 8 (Sept. 2017), p. 627. URL: https://pubmed.ncbi.nlm.nih.gov/28928669%20https://www.ncbi.nlm.nih.gov/pmc/articles/PMC5591378/.

[219] Arthur Prindle et al. “Ion channels enable electrical communication in bacterial communities”. In: *Nature* 527.7576 (2015), pp. 59–63. URL: https://doi.org/10.1038/nature15709.

[220] A L HODGKIN and A F HUXLEY. “A quantitative description of membrane current and its application to conduction and excitation in nerve”. eng. In: *The Journal of physiology* 117.4 (Aug. 1952), pp. 500–544. URL: https://pubmed.ncbi.nlm.nih.gov/12991237%20https://www.ncbi.nlm.nih.gov/pmc/articles/PMC1392413/.

[221] Aloysio Luigi Galvani. “The Effects of Artificial Electricity on Muscular Motion”. In: *Clinical Orthopaedics and Related Research®* 88 (1972). URL: https://journals.lww.com/clinorthop/Fulltext/1972/10000/The_Effects_of_Artificial_Electricity_on_Muscular.1.aspx.

[222] Kristoffer Famm et al. “A jump-start for electroceuticals”. In: *Nature* 496.7444 (2013), pp. 159–161. URL: https://doi.org/10.1038/496159a.

[223] Shiksha Mantri et al. “An engineered dimeric protein pore that spans adjacent lipid bilayers”. In: *Nature Communications* 4.1 (2013), p. 1725. URL: https://doi.org/10.1038/ncomms2726.

[224] Yuval Elani, Robert V Law, and Oscar Ces. "Vesicle-based artificial cells as chemical microreactors with spatially segregated reaction pathways". In: *Nature Communications* 5.1 (2014), p. 5305. URL: https://doi.org/10.1038/ncomms6305.

[225] Thomas B H Schroeder et al. "An electric-eel-inspired soft power source from stacked hydrogels". In: *Nature* 552.7684 (2017), pp. 214–218. URL: https://doi.org/10.1038/nature24670.

[226] Tarryn E Miller et al. "Light-powered CO₂ fixation in a chloroplast mimic with natural and synthetic parts". In: *Science* 368.6491 (May 2020), p. 649. URL: http://science.sciencemag.org/content/368/6491/649.abstract.

[227] B V V S Pavan Kumar et al. "Chloroplast-containing coacervate micro-droplets as a step towards photosynthetically active membrane-free protocells". In: *Chemical Communications* 54.29 (2018), pp. 3594–3597. URL: http://dx.doi.org/10.1039/C8CC01129J.

[228] Royal Society. *iHuman perspective: Blurring the lines between mind and machine. ISBN: 978-1-78252-420-5.* Sept. 2019. URL: https://royalsociety.org/topics-policy/projects/ihuman-perspective/?utm_source=ihuman-perspective&utm_medium=print&utm_campaign=report.

[229] Tessa Gordon. "Electrical Stimulation to Enhance Axon Regeneration After Peripheral Nerve Injuries in Animal Models and Humans". In: *Neurotherapeutics* 13.2 (2016), pp. 295–310. URL: https://doi.org/10.1007/s13311-015-0415-1.

[230] Grand View Research. *Bioelectric Medicine Market Size, Share & Trends Analysis Report By Product (Implantable Cardioverter Defibrillators, Cardiac Pacemakers, Cochlear Implants), By Type, By Application, By End-Use, And Segment Forecasts, 2019 - 2026. Report ID: GVR-1-68038-899-2.* Sept. 2019. URL: https://www.grandviewresearch.com/industry-analysis/electroceuticals-bioelectric-medicine-market.

[231] W M M Schuepbach et al. "Neurostimulation for Parkinson's Disease with Early Motor Complications". In: *New England Journal of Medicine* 368.7 (Feb. 2013), pp. 610–622. URL: https://doi.org/10.1056/NEJMoa1205158.

[232] Andres M Lozano et al. "Deep brain stimulation: current challenges and future directions". In: *Nature Reviews Neurology* 15.3 (2019), pp. 148–160. URL: https://doi.org/10.1038/s41582-018-0128-2.

[233] Helen S Mayberg et al. "Deep Brain Stimulation for Treatment-Resistant Depression". In: *Neuron* 45.5 (2005), pp. 651–660. URL: https://www.sciencedirect.com/science/article/pii/S089662730500156X.

[234] Nir Lipsman et al. "Subcallosal cingulate deep brain stimulation for treatment-refractory anorexia nervosa: a phase 1 pilot trial". In: *The Lancet* 381.9875 (2013), pp. 1361–1370. URL: https://www.sciencedirect.com/science/article/pii/S0140673612621886.

[235] Stéphanie P Lacour, Grégoire Courtine, and Jochen Guck. "Materials and technologies for soft implantable neuroprostheses". In: *Nature Reviews Materials* 1.10 (2016), p. 16063. URL: https://doi.org/10.1038/natrevmats.2016.63.

[236] Enming Song et al. “Materials for flexible bioelectronic systems as chronic neural interfaces”. In: *Nature Materials* 19.6 (2020), pp. 590–603. URL: https://doi.org/10.1038/s41563-020-0679-7.

[237] Héctor Acarón Ledesma et al. “An atlas of nano-enabled neural interfaces”. In: *Nature Nanotechnology* 14.7 (2019), pp. 645–657. URL: https://doi.org/10.1038/s41565-019-0487-x.

[238] Xiao Yang et al. “Bioinspired neuron-like electronics”. In: *Nature Materials* 18.5 (2019), pp. 510–517. URL: https://doi.org/10.1038/s41563-019-0292-9.

[239] Jonathan Viventi et al. “Flexible, foldable, actively multiplexed, high-density electrode array for mapping brain activity in vivo”. In: *Nature Neuroscience* 14.12 (2011), pp. 1599–1605. URL: https://doi.org/10.1038/nn.2973.

[240] Nipun Misra et al. “Bioelectronic silicon nanowire devices using functional membrane proteins”. In: *Proceedings of the National Academy of Sciences* 106.33 (Aug. 2009), p. 13780. URL: http://www.pnas.org/content/106/33/13780.abstract.

[241] Suji Choi et al. “Highly conductive, stretchable and biocompatible Ag–Au core–sheath nanowire composite for wearable and implantable bioelectronics”. In: *Nature Nanotechnology* 13.11 (2018), pp. 1048–1056. URL: https://doi.org/10.1038/s41565-018-0226-8.

[242] Dae-Hyeong Kim et al. “Epidermal Electronics”. In: *Science* 333.6044 (Aug. 2011), p. 838. URL: http://science.sciencemag.org/content/333/6044/838.abstract.

[243] Suk-Won Hwang et al. “A Physically Transient Form of Silicon Electronics”. In: *Science* 337.6102 (Sept. 2012), p. 1640. URL: http://science.sciencemag.org/content/337/6102/1640.abstract.

[244] Jonathan Rivnay, Róisín M Owens, and George G Malliaras. “The Rise of Organic Bioelectronics”. In: *Chemistry of Materials* 26.1 (Jan. 2014), pp. 679–685. URL: https://doi.org/10.1021/cm4022003.

[245] Stefan C B Mannsfeld et al. “Highly sensitive flexible pressure sensors with microstructured rubber dielectric layers”. In: *Nature Materials* 9.10 (2010), pp. 859–864. URL: https://doi.org/10.1038/nmat2834.

[246] Martin Kaltenbrunner et al. “An ultra-lightweight design for imperceptible plastic electronics”. In: *Nature* 499.7459 (2013), pp. 458–463. URL: https://doi.org/10.1038/nature12314.

[247] Hyunwoo Yuk et al. “Skin-inspired hydrogel–elastomer hybrids with robust interfaces and functional microstructures”. In: *Nature Communications* 7.1 (2016), p. 12028. URL: https://doi.org/10.1038/ncomms12028.

[248] Yeongin Kim et al. “A bioinspired flexible organic artificial afferent nerve”. In: *Science* 360.6392 (June 2018), p. 998. URL: http://science.sciencemag.org/content/360/6392/998.abstract.

[249] Jordi March i Nogué. *Lateral X-ray of the head: Deep brain stimulation in obsessive–compulsive disorder (Medtronic 3391). Men 42 years old, surgery in 2013.* Jan. 2021. URL: https://commons.wikimedia.org/wiki/File:X-ray_of_deep_brain_stimulation_in_OCD,_L.png#filelinks.

[250] Yuxin Liu et al. “Soft and elastic hydrogel-based microelectronics for localized low-voltage neuromodulation”. In: *Nature Biomedical Engineering* 3.1 (2019), pp. 58–68. URL: https://doi.org/10.1038/s41551-018-0335-6.

[251] Christoph Keplinger et al. “Stretchable, Transparent, Ionic Conductors”. In: *Science* 341.6149 (Aug. 2013), p. 984. URL: http://science.sciencemag.org/content/341/6149/984.abstract.

[252] Hyunwoo Yuk, Baoyang Lu, and Xuanhe Zhao. “Hydrogel bioelectronics”. In: *Chemical Society Reviews* 48.6 (2019), pp. 1642–1667. URL: http://dx.doi.org/10.1039/C8CS00595H.

[253] Jeong-Yun Sun et al. “Ionic skin”. In: *Advanced Materials* 26.45 (Dec. 2014), pp. 7608–7614. URL: https://doi.org/10.1002/adma.201403441.

[254] Siwei Zhao et al. “Programmable Hydrogel Ionic Circuits for Biologically Matched Electronic Interfaces”. In: *Advanced Materials* 30.25 (June 2018), p. 1800598. URL: https://doi.org/10.1002/adma.201800598.

[255] Jianyu Li and David J Mooney. “Designing hydrogels for controlled drug delivery”. eng. In: *Nature reviews. Materials* 1.12 (Dec. 2016), p. 16071. URL: https://pubmed.ncbi.nlm.nih.gov/29657852%20https://www.ncbi.nlm.nih.gov/pmc/articles/PMC5898614/.

[256] Naomi A Staples et al. “Conductive Hydrogel Electrodes for Delivery of Long-Term High Frequency Pulses”. eng. In: *Frontiers in neuroscience* 11 (Jan. 2018), p. 748. URL: https://pubmed.ncbi.nlm.nih.gov/29375292%20https://www.ncbi.nlm.nih.gov/pmc/articles/PMC5768631/.

[257] Sang Min Won et al. “Wireless and battery-free technologies for neuroengineering”. In: *Nature Biomedical Engineering* (2021). URL: https://doi.org/10.1038/s41551-021-00683-3.

[258] Benjamin I Rapoport, Jakub T Kedzierski, and Rahul Sarpeshkar. “A Glucose Fuel Cell for Implantable Brain–Machine Interfaces”. In: *PLOS ONE* 7.6 (June 2012), e38436–. URL: https://doi.org/10.1371/journal.pone.0038436.

[259] Dongjin Seo et al. “Wireless Recording in the Peripheral Nervous System with Ultrasonic Neural Dust”. In: *Neuron* 91.3 (Aug. 2016), pp. 529–539. URL: https://doi.org/10.1016/j.neuron.2016.06.034.

[260] David K Piech et al. “A wireless millimetre-scale implantable neural stimulator with ultrasonically powered bidirectional communication”. In: *Nature Biomedical Engineering* 4.2 (2020), pp. 207–222. URL: https://doi.org/10.1038/s41551-020-0518-9.

[261] Aaron D Mickle et al. “A wireless closed-loop system for optogenetic peripheral neuromodulation”. In: *Nature* 565.7739 (2019), pp. 361–365. URL: https://doi.org/10.1038/s41586-018-0823-6.

[262] Han Ouyang et al. “Symbiotic cardiac pacemaker”. In: *Nature Communications* 10.1 (2019), p. 1821. URL: https://doi.org/10.1038/s41467-019-09851-1.

[263] Ron Feiner and Tal Dvir. “Tissue-electronics interfaces: From implantable devices to engineered tissues”. In: *Nature Reviews Materials* 3 (Mar. 2017), p. 17076.

[264] A Sydney Gladman et al. “Biomimetic 4D printing”. In: *Nature Materials* 15.4 (2016), pp. 413–418. URL: https://doi.org/10.1038/nmat4544.

[265] Canhui Yang and Zhigang Suo. "Hydrogel ionotronics". In: *Nature Reviews Materials* 3.6 (2018), pp. 125–142. URL: https://doi.org/10.1038/s41578-018-0018-7.

[266] Tae Soup Shim et al. "Controlled Origami Folding of Hydrogel Bilayers with Sustained Reversibility for Robust Microcarriers". In: *Angewandte Chemie International Edition* 51.6 (Feb. 2012), pp. 1420–1423. URL: https://doi.org/10.1002/anie.201106723.

[267] Georgi Stoychev, Nikolay Puretskiy, and Leonid Ionov. "Self-folding all-polymer thermoresponsive microcapsules". In: *Soft Matter* 7.7 (2011), pp. 3277–3279. URL: http://dx.doi.org/10.1039/C1SM05109A.

[268] Joyce C Breger et al. "Self-Folding Thermo-Magnetically Responsive Soft Microgrippers". In: *ACS Applied Materials & Interfaces* 7.5 (Feb. 2015), pp. 3398–3405. URL: https://doi.org/10.1021/am508621s.

[269] Michael Wehner et al. "An integrated design and fabrication strategy for entirely soft, autonomous robots". In: *Nature* 536.7617 (2016), pp. 451–455. URL: https://doi.org/10.1038/nature19100.

[270] Sung-Jin Park et al. "Phototactic guidance of a tissue-engineered soft-robotic ray". In: *Science* 353.6295 (July 2016), p. 158. URL: http://science.sciencemag.org/content/353/6295/158.abstract.

[271] Hen-Wei Huang et al. "Soft micromachines with programmable motility and morphology". In: *Nature Communications* 7.1 (2016), p. 12263. URL: https://doi.org/10.1038/ncomms12263.

[272] Chengzhi Hu, Salvador Pané, and Bradley J Nelson. "Soft Micro- and Nanorobotics". In: *Annual Review of Control, Robotics, and Autonomous Systems* 1.1 (May 2018), pp. 53–75. URL: https://doi.org/10.1146/annurev-control-060117-104947.

[273] Lewis Grozinger et al. "Pathways to cellular supremacy in biocomputing". In: *Nature Communications* 10.1 (2019), p. 5250. URL: https://doi.org/10.1038/s41467-019-13232-z.

[274] L M Adleman. "Molecular computation of solutions to combinatorial problems". In: *Science* 266.5187 (Nov. 1994), p. 1021. URL: http://science.sciencemag.org/content/266/5187/1021.abstract.

[275] Yaniv Erlich and Dina Zielinski. "DNA Fountain enables a robust and efficient storage architecture". In: *Science* 355.6328 (Mar. 2017), p. 950. URL: http://science.sciencemag.org/content/355/6328/950.abstract.

[276] George M Church, Yuan Gao, and Sriram Kosuri. "Next-Generation Digital Information Storage in DNA". In: *Science* 337.6102 (Sept. 2012), p. 1628. URL: http://science.sciencemag.org/content/337/6102/1628.abstract.

[277] Seth L Shipman et al. "CRISPR–Cas encoding of a digital movie into the genomes of a population of living bacteria". In: *Nature* 547.7663 (2017), pp. 345–349. URL: https://doi.org/10.1038/nature23017.

[278] Yaakov Benenson. “Biocomputers: from test tubes to live cells”. eng. In: *Molecular bioSystems* 5.7 (July 2009), pp. 675–685. URL: https://pubmed.ncbi.nlm.nih.gov/19562106%20https://www.ncbi.nlm.nih.gov/pmc/articles/PMC2714485/.

[279] Alexander A. Green et al. “Toehold Switches: De-Novo-Designed Regulators of Gene Expression”. In: *Cell* 159.4 (Nov. 2014), pp. 925–939. URL: https://doi.org/10.1016/j.cell.2014.10.002.

[280] Simon Ausländer et al. “Programmable single-cell mammalian biocomputers”. In: *Nature* 487.7405 (2012), pp. 123–127. URL: https://doi.org/10.1038/nature11149.

[281] Lulu Qian and Erik Winfree. “Scaling Up Digital Circuit Computation with DNA Strand Displacement Cascades”. In: *Science* 332.6034 (June 2011), p. 1196. URL: http://science.sciencemag.org/content/332/6034/1196.abstract.

[282] Georg Seelig et al. “Enzyme-Free Nucleic Acid Logic Circuits”. In: *Science* 314.5805 (Dec. 2006), p. 1585. URL: http://science.sciencemag.org/content/314/5805/1585.abstract.

[283] Hubert Hug and Rainer Schuler. “Strategies for the development of a peptide computer”. In: *Bioinformatics* 17.4 (Apr. 2001), pp. 364–368. URL: https://doi.org/10.1093/bioinformatics/17.4.364.

[284] John E Dueber et al. “Reprogramming Control of an Allosteric Signaling Switch Through Modular Recombination”. In: *Science* 301.5641 (Sept. 2003), p. 1904. URL: http://science.sciencemag.org/content/301/5641/1904.abstract.

[285] Alec A K Nielsen et al. “Genetic circuit design automation”. In: *Science* 352.6281 (Apr. 2016), aac7341. URL: http://science.sciencemag.org/content/352/6281/aac7341.abstract.

[286] Abigail J. Smith et al. “Guiding Biomolecular Interactions in Cells Using de Novo Protein–Protein Interfaces”. In: *ACS Synthetic Biology* 8.6 (June 2019), pp. 1284–1293. URL: https://doi.org/10.1021/acssynbio.8b00501.

[287] James Hemphill and Alexander Deiters. “DNA Computation in Mammalian Cells: MicroRNA Logic Operations”. In: *Journal of the American Chemical Society* 135.28 (July 2013), pp. 10512–10518. URL: https://doi.org/10.1021/ja404350s.

[288] Yaniv Amir et al. “Universal computing by DNA origami robots in a living animal”. In: *Nature Nanotechnology* 9.5 (2014), pp. 353–357. URL: https://doi.org/10.1038/nnano.2014.58.

[289] Zibo Chen et al. “De novo design of protein logic gates”. In: *Science* 368.6486 (Apr. 2020), p. 78. URL: http://science.sciencemag.org/content/368/6486/78.abstract.

[290] Zhen Xie et al. “Multi-Input RNAi-Based Logic Circuit for Identification of Specific Cancer Cells”. In: *Science* 333.6047 (Sept. 2011), p. 1307. URL: http://science.sciencemag.org/content/333/6047/1307.abstract.

[291] Juan Manuel Parrilla-Gutierrez et al. “A programmable chemical computer with memory and pattern recognition”. In: *Nature Communications* 11.1 (2020), p. 1442. URL: https://doi.org/10.1038/s41467-020-15190-3.

[292] Konrad Gizynski and Jerzy Gorecki. “Chemical memory with states coded in light controlled oscillations of interacting Belousov–Zhabotinsky droplets”. In: *Physical Chemistry Chemical Physics* 19.9 (2017), pp. 6519–6531. URL: http://dx.doi.org/10.1039/C6CP07492H.

[293] L Kuhnert, K I Agladze, and V I Krinsky. “Image processing using light-sensitive chemical waves”. In: *Nature* 337.6204 (1989), pp. 244–247. URL: https://doi.org/10.1038/337244a0.

[294] Gerd Gruenert et al. “Understanding Networks of Computing Chemical Droplet Neurons Based on Information Flow”. In: *International Journal of Neural Systems* 25.07 (Oct. 2014), p. 1450032. URL: https://doi.org/10.1142/S0129065714500324.

[295] Georgios Katsikis, James S Cybulski, and Manu Prakash. “Synchronous universal droplet logic and control”. In: *Nature Physics* 11.7 (2015), pp. 588–596. URL: https://doi.org/10.1038/nphys3341.

[296] Keiichi Inoue et al. “A natural light-driven inward proton pump”. In: *Nature Communications* 7.1 (2016), p. 13415. URL: https://doi.org/10.1038/ncomms13415.

[297] Bruce P Bean. “The action potential in mammalian central neurons”. In: *Nature Reviews Neuroscience* 8.6 (2007), pp. 451–465. URL: https://doi.org/10.1038/nrn2148.

[298] Myron Yanoff and Joseph W Sassani. “13 - Optic Nerve”. In: *Ocular Pathology (Eighth Edition)*. Ed. by Myron Yanoff and Joseph W Sassani. London: Elsevier, 2020, pp. 494–518. URL: https://www.sciencedirect.com/science/article/pii/B9780323547550000139.

[299] Philip Serwer. “Agarose gels: Properties and use for electrophoresis”. In: *ELECTROPHORESIS* 4.6 (Feb. 1983), pp. 375–382. URL: https://doi.org/10.1002/elps.1150040602.

[300] Alberto E Pereda. “Electrical synapses and their functional interactions with chemical synapses”. In: *Nature Reviews Neuroscience* 15.4 (2014), pp. 250–263. URL: https://doi.org/10.1038/nrn3708.

[301] Jianyang Du, Zubayer Hossain Saad, and Juthika Mandal. “Protons: A neurotransmitter in the brain”. In: *Edorium J Cell Biol* 3 (Mar. 2017), pp. 1–3.

[302] Geoffrey Burnstock. “Historical review: ATP as a neurotransmitter”. In: *Trends in Pharmacological Sciences* 27.3 (Mar. 2006), pp. 166–176. URL: https://doi.org/10.1016/j.tips.2006.01.005.

[303] Ron Milo and Rob Phillips. *Cell Biology by the Numbers*. 1st. Garland Science, Dec. 2015.

[304] Enrique Soto, Audrey Ortega-Ramírez, and Rosario Vega. “Protons as Messengers of Intercellular Communication in the Nervous System”. eng. In: *Frontiers in cellular neuroscience* 12 (Oct. 2018), p. 342. URL: https://pubmed.ncbi.nlm.nih.gov/30364044%20https://www.ncbi.nlm.nih.gov/pmc/articles/PMC6191491/.

[305] Asim A Beg et al. “Protons Act as a Transmitter for Muscle Contraction in C. elegans”. In: *Cell* 132.1 (2008), pp. 149–160. URL: https://www.sciencedirect.com/science/article/pii/S0092867407014791.

[306] Sónia Guerra-Gomes et al. “Functional Roles of Astrocyte Calcium Elevations: From Synapses to Behavior”. In: *Frontiers in Cellular Neuroscience* 11 (2018), p. 427. URL: https://www.frontiersin.org/article/10.3389/fncel.2017.00427.

[307] Juan Liu et al. *Hydrogels for engineering of perfusable vascular networks*. July 2015.

[308] Linna Zhou et al. “Lipid-Bilayer-Supported 3D Printing of Human Cerebral Cortex Cells Reveals Developmental Interactions”. In: *Advanced Materials* 32.31 (Aug. 2020), p. 2002183. URL: https://doi.org/10.1002/adma.202002183.

[309] Ravinash Krishna Kumar et al. “Droplet printing reveals the importance of micron-scale structure for bacterial ecology”. In: *Nature Communications* 12.1 (2021), p. 857. URL: https://doi.org/10.1038/s41467-021-20996-w.

[310] Hiroki Yasuga et al. “Logic Gate Operation by DNA Translocation through Biological Nanopores”. In: *PLOS ONE* 11.2 (Feb. 2016), e0149667–. URL: https://doi.org/10.1371/journal.pone.0149667.

[311] Chi Long Chan et al. “DROPLAY: laser writing of functional patterns within biological microdroplet displays”. In: *Lab on a Chip* 16.23 (2016), pp. 4621–4627. URL: http://dx.doi.org/10.1039/C6LC01219A.

[312] Stéphanie P Lacour, Grégoire Courtine, and Jochen Guck. “Materials and technologies for soft implantable neuroprostheses”. In: *Nature Reviews Materials* 1.10 (2016), p. 16063. URL: https://doi.org/10.1038/natrevmats.2016.63.

[313] Michael E Todhunter et al. “Programmed synthesis of three-dimensional tissues”. In: *Nature Methods* 12.10 (2015), pp. 975–981. URL: https://doi.org/10.1038/nmeth.3553.

[314] Satoshi Toda et al. “Programming self-organizing multicellular structures with synthetic cell-cell signaling”. In: *Science* 361.6398 (July 2018), p. 156. URL: http://science.sciencemag.org/content/361/6398/156.abstract.

[315] Nitzan Krinsky et al. “Synthetic Cells Synthesize Therapeutic Proteins inside Tumors”. eng. In: *Advanced healthcare materials* 7.9 (May 2018), e1701163–e1701163. URL: https://pubmed.ncbi.nlm.nih.gov/29283226%20https://www.ncbi.nlm.nih.gov/pmc/articles/PMC6684359/.

[316] Alexander V Gourine et al. “Astrocytes Control Breathing Through pH-Dependent Release of ATP”. In: *Science* 329.5991 (July 2010), p. 571. URL: http://science.sciencemag.org/content/329/5991/571.abstract.

[317] Robert R Ishmukhametov, Aidan N Russell, and Richard M Berry. “A modular platform for one-step assembly of multi-component membrane systems by fusion of charged proteoliposomes”. In: *Nature Communications* 7.1 (2016), p. 13025. URL: https://doi.org/10.1038/ncomms13025.

[318] Dominique Boeuf et al. “MicRhoDE: a curated database for the analysis of microbial rhodopsin diversity and evolution”. In: *Database* 2015 (Jan. 2015). URL: https://doi.org/10.1093/database/bav080.

[319] Xiaoyang Long et al. “Magnetogenetics: remote non-invasive magnetic activation of neuronal activity with a magnetoreceptor”. In: *Science Bulletin* 60.24 (2015), pp. 2107–2119. URL: https://www.sciencedirect.com/science/article/pii/S2095927316302407.

[320] Koki Kamiya et al. “Electrophysiological measurement of ion channels on plasma/organelle membranes using an on-chip lipid bilayer system”. In: *Scientific Reports* 8.1 (2018), p. 17498. URL: https://doi.org/10.1038/s41598-018-35316-4.

[321] Clementine M Boutry et al. “Biodegradable and flexible arterial-pulse sensor for the wireless monitoring of blood flow”. In: *Nature Biomedical Engineering* 3.1 (2019), pp. 47–57. URL: https://doi.org/10.1038/s41551-018-0336-5.

[322] Khanh T M Tran and Thanh D Nguyen. “Lithography-based methods to manufacture biomaterials at small scales”. In: *Journal of Science: Advanced Materials and Devices* 2.1 (2017), pp. 1–14. URL: https://www.sciencedirect.com/science/article/pii/S2468217916301927.

[323] Sophie Aimon et al. “Functional Reconstitution of a Voltage-Gated Potassium Channel in Giant Unilamellar Vesicles”. In: *PLOS ONE* 6.10 (Oct. 2011), e25529–. URL: https://doi.org/10.1371/journal.pone.0025529.

[324] A Studer et al. “Integration and recording of a reconstituted voltage-gated sodium channel in planar lipid bilayers”. In: *Biosensors and Bioelectronics* 26.5 (2011), pp. 1924–1928. URL: https://www.sciencedirect.com/science/article/pii/S095656631000309X.

[325] Emeline Rideau, Frederik R Wurm, and Katharina Landfester. “Giant polymersomes from non-assisted film hydration of phosphate-based block copolymers”. In: *Polymer Chemistry* 9.44 (2018), pp. 5385–5394. URL: http://dx.doi.org/10.1039/C8PY00992A.

[326] Dae-Woong Jeong et al. “Enhanced stability of freestanding lipid bilayer and its stability criteria”. In: *Scientific Reports* 6.1 (2016), p. 38158. URL: https://doi.org/10.1038/srep38158.

[327] Hagyoul Bae et al. “Physically Transient Memory on a Rapidly Dissoluble Paper for Security Application”. In: *Scientific Reports* 6.1 (2016), p. 38324. URL: https://doi.org/10.1038/srep38324.

[328] Kun Fu et al. “Transient Rechargeable Batteries Triggered by Cascade Reactions”. In: *Nano Letters* 15.7 (July 2015), pp. 4664–4671. URL: https://doi.org/10.1021/acs.nanolett.5b01451.

[329] Langzhou Song et al. “Structure of Staphylococcal α-Hemolysin, a Heptameric Transmembrane Pore”. In: *Science* 274.5294 (Dec. 1996), p. 1859. URL: http://science.sciencemag.org/content/274/5294/1859.abstract.

[330] Lukas Herwig et al. “Directed Evolution of a Bright Near-Infrared Fluorescent Rhodopsin Using a Synthetic Chromophore”. eng. In: *Cell chemical biology* 24.3 (Mar. 2017), pp. 415–425. URL: https://pubmed.ncbi.nlm.nih.gov/28262559%20https://www.ncbi.nlm.nih.gov/pmc/articles/PMC5357175/.

[331] Stephan Preibisch, Stephan Saalfeld, and Pavel Tomancak. “Globally optimal stitching of tiled 3D microscopic image acquisitions”. eng. In: *Bioinformatics (Oxford, England)* 25.11 (2009), pp. 1463–1465. URL: http://europepmc.org/abstract/MED/19346324%20http://bioinformatics.oxfordjournals.org/cgi/content/abstract/25/11/1463%20http://bioinformatics.oxfordjournals.org/cgi/content/full/25/11/1463%20http://bioinformatics.oxfordjournals.org/cgi/reprint/25/11/1463%20https://www.ncbi.nlm.nih.gov/pmc/articles/pmid/19346324/?tool=EBI%20https://www.ncbi.nlm.nih.gov/pmc/articles/pmid/19346324/pdf/?tool=EBI%20https://doi.org/10.1093/bioinformatics/btp184%20https://europepmc.org/articles/PMC2682522%20https://europepmc.org/articles/PMC2682522?pdf=render.